THE UNIVERSITY
of EDINBURGH

Hydrological controls on Greenland Ice Sheet motion

Andrew J. Tedstone

Thesis submitted in fulfilment of the requirements for the degree of

Doctor of Philosophy

to the

University of Edinburgh

2015

Declaration

The work presented in this thesis is original and my own, unless indicated otherwise. No part of the thesis has been submitted for any other award or professional qualification.

The candidate confirms that the work submitted is his/her own, except where work which has formed part of jointly-authored publications has been included. The contribution of the candidate and the other authors to this work has been explicitly indicated below. The candidate confirms that appropriate credit has been given within the thesis where reference has been made to the work of others.

Chapter 4

Citation: Tedstone, A. J., P. W. Nienow, A. J. Sole, D. W. F. Mair, T. R. Cowton, I. D. Bartholomew and M. A. King (2013), Greenland Ice Sheet motion insensitive to exceptional melt water forcing, *Proc. Nat. Acad. Sci. USA*, **110**(9), 19719-19724. DOI: 10.1073/pnas.1315843110

Author contributions: P.W.N. and D.W.F.M. designed research; A.J.T., P.W.N., A.J.S., D.W.F.M., T.R.C., and I.D.B. performed research; A.J.T., A.J.S., I.D.B., and M.A.K. contributed new analytic tools; A.J.T., A.J.S., T.R.C., I.D.B., and M.A.K. analyzed data; and A.J.T. wrote the paper with assistance from P.W.N.

Chapter 5

Citation: Tedstone, A. J., P. W. Nienow, N. Gourmelen and A. J. Sole (2014), Greenland Ice Sheet annual motion insensitive to spatial variations in subglacial hydraulic structure, *Geophys. Res. Lett.*, **41**(24), 8910-8917. DOI: 10.1002/2014GL062386.

Author contributions: A.J.T. and P.W.N. designed research; A.J.T., P.W.N. and A.J.S. collected field observations; N.G. processed the radar data; A.J.T., N.G. and A.J.S contributed new analytic tools; A.J.T. analysed the data; and A.J.T. wrote the paper with assistance from P.W.N.

Chapter 6

Citation: Tedstone, A. J., P. W. Nienow, N. Gourmelen, A. Dehecq, D. Goldberg and E. Hanna, Decadal slowdown of a land-terminating sector of the Greenland Ice Sheet despite warming. *Nature*, in press, September 2015.

Author contributions: A.J.T., P.W.N. and N.G. designed this study. A.D., N.G. and A.J.T. developed the processing chain used for feature tracking of Landsat imagery. A.J.T., A.D. and N.G. processed the Landsat imagery. A.J.T. and D.G. calculated the impact of changing ice geometry upon ice motion. E.H. processed the melt data. A.J.T., N.G. and P.W.N. analyzed the results. A.J.T., P.W.N. and N.G. wrote the manuscript. All authors discussed the results and edited the manuscript. A.J.T. was the lead author of this work.

Andrew Tedstone

September 2015

Abstract

An improved understanding of the processes controlling the dynamics of the Greenland Ice Sheet is needed to enable more accurate determination of the response of the ice sheet to projected climate change. Meltwater produced on the ice sheet surface can penetrate to the bed and cause ice motion to speed up through enhanced basal sliding. However, the importance of coupled hydro-dynamics both to current ice sheet motion and future stability over the coming century is unclear.

This thesis presents observations from the south-west Greenland Ice Sheet which improve our understanding of coupled hydro-dynamics. It commences with an investigation of the response of ice motion to exceptional meltwater forcing during summer 2012. Simultaneous field observations of ice motion (by GPS) and proglacial discharge show that, despite two extreme melt events during July 2012 and summer ice sheet runoff 3.9 s.d. above the 1958–2011 mean which resulted in faster summer motion, net annual motion was slower than in the average melt year of 2009. This suggests that surface melt-induced acceleration of land-terminating regions of the ice sheet will remain insignificant even under extreme melting scenarios.

The thesis then examines spatial variability in ice motion, in relation to an inferred subglacial drainage axis, using GPS and satellite radar observations from a land-terminating margin up to 20 km inland where ice is 800 m thick. Whilst spatial variability in subglacial drainage

system configuration is found to control ice motion at short timescales, the proportional contribution of summer motion to annual motion is almost invariant. The structure of the subglacial drainage system does not therefore appear to significantly influence spatial variations in net summer speedup.

Lastly, observations are made by applying feature tracking to 30 years of optical satellite imagery in a ~170 by 50 km area along the ice sheet margin (where ice reaches ~850 m thick) to examine whether coupled hydrology-dynamics affects inter-annual ice motion. Hydro-dynamic coupling resulted in net ice motion slowdown during a period of clear climate warming. Further increases in meltwater production may therefore reduce ice sheet motion.

The thesis concludes that at land-terminating margins of the Greenland Ice Sheet, (1) larger annual meltwater volumes do not result in faster annual ice motion; (2) the detailed structure of the subglacial drainage network appears unimportant to the role of summer motion in determining annual motion; and (3) atmospheric warming over several decades has been accompanied by a slowdown in ice motion. As such, hydro-dynamic coupling is unlikely to form a significant positive feedback between surface melting and ice motion in response to projected climate warming. The wider relevance of these findings to tidewater systems requires further investigation.

Lay Summary

In the last two decades summer air temperatures over the Greenland Ice Sheet have increased, causing more ice to melt and be lost to the oceans, raising global sea level. Surface meltwater gathers in lakes and rivers, before abruptly draining to the bed of the ice sheet and then out to the ice-sheet edge.

The drainage of surface meltwater to the bed of the ice sheet can also change the speed at which the ice flows, termed 'hydro-dynamic coupling'. Previously, observations made during the summer melt season have shown that the ice speeds up when more surface meltwater drains to the ice-sheet bed, as the meltwater lubricates the bottom of the ice sheet which reduces the friction, allowing the ice to slide more quickly over its bed. These observations led to suggestions that the Greenland Ice Sheet will flow more quickly as the climate warms during the 21st century, increasing mass losses both by melting (as more ice is pulled down to lower, warmer elevations) and iceberg calving (as glaciers finishing in the sea speed up) and in turn causing more sea level rise. However, meltwater at the ice-sheet bed also melts out subglacial channels which allow the water to drain away to the margins of the ice sheet more quickly, in turn reducing lubrication, and this means that the overall impact of surface melting on ice flow is unclear.

This thesis presents observations of hydro-dynamic coupling from the south-west Greenland Ice Sheet over annual and decadal periods. Firstly, it examines the response of ice flow

to exceptional melting which occurred during summer 2012. It shows that, although two extreme melt events during July 2012 and the highest surface melting on record caused slightly faster ice flow than during the average summer of 2009, total annual ice flow in 2012 was slightly slower than in 2009. This suggests that hydro-dynamic coupling in areas which finish on land will not cause ice speed-up even under future extreme melting.

The thesis then examines spatial variability in ice flow in relation to inferred locations of drainage channels beneath the ice where meltwater is concentrated. While the locations of these drainage channels control spatial variability in ice flow over short hours to days, they make almost no impact on spatial variability in annual ice flow.

Lastly, observations of ice flow in the melt zone of the ice sheet are made from 30 years of satellite images to examine whether surface meltwater can affect ice flow over decadal timescales. The observations show that a 50 % rise in surface melting over the last twenty years has led to a slow-down in ice flow. This is likely to be because, each summer, the initial increase in sliding caused by more melting is then more than offset by the quicker drainage of meltwater from the ice-sheet bed, resulting in higher friction and less sliding during the following winter than if there had been less summer melting.

These findings therefore suggest that hydro-dynamic coupling is unlikely to cause land-terminating margins of the ice sheet to speed up in response to 21st century climate warming. The wider relevance of these findings to ocean-terminating glaciers, and at high elevations of the ice sheet, requires further investigation.

Acknowledgements

I am especially indebted to my principal supervisor Peter Nienow. Pete has steered me unerringly through the maze of research ideas, funding, fieldwork, presentations and publishing papers. He has done all of this with exceptional humour and has been at the centre of many memorable moments in Greenland, the Highlands and the Lake District along the way. Andrew Sole has been a fantastic second supervisor with his keen attention to detail, wealth of practical knowledge and penchant for heavy rucksacks. In return for deliveries of Reblochon and Chartreuse, Noel Gourmelen has lent his remote sensing expertise, enabling me to undertake more exciting research than would otherwise have been possible. Thanks to Amaury Dehecq for sharing his Landsat processing tools and for being an excellent host during my exchange visits to Annecy, especially on the local crags and ski slopes. Among the wider glaciology community at Edinburgh I thank Tom Cowton for many hours of patient responses to my questions, and for passing on his fieldwork knowledge during two muddy weeks at Leverett Glacier; Donald Slater for keeping me on my toes; Alex Ingle for committing 2012's fieldwork to film; and David Sugden for sage words of advice.

I am immensely grateful to those who have supported me through funding. The Natural Environment Research Council provided me with a fully-funded studentship plus fieldwork expenses. We would not have been able to continue our GPS observations for as long as we did without the generosity of Derek and Maureen Moss, together with the Mackay Greenland Fund, the University of Edinburgh Development Trust and the Carnegie Trust for

the Universities of Scotland. Furthermore, funding from the Scottish Alliance for Geosciences, Environment and Society (SAGES), the Institute of Geography and the Edinburgh University Club of Toronto (EDUCT) has enabled me to attend conferences and workshops and to undertake exchanges.

Much of my fieldwork was enabled by collaboration with Bristol via Jemma Wadham and Aberdeen via Doug Mair. Jon Hawkings and Ben Linhoff were fantastic company throughout the whole 2012 field season, especially when they put their chemistry know-how to good use — who needs duty-free? Thanks also to all of the others in the 2012 field team. More broadly, Kangerlussuaq International Scientific Support, Air Greenland, Heli Greenland and a number of Kangerlussuaq locals provided logistical support (and invoices). Alan Hobbs and the NERC Geophysical Equipment Facility provided equipment, help and advice.

I've been privileged to be involved in teaching at Edinburgh. In particular, Anthony Newton has always taken the time to lend a friendly ear while making tutorial arrangements or during a game of table football after a day's fieldwork in the Cairngorms. Over the course of three undergraduate field courses to Iceland I have benefited hugely from Andrew Dugmore's wisdom and advice. I have also developed both a niche skill in changing Land Rover wheels and a distrust of hot tubs.

For the enjoyable times in Edinburgh and away I thank all the friends who I have shared the last few years with, especially Ed, Ben, Donald, Damon and Tom. The hillwalking exploits have been particularly entertaining. Thanks to my fellow Lower Lewis inmates for their boundless mischief. Thank you to Bella for your good company and humour, both in Edinburgh and the Alps. Lastly, my family have given unwavering support, as have CEM and HJFM; thank you for all of the encouragement that you have given.

Contents

List of Figures

List of Tables

Chapter 1

Introduction

To many the Greenland Ice Sheet is simply a vast, frozen expanse. High above it, air travellers close their window blinds against the the glare of the sun's rays reflected off the snow and ice below. But in recent years the Greenland Ice Sheet has become increasingly difficult to ignore. Warmer air temperatures in summer cause the surface of the ice sheet to melt. These meltwaters gather in strikingly blue lakes and rivers, before abruptly pouring into the dark depths of the ice below, not to be seen again until they emerge at the edge of the ice sheet hours to days later and discharge to the oceans, reducing the mass of the ice sheet. During the last two decades summer air temperatures over the ice sheet have increased, causing more ice to melt and be lost as runoff to the oceans, raising global sea level.

What is less clear, however, is the impact of these vast volumes of meltwater upon ice motion as they make their journey from surface to sea. Dynamic coupling between surface melting and ice motion enables changing air temperatures to influence the flow of the Greenland Ice Sheet by altering the 'slipperiness' of the interface between the base of the ice and its bed. If the flow of the ice sheet speeds up in response to additional meltwater at the ice-bed interface then mass losses may accelerate. This thesis seeks to improve our understanding of coupled hydrology-dynamics of the Greenland Ice Sheet, in order that the sensitivity of

ice sheet motion to climate changes projected to occur during the 21st century may be better constrained.

1.1 The Greenland Ice Sheet and climate change

Together with the atmosphere, oceans, continental surface and biosphere, ice sheets and the rest of the cryosphere compose the Earth system, an interlocked set of processes ultimately driven by solar energy (Cuffey and Paterson, 2010). Over long (1,000 year plus) timescales, changes to the Earth system are driven by changes in the seasonality and location of solar energy inputs around the Earth, which is determined by Milankovitch cycles — variations in the Earth's eccentricity, axial tilt and precession (Alley, 2000). Changes in the extent and mass of the Earth's ice sheets controlled by Milankovitch cycles have been particularly dramatic during the Quaternary (the last 2.5 million years). During this time, 'cold' glacial maximum periods of approximately 100,000 years have been interspersed with warmer inter-glacial periods of around 10,000 years during which ice sheets and glaciers have retreated (Cuffey and Paterson, 2010).

Today, in the warm inter-glacial Holocene period, the landscapes of deglaciated areas such as North America (previously covered by the Laurentide Ice Sheet) and the Scottish Highlands are rich in geomorphological evidence that can offer glimpses of the extent of ice masses during the Last Glacial Maximum approximately 18,000 years ago and during subsequent still-stands and retreat (e.g. Benn and Evans, 2010). Some previous inter-glacial periods were warmer than the present. For instance, sedimentological evidence indicates that during Marine Isotope Stage 11 (420,000-400,000 years ago), global sea level was 6–13 m higher than present, suggesting that the Greenland Ice Sheet crossed a climate/ice-sheet stability threshold that may have been only several degrees warmer than pre-industrial temperatures (Reyes et al., 2014).

The present distribution of the Earth's ice sheets is essentially a function of orbital forcing

and Earth's topography. However, ice masses also respond to changes in the Earth system over much shorter timescales. Human activity has resulted in significant changes in the Earth system, principally through the emission of greenhouse gases to the atmosphere, for instance through the burning of fossil fuels, which causes more solar energy to be trapped in the Earth system (Stocker et al., 2013). As a result, since 1970 the Earth has been in radiative imbalance, with more energy from the sun entering than exiting the top of the atmosphere, causing rising global air and ocean temperatures and associated changes in global circulation patterns and land surface cover (Stocker et al., 2013). In 1750 the mean atmospheric carbon dioxide concentration was 278 ppm but by 2010 it was >390 ppm, and it continues to rise by approximately 2 ppm yr^{-2}, a rate which is unprecedented in the last 22,000 years (Stocker et al., 2013). Changes to the Earth system are likely to be irreversible and catastrophic over societal timescales if atmospheric carbon dioxide remains over 350 ppm for longer than a few decades (Hansen et al., 2008).

Ice sheets constitute some of the most sensitive components of the Earth system to climate change. They gain mass from snowfall, and lose it through two broad processes: (i) surface melting and runoff, and (ii) outlet glacier flow dynamics leading to iceberg calving from marine-terminating margins (Figure 1.1). Ice flow provides a transport mechanism to move ice in the accumulation zone down to lower, warmer elevations, into the ablation zone of the ice sheet where it will melt. If over the course of a full melt-year the mass gained equals the mass lost then the ice sheet is 'in balance'. However, if more mass is lost than gained each year then the ice sheet will have a negative mass balance. Observations indicate that the Greenland Ice Sheet, the West Antarctic Ice Sheet and many mountain glaciers and ice caps presently have an overall negative mass balance (Vaughan et al., 2013).

The present-day Greenland Ice Sheet contains ~2.9 million km^3 of ice, equivalent to 7.4 m of global sea level rise (Bamber et al., 2013). Until recently it had been widely assumed that the mass balance of the Greenland and Antarctic Ice Sheets took thousands of years to respond to climate forcing, but observations in the last two decades have revealed that major

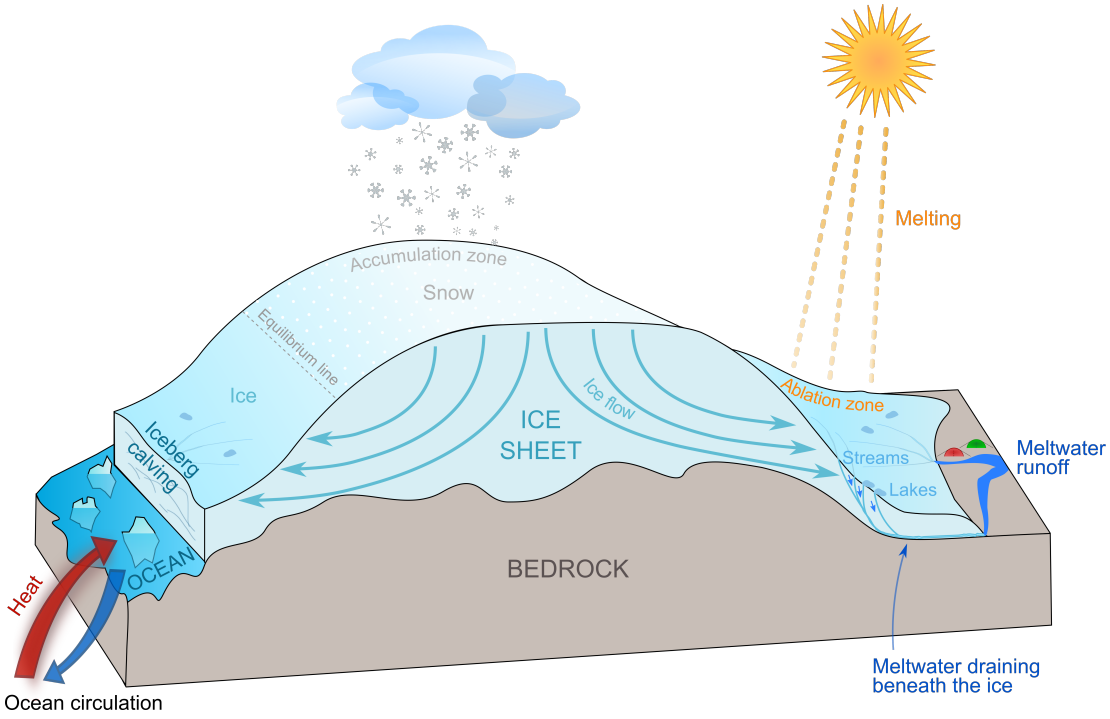

Figure 1.1: Components of the Greenland Ice Sheet mass budget.

changes in the flow dynamics of the ice sheet can occur over timescales of years (Bamber et al., 2007). The 4th Assessment Report (AR4) by the Intergovernmental Panel on Climate Change (IPCC) released in 2007 was unable to quantify the impact of dynamic changes to ice sheets as the models available at the time did not incorporate the processes responsible (Meehl et al., 2007).

Overall mass losses from the Greenland Ice Sheet have increased substantially since the early 1990s (Rignot and Kanagaratnam, 2006; Velicogna and Wahr, 2006; Rignot et al., 2011; Shepherd et al., 2012) with concomitant increases in global sea level (Pritchard et al., 2009; Vaughan et al., 2013). One recent estimate suggests that the Greenland Ice Sheet lost 142 ± 49 gigatonnes (Gt) more mass than it gained each year on average between 1992 and 2011 (Shepherd et al., 2012). Mass losses during this period increased by 21.9 ± 1 Gt yr^{-2} (Rignot et al., 2011), despite slight thickening at higher elevations (Thomas et al., 2009; Pritchard et al., 2009). The IPCC's 5th Assessment Report (AR5) estimated that the average rate of mass loss increased from 34 Gt yr^{-1} during 1992–2001 to 215 Gt yr^{-1} during

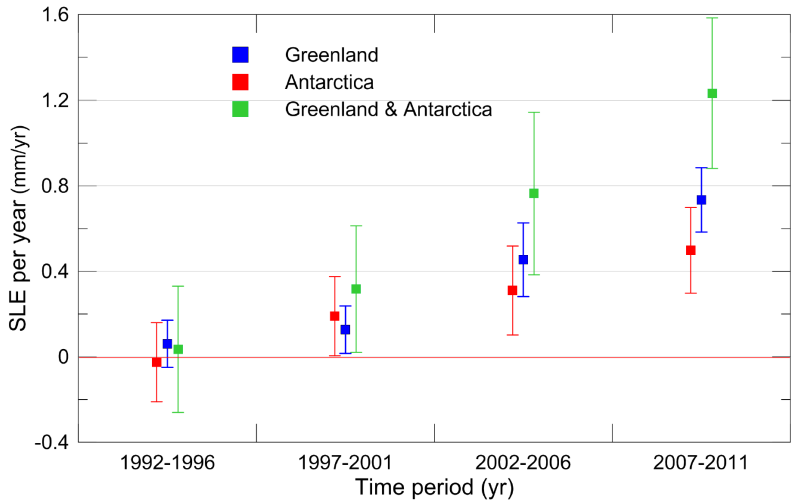

Figure 1.2: Rates of ice sheet mass loss in sea level equivalent averaged over 5-year periods between 1992 and 2011. Figure reproduced from Vaughan et al. (2013).

2002-2011, equivalent to a sea level rise contribution of 0.59 mm yr^{-1} (Vaughan et al., 2013, and Figure 1.2). In recent years mass losses from the Greenland Ice Sheet have contributed ∼1 mm yr^{-1} to global sea levels (Vaughan et al., 2013). The impact of fluctuations in the mass of ice sheets is therefore of enormous societal importance (Shepherd et al., 2012).

During the 2000s mass losses from the Greenland Ice Sheet were split approximately equally between surface melting and ice discharge (Hanna et al., 2008; van den Broeke et al., 2009; Vaughan et al., 2013). However, between 2009 and 2012 the relative contribution of ice discharge to total loss decreased from ∼50% to 32% and as a result, 84% of the increase in mass loss after 2009 was due to surface runoff rather than ice discharge (Enderlin et al., 2014). Surface melting and runoff have increased over the last two decades (Hanna et al., 2005; Mote, 2007; Mernild et al., 2010) coincident with a global warming signal (Hanna et al., 2008). During 1995–2007 the average freshwater flux to the ocean was 786 km^3 yr^{-1} (Mernild et al., 2009) compared to 1953–2003 rates of 281 km^3 yr^{-1} (Janssens and Huybrechts, 2000); high summer melt rates have intensified further since 2006 (Mote, 2007; van den Broeke et al., 2009; Fettweis et al., 2013).

Dynamic thinning (caused by changes in ice flow, rather than simply by increased ablation

and/or reduced accumulation) of marine-terminating margins has been observed at latitudes south of 70°N (Rignot and Kanagaratnam, 2006) and, more recently, at all latitudes penetrating up to 120 km into the ice sheet interior (Pritchard et al., 2009). Most fast flow (>400 m y^{-1}) is limited to narrow, well-defined trunks of outlet glaciers, likely determined by subglacial topography (Joughin et al., 2010). The four largest outlet glaciers (Jakobshavn Isbrae in the west; Petermann Glacier in the north; and Kangerdlussuaq and Helheim Glaciers in the east) are marine-terminating and collectively drain about 22% of the area of the Greenland Ice Sheet and are projected to contribute 19–30 mm of sea level rise by 2200 through changes in their dynamics (Nick et al., 2013). Between 2000–2012 these four outlet glaciers accounted for ∼50% of ice lost due to flow acceleration (Enderlin et al., 2014).

Various dynamic mechanisms of mass loss from marine-terminating margins have been identified. These include (a) the warming of fjord waters associated with atmospheric forcing and modifications to fjord circulation patterns driven by enhanced submarine melt rates (Murray et al., 2010; Straneo et al., 2011; Christoffersen et al., 2011); (b) the disintegration of buttressing floating ice tongues and sikkusak (mélange), resulting in reduced back-stress (Thomas et al., 2009; Howat et al., 2010); (c) enhanced submarine melt rates associated with subglacial discharge from the glacier terminus which upwells in a turbulent plume against the glacier front (Jenkins, 2011); and (d) iceberg calving due to fracture (crevasse) propagation, which is in turn inseparably coupled to glacier dynamics (Benn et al., 2007). The relative importance of each of these mechanisms and the ways in which they interact are presently poorly understood but, given their significant role in recent mass losses, tidewater glaciers are a major area of ongoing research (Straneo et al., 2013).

The Greenland Ice Sheet flows not only under its own weight due to gravity, but also by sliding along its bed. Ice motion has been observed to accelerate coincident with increases in meltwater inputs to the subglacial environment which enhance sliding of the ice sheet along its bed, predominantly in land-terminating regions (Zwally et al., 2002; Bartholomaus et al., 2008; van de Wal et al., 2008; Shepherd et al., 2009; Bartholomew et al., 2010, 2011a,

2012; Palmer et al., 2011) but also at marine-terminating glaciers including Helheim Glacier, east Greenland (Andersen et al., 2010) and Kangiata Nunata Sermia, south-west Greenland (Sole et al., 2011). The mechanism enables changing air temperature to perturb the speed at which the margins of the Greenland Ice Sheet flows by changing rates of surface melting.

Initially it was suggested that enhanced surface meltwater production could lead to faster net annual ice flow (Zwally et al., 2002), accelerating dynamic mass losses in a warming climate as more ice would be drawn down to lower elevations resulting in higher ablation rates, additional thinning and marginal retreat (Parizek and Alley, 2004), threatening the 'loss' of the Greenland Ice Sheet (Gregory, 2004). Theoretical considerations and observations in south-west Greenland revealed that supraglacial lakes could drain suddenly by hydro-fracture, providing a mechanism to initiate surface-to-bed hydrological connections (Alley et al., 2005b; Das et al., 2008). However, some recent studies have suggested that, over annual timescales, the ice sheet might instead flow more slowly in response to increasing summer meltwater volumes (van de Wal et al., 2008; Sundal et al., 2011).

The overall relationship between surface meltwater volume and ice motion is elusive because the ice-bed interface changes in response both to varying meltwater inputs and to sliding, and it is difficult to make direct observations of the ice-bed interface. Transient periods of faster ice motion occur when subglacial water pressure rises enough to 'lift' the ice up, causing ice-bed separation over a wide enough area to reduce basal traction and enable slip (Iken and Bindschadler, 1986). During such periods, ice velocities can increase by ∼200-300% of their winter velocities (e.g. Bartholomew et al., 2010). However, as the ice slides over its bed, cavity spaces open up, increasing the capacity of the subglacial drainage system and lowering water pressure which in turn increases basal traction and reduces slip (Iken and Truffer, 1997). Moreover, the morphology of the subglacial drainage system adapts to evacuate larger fluxes of water at lower pressure as water incises channels into the overlying ice and/or into the substrate (Hubbard and Nienow, 1997). Thus, whilst meltwater inputs to the ice sheet bed initially cause transient acceleration, negative feedbacks then act to reduce

ice motion by lowering water pressure and increasing basal traction (Iken and Truffer, 1997). In order to understand the net impact of surface meltwater production on ice motion it is therefore necessary to consider how short-term variability aggregates to control ice motion over seasonal, annual and longer timescales. Only then can we begin to identify where the balance in a warming climate lies between (1) meltwater inputs and water pressure, (2) the impact of subglacial drainage system evolution upon water pressure, and (3) the effect of water pressure upon ice motion.

1.2 Outline of thesis

This thesis aims to improve our understanding of the coupling between hydrology and dynamics along land-terminating margins of the south-west Greenland Ice Sheet. It uses both field and remotely sensed observations to understand the potential hydro-dynamic responses of the Greenland Ice Sheet to Earth's changing climate, and specifically seeks to establish whether enhanced melting is able to generate spatially significant ice motion speed-up over annual and longer timescales. The thesis is organised into three complementary research themes:

1. **The impact of extreme meltwater supply rates and extreme meltwater volumes on ice motion.** Contrasting hypotheses have been developed to address which of meltwater supply *rates* versus *volumes* is most important to generating ice motion. In the first key study to examine the coupled hydrology-dynamics of the Greenland Ice Sheet, Zwally et al. (2002) suggested that ice motion could be faster in years when meltwater volumes were larger. In contrast, van de Wal et al. (2008) and Sundal et al. (2011) suggested that larger seasonal meltwater volumes result in slower annual ice motion due to the development of efficient subglacial drainage earlier in summer, resulting in lower velocities during the remainder of the melt season. Conversely, some field-based (Bartholomew et al., 2011a) and theoretical (Schoof, 2010) studies have shown that rapid increases in the rate of meltwater supply to the ice sheet bed

can cause spikes in subglacial water pressure, leading to transient ice acceleration. Bartholomew et al. (2011a) therefore proposed that net annual ice motion is likely to be faster in a warmer climate as a consequence of higher meltwater supply rates.

A major reason for these continuing uncertainties is that few observations have been made over complete melt-years (i.e., spring to the end of the following winter) when the net impact of coupled hydrology-dynamics upon annual ice motion becomes apparent. This theme aims to identify whether more melting results in faster net annual ice motion by utilising observations made over the two complete melt-years of 2009 and 2012. During 2012 there were two melt events which resulted in extreme rates of meltwater supply (unprecedented since 1889 (Nghiem et al., 2012)) and total Greenland-wide runoff was 3.9 σ above the 1958–2011 mean (Tedesco et al., 2013a). Conversely, 2009 was an 'average' melt-year in which extreme melt events did not occur. These two melt-years are therefore ideal candidates for testing the impact of varying meltwater volumes and supply rates on annual ice motion.

2. **The impact of subglacial drainage system structure on ice motion.** Field studies of alpine glaciers have revealed significant spatial hetereogeneity in the morphology of the subglacial drainage system, with associated spatial variability in ice surface motion (e.g. Nienow et al., 2005). Similarly, interferometric synthetic aperture radar (InSAR) observations of ice motion over a section of the south-west Greenland Ice Sheet during late summer show that faster ice motion is coincident with supraglacial meltwater input points, indicating that routing of meltwater at the ice sheet bed closely resembles routing at the surface (Palmer et al., 2011). This theme aims to identify the magnitude of spatial variations in ice motion driven by water pressure variability in the underlying subglacial drainage system through two approaches. Firstly, it uses detailed field observations to examine transient variations in ice motion adjacent to and distal from an inferred subglacial channel during the 2012 melt season. Secondly, it uses satellite synthetic aperture radar and GPS observations to examine net ice motion during summer and over the full 2012–2013 melt-year, in order to examine spatial

variations in the proportion of annual ice motion attributable to hydrologically-forced ice motion.

3. **Coupled hydrology-dynamics over decadal timescales.** Air temperatures over the south-west Greenland Ice Sheet have warmed during the last two decades (Box et al., 2009; Hanna et al., 2012), leading to the production of more surface meltwater (Fettweis et al., 2013). However, for reasons outlined above, it remains unclear whether increasing meltwater production will cause ice sheet motion to increase over decadal timescales. Utilising feature tracking of the Landsat Program archive of satellite imagery, this theme quantifies changes in annual ice motion from 1985 to 2014 over an 8000 km^2 area along the margins of the south-west Greenland Ice Sheet. Examining ice motion at unprecedented combined temporal and spatial resolution, this theme investigates how decadal changes in surface melting have impacted upon ice motion.

This thesis specifically addresses the land-terminating margins of the Greenland Ice Sheet. This is because these are the margins at which proglacial discharge can be measured to help understand links between melting, runoff and ice motion, and the impact of coupled hydrology-dynamics can be separated from the other numerous and complex dynamic mechanisms which perturb the flow of marine-terminating glaciers.

Chapter 2 provides a more detailed review of subglacial hydrology and the role of water at the ice-bed interface in controlling ice motion. It summarises findings made both at alpine glaciers and on the Greenland Ice Sheet. Chapter 3 introduces the study areas and the methods used to collect field observations and to analyse remotely sensed data.

Chapters 4, 5 and 6 examine each of the three research themes outlined above. Chapter 7 summarises and synthesises these findings in the context of other research undertaken on the Greenland Ice Sheet, and highlights a number of critical outstanding issues which need to be addressed to reduce the errors on predictions of the stability of the Greenland Ice Sheet in a warming world.

1.3 Format of thesis

Chapters 4, 5 and 6 have been written in the format of standalone papers to facilitate rapid dissemination of their findings to the research community. Chapters 4 and 5 have already been published, whilst Chapter 6 is in review. Each of these chapters lists a number of co-authors, along with a summary of their contributions. In addition, I am a co-author on three further published papers related to my doctoral studies. All of these papers are included in their published format as appendixes at the end of this thesis.

Chapter 2

Background

During the second half of the 20th century the field of glaciology began to grow dramatically. Initially many studies were numerical and theoretical in approach, concerning themselves with physical formulations to describe glacier flow, basal slip and subglacial drainage channels. From around the 1970s a number of field campaigns began to record complementary observational data both in the European Alps and further afield. However, it was only at the turn of the 21st century that the hydrology and dynamics of the Greenland Ice Sheet started to receive substantial research attention.

Much of the existing body of glaciological knowledge derived from alpine glaciers is applicable to the Greenland Ice Sheet. This chapter therefore first briefly reviews some essential theoretical aspects of glacier hydrology and ice motion. It then examines observations of hydrologically-controlled ice flow variability made at alpine glaciers before moving on to summarise the current state of knowledge of coupled hydrology-dynamics of the Greenland Ice Sheet gained from field observations, remote sensing measurements and modelling approaches.

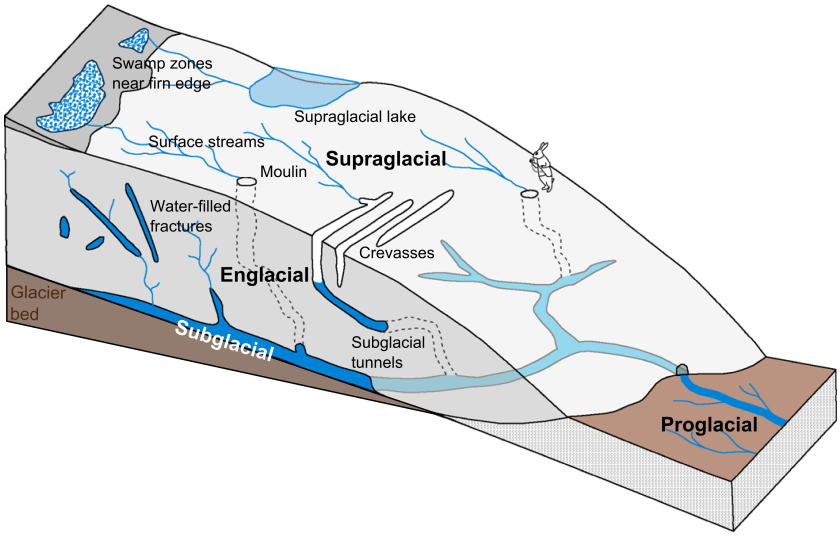

Figure 2.1: Elements of the glacier water system, reproduced with modifications from Figure 6.1, Cuffey and Paterson (2010).

2.1 The glacier hydrological system

The hydrological system of a glacier has three main elements: meltwater production on the surface of the glacier (supraglacial hydrology), routing of surface meltwater through the ice to the glacier bed (englacial hydrology), and the drainage of water beneath the ice (subglacial hydrology). Each element has a number of features, as shown in Figure 2.1.

2.1.1 Surface meltwater production

Meltwater is produced on the glacier surface in quantities largely determined by the energy balance at the glacier-atmosphere interface (Hock, 2005). For the same amount of radiation input, snow-covered surfaces produce less melt per unit of radiation input than bare-ice surfaces as they have a higher albedo, resulting in a higher proportion of the shortwave radiation being reflected.

Melting is more rapid during the daytime when more radiation reaches the ice sheet surface. The flux of meltwater is greater in the ablation zone than the accumulation zone as the

lower albedo and warmer temperatures at lower elevations act to increase the melt rate (Fountain and Walder, 1998).

2.1.2 Routing to the glacier bed

The processes controlling the routing of surface meltwater to the subglacial environment govern the rate at which surface meltwater reaches the bed. Routing pathways evolve in response to supraglacial meltwater production. Broadly, they may be characterised as 'slow', where meltwater percolates through snowpack, or 'fast', where meltwater flows across bare ice surfaces.

Mediation by snowpack facies

Meltwater produced where snow and/or firn is present has to percolate through the snowpack/firn in order to reach the impermeable ice surface. Transmission through the interstitial pores introduces significant lags in discharge (Fountain, 1996; Fox et al., 2008). Early in the melt season, when the snowpack is cold, meltwater will refreeze in the interstitial structure, reducing the meltwater flux. Snowpack/firn temperature and porosity control the percolation rate (Jezek et al., 1994). As meltwater passes through the snowpack/firn, it causes the surrounding snowpack/firn to warm, thus the transmission efficiency of the snowpack/firn increases with surface melting (Campbell et al., 2006).

Supraglacial streams

Water percolates through the snow and firn to the impermeable ice interface, where it begins to flow downslope. As water from the melting of snow/firn and ice flows into topographic lows, it coalesces, and supraglacial channel incision by frictional melting occurs (Isenko et al., 2005). The width of supraglacial channels is proportional to the square root of their discharge (Ferguson, 1973). Near the ice sheet margin, these streams may discharge directly

to the proglacial environment, but further inland they either drain to the glacier bed via crevasses and moulins, or pond into supraglacial lakes.

Hydro-fracture

Unlike alpine valley glaciers, which are usually at the melting point throughout their depth, the ice of glaciers in the High Arctic and Greenland tends to be either cold apart from a basal layer of finite thickness at the melting point, or cold throughout the vertical profile and frozen to the underlying bed (Cuffey and Paterson, 2010). Englacial conduits therefore cannot propagate down towards the bed by the melting of their walls through heat generated by viscous dissipation as the surrounding ice is too cold (Shreve, 1972; Röthlisberger, 1972). In principle this has the potential to limit hydrological connections from the surface to the bed (Boon and Sharp, 2003). However, crevasses can propagate from the glacier surface to the bed via hydro-fracture. Water has a slightly greater density than ice. Provided the crevasse is water-filled, the weight of the water can overcome the lithostatic stress of the ice, enabling the crevasse to propagate to the glacier bed (van der Veen, 2007). Such a mechanism appears to explain surface-bed connectivity in the polythermal John Evans Glacier, Ellesmere Island (Boon and Sharp, 2003).

The locations of crevasse formation are governed by ice tensile stress and mechanical strength (i.e. fracture toughness), but once hydro-fracture is initiated then propagation proceeds independently of these initial conditions (van der Veen, 2007). Modelling has suggested that the crevasse must fracture quickly enough that the water inside is not able to refreeze, which requires that the crevasse be deeply filled with water initially (Alley et al., 2005b), although observations in the High Arctic suggest that the process proceeds by multiple small fracture events, each halted by re-freezing (Boon and Sharp, 2003). If the crack is large enough it propagates easily; hydro-fracture to the bed is thus likely to be most successful when the initial crevasse depth is on the order of tens of metres (Alley et al., 2005a). The supply of water to the crevasse must continue during propagation, and

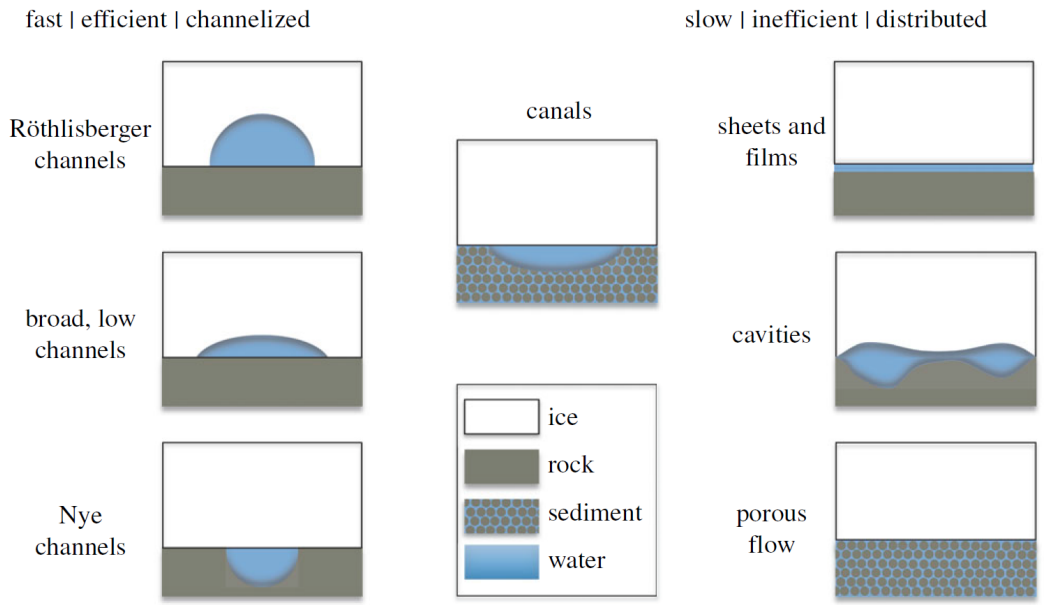

Figure 2.2: Idealized elements of the subglacial drainage system, grouped into 'fast', 'efficient' or 'channelised' drainage, versus 'slow', 'inefficient' or 'distributed' drainage. Canals may be classified either way. Reproduced from Flowers (2015).

forms the chief control on the rate at which propagation proceeds (van der Veen, 2007). If a crevasse subsequently develops into a moulin then the lag time between surface melting and delivery to the bed will decrease (Colgan et al., 2011).

2.1.3 Subglacial hydrology

Surface meltwater travels through englacial pathways to the glacier bed where it meets relatively impermeable bedrock or unconsolidated sediments (Hubbard and Nienow, 1997). The glacier bed may be frozen, such as beneath the ice divide region of the Greenland Ice Sheet (Parizek and Alley, 2004), or it may be temperate — maintained at the pressure melting point as is the case at most alpine glaciers and also for the margins of the south-west Greenland Ice Sheet (Parizek and Alley, 2004). When the ice-bed interface is at the pressure melting point, liquid water will be present. In water-filled, ice-bounded channels this water will flow in the direction of the hydraulic gradient, which is a function of both the bed slope and the overlying ice mass (Shreve, 1972). The morphology of the subglacial drainage system

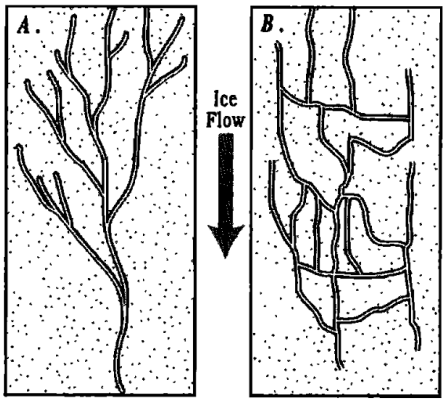

Figure 2.3: Idealised plan view of (a) an arborescent hydraulic system composed of channels and (b) a non-arborescent inefficient hydraulic system. Reproduced from Fountain and Walder (1998).

evolves in response to meltwater supply rates. Frictional viscous melting by water flowing under pressure must counteract the rate of ice deformation if an ice-incised passage is to remain open (Shreve, 1972). Water flow also erodes, mobilises and transports sediments, resulting in an ever-changing subglacial drainage system. Various elements composing the subglacial drainage system have been proposed, broadly grouped by their hydraulic efficiency and/or speed of water routing (Figure 2.2; Hubbard and Nienow, 1997; Fountain and Walder, 1998).

Early in the melt season drainage is thought to occur primarily via a distributed system with low hydraulic efficiency (Hubbard and Nienow, 1997, and Figure 2.3b). As a result, water pressure (hereafter P_w) is high even though the meltwater flux is small. As surface melting intensifies, P_w will increase if the rate of meltwater supply is faster than the rate at which the subglacial drainage system can grow and/or increase its efficiency to accommodate the increased meltwater inputs. Beyond a critical P_w-size threshold, elements of the distributed system become unstable and collapse (Kamb, 1987), resulting in the development of channelised structures which evolve into an arborescent system (Fountain and Walder, 1998, and Figure 2.3a). These channels could operate as central variable pressure axes characterised by low minimum diurnal P_w and high diurnal P_w variations in a narrow zone, transitioning over several tens of metres to more stable P_w in adjacent distributed drainage areas (Hubbard et al., 1995). This hydraulically efficient arborescent

system expands up-glacier at the expense of the widespread inefficient drainage system as the snow-line retreats and surface-to-bed connections are established which enable diurnally varying inputs of surface meltwater (Nienow et al., 1998). As melt fluxes reduce towards the end of the summer, ice deformation will cause the gradual closure of channelised drainage structures until ice overburden pressure (P_i) is balanced by P_w.

The foregoing description of the subglacial drainage system concentrates on its evolution over the full length of the melt season as a function of seasonal variations in meltwater supply. Over diurnal timescales, meltwater supply rates vary substantially, resulting in transient periods of over-pressurisation and, conversely, periods during which elements of the system may be at atmospheric pressure (Fountain and Walder, 1998).

2.2 Subglacial hydrology and ice motion

The presence of water at the glacier bed plays a critical role in controlling spatial and temporal variations in ice motion. It influences the stress distribution at the ice-bed interface by modifying the degree of contact between the bed and overlying ice, thereby controlling basal traction and thus the rate at which ice slips over the bed (Fountain and Walder, 1998; Cuffey and Paterson, 2010). Particularly important to the control of basal slip is P_w, with high P_w providing the potential to initiate slipping (Clarke, 2005). However, P_w in turn depends on meltwater supply and subglacial drainage system structure, which complicates the specific relationship between surface melting and ice motion. Changes in system morphology and meltwater supply can induce variations in ice motion over diurnal to seasonal timescales (e.g. Willis, 1995).

2.2.1 Basal slip

The theory of ice sliding over a hard bed has its origins in the mechanisms of regelation (pressure melting) and enhanced ice creep proposed by Weertman (1957). Both assume a

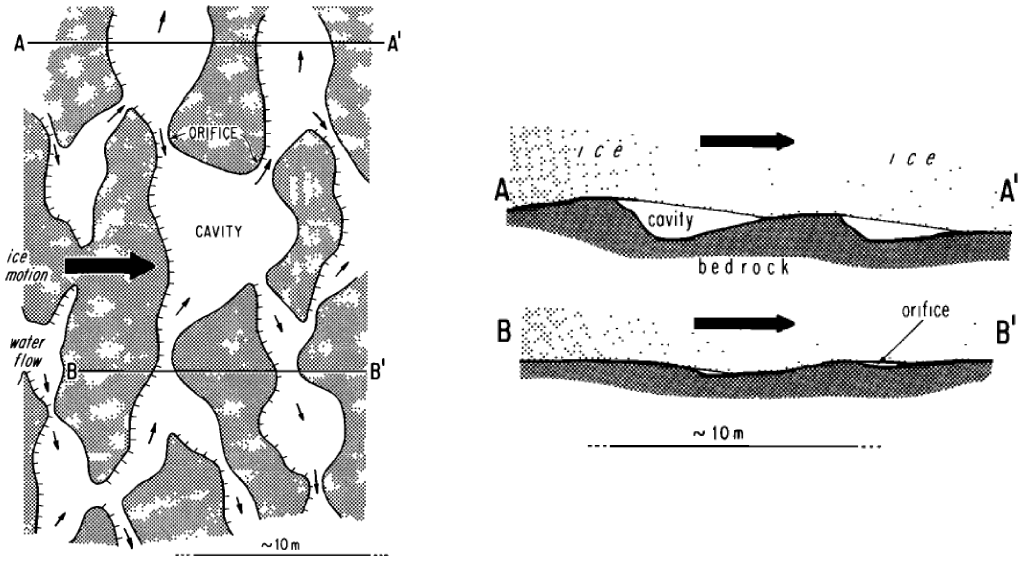

Figure 2.4: A model of linked cavity drainage, reproduced from Kamb (1987). Large black arrows indicate the direction of ice flow. Left: Map view of the glacier bed. Areas of ice contact with the bed are shaded. Vertical cross-sections along AA' and BB' are shown in the right-hand panel. Directions of water flow through the system are identified with small black arrows. Right: Vertical cross-sections through AA' and BB'.

temperate ice mass overlying impermeable hard bedrock with irregular topography where a widespread uniform film of water, produced by pressure and geothermal melting, separates the ice from its bed. With this theory, it is simple to understand that if meltwater is present at the glacier bed in quantities greater than can immediately be drained, the water film will thicken, resulting in more bed separation as more bed obstacles are submerged. The reduction in ice-bed contact reduces friction and drives increases in sliding.

The mechanism proposed by Weertman is unlikely to be physically realistic as it fails to account for the role of bed topography in promoting the development of cavities — pockets where water concentrates. This led to the development of a model of sliding based on cavities (Figure 2.4; Lliboutry, 1968, 1979; Kamb, 1987) in which water concentrates in cavities which form in the lee of bedrock bumps, where the pressure exerted by the overlying ice is lowest. Simple channels provide links between the cavities.

Under increased P_w the cavities become enlarged, which reduces the degree of contact

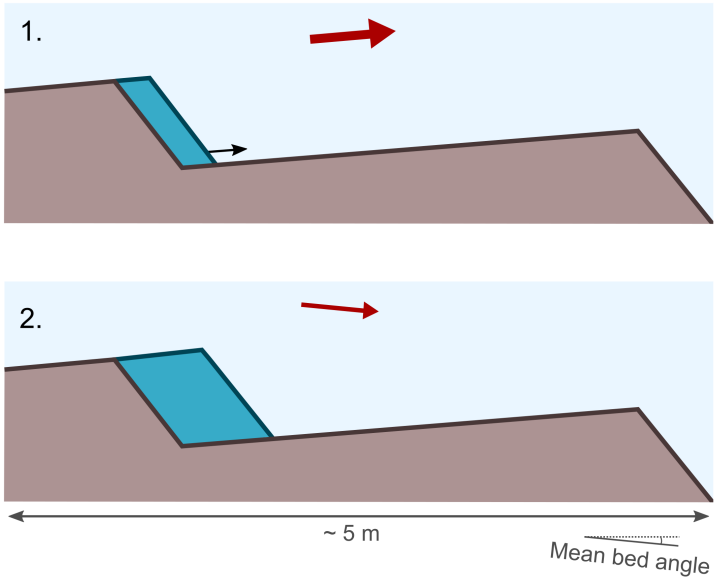

Figure 2.5: Conceptual process of transient cavity growth and its effect on ice motion, as envisaged by Iken (1981). Red arrows indicate the direction and magnitude of ice motion. As the cavity grows (1), ice velocities increase in the horizontal direction, and ice uplift occurs. When the cavity stops growing (2), horizontal ice velocities decrease and become bed-parallel.

between the ice and bed, concentrating the stresses onto the remaining points of contact (Lliboutry, 1979). For enhanced rates of sliding to occur, the effective pressure N (the difference between P_i and P_w in the cavity) must tend to 0, enabling flotation. The minimum value at which this occurs is termed the separation pressure P_s. As P_w increases above P_s it reaches a critical point P_c ($< P_i$) at which sliding becomes unstable (Iken, 1981; Cuffey and Paterson, 2010). Thus, when $P_w < P_s$, sliding is constant and depends on Weertman-derived processes of regelation and enhanced creep. As P_w approaches P_s, water-filled cavities begin to form, reducing ice-bed contact and causing glacier surface uplift when $P_w > P_s$. At $P_w = P_c$ sliding becomes unstable and non-linear acceleration may occur (Iken, 1981). Water supply to the ice-bed interface, together with the drainage system that it encounters, are therefore the key controls on the contribution of cavity growth to enhanced ice motion (Fowler, 1987).

The foregoing mechanism fails to explain why peak horizontal velocities are often observed to occur while the rate of surface uplift is greatest, rather than when the upward motion of the ice has reached the maximum elevation (Iken, 1981). Iken therefore suggests that the

greatest sliding velocities occur at the beginning of cavity growth, when P_w is between P_s and P_c. After initial separation, the cavity grows (Figure 2.5:1), increasing the area of the ice supported by P_w. Ice at the down-glacier edge of the cavity moves further along the bed than that at the up-glacier edge. Only when the cavity reaches the steady-state size for the given water pressure does the ice at the ceiling move parallel to the bed, resulting in slower sliding velocities and the cessation of surface uplift (Figure 2.5:2). This mechanism in turn explains why glaciers slide faster during periods when P_w is increasing rather than decreasing. However, it is important to note that this mechanism assumes steady-state conditions. In reality, cavity growth increases the capacity of the subglacial drainage system, which acts to reduce P_w and in turn reduce ice motion.

Unlike sliding over a hard bed, sliding over a soft bed introduces a dynamic role for underlying sediments at the ice-bed interface (Fowler, 2003). Whereas hard beds promote enhanced ice motion by flotation when sufficient water is present, glaciers underlain by soft sediments theoretically undergo elevated ice motion as a consequence of bed deformation.

Water-saturated till can deform at high pore water pressure (Boulton and Jones, 1979). High pore water pressure occurs when drainage of water is slower than the rate of meltwater input into the till. Effective stress (N) is reduced as high P_w reduces the force per area given by grain-to-grain contact (Cuffey and Paterson, 2010). Thus, as P_w approaches P_i, subglacial till becomes weaker than the overlying ice. The more readily the sediments deform, the smaller the resisting forces, so the faster the ice will be transported by the deforming substrate. However, elevated P_w does not necessarily lead to deformation (and consequent ice motion), as at low N the ice is nearly afloat so transmits very little shear stress to the sediment (Clarke, 2005). This negative feedback reduces the propensity for sliding by sediment deformation and instead tends to favour sliding by decoupling of the ice from the bed. At Storgläciaren, Sweden, a reduction in N was observed to correspond to an increase in ice motion but a decrease in the strain rate in the subglacial sediment as the decoupling reduced shearing (Iverson et al., 1995). Surface uplift during ice speed-up events is also consistent with ice-bed

decoupling rather than sediment deformation. Iverson et al. (1995) therefore suggested that the most important aspect of sediment deformation could be in providing a smooth surface over which the ice can slide by ice-bed decoupling. Overall, it is possible that the importance of sliding caused by bed deformation has been overstated (Piotrowski et al., 2001).

2.2.2 Temporal variability in hydrology and dynamics

Variability in ice motion is associated both with variations in the rate of meltwater supply and the evolution of an increasingly efficient channelised subglacial drainage system, resulting in variable P_w. Coupled hydrology-dynamics has been observed at alpine glaciers such as the Haut Glacier d'Arolla, Switzerland (Mair et al., 2002) and at High Arctic glaciers such as John Evans Glacier, Ellesmere Island (Bingham et al., 2003) and Midre Lovénbreen, Svalbard (Rippin et al., 2005).

A subglacial drainage system consisting of cavities and/or patches of porous sediment is hydraulically inefficient and is therefore unable to route meltwater quickly (Figure 2.6:1). Once surface melting commences at the start of the melt season and meltwater reaches the glacier bed, high velocity events occur, commonly termed 'spring events' (Mair et al., 2003). They are associated with the initiation of surface-to-bed connections, large increases in proglacial discharge and high subglacial P_w, resulting in widespread decoupling of the ice from its bed (Mair et al., 2003; Bingham et al., 2006) (Figure 2.6:2). During these spring events P_w in the existing 'distributed' drainage system rises and hydraulic jacking occurs as cavities grow in response to rising P_w, causing ice motion to speed up (Figure 2.6 box a).

Beyond P_c, cavities become unstable and the morphology of the subglacial drainage system therefore adapts to improve the efficiency of water routing. Channels form as the flowing water melts the walls of the surrounding ice by friction (Figure 2.6:3). For a given meltwater supply rate, the increasing capacity of the subglacial drainage system works to lower P_w and hydraulic jacking therefore becomes less widespread, causing ice velocity to fall

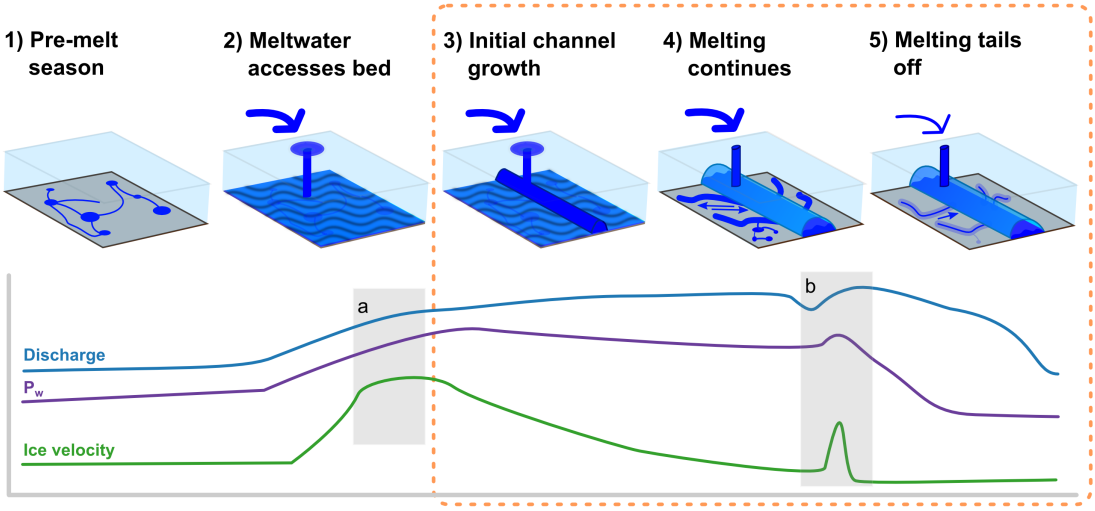

Figure 2.6: A cartoon of coupled hydrology-dynamics, after Iken and Bindschadler (1986); Bingham et al. (2003); Bartholomew et al. (2010). Steps 1–5 occur over the course of the summer. Steps 3–5, outlined in orange, can additionally occur each time there is a step increase in the rate of meltwater supply to the ice sheet bed. Arrows in steps 4 and 5 show the direction of diurnal P_w gradients. Boxes (a) and (b) refer to specific periods discussed in the text.

(Figure 2.6:4). Over diurnal timescales, varying surface meltwater inputs cause pressure gradients between the efficient channelised system and the surrounding distributed system to oscillate (Figure 2.6:4). During high rates of meltwater supply in the daytime, water is forced out of channels to the surrounding bed, whilst at night when melting decreases, water drains out of the surrounding bed into the channelised drainage system (Hubbard et al., 1995). This causes diurnal oscillations in ice motion, which are strongest in amplitude directly above the subglacial channel (Nienow et al., 2005). As the meltwater supply rate falls towards the end of the melt season, the pressure in the efficient channelised regions of the drainage system falls to become lower than surrounding areas of the inefficient unchannelised glacier bed, and water from these areas is drained into the channelised system (Figure 2.6:5), much as over diurnal timescales. Ice velocities therefore drop as basal traction increases. Steps 3 and 4 in Figure 2.6 occur each time there is a step increase in the rate of meltwater supply to the ice sheet bed that overwhelms the routing capacity of the existing drainage system, resulting in transient over-pressurisation and ice speedup akin to that illustrated in Figure 2.6, box b.

Upglacier expansion of an efficient subglacial drainage system is broadly synchronous with

the expanding melt area (Nienow et al., 1998; Bingham et al., 2003). The evolution of a more hydraulically efficient subglacial drainage system in response to meltwater inputs has an important negative feedback on ice flow, reducing the sensitivity of basal sliding to meltwater inputs. This has a number of ramifications for spatial variability in ice motion, on timescales from sub-diurnal to inter-annual.

2.2.3 Spatial variability in hydrology and dynamics

Initially, investigations of spatial variability in ice motion largely ignored the role of hydrology. One of the first examples of numerical modelling in glaciology, by Nye (1965), investigated ice flow through idealized glacier cross-sections of different geometries, examining the impact that factors such as drag on the valley sides have on velocities at the bed and the surface. However, Nye neglected basal slip, primarily due to inadequate constraints from field data. Motivated by Nye, Raymond (1971) measured ice deformation at the surface and at depth through a cross-section of Athabasca Glacier in the Canadian Rockies. His observations differed significantly from the theoretical predictions of Nye (1965) due primarily to the identification of a spatially variable slip component, rather than a constant sliding velocity for which Nye's analysis would have held. Basal sliding was found to contribute proportionally more motion towards the centre line than at the margins, rather than to occur uniformly throughout the cross-section.

To investigate the amount of basal sliding that would be expected at the ice surface, Balise and Raymond (1985) modelled the impact of different length scales of basal velocity anomalies on the distribution of ice surface motion. They found that over length scales >10 ice thicknesses ($10H$) the velocity anomaly at the surface is essentially the same as the anomaly at the bed. However, at length scales $<10H$, the velocity anomaly expressed at the surface becomes different to that at the bed. The propagation of the basal perturbation in ice motion is smoothed and dampened as it propagates upwards, resulting in a smaller surface expression of the original basal perturbation. At $<5H$ the position of velocity peak at the

surface shifts away from the peak perturbation at the bed and additional surface peaks may also be introduced. At very short spatial scales of basal perturbation ($<1H$) there is no corresponding change in the surface velocity field. The theoretical findings of Balise and Raymond (1985) highlight the difficulties associated with inferring basal conditions from surface properties.

During the 1980s and 1990s a number of field campaigns on alpine glaciers seeked to elucidate the mechanisms by which hydrology and ice motion might be linked. Dense grids of boreholes were drilled at glaciers such as Findelengletscher (Iken and Truffer, 1997) and Haut Glacier d'Arolla (Harbor et al., 1997; Gordon et al., 1998) in the European Alps, Storglaciären in Sweden (Hooke et al., 1989), South Cascade Glacier in the USA (Fountain, 1994) and Trapridge Glacier in the Yukon Territory, Canada (Murray and Clarke, 1995). Water levels measured in the boreholes were used as proxies for subglacial P_w. The spatial relationships between water levels across the borehole grids were seen to change both over the course of a melt season and from one hour to the next. Critically, the borehole observations suggested that glacier beds are spatially non-uniform in their hydrology and their substrate over length scales from less than one to several ice thicknesses (e.g. Harbor et al., 1997). Observations at the Haut Glacier d'Arolla revealed that diurnally variable water pressures tended to be restricted to an area relatively narrow in cross-glacier direction, and associated with an efficient subglacial Röthlisberger channel (e.g. Figure 2.2, top-left), forming variable pressure axes (VPAs; see also Section 2.1.3) (Hubbard et al., 1995). Away from these zones water pressures tended to be higher and less variable, implying that at any one time some areas of the glacier bed are more hydrologically connected than others.

Spatio-temporal patterns in borehole water levels show relatively close correspondence to surface ice motion (within a distance <= 1 ice thickness). Increasing P_w leads to more spatially extensive ice-bed decoupling, with ice uplift likely to occur once the meltwater supply rate is large enough to raise P_w in the adjacent unchannelised regions of the subglacial drainage system (Murray and Clarke, 1995). The greatest diurnal variability and highest

peak velocities tend to occur over the VPA and attenuate with distance from the VPA as the impact of the VPA on P_w decreases (Hubbard et al., 1995; Nienow et al., 2005).

Stake networks used to observe ice surface strain rates have provided further insights into how basal motion perturbations are expressed at the glacier surface. Mair et al. (2001) observed that during spring events on Haut Glacier d'Arolla, enhanced glacier motion was dependent on a change in the spatial distribution of areas of high drag across the glacier. Specifically, they concluded that 'sticky spots' would have to be removed over length scales >4 ice thicknesses before a high velocity event could occur. The pattern of 'sticky' and 'slippery' spots was spatially and temporally variable. Moreover, at horizontal scales <1 ice thickness, ice coupling to surrounding areas obfuscated any local relationship between basal drag and glacier motion.

The importance of 'sticky' spots for regulating ice surface motion implicates stick-slip motion at the glacier bed (e.g. Fischer and Clarke, 1997; Kavanaugh and Clarke, 2001; Nienow et al., 2005). Stick-slip motion assumes a network of water-filled cavities at the ice-bed interface which can grow and shrink; sliding velocity is greatest when cavities are growing in response to rising P_w, rather than when they reach a steady-state size (Iken, 1981). However, stick-slip also incorporates cyclic momentary speed-up as the accumulated local elastic strain associated with increasing P_w is released (Fischer and Clarke, 1997).

Combining observations of proxy P_w from boreholes with records of ice surface motion yields a complex picture in which variable P_w is clearly responsible for some variability in ice motion, yet the extent to which P_w can directly explain ice surface motion is somewhat spatially and temporally discontinuous. Much of this uncertainty arises from how the configuration of the subglacial drainage system at any point in time is able to drive fluctuations in P_w both locally and further away, together with the flux of water delivered to the system (Kamb, 1987 in Nienow et al., 2005). Building on the suite of observations collected at Haut Glacier d'Arolla, Nienow et al. (2005) modelled the observed diurnal velocity field. They found that reductions in basal shear traction were required over a substantially larger area of the bed

than just in the vicinity of the subglacial channel and VPA to explain the observed velocity patterns. They therefore suggested that P_w needed to act over length scales of at least several ice thicknesses to produce the observed surface expression of ice motion.

As variations in subglacial hydrological conditions affect rates of basal motion, in turn creating longitudinal and transeverse stress gradients in the ice (Harbor et al., 1997), the surface expression of basal motion will be modified and attenuated. There was some evidence of faster surface motion in the vicinity of the VPA during the summer season at Haut Glacier d'Arolla, but over the course of a full year, compensating ice deformation via transverse coupling appeared to suppress surface expression of the VPA (Harbor et al., 1997).

2.3 Hydrology and dynamics of the Greenland Ice Sheet

One of the first indications that surface melting could influence the ice motion of the Greenland Ice Sheet came from satellite radar interferometry data of Ryder Glacier, north Greenland, which sped up around three-fold during a period when lakes on the surface of the ice sheet were inferred to have drained, somehow influencing basal P_w (Joughin et al., 1998). This was followed by observations made at Swiss Camp, west Greenland during the 1990s which showed near-coincidence of ice acceleration with the duration of summer melting, and deceleration upon the cessation of melting (Zwally et al., 2002). With the realisation that coupled surface melting and ice motion might provide a dynamic mechanism by which the ice sheet could respond rapidly to climate warming, the investigation of coupled hydrology-dynamics in the Greenland Ice Sheet has become a key research priority.

To date most research into coupled hydrology-dynamics has focused on understanding the behaviour of land-terminating margins of the ice sheet. Marine-terminating margins are sensitive to a number of other potential dynamic thinning mechanisms, including iceberg calving (e.g. Benn et al., 2007) and submarine melting of the terminus (e.g. Chauché et al., 2014), making it difficult to discern signatures of hydrologically-forced ice motion.

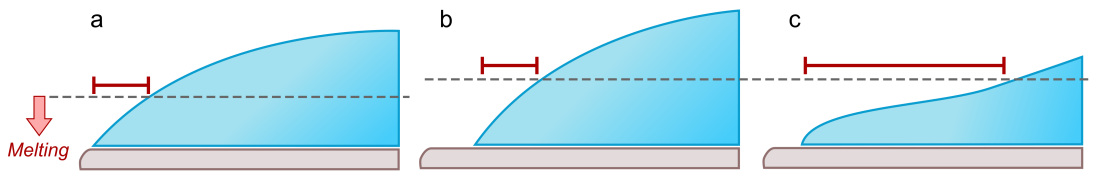

Figure 2.7: Response of land-terminating margins of the Greenland Ice Sheet to coupled hydrology-dynamics. Red bars show the size of the ablation zone. a: the margins in their present state. b: under projected climate change, the equilibrium line will rise and the interior of the ice sheet will thicken by accumulation while the margins will thin (e.g. Stocker et al., 2013; Shepherd et al., 2012). c: if coupled hydrology-dynamics has a positive feedback effect, ice will be moved more quickly from higher elevations into the ablation zone, causing melting over larger areas of the ice surface.

The speed at which land-terminating margins flow relative to up-glacier regions is important because it acts to determine the size of the ablation zone (Figure 2.7a). Climate change is predicted to result in more accumulation at higher elevations but also to cause thinning at lower elevations (Vaughan et al., 2013), which may cause the ablation zone to steepen and get smaller over time (Figure 2.7b). However, if coupled hydrology-dynamics has a positive feedback effect such that enhanced melting of the ice sheet results in faster ice motion, it will lead to faster ice drawdown from higher elevations, likely causing the ablation zone of the ice sheet to expand despite increased accumulation at higher elevations (Figure 2.7c; Parizek and Alley, 2004).

Research into the coupled hydrology-dynamics of the Greenland Ice Sheet has two major elements. The first element is to understand how meltwater generated on the ice sheet surface can force its way through thick ice to reach the ice sheet bed. Previous research on John Evans Glacier in the High Arctic has shown that ponded meltwater can initiate hydro-fracture through ice 150 m thick (Boon and Sharp, 2003). Further into the interior of the Greenland Ice Sheet, ice is over a kilometre thick, which has led to several major investigations into how the drainage of supraglacial lakes drives hydro-fracture to the ice sheet bed. The second element is to understand how variations in the rate of meltwater supply to the ice sheet bed change ice motion in both time and space, which is the focus of this thesis.

2.3.1 Supraglacial lake drainage and moulins

During the melt season many supraglacial lakes form in the ablation zone, with dimensions on the order of kilometres and depths in the region of tens of metres (e.g. Das et al., 2008; Sundal et al., 2009). Low surface gradients and back-slopes provide topographic depressions conducive to lake formation (Lüthje et al., 2006; Sundal et al., 2009), often spatially fixing the position of lakes (Box and Ski, 2007; Fitzpatrick et al., 2014). Lakes are more common higher in the ablation zone as longitudinal stretching nearer the ice sheet margin increases the likelihood of bed-connected crevasses and steeper margins provide less potential for ponding of meltwater in back-slope areas (Sneed and Hamilton, 2007), thereby allowing water to drain away without ponding. The number and size of supraglacial lakes have increased substantially at higher elevations during the last 40 years, closely following the mass balance equilibrium line (Howat et al., 2013).

Hydro-fracture models (e.g. Alley et al., 2005a; van der Veen, 2007; Krawczynski et al., 2009) suggest that large quantities of water are required to initiate penetration of a pathway to the ice sheet bed. Supraglacial lakes coalesce and store meltwater generated over days to weeks, which enables them to provide the quantities of meltwater required for hydro-fracture through ice as much as ∼2 km thick.

Lake drainage events have been widely observed both in the field (Boon and Sharp, 2003; Das et al., 2008; Doyle et al., 2013) and via remote sensing (McMillan et al., 2007; Box and Ski, 2007; Sneed and Hamilton, 2007; Sundal et al., 2009; Liang et al., 2012). The evolution and subsequent rapid drainage of supraglacial lakes is particularly common in the south-west of the ice sheet (Selmes et al., 2011). Lakes at lower elevations drain earlier in the melt season whilst those located further inland tend to drain later (Sundal et al., 2009), a pattern which is strongly correlated with air temperatures (Fitzpatrick et al., 2014).

Models indicate that successful hydro-fracture to the bed through ∼1 km of ice requires supraglacial lakes of dimensions ∼250–800 m across and ∼2–5 m deep in order to supply

sufficient meltwater to keep the crack full (Krawczynski et al., 2009). Complete drainage usually occurs in a matter of hours, rapidly introducing a large pulse of meltwater to the subglacial environment. Field observations show that during this time ice uplift occurs, causing widespread hydraulic separation and enhanced basal motion followed by subsidence within hours (Das et al., 2008; Doyle et al., 2013; Hoffman et al., 2011; Bartholomew et al., 2011a). Often, clusters of lakes drain at the same time, forcing extensive ice motion speedup over wider areas (Joughin et al., 2013; Fitzpatrick et al., 2014). If supraglacial meltwater continues to drain to the bed via the newly opened drainage pathway then a seasonally persistent moulin is likely to form. Lakes at higher elevations sometimes fill and drain multiple times during a melt season, suggesting that hydro-fracture by supraglacial lake drainage does not always result in persistent moulins in locations where ice is thicker and the hydraulic gradient shallower (Fitzpatrick et al., 2014).

Ice-penetrating radar surveys suggest that moulin locations are more correlated with areas of elevated along-flow tension (which promotes surface crevassing, providing an entry point for meltwater) than with the locations of supraglacial lakes (Catania et al., 2008). Furthermore, annually persistent moulins route a greater volume of water than one lake drainage (Catania et al., 2008). As evidence from south-west Greenland indicates that lakes delay the transmission of 7–14% of surface-generated meltwater (Fitzpatrick et al., 2014), the most important role of supraglacial lake drainage is therefore in controlling the timing of when many surface-to-bed connections are first established (Joughin et al., 2013), particularly further inland where ice is much thicker and it is therefore less likely that crevasses and persistent moulins are present. Subsequently, meltwater inputs to the ice sheet bed are controlled mainly by continuous supraglacial stream discharge into moulins.

Aerial photography and satellite imagery have shown that moulins in the western ablation zone of the Greenland Ice Sheet tend to persist in the same locations from one year to the next and may contribute to an established network of englacial channels (Chu, 2013). Between 300 m asl and 800 m asl they are present with a density of $\sim$12 moulins km^{-2} (Phillips et al.,

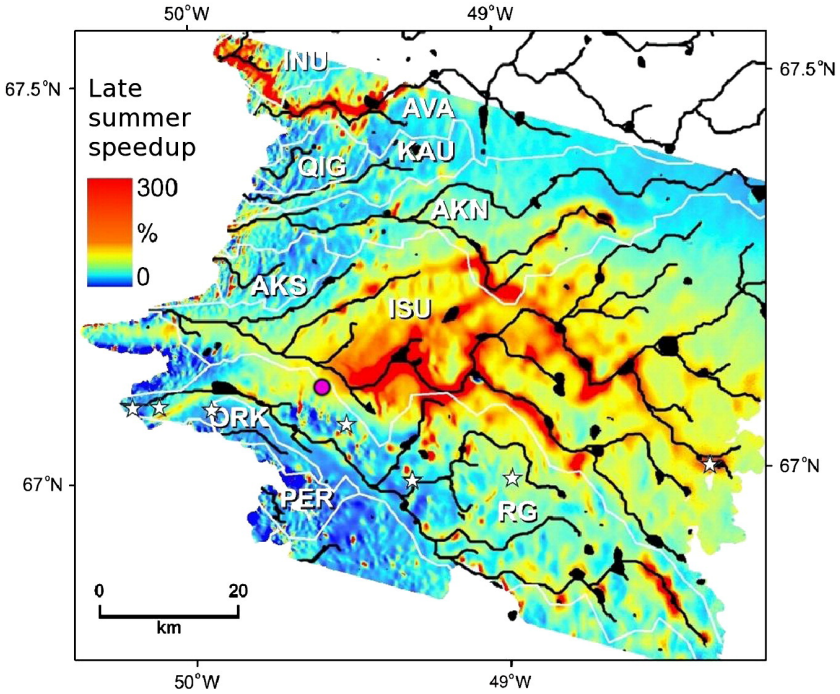

Figure 2.8: Late summer speedup in south-west Greenland. Supraglacial hydrological catchments (white lines) superimposed on late-summer minus winter-average velocity change (colour scale), together with supraglacial streams (black lines), topographic sinks (coloured black) and K-transect sites (white stars). The Leverett Glacier catchment is denoted 'RG'. Reproduced from Palmer et al. (2011).

2011). This is much greater than the density of supraglacial lakes (e.g. Sundal et al., 2009), which suggests that moulins drain the volumetric equivalent of multiple supraglacial lakes each year (Catania and Neumann, 2010).

2.3.2 Hydrologically-forced ice motion

The ablation zone of land-terminating regions of the Greenland Ice Sheet responds dynamically to meltwater in a similar way to alpine glaciers. The coincidence of enhanced surface melting with transient increases in ice motion is widespread amongst land-terminating outlet glaciers along the western margin of the ice sheet (Joughin et al., 2008). Observations of individual Greenland outlet glaciers indicate that meltwater can cause variability in ice motion from sub-diurnal to inter-annual timescales. Volumes of surface melting in individual supraglacial catchments are positively correlated with speedup observed during late summer

compared to winter and correspond closely with the locations of supraglacial sinks including lakes (Palmer et al., 2011, and Figure 2.8).

Over short timescales, Shepherd et al. (2009) found that Russell Glacier in south-west Greenland accelerated to peak daily velocity within ∼1–2 hours of peak melting as calculated by a positive degree day model. Surface uplift (1–4 cm) was consistent with hydraulic jacking, implying a role for transient cavity growth. Ice speedup was most pronounced after a cycle of lake drainage and thereafter was sustained at lower magnitude by continued routing of surface meltwater to the bed.

Episodic inputs of meltwater and coincident variations in proglacial discharge point to the timing and rate of meltwater supply as key controls upon the subglacial drainage system and thus hydrologically-controlled ice motion (Bartholomew et al., 2011a). Meltwater *volume* is of secondary importance. Thus, although the sensitivity of the subglacial drainage system to absolute meltwater inputs decreases over the "course of the melt season as the system increases its capacity and becomes more efficient, sufficiently large transient inputs of meltwater can still overfill the system, causing transient increases in P_w (Bartholomew et al., 2012; Cowton et al., 2013). Cyclical diurnal meltwater inputs related to air temperature produce a coincident response in ice motion, where diurnal melt maxima are associated with diurnal motion maxima (Bartholomew et al., 2011a). Similarly, short-term increases in the proglacial runoff hydrograph coincide with enhanced ice motion at nearby observation sites (Bartholomew et al., 2011a). Peak horizontal velocities occur when the rate of surface uplift is greatest, implicating 'stick-slip' motion. Stresses built up in the ice as the subglacial drainage system accommodates additional meltwater by raising P_w are released through transient decoupling of the ice from its bed (Bartholomew et al., 2012). This agrees with conclusions reached 30 years ago, that horizontal velocities are greatest during cavity growth (Iken, 1981). Moreover, the foregoing mechanism suggests that seasonal changes in ice motion are caused by the cumulative effect of varying meltwater supply rates over diurnal timescales (Bartholomew et al., 2012).

Working on the assumption that coupled hydro-dynamics is only active during the summer melt season when there is a meltwater supply, Sundal et al. (2011) seeked to quantify the net annual impact of hydrologically-forced ice motion by observing ice motion at sub-seasonal timescales, using 35-day mean velocities captured by satellite radar over multiple years. They found that in years of stronger melting the ice sheet appeared to flow more slowly — late-summer velocities were 39 ± 14% above mean winter 'background' values in years of higher melting but 102 ± 9% above mean winter 'background' values in years of lower melting along the south-west Greenland margin. Drawing on Schoof (2010), these findings led them to suggest that there was a critical runoff threshold beyond which the subglacial drainage system would switch to an efficient channelised system, resulting in overall slower motion during warmer years as the drainage system would transition to an efficient state earlier in the melt season due to larger meltwater inputs.

Observations made at high temporal resolution over the duration of several years show that the mechanism proposed by Sundal et al. (2011) to explain the lack of ice motion sensitivity to meltwater supply is incorrect. Seasonal ice acceleration is predominantly a function of locally-forced shorter-term speedup events of 1 day to 1 week in duration (Bartholomew et al., 2012). Ice acceleration as meltwater accesses the unchannelised, inefficient subglacial drainage system for the first time in the melt season is similar to 'spring events' observed on alpine and polythermal glaciers which are typically of a few days duration (Mair et al., 2003; Copland et al., 2003; Bingham et al., 2008). At Leverett Glacier, the magnitude of these events is greatest nearer the ice margin as ice motion increases by 300–400% above pre-summer velocities with significant uplift (implicating local hydrological forcing), compared to further inland where the spring events occur progressively later in the melt season, with velocity increases of 50–100% above pre-summer velocities and more subdued surface uplift (Bartholomew et al., 2012). Multi-day speedup events are widespread up to ∼50 km inland, likely associated with increased meltwater delivery from increased ablation or drainage of stored water which overwhelms the subglacial drainage system (Das et al., 2008).

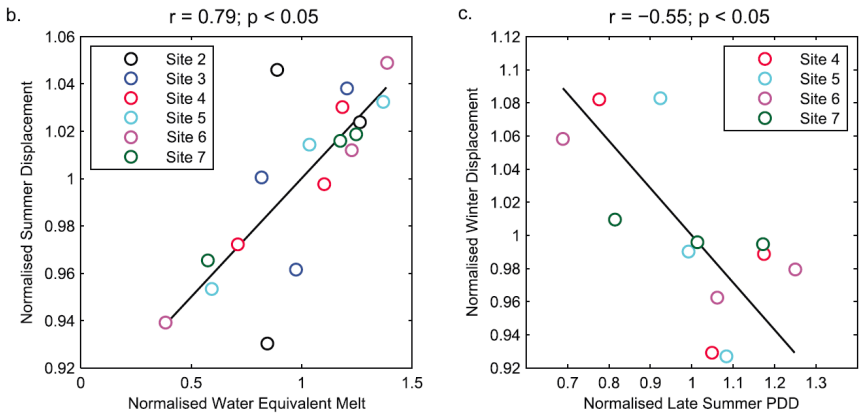

Figure 2.9: Seasonal relationships between melting and ice motion reproduced from Sole et al. (2013). Absolute differences in the magnitude of ice displacement and water equivalent melt between sites were normalized by dividing each value by the mean of values for all years at a particular site. (b) Relationship between normalized water equivalent melt and normalized summer ice displacement. (c) Relationship between normalized late summer positive degree days and normalized winter ice displacement.

After the spring event has occurred, ice motion tends to slow down from the spring event peak velocity, even if meltwater continues to be supplied to the the ice sheet bed at the same rate as during the spring event. Hydrological and tracing investigations undertaken at Leverett Glacier show that the subglacial drainage system quickly develops efficient drainage pathways and expands upglacier in response to melt onset (Bartholomew et al., 2011b; Cowton et al., 2013), which increases the capacity of the subglacial drainage system and enables meltwater to be evacuated more quickly. These efficient drainage pathways develop to at least 40 km inland, where the ice is 1 km thick (Chandler et al., 2013). Subsequent periods of faster ice motion will only occur when the rate of meltwater supply exceeds the routing capacity of the subglacial drainage system, causing P_w to increase and leading to transient ice-bed separation and enhanced basal sliding until the drainage system adapts to the increased rate of meltwater supply (Bartholomew et al., 2012; Cowton et al., 2013).

These observations show that an increase in the rate of meltwater supply which overwhelms the routing capacity of the drainage system — channelised or not — will always lead to transient periods of faster ice motion during summer compared to if the increase in the rate of meltwater supply had not occurred. Longer melt seasons are therefore likely to result in

more ice flow during summer (Sole et al., 2013). The subglacial drainage system does not become so efficient that it reduces ice flow during summer as has been posited previously (van de Wal et al., 2008; Sundal et al., 2011). Three years of data from Leverett Glacier show that warmer summers result in more summer ice flow (Figure 2.9b), but less ice flow during the subsequent winter (Figure 2.9c) compared to the 'average' melt-year of 2009, such that over the course of a full melt-year there is no significant correlation between summer melting and annual ice flow (Sole et al., 2013). Flow during the winter is therefore a function of the preceding summer, in terms of the duration and volume of melting and the subglacial drainage system morphology which evolved in response.

Andrews et al. (2014) made simultaneous observations of hydraulic head in both moulins and boreholes in the ablation zone of the western Greenland Ice Sheet. They found that as the melt season progressed, moulin hydraulic head underwent large diurnal oscillations, but neither the minimum nor maximum daily moulin hydraulic head decreased, leading them to suggest that P_w decreases in the efficient, channelised system do not control decreases in ice motion later in the melt season. Meanwhile, hydraulic head in the boreholes oscillated at much lower amplitude, and was anti-correlated with diurnal velocity maxima, suggesting that they were connected to hydrologically isolated areas of the ice sheet bed. Andrews et al. (2014) proposed that pressurisation of hydrologically connected areas of the bed induces sliding in those areas, which is transmitted to hydraulically isolated areas by stress transfer laterally through the ice. The consequent sliding of hydraulically isolated areas increases the volume of cavities, reducing P_w, which in turn acts to limit sliding. Andrews et al. (2014) therefore suggested that decreases in P_w in the isolated areas of the bed over the course of the melt season may explain the winter mediation of summer acceleration as identified by Sole et al. (2013) and Tedstone et al. (2013).

Over inter-annual timescales the net impact of coupled hydrology-dynamics is unclear. Few observations of ice motion over inter-annual and decadal timescales have been made. The K-transect, consisting of 8 GPS stations on the south-west Greenland Ice Sheet, showed an

average 10% decrease from 1991 to 2007 (van de Wal et al., 2008); the slow-down trend at lower sites continued into 2012 (van de Wal et al., 2012) but small acceleration signals (2% net increase in annual flow over 2009–2012) were identified above the equilibrium line (Doyle et al., 2014). Using a combination of boreholes and modelling, some studies have proposed that shallow bed gradients coupled with >1 km thick ice prevent the evolution of channelised subglacial drainage systems further into the ice sheet interior. They therefore suggest that higher elevations may be sensitive to enhanced meltwater inputs in a warming climate as drainage system morphology cannot easily evolve to reduce P_w (Dow et al., 2014; Meierbachtol et al., 2013).

Remote sensing campaigns undertaken over inter-annual timescales have concentrated on seasonal and sub-seasonal snapshots of ice motion. Moon et al. (2012) compiled winter velocity maps for 2000/2001 and then every winter from 2005/6 to 2010/11. In the land-terminating regions of the south-west Greenland Ice Sheet, they found that in winter 70% of surveyed glaciers with a notable trend slowed down from 2005 to 2010. However, because they were unable to capture observations of summer ice motion, annual ice motion is unknown. Fitzpatrick et al. (2013) used sub-seasonal snapshots of summer and winter motion to show that 48% of their study catchment slowed down to less than the winter flow mean by the end of summer, but they did not have observations with which to examine variability in ice motion during the subsequent winter.

Theoretical and modelling studies provide a complementary perspective to observations of coupled hydrology-dynamics. The recent observations made over the Greenland Ice Sheet have renewed community interest in modelling subglacial drainage and its impact on ice motion (Flowers, 2015). Modelling enables the impact of future climate scenarios upon ice sheet dynamics to be estimated, and the sensitivity of different processes and parameters to be tested, with the ultimate aim of improving sea level rise projections for the next century. There have been some important specific advances since the IPCC's 4$^{\text{th}}$ Assessment Report (Meehl et al., 2007), which omitted dynamic responses of the ice sheet to climate change.

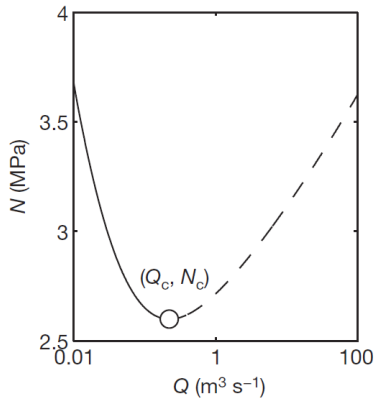

Figure 2.10: Steady-state effective pressure (N) versus discharge (Q) in a conduit. Below the critical discharge Q_c the conduit remains a cavity (solid line). A conduit becomes a channel (dashed line) at the point Q_c is exceeded (circle). Reproduced from Schoof (2010), Figure 1d.

Schoof (2010) developed a model which captures for the first time the dynamic switching between 'distributed' (cavity) and 'efficient' (channelised) subglacial drainage over seasonal timescales based on effective pressure (Figure 2.10). It accommodates short-term fluctuations in P_w as conduit size evolves slowly in response to rising melt inputs, such that large but short-lived pulses of meltwater supply can only be accommodated by increased P_w rather than by channel growth. This is presumed to lead to hydraulic jacking and transiently faster ice motion. Schoof (2010) proposed that over longer timescales, however, higher rates of steady water supply should suppress rather than enhance ice motion, due to expanding channelisation of the drainage system. This does not agree with observations which show that ice motion is faster during warmer summers, when the subglacial drainage system is challenged to evacuate larger rates of meltwater supply for longer, resulting in longer periods of over-pressurisation (Sole et al., 2013).

Subglacial drainage modelling by Werder et al. (2013) showed that water can flow in and out of channels over diurnal timescales, resulting in complex spatio-temporal patterns of P_w across the subglacial drainage system. However, the evolution of a modelled efficient subglacial drainage system takes months, as opposed to days, according to tracer observations from the ice sheet margin (Cowton et al., 2013).

Models which physically link hydrology and ice motion are in a state of rapid development and while they now capture a number of essential aspects of the coupled system, calibration tends to remain out of reach, particularly as direct observations of the ice sheet bed remain a significant challenge (Flowers, 2015). For example, Pimentel and Flowers (2011) found that over seasonal timescales they could generate results that qualitatively compared well with observations made by Shepherd et al. (2009) but, despite driving the model with diurnally varying meltwater inputs, they were unable to reproduce corresponding diurnal variability in ice motion. Hewitt (2013), using the same essential hydrology formulation as Schoof (2010), suggested that increased melting associated with future climate scenarios will result in *faster* summer ice motion despite the establishment of an efficient channelised drainage system, particularly further inland where the drainage system capacity is overwhelmed, leading to higher P_w all summer. Meanwhile, Mayaud et al. (2014) applied a model originally designed to simulate sewage pipe systems to simulate P_w in response to projected runoff during the 21st century. This model, previously used in the Swiss Alps, is inherently channelised — the interaction of channelised drainage with surrounding areas of distributed drainage is not accounted for (Arnold et al., 1998; Banwell et al., 2013). They concluded that in years of more melting, channelization will occur earlier, leading to *slower* summer ice motion. Thus, the choice of model physics can strongly affect the overall conclusion reached.

Nevertheless, the diagnostic capabilities of models are beginning to provide useful constraints on dynamic sensitivities. Hoffman and Price (2014) found that the dominant feedback between subglacial hydrology and dynamics is negative: sliding over bedrock bumps opens additional cavity space, lowering P_w and in turn reducing ice motion, which is similar to the slowdown mechanism proposed by Andrews et al. (2014). The positive feedbacks of (1) increasing P_w through frictional melting during sliding and (2) strain softening of basal ice during localized speedup causing cavities to close more quickly, are less important (Hoffman and Price, 2014). Moreover, the results of Hoffman and Price (2014) also indicate that sustained input to the distributed drainage system leads to the gradual decay of ice

motion even in the absence of channelisation, due to the aforementioned increases in cavity capacity which causes P_w to decrease.

While the precise physics of coupled hydrology-dynamics remains a significant topic of research, useful progress is being made via the parameterisation of basal lubrication in higher-order ice sheet models. Shannon et al. (2013) calculated a best-fit parameterisation using observations of melting and ice motion from south-west Greenland. Like the selection of observations presently available, the parameterisation is equivocal as to whether subglacial hydrology will limit the potential for speedup of flow. Shannon et al. (2013) applied the best-fit parameterisation to higher-order ice sheet models forced by climate projections for the coming century and found that whilst basal lubrication will change the form and flow of the ice sheet, the mechanism is unlikely to increase the contribution of the ice sheet to sea level rise by more than 5% of the contribution expected from the negative surface mass budget alone.

2.4 Research at Leverett Glacier

The research presented in this thesis has been undertaken as part of a broader collaborative project investigating the hydrology and dynamics of Leverett Glacier, a land-terminating glacier in south-west Greenland. The project was initiated in 2008 by Peter Nienow (University of Edinburgh), Doug Mair (University of Aberdeen) and Jemma Wadham (University of Bristol) and has been principally funded by two Natural Environment Research Council grants. The fieldwork programme ran from 2008 to 2012. The project has resulted in a significant range of published findings, ranging from subglacial drainage system morphology (Bartholomew et al., 2011b; Cowton et al., 2013; Chandler et al., 2013) and coupled hydrology-dynamics (Bartholomew et al., 2010, 2011a, 2012; Sole et al., 2013) which are summarised below, to subglacial erosion rates (Cowton et al., 2012), nitrogen fixation by microbial communities (Telling et al., 2012) and the export of labile carbon

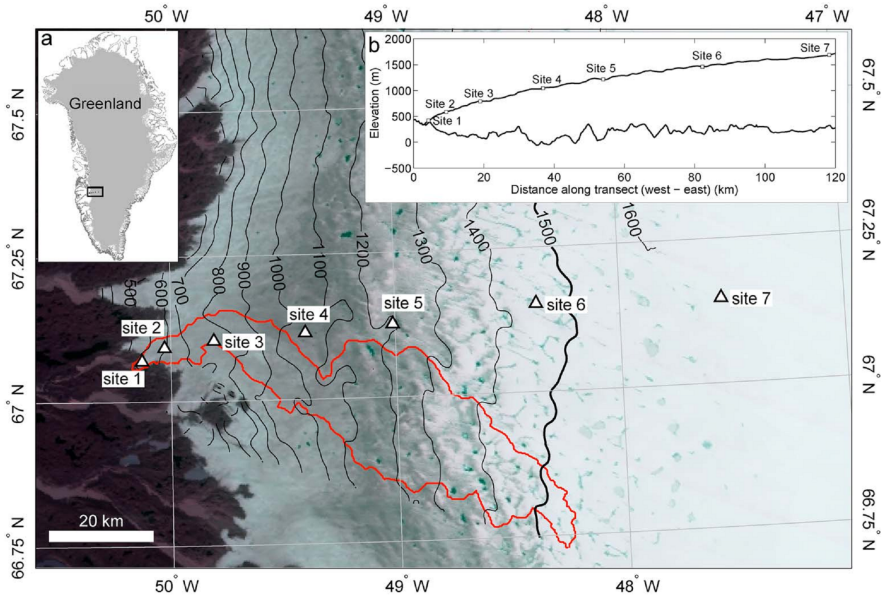

Figure 2.11: (a) Location of the Leverett Glacier study region on the western margin of the Greenland Ice Sheet. (b) Ice surface and bed elevation along the transect of sites 1–7. Main panel: location of GPS sites. Contours at 100 m intervals. The bold contour represents the approximate equilibrium line altitude estimated by van de Wal et al. (2008). The Leverett Glacier hydrological catchment is shown in red. Figure reproduced from Sole et al. (2013).

(Lawson et al., 2014) and iron (Hawkings et al., 2014) to the ocean — potentially with important ramifications for marine productivity and carbon cycling.

During the first season of fieldwork in 2008, observations of melting and ice motion were made at four transect sites on Russell Glacier, the land-terminating glacier immediately to the north of Leverett Glacier. These observations showed that surface meltwater inputs to the glacier bed cause seasonal acceleration of ice motion, but that the relationship between melt and ice motion varies both through the melt season and according to the distance from the glacier margin. Greater increases in melting are required to sustain higher velocities as the melt season continues, suggesting that the drainage system becomes more efficient and expands up-glacier during the melt season in a manner similar to alpine glacier systems (Bartholomew et al., 2010).

Work at Russell Glacier was to become a pilot project for the following four years of work at Leverett Glacier, commencing in 2009. Leverett Glacier (Figure 2.11) drains a much larger

hydrologic catchment than Russell Glacier. An ice-marginal camp was established to enable the collection of hydrological data throughout the melt season. On the ice sheet, the transect of observation sites established on Russell Glacier in 2008 was extended to 115 km inland, thereby extending above the equilibrium line estimated by van de Wal et al. (2008).

The more extensive observations from Leverett Glacier showed that seasonal upglacier expansion of an efficient subglacial drainage system occurred across a catchment of >600 km^2, beyond 50 km from the ice sheet margin, in response to surface meltwater inputs accessing previously unchannelised regions of the bed (Bartholomew et al., 2011b). Coincident measurements of ice motion showed that in the lower ablation zone, the evolution of the subglacial drainage system limited the contribution that enhanced motion due to coupled hydrology-dynamics could make to annual motion, while in the upper ablation zone the key limitation on enhanced ice motion was the short timeframe during which meltwater was able to access the ice sheet bed (Bartholomew et al., 2011a). Comparison of dynamics data collected over two melt seasons — 2009 and 2010 — showed that seasonal changes in ice velocity were dominated by rapid variations in meltwater inputs from the glacier surface. Together with subglacial conduit modelling, this led Bartholomew et al. (2012) to conclude that the duration and rate, rather than absolute volume of meltwater delivery to the subglacial drainage system, are critical to controlling seasonal ice velocity variations.

Up to this stage conclusions pertaining to the structure of the subglacial drainage system had been made only by reference to observations of surface melting, proglacial runoff characteristics (discharge, suspended sediments and electrical conductivity) and ice motion. No detailed investigations of the subglacial drainage system structure had been made. Cowton et al. (2013) deployed pressure sensors in moulins, and undertook multiple dye tracer investigations along the lower 14 km of Leverett Glacier. They found that following melt onset in spring, the englacial water table regularly rose, indicating that local inputs to the drainage system were exceeding the drainage capacity, causing P_w to rise. Transition from the winter distributed drainage morphology to channelised drainage occurred rapidly following

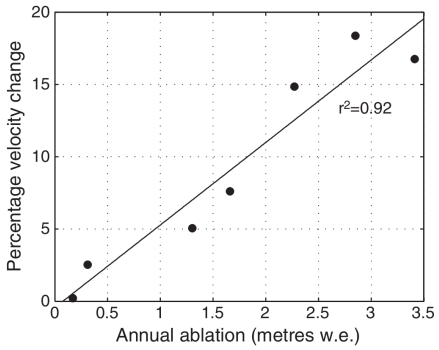

Figure 2.12: Percentage change in mean annual ice velocity vs. total surface ablation (m w.e.) at Leverett Glacier GPS sites during 2009. The increase in annual ice velocity is calculated as the percentage by which the observed annual displacement exceeds that which would occur if the ice moved at a steady winter rate (net displacement from 1 September to 30 April of following year) all year round. Figure reproduced from (Bartholomew et al., 2011a), Figure 6. Note that the interpretation of this figure in Bartholomew et al. (2011a) is no longer considered to be correct.

melt onset, although high velocity events continued to occur, indicating that hydrological forcing of ice motion by transient increases in P_w is possible even in a channelized drainage system. Further upglacier, tracer investigations using sulfur hexafluoride (SF_6) revealed the evolution of a fast, efficient channelised drainage system to at least 41 km from the ice margin, where the ice is approximately 1 km thick (Chandler et al., 2013).

Data collection at Leverett Glacier was initially intended to yield two summer seasons of observations during 2009 and 2010 plus observations of the intervening winter. These were two very different melt seasons: 2009 was 'average' compared to the last fifty years of melting, whilst 2010 saw melt volumes unprecedented in the previous few decades. A story of warmer summers forcing faster annual ice motion started to emerge — suggesting that coupled hydrology-dynamics could have a runaway, positive feedback effect on ice motion in a warming climate (Figure 2.12 and Sole et al., 2010). However, an opportunity to continue the campaign into 2011 enabled additional observations of summer and winter ice motion to be made. Comparison of these three years of data revealed a very different story: whilst larger melt volumes were positively correlated with summer motion, they were negatively correlated with net winter motion (Sole et al., 2013), whereas winter motion had previously been assumed to occur at a constant rate (Figure 2.12 and Bartholomew et al., 2011a). As

a result, melting was found to *not* be correlated with annual ice motion. Increased summer melting preconditions the subglacial drainage system for reduced winter motion as larger, more extensive subglacial channels drain high basal water pressure regions, resulting in limited dynamic sensitivity to inter-annual variations in surface melting (Sole et al., 2013).

Research at Leverett Glacier has therefore shown that many of the previous findings undertaken at alpine and High Arctic glaciers are applicable to the margins of the Greenland Ice Sheet. The body of literature which addresses the hydro-dynamics of the Greenland Ice Sheet has grown rapidly during the last decade in particular, with many significant findings made at Leverett Glacier. However, considerable uncertainties remain. These include (1) which of meltwater supply rates versus volumes is most important to generating ice motion; (2) the impact of a spatially heterogeneous subglacial drainage system upon ice motion; (3) the net impact of coupled hydrology-dynamics upon ice motion over timescales commensurate with climate change; and (4) the role of coupled hydrology-dynamics at higher elevations where water does not often reach the ice sheet bed. In the rest of this thesis various aspects of these uncertainties are explored, with the overall aim of constraining more accurately the likely hydro-dynamic response of the Greenland Ice Sheet to Earth's changing climate.

Chapter 3

Methods

The research presented in this thesis utilises data from the south-western Greenland Ice Sheet. Most of the field data presented in this thesis were collected during the 2012 melt season at Leverett Glacier, west Greenland (Figure 3.1 box A). Data presented from previous field campaigns at Leverett Glacier were collected by other researchers and many of the findings from those earlier field campaigns are summarised in Chapter 2. Satellite remote sensing was used to examine ice motion across the lower ablation zone of Leverett Glacier (box B) and across the neighbouring 170 km stretch of ice sheet margin which continues northwards to Jakobshavn Isbrae (box C). The region corresponding to box C was chosen to take advantage of an extensive archive of satellite data, yielding significantly finer spatio-temporal resolution than is possible in the region centred on Leverett Glacier.

The results chapters 4–6 which follow each have their own Methods section which detail the most relevant information for that chapter. This chapter provides a broader overview and context together with more detailed descriptions of all the methods used.

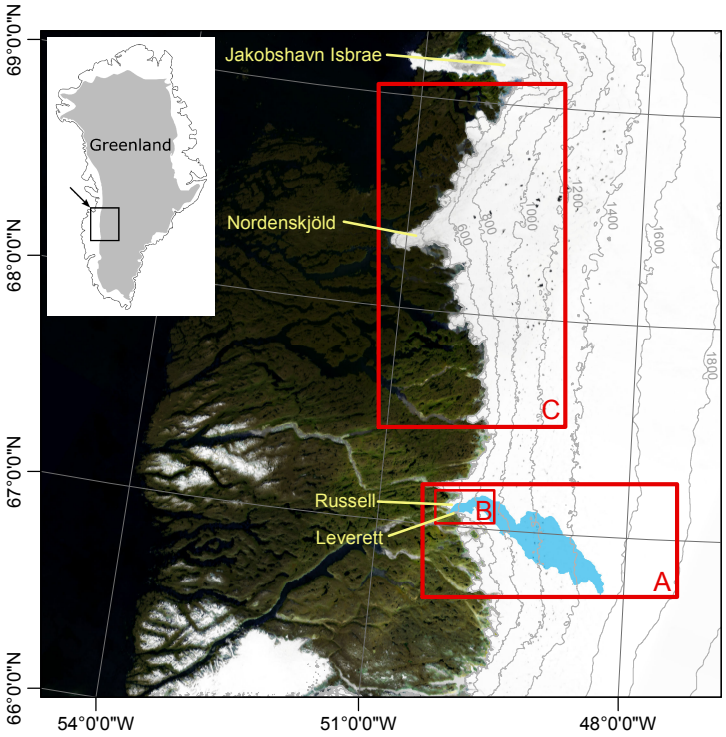

Figure 3.1: Location of study areas along the south-west margin of the Greenland Ice Sheet, with True Marble 500 m background derived from Landsat 7 ETM+ data (copyright Unearthed Outdoors LLC). Red boxes indicate approximate bounds of study areas used in chapters 4 (A), 5 (B) and 6 (C). Leverett Glacier's surface hydrological catchment (shaded blue) derived from a surface digital elevation model (Palmer et al., 2011). Names of selected outlet glaciers (yellow). Ice surface contours (grey) derived from Howat et al. (2014).

3.1 Field area

Leverett Glacier (67°03'N, 50°07'W) is a land-terminating glacier on the western margin of the Greenland Ice Sheet (Figure 3.2). Its tongue lies directly to the south of the neighbouring Russell Glacier (Figure 3.3), and it has a potential hydrological catchment of ~1200 km^2 defined by the supraglacial topography (Palmer et al., 2011). During summer months, Leverett Glacier has an order of magnitude more proglacial meltwater discharge than Russell Glacier (I.D. Bartholomew, *pers. comm.*). Hydraulic potential analysis suggests that subglacial water pressure must rise towards ice overburden pressure near to the margin in order to enable water to flow through a basal over-deepening located a few kilometres upglacier

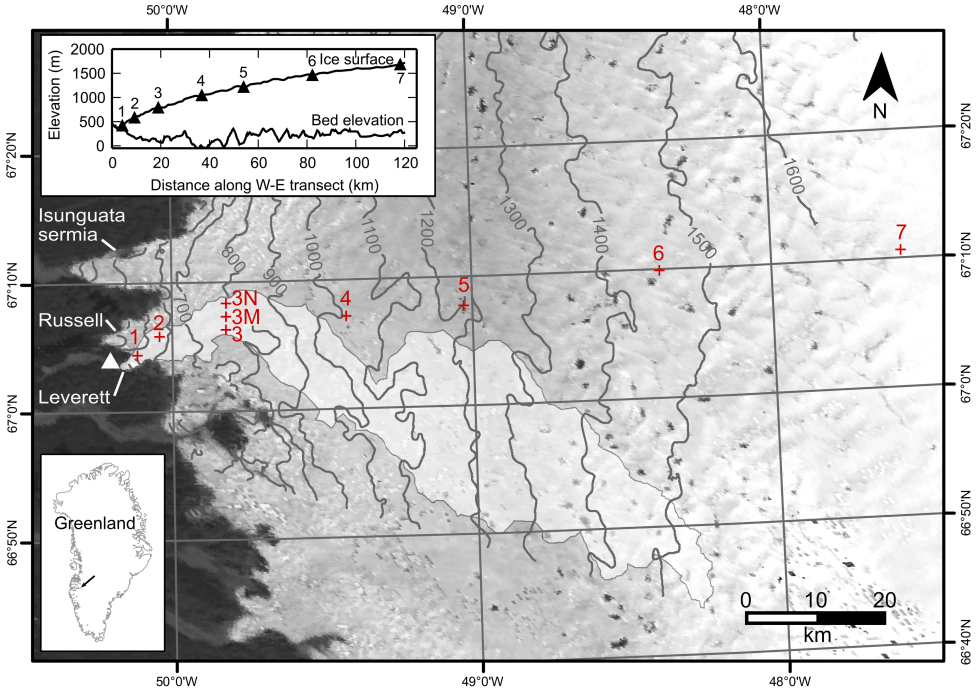

Figure 3.2: Leverett Glacier and the surrounding area, on the western margin of the Greenland Ice Sheet. Crosses indicate sites where ice motion, air temperature and total seasonal surface melting were measured. The triangle indicates where proglacial discharge was measured and the GPS base station and field camp were located. Contours (metres) are from a digital elevation model (DEM) of the ice sheet surface produced from InSAR (Palmer et al., 2011). The inferred hydrological catchment of Leverett Glacier, delineated in light grey, was calculated from the ice sheet surface DEM. Inset: surface and bed elevation along our transect measured by IceBridge ATM (ILATM2) and MCoRDS (IRMCR2) in 2010 and 2011 respectively (Allen, 2011).

(Figure 3.2 inset, as identified by airborne geophysical surveys; see Section 5.2 for more information) before draining from the portal at the snout of Leverett Glacier (Figure 3.4).

Most of the field data presented in this thesis were collected during the 2012 melt season. The data presented from previous years were collected by other researchers and many of the findings from those earlier field campaigns are summarised in Chapter 2.

There were two components to the 2012 field campaign. The first involved the use of Global Navigation Satellite Systems (GNSS) to measure ice motion at diurnal, seasonal and annual timescales at nine sites up to 120 km from Leverett Glacier's tongue into the ice sheet interior.

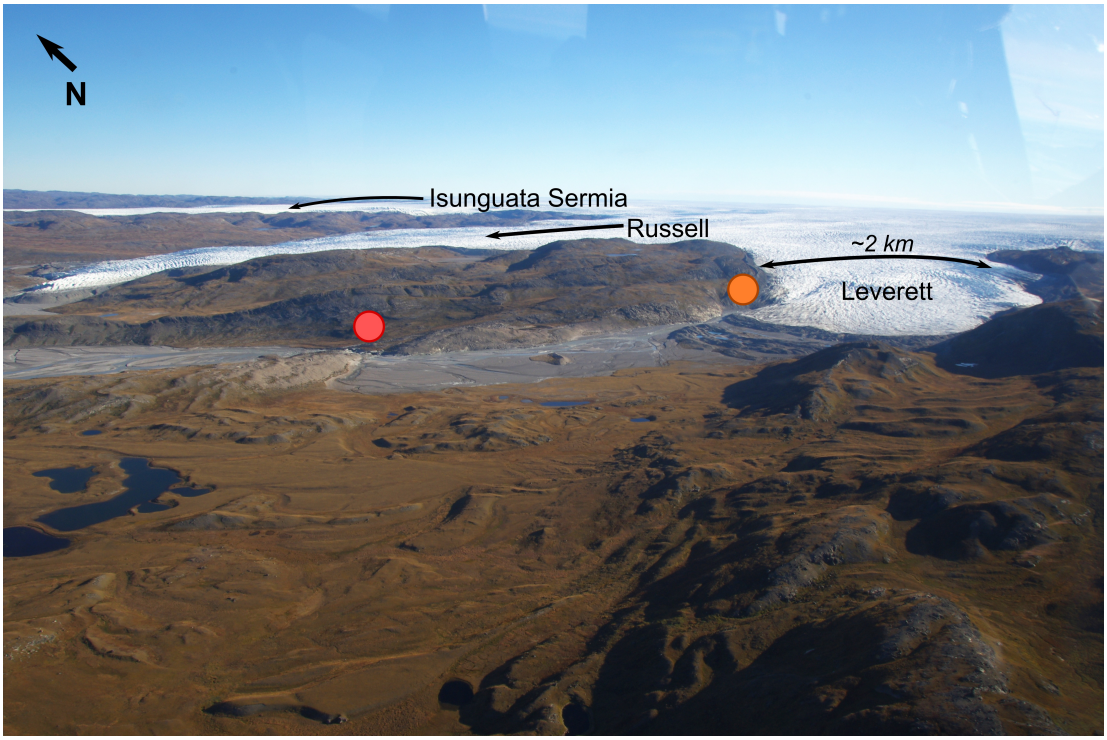

Figure 3.3: An oblique view of Leverett Glacier, with Russell Glacier and Isunguata Sermia to the north. Water exits Leverett Glacier below the orange circle. The stable bedrock section approximately 2 km downstream through which proglacial discharge is gauged is below the red circle. Photograph taken in August 2012.

The second field component monitored the hydrology of the meltwaters draining from the Leverett Glacier portal (Figure 3.4). The methods used for these components are described in more detail in the following sections.

3.2 Sites S1 to S7

Seven on-ice transect sites (Figure 3.2) operated for the full duration of the 2009–2013 field campaign. The sites were deployed along Leverett Glacier's flow-line (S. Palmer, pers. comm.) which, beyond ∼35 km inland, diverges from the supraglacial hydrological catchment. Dynamics records collected at sites further inland than S3 therefore cannot be directly compared with bulk proglacial runoff records. Two further sites were installed for

Figure 3.4: The single meltwater discharge portal at Leverett Glacier's terminus in September 2012, located at the orange circle in Figure 3.3. The portal is ~30 m wide. Note the ice surface depression up-ice of the portal, which is evidence of a large subglacial channel draining from the ice sheet interior.

the research conducted in this thesis: S3N (June 2011–May 2013) and S3M (May 2012–May 2013), to provide observations of ice surface velocity transverse to an inferred efficient subglacial drainage axis within Leverett Glacier's supraglacial hydrological catchment.

Each transect site recorded ice motion, near-surface air temperature and total seasonal melt, whilst selected sites also measured melt rates at 15 minute intervals and observed supraglacial lake filling and drainage using hourly photos from time-lapse cameras. An example of the data collection set-up at a transect site is shown in Figure 3.5. Sensors and solar panels were mounted on a support pole drilled up to 6 m into the ice which froze in subsequently. Data loggers and batteries were installed in enclosures tethered to the support pole, allowing the enclosures to move with surface melting.

All transect sites were visited by helicopter at the beginning and end of the melt season

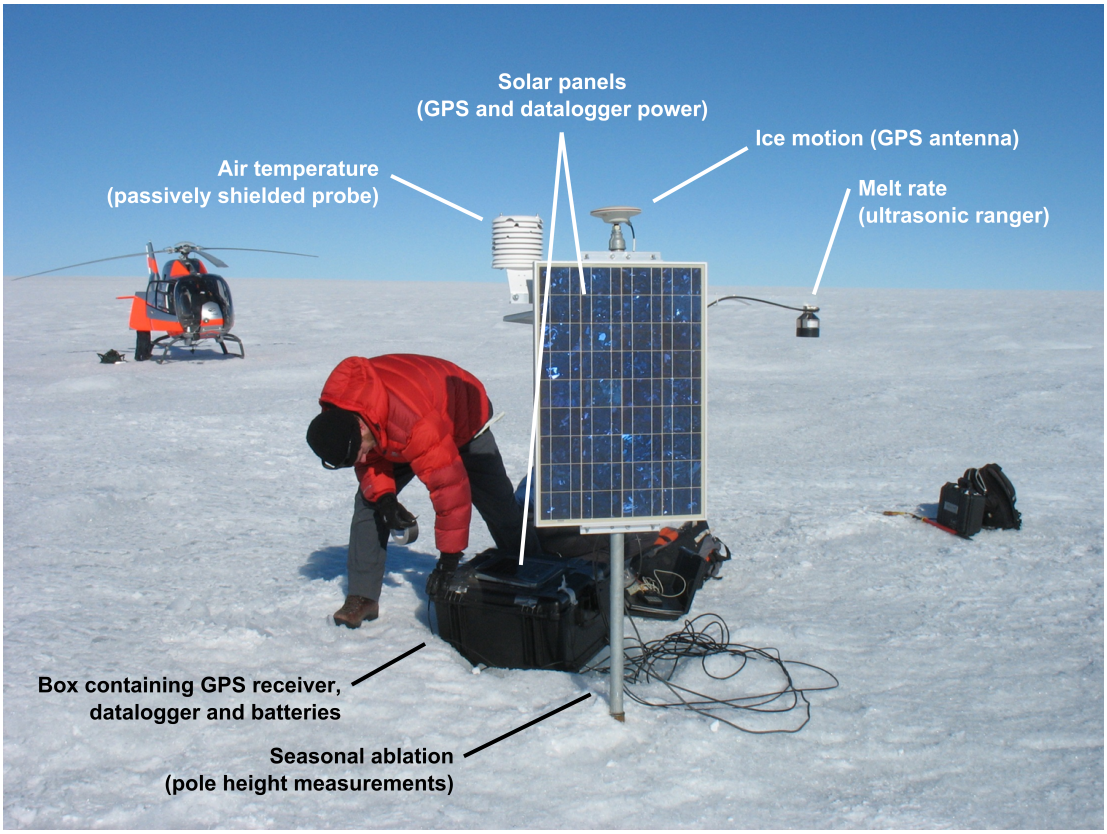

Figure 3.5: Instrumentation deployed at transect observation site S4. Photo: P. Nienow.

each year to download data and undertake essential maintenance including redrilling of the support poles (due to exposure by surface melting) and replacing batteries. Sites S1 and S2 were accessible on foot from the field camp near to the ice sheet margin and therefore received maintenance visits more frequently during the melt season.

3.2.1 Air temperature, accumulation and melting

Leverett Glacier is situated in a semi-arid region of the ice sheet (Ohmura and Reeh, 1991). During 2001–2012, average annual precipitation at Kangerlussuaq (~20 km away from the glacier margin) was 258 ±63 mm w.e. y^{-1} (Mernild et al., 2014). The majority of the annual precipitation falls as snow during the winter season, whilst during the summer model findings indicate that runoff is dominated by melting of the ice sheet surface (Mernild et al., 2010). As a result, measurements of snow accumulation are necessary but measurements

of rainfall are not, apart from on rare occasions such as at the end of the 2011 melt season (Sole et al., 2013). Near-surface air temperatures, surface melting and snow accumulation immediately prior to the onset of the melt season were measured at each transect site to constrain the hydrological forcing of ice motion by surface melting.

At S1, S3 and S6, air temperatures were measured using shielded Campbell Scientific (CS) T107 temperature sensors and melt rates were measured using CS SR50A ultrasonic ranging devices. Both sensors were connected to CS CR800 data loggers. At all other sites air temperatures were measured using shielded HOBO U21-004 temperature sensors. All sensors sampled once per minute and stored a mean value every 15 minutes.

Net seasonal melting was measured at each site apart from S1 using ablation stakes. Snow accumulation since the end of the previous melt season was measured shortly prior to melt onset each year by using a probe to measure the depth to the previous summer's surface in order to split subsequent melting into snow and ice components and subsequently into water equivalent totals. In conjunction with the snow accumulation measurements, at transect sites with ultrasonic ranging devices the date of the transition from snow to bare ice could be identified, enabling calculation of melt rates specific to the snow and ice components.

Lastly, the observations of wind speed used in Chapter 4 were obtained from several Programme for Monitoring of the Greenland Ice Sheet (PROMICE)/Greenland Analogue Project (GAP) sites (www.promice.org), the locations of which are shown in Figure 4.1. Automatic weather station are maintained at each of these sites by the Geological Survey of Denmark and Greenland (GEUS) and measure wind speed as well as several other meteorological parameters once per hour.

3.2.2 Ice surface motion

Global Navigation Satellite Systems (GNSS) were used to observe ice surface motion at each transect site. GNSS has a number of benefits over the traditional surveying techniques

commonly employed at alpine glaciers. Receivers can be deployed out of view of stable reference points and will operate autonomously with infrequent manual intervention. Temporal resolution is much higher and uncertainties can be reduced to millimetres if processed appropriately (King, 2004). However, the expense of deploying GNSS receivers limits their spatial coverage to only a few locations on the ice sheet surface, unlike satellites which can observe velocities over wide areas but at lower temporal resolution (see Section 3.4).

A GNSS receiver calculates the position of its antenna by measuring the apparent transmission time of timing signals broadcast from GNSS satellites in the L1 band. The two operational GNSS constellations, GPS and GLONASS, each provide continuous global coverage, enabling position calculations to be made anywhere on Earth. The number of GNSS satellites visible in the sky from any one point on the Earth varies through time. A receiver must acquire signals from at least four satellites to calculate its position using a form of trilateration (the process of determining location using measurements of the distance between the antenna and each receiver). The accuracy of the position fix increases with the number of satellites visible to the antenna.

Unlike ordinary GNSS receivers, which only receive a single-frequency (the timing signal), dual-frequency receivers also receive a signal transmitted in band L2 containing the satellite ephemeris data (location and health). This enables the position of the receiver to be determined more accurately than by L1 signals alone and 'bad' satellites to be removed from the location solution calculated by the receiver.

Precision of the position fix can be further improved by use of a static, stable ground reference station. This correction signal can either be applied in real-time or during post-processing. In the first year of the campaign (2009) post-processing utilised the International GNSS Service (IGS) reference station located at Kelyville, ∼40 km west from S1. However, the quality of the correction signal decays with distance from the reference station, and Kelyville only records observations every 30 seconds, which resulted in two thirds of the recorded

data from the several transect sites that recorded every 10 seconds being discarded. During 2010–2013, we therefore maintained our own GNSS reference station at the ice-marginal field camp, ∼4 km from S1, which recorded an observation every 10 seconds.

At each transect site a dual-frequency GNSS receiver, either a Leica System 500 or Leica System 1200, was mounted on a pole drilled and frozen into the ice, providing measurements of movement independent of ablation. Both receiver types utilised the GPS constellation of satellites. Each receiver was powered by a lead acid or dry cell battery charged by a solar panel mounted on the same pole, with sufficient capacity for observations to be made every 10 seconds or 30 seconds (determined during system configuration at the start of the 2009 field campaign) throughout the melt season. Power supplies were configured to maximise data acquisition during autumn as the sun's position in the sky progressively lowered. Data acquisition stopped during the dark polar winter as power supplies were depleted, and in most cases did not re-start until the sites were visited prior to the start of the following melt season. However, it was still possible to calculate net winter ice motion by recording the absolute position of the support pole in spring prior to melt onset.

During post-processing, data from each receiver were first converted to the RINEX format using TEQC (Estey and Meertens, 1999). Position observations from each site were then corrected using TRACK 1.27 (Chen, 1999), which first applies the correction signal from a static reference station and then computes the kinematic trajectory of the corrected data. Processing utilised the Final Orbit solutions produced by the International GNSS Service, in which satellite orbits have a stated accuracy of ∼2.5 cm. Observations were split into overlapping 28 h windows to negate edge effects when the windows of data were subsequently spliced back together. Each window of data was processed individually using a semi-automated, quality-controlled processing chain developed for this thesis (based on the existing chain created by M. King, I. Bartholomew and A. Sole, pers. comm.). A-priori coordinates for each window were taken from the solution for the previous window, or from Precise Point Positioning (PPP) if the window was the first in the time series.

The windowed approach enabled immediate isolation during processing of windows of data in which many ambiguities remained unresolved, as data in the 28-h window would display high scatter. These ambiguities are often due to ionosphere effects which alter the propagation of the L1 and L2 signals, for instance by range errors (varying total electron content changes the effective path length of the signal) or scintillation (small scale irregularities in electron density cause cycle slippage or loss of signal lock) (Klobuchar, 1991). Ambiguous windows of data were therefore reprocessed using modified ionosphere correction parameters, specifically (1) increasing the ion delay period allowed before flagging data biases; (2) reducing the weighting given in the solution to the deviation of the Melbourne-Wubbena wide lane (which gives the difference between the biases in the L1 and L2 signal frequencies) and (3) reducing the weight given to the deviation of the ionospheric delay from zero. Windows of data which remained ambiguous despite re-processing were discarded. Once post-processed, the first and last two hours of each window were discarded and the whole time-series was spliced back together.

Post-processed observations were converted to maximum along-track and cross-track displacements, filtered using a high-pass Gaussian filter and then differenced every 24 hours to calculate daily velocities. Shorter-term variations in ice velocities were obtained by differencing positions observed 6 hours apart. Horizontal velocity uncertainties are approximately ±1 cm at each epoch and 5.2 m yr^{-1} for daily velocities (Bartholomew et al., 2011a). Vertical displacements were estimated from the elevation observations by removing the linear trend attributable to down- or up-slope movement, retaining just the signal attributable to dynamic ice motion. The uncertainty in vertical displacement is <1 cm (Bartholomew et al., 2012).

3.3 Proglacial hydrology

Meltwater from Leverett Glacier's hydrological catchment drains through a single portal at the glacier terminus. After ∼2 km of slightly braided river system (Figure 3.3) all the

Figure 3.6: Gauging through the stable bedrock section. In the foreground (but submerged below the water), a pressure transducer, turbidity sensor and electrical conductivity sensor logged by a Campbell Scientific CR800 data logger were deployed on a metal support which was re-positioned as the water level rose and fell. On the far side of the channel a permanent gauging station (inaccessible during the melt season) recorded the same parameters using a Campbell Scientific CR1000 logger until it was destroyed in July 2012 by record water levels.

water coalesces into a single stable bedrock section located above a waterfall (Figure 3.6). The short distance between the portal and the single stable bedrock section make Leverett Glacier an ideal candidate for research which requires gauging of proglacial discharge.

In 2012, pressure transducers deployed at fixed locations in the stable bedrock section recorded variations in river water level (stage) throughout the melt season. Two Druck pressure transducers were deployed at the top of the stable bedrock section (Figure 3.6) and two further Onset HOBO U20-001-03 autonomous pressure transducers were bolted to the bedrock at the base of the section prior to melt onset to be retrieved at the end of the melt season. An Onset HOBO U20-001-04 pressure transducer recorded barometric pressure at the top of the stable bedrock section for correction of the HOBO stage records.

In post-processing the best (i.e. least noisy) segments of each stage record were identified and spliced together.

Stage was converted into discharge using rating curves calculated from repeat Rhodamine dye dilution injections conducted through the stable bedrock section across the full range of observed river discharge. Dye was injected at the top of the stable bedrock section (e.g. Figure 3.7) and allowed to disperse until mixed uniformly in the rapids prior to detection using a Turner Designs Cyclops 7 fluorometer logged once per second by a Campbell Scientific CR800 data logger.

Discharge gauging during the 2012 season was made particularly difficult by (1) the extreme melt event on 12 July (Nghiem et al., 2012) and (2) the record melt volumes recorded over the full season, both at Leverett and from the whole ice sheet (Tedesco et al., 2013a). Peak discharge of over 800 m^3s^{-1}, double that seen in previous years and similar to the discharge shown in Figure 3.8, made selection of safe dye injection and detection sites difficult. As discharge peaked on 12 July, detection sites were established on the floodplain, ∼1 km downstream of the injection point, as access to the normal detection sites located in the stable bedrock section directly above the lower waterfall (Figure 3.8) became too dangerous.

The extreme peak discharge exhausted camp's supplies of Rhodamine WT (aqueous), necessitating the use of Rhodamine B (solid) for the three discharge estimates above 800 m^3s^{-1} (Figure 3.9b). In principle Rhodamine B is susceptible to adsorption, where the dye bonds to freshly weathered sediment, thereby reducing recorded fluorescence, which in turn will erroneously increase estimates of discharge. Lab experiments undertaken with Rhodamine B and sediment collected from the proglacial sediment after the 2012 melt season were inconclusive because the fluorescence decayed over time whether the sample was made up with river sediment or only de-ionised water. However, the fit of the final rating curve (Figure 3.9b) is determined primarily by the Rhodamine WT estimates of discharge, making the estimates of discharge at peak stage significantly lower than the

Figure 3.7: Injecting Rhodamine WT at the top of the stable bedrock section on 18 July 2012. The river was flowing at approximately 350 m^3s^{-1}. Photo: B. Linhoff.

discharge values obtained by Rhodamine B injection, and so it is unlikely that total runoff has been over-estimated as would be expected if relying solely on Rhodamine B.

Unprocessed dye return curves all had a non-zero and usually non-constant background. This background was removed from the curve using linear interpolation through the curve based on smoothed background values recorded at least 10 minutes before and after the dye return curve. Corrected readings were then converted to Rhodamine concentration using calibration gradients derived from *in situ* calibration tests undertaken with each batch of Rhodamine. Specific calibration gradients for each dye batch are important; the gradient can vary by as much as a factor of two between batches, strongly affecting the accuracy of

Figure 3.8: Discharge through the lower waterfall of the stable bedrock section on 10 July 2012, ~600 m^3s^{-1}.

the discharge estimates. Finally, the discharge was calculated by dividing the amount of dye injected by the area under the return curve.

The rating curves are of the form $Q = aS^b$, where Q is discharge, S is stage, and a and b are parameters determined by iterative non-linear regression. One curve was designed for discharge from the start of the melt season to 29 May (Figure 3.9a) in order to sensitively capture small variations in discharge at low stage, while another was designed for discharge after 29 May (Figure 3.9b). Following Bartholomew et al. (2011b) the uncertainty related to the rating curve is represented by the (Normalised) Root Mean Squared Deviation ([N]RMSD) between discharge measured by dye injections compared to discharge estimated from the rating curve using stage observations. For the 2012 discharge record, the RMSD is 96.2 m^3s^{-1} and the NRMSD is 10.7%. The overall discharge error is ±10%.

In addition to discharge, suspended sediment concentration (SSC) and electrical conductivity

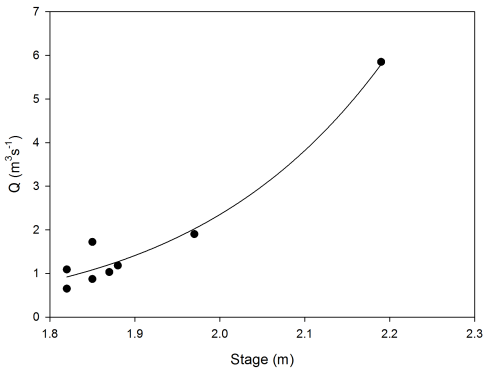

(a) Rating curve from the start of the melt season on 13 May 2012 to 29 May 2012. $a = 0.0024, b = 0.9494, R^2 = 0.87, P < 0.01$.

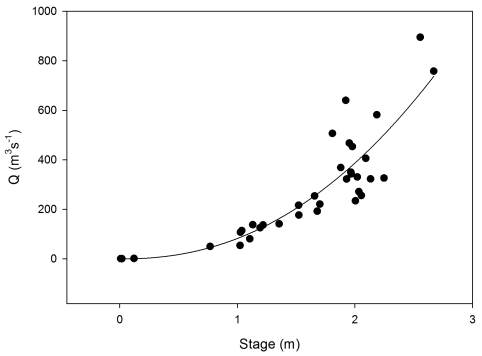

(b) Rating curve from 29 May 2012 onwards. $a = 82.5393, b = 2.2297, R^2 = 0.87, P < 0.01$.

Figure 3.9: Discharge rating curves for 2012 melt season.

(EC) in water flowing through the stable bedrock section were recorded using Partech IR15C and Campbell CS547A sensors respectively, to aid identification of varying meltwater routing through the subglacial drainage system. SSC was calibrated using manual gulp samples collected with a USDH-48 depth-integrated water sampler and filtered under vacuum through 0.45μm papers which were dried and weighed in the laboratory. Previous work at Leverett Glacier has established that SSC remains broadly constant once the meltwater exits the glacier portal (Cowton, 2013). The EC and SSC records are not utilised directly in this thesis but are integral to hydro-chemical research findings made by others (see e.g. Appendix D Hawkings et al., 2014).

3.4 Remote sensing of ice motion

Ice motion measurements made using GNSS during the field campaign are of very high temporal resolution, yielding crucial insights into the short-term ice dynamics which aggregate into longer-term ice motion. However, they are also logistically and financially constrained to only 9 locations over a study area that extends 120 km into the ice sheet interior. Satellite-based remote sensing provides a means of acquiring complementary, spatially extensive observations of ice motion at the expense of temporal resolution.

In this thesis, two sources of satellite data are used: Synthetic Aperture Radar to advance our understanding of spatial variations in hydro-dynamic coupling over seasonal and annual timescales, and images acquired in the visible spectrum by the Landsat Program to explore decadal trends in ice motion using an unprecedented combination of spatial resolution and time series duration.

3.4.1 Synthetic Aperture Radar

The TerraSAR-X and TanDEM-X (TSX/TDX) satellites are Synthetic Aperture Radar (SAR) Earth observation satellites which acquire radar images with up to 1 m ground resolution. The satellites are tasked to acquire data for specific regions. TSX/TDX were tasked to acquire data over the lower Leverett Glacier area every 11 days from June 2011 and data for this thesis were available into summer 2013. These data were processed using feature tracking (Paul et al., 2013) to yield ice displacement maps. This thesis does not discuss the data acquisition and processing further as the ice displacement maps were processed by Noel Gourmelen (University of Edinburgh) and provided in a format ready for interpretation.

The 11-day repeat period of the ice displacement maps derived from TSX/TDX makes it possible to sub-divide annual motion into seasonal components, enabling exploration of the contribution of differing ice motion during the summer melt season versus the subsequent winter. The displacement maps have a nominal spatial resolution of 60 m, enabling identification of changes in the spatial pattern of ice motion at scales less than one ice thickness ($\sim$400–1000 m).

3.4.2 Landsat program

The Landsat program captures optical satellite imagery over a number of spectral bands. The first satellite, Landsat 1, was launched in 1972, and observations have been captured ever since. Landsat 8 is currently in orbit. Whilst the design of the imaging sensors onboard

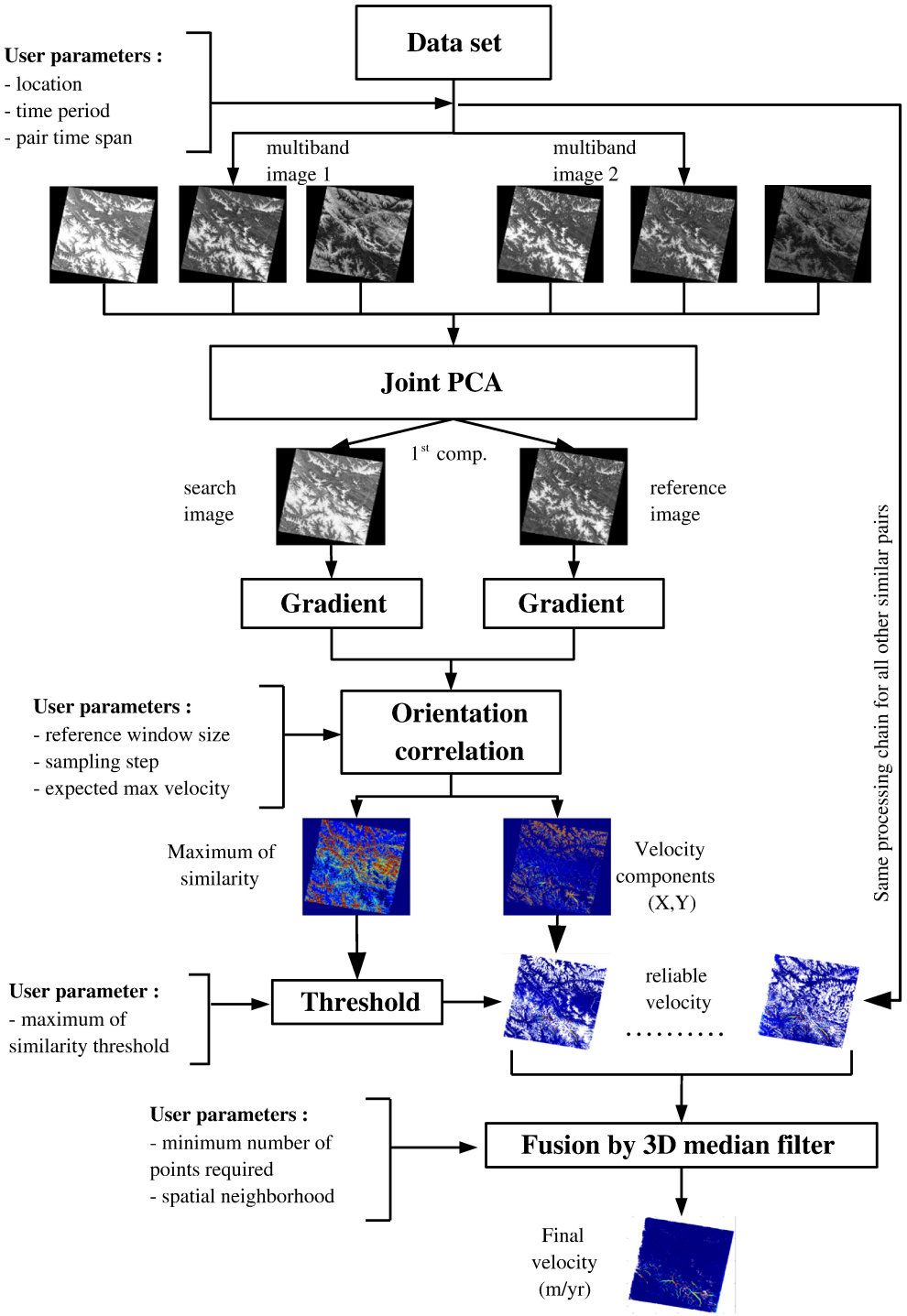

Figure 3.10: Processing strategy to derive glacier velocities from a complete multispectral satellite archive such as the Landsat program. Reproduced from Dehecq et al. (2015), Figure 1.

each successive satellite has changed over time, the overall characteristics of these data (e.g. 30 m resolution, multi-spectral acquisition, 16 day temporal resolution) have remained the same. Until recently, many of these data were unavailable to end users, preventing full exploitation of one of the longest time records of environmental change. However, major data re-processing and archival programs are now being undertaken by the United States Geological Survey (USGS) and the European Space Agency (ESA), delivering an unprecedented volume of observations in both time and space, captured during a period of rapid climate change (e.g. Stocker et al., 2013).

This enlarged archive of optical (i.e. visible) observations of the Earth's surface makes it possible to measure a wide variety of parameters of environmental change. One of these parameters is ice flow velocity, which may be obtained over seasonal to inter-annual timescales through tracking of surface feature motion in optical images of the same geographic area but separated in time, yielding a spatial resolution on the order of hundreds of metres (Paul et al., 2013). The technique itself is not new: Scambos et al. (1992) used feature tracking of Landsat TM images to obtain velocities of regions of the Antarctic Ice Sheets. However, the release of new data, coupled with significant advances in computational power, have substantially enhanced the scope of the technique.

Development of the processing chain used to extract the ice velocity fields from the Landsat images was initiated by A. Dehecq (Université de Savoie, France) for use with data from the Himalayas. Dehecq et al. (2015) contains a detailed description of the chain methodology. The overall processing strategy builds individual, approximately annual velocity fields from feature tracking of Landsat pairs, overlapping in time and space. These velocity fields are then combined over inter-annual time periods in order to increase the robustness of the velocity estimates and to enable statistical determination of uncertainties.

I made collaborative changes to improve the usability, portability and speed of the chain for super-computer deployment and to enable the chain's use for the Greenland Ice Sheet. We used the Git distributed version control system with Bitbucket to keep track of changes. For

the research presented in this thesis the processing chain was deployed on the Edinburgh Compute and Data Facility super-computer, Eddie.

There are a number of steps required to extract ice velocities from Landsat imagery (Figure 3.10). Firstly, pairs of images must be identified based on the desired temporal baseline separation, which in this thesis is one year, in order to minimize the impact of seasonal flow variability upon inter-annual trends in ice velocity. Then, the images are imported and cropped to uniform geographic extents. Next, the first Principal Component from the optimum combination of spectral bands is calculated (see 'Determination of processing parameters' below). Sobel kernels are used to compute the intensity gradient in the x and y directions, enhancing surface features such as crevasses. Then, the motion of surface features over the temporal baseline between the two images is tracked (Figure 3.11) using a coherence tracking function that tracks the gradient orientation contained in the phase of the orientation image (Strozzi et al., 2002) to extract displacement from the intensity gradients, resulting in a field of velocity estimates for the baseline duration.

All the pairs of images in the desired study area are processed, which yields multiple estimates of ice motion at any one location over the ∼annual baseline period separating the two images. Then, the redundancy offered by these multiple spatio-temporal estimates of ice velocity is exploited by calculating spatio-temporal neighbourhood medians to efficiently remove outliers and produce robust fused velocity fields on a common polar stereographic grid projection with little user interaction. Each velocity field presented in Chapter 6 is therefore a composite created from several individual annual velocity estimates. Thus, annual composite velocity fields, such as 2013–2014, are created from individual velocity estimates, some of which have baselines as early as May 2013–May 2014, and others as late as September 2013–September 2014. A full discussion of of the approach used to remove outliers in the composite velocity fields, and to calculate uncertainties, can be found in Chapter 6.

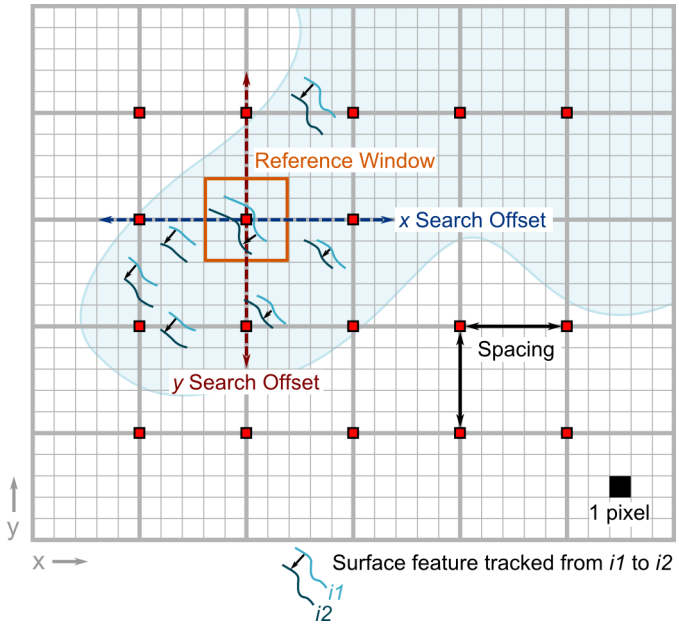

Figure 3.11: Schematic of feature-tracking methodology (not to scale). Red squares mark each sampling point at which a displacement estimate is calculated, defined by the 'spacing' parameter. The reference window is centred over each of the sampling points in turn. The search area over which the reference window may move to track surface features is defined by the '*x* search offset' and '*y* search offset' parameters.

Determination of processing parameters

'Annual' pairs cannot be created from images acquired exactly 1 year apart. Rather, the Landsat satellites acquire images of the same location every 16 days, which yields pairs of images with temporal baselines of 336–400 days, but ideally 352 or 368 days. The precision of the 'annual' baseline therefore determines which images can be paired together: the more precise the baseline, the fewer the number of pairs of images are generated.

The most appropriate spectral bands to enable identification of ice surface features need to be picked. Radiation is reflected, and emitted from, the ice sheet surface over a wide range of wavelengths. The wavelengths that the Landsat sensors observe and which are most useful to the identification of surface features fall within the range ~0.45-0.90 μm. The precise wavelength ranges of each spectral band designation vary by Landsat sensor but are broadly equivalent between the Thematic Mapper (TM), Enhanced Thematic Mapper Plus (ETM+) and Operational Land Imager (OLI) sensors. Thus, the most appropriate bands are 2–4. In

older Multi Spectral Scanner (MSS) images, the most appropriate bands are 4–5, but we are unable to utilise MSS images in this study as insufficient acquisitions are available from which to form pairs.

Whilst feature tracking could utilise just one spectral band, it is possible to extract more information for tracking from the available observations by calculating the first Principal Component (PC) of a combination of spectral bands. The optimum combination of spectral bands is identified by running PC analysis with a number of different spectral band combinations, calculating the velocity fields, then computing the success rate (the percentage of velocity estimates in a defined area which have a signal-to-noise value calculated by the feature tracking algorithm greater than a user-prescribed threshold) of velocity extraction in both stable (off-ice) and glaciated regions. Testing showed that, on average, the first PC of bands 2 and 3 yielded the highest success rates, based on inter-comparison of four cloud-free annual image pairs acquired in the study area examined in Chapter 6 of this thesis (Figure 3.1 box C).

The feature tracking algorithm itself has a number of parameters which are determined based on the characteristics of the study area. Figure 3.11 provides a pictorial overview of the relationship between the parameters.

Reference Window The reference window defines the 'chip size' of the area centred around the sampling pixel in the master image to treat as the reference pattern to be matched in the search area of the slave image. The dimensions of the reference window therefore characterize the spatial scale of patterns which will be matched by the algorithm. It is desirable to identify the smallest possible reference window which yields an acceptable success rate without compromising the spatial precision lost at larger window sizes or capturing deformation of objects within the window.

Identification of the optimum reference window size is complicated because the quality product of the feature tracking algorithm — the signal-to-noise-ratio (SNR) —

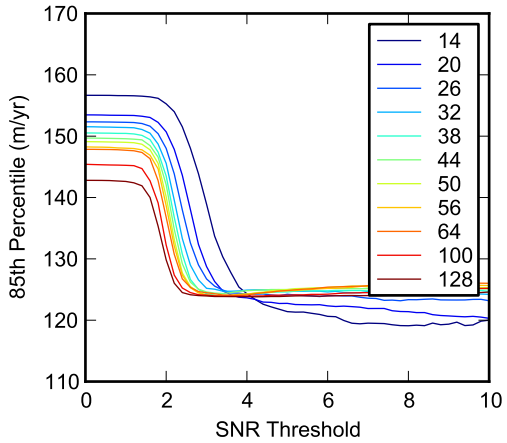

(a) 85th Percentile of stable (off-ice) area velocities at signal-to-noise-ratio thresholds from 0 to 10 across a range of reference window sizes from 14 to 128 pixels.

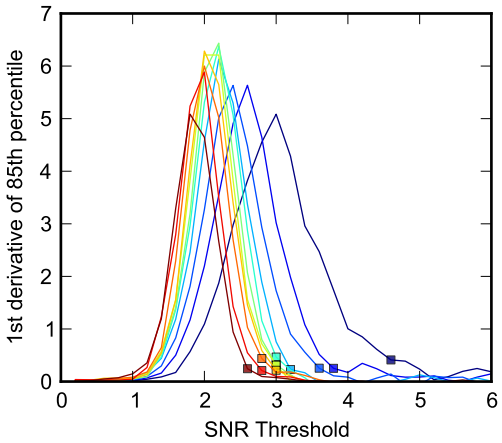

(b) 1st derivative of velocities shown in (a). Coloured squares indicate the chosen SNR threshold for each reference window size.

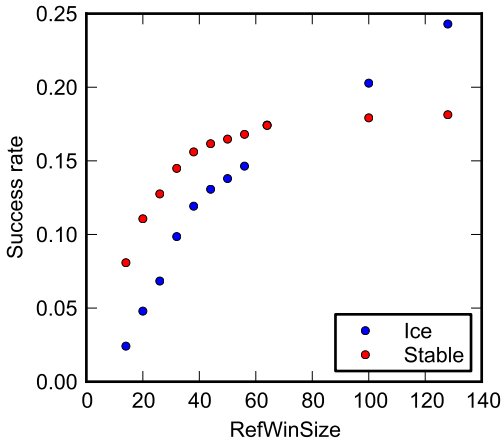

(c) Success rate in stable (off-ice) and ice regions for different reference window sizes (pixels), after bad data have been masked out using the SNR threshold identified in (b).

Figure 3.12: Example determination of optimum reference window size, using Landsat 5 images acquired on day 239, 1990 and day 242, 1991 in PR(008,012). I use the term 'stable' to describe off-ice regions after Dehecq et al. (2015).

increases with reference window size, preventing application of a fixed SNR threshold to calculate the success rates at different reference window sizes. Thus, a more sophisticated approach to picking the optimum reference window size is required.

First, the feature tracking algorithm is run for an image pair at a variety of reference window sizes. Figure 3.12a shows the value of the 85^{th} percentile velocities estimated in stable (off-ice, i.e. non-moving areas) areas for different SNR thresholds. In all cases there is a clear step-change in the value of the 85^{th} percentile at a certain SNR threshold; however, the optimum SNR threshold varies by reference window size. It is therefore necessary to first identify the most appropriate SNR threshold for each reference window size by finding the break in slope of the first derivative of the 85^{th} percentile velocities (Figure 3.12b). Then, the SNR threshold identified for each reference window size is applied and the success rate of remaining observations is calculated; the final choice of reference window is based on when the increase in stable ground success rate becomes asymptotic (Figure 3.12c), corresponding to an average of 44 pixels.

Search Windows The range and azimuth search windows define the region in which the reference window 'chip' searches for matching offsets. The size of each window is set to correspond to the maximum expected displacement over the baseline between the two images based on previous observations (e.g. Joughin et al., 2010), plus three pixels (90 m). Larger search windows increase the computation time required for feature tracking. In the land-terminating sector of west Greenland under examination here, the ice moves slowly enough ($\sim$100 m yr^{-1}) to allow feature tracking of images acquired approximately one year apart within an acceptable amount of computational time, but, for faster-moving tidewater glaciers, pairs of images with shorter baselines would be necessary.

Spacing This parameter essentially defines the spatial resolution of the calculated velocity field, by setting the grid spacing at which offsets are calculated (Figure 3.11). Higher

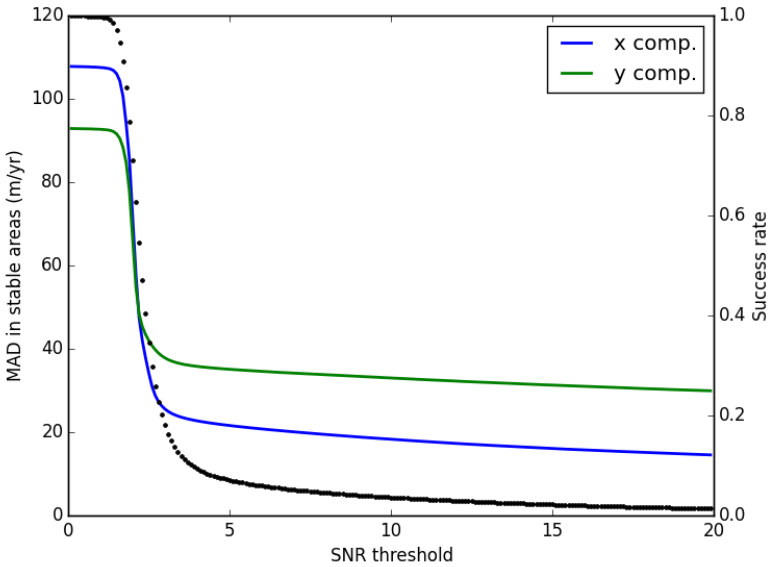

Figure 3.13: Median Absolute Deviation (MAD) of the x and y velocity components in stable areas (plain lines), and the success rate (black dots), for different SNR thresholds. This example is for all the velocity fields extracted from Landsat 5 TM imagery.

spacing values decrease computation time at the expense of spatial resolution. However, very small values of spacing are also undesirable, not only because computation times increase dramatically, but also because there is an inherent limit on the spatial resolution that can be achieved with a reference window on the order of 40 pixels and a search window of ∼15 pixels. Spacing is therefore set to 8 pixels as a compromise between these considerations.

Further parameters define the way in which the velocity fields calculated from individual image pairs are fused into annual composite velocity fields.

SNR Threshold Velocities below a minimum SNR value are removed prior to merging. Figure 3.13 shows that the median absolute deviation of velocities decreases to become asymptotic above a certain SNR threshold, in this case SNR≈3. However, it is undesirable to use too high a SNR threshold because the success rate decreases as more of the velocity field is removed. The most appropriate SNR threshold is therefore

a compromise between retaining the maximum number of velocity estimates versus enhancing certainty (expressed through the Median Absolute Deviation) in those retained velocity estimates.

Fusion Baseline This parameter determines the period over which velocity estimates from individual pairs are selected from. As the individual pairs have essentially annual baselines, annual baselines are also used during fusion. Inter-annual reference velocity fields were also computed; see Chapter 6 for more details.

Search Radius Fusion utilises a 'k-d tree' which organises data points for quick nearest-neighbour look-up in order to find velocity estimates within a specified radius of each common grid coordinate. The median velocity is then calculated from all the retrieved estimates. The minimum search radius corresponds to the pixel size of the individual velocity fields. At 8 pixel spacing and 30 m resolution this yields a search radius of 340 m. Larger search radiuses tend to simply spatially smooth the velocity field without adding information, so 340 m was chosen.

For the first time, therefore, it is possible, data quality permitting, to retrieve a 40-year record of seasonal, annual and inter-annual ice motion from the Landsat Program archive for almost any glaciated region on the globe, at relatively fine (∼km) resolution. In practice, poor image quality from Landsat missions 1–3 means that the record of ice motion retrieved here begins in 1985.

Chapter 4

Greenland Ice Sheet motion insensitive to exceptional melt water forcing

Published in **Proceedings of the National Academy of Sciences of the United States of America**, December 2013.

Authors: Andrew J. Tedstone[1], Peter W. Nienow[1], Andrew J. Sole[1,2], Douglas W. F. Mair[3], Thomas R. Cowton[1,2], Ian D. Bartholomew[1] and Matt A. King[4,5].

1. School of GeoSciences, University of Edinburgh, Edinburgh, EH8 9XP, UK
2. Department of Geography, University of Sheffield, Sheffield, S10 2TN, UK
3. School of Geosciences, University of Aberdeen, Aberdeen, AB24 3UF, UK
4. School of Geography and Environmental Studies, University of Tasmania, Hobart, TAS 7001, Australia
5. School of Civil Engineering and Geosciences, Newcastle University, Newcastle upon Tyne, NE1 7RU, UK

Citation: Tedstone, A. J., P. W. Nienow, A. J. Sole, D. W. F. Mair, T. R. Cowton, I. D. Bartholomew and M. A. King (2013), Greenland Ice Sheet motion insensitive to exceptional melt water forcing, *Proc. Nat. Acad. Sci. USA*, 110(9), 19719-19724. DOI: 10.1073/pnas.1315843110

Author contributions: P.W.N. and D.W.F.M. designed research; A.J.T., P.W.N., A.J.S., D.W.F.M., T.R.C., and I.D.B. performed research; A.J.T., A.J.S., I.D.B., and M.A.K. contributed new analytic tools; A.J.T., A.J.S., T.R.C., I.D.B., and M.A.K. analyzed data; and A.J.T. and P.W.N. wrote the paper.

Abstract

Changes to the dynamics of the Greenland Ice Sheet can be forced by various mechanisms including surface-melt-induced ice acceleration and oceanic forcing of marine-terminating glaciers. We use observations of ice motion to examine the surface melt-induced dynamic response of a land-terminating outlet glacier in south-west Greenland to the exceptional melting observed in 2012. During summer, meltwater generated on the Greenland Ice Sheet (GrIS) surface accesses the ice sheet bed, lubricating basal motion and resulting in periods of faster ice flow. However, the net impact of varying meltwater volumes upon seasonal and annual ice flow, and thus sea level rise, remains unclear. We show that two extreme melt events (98.6% of the GrIS surface experienced melting on 12 July — the most significant melt event since 1889 — and 79.2% on 29 July) and summer ice sheet runoff $\sim 3.9\sigma$ above the 1958–2011 mean resulted in enhanced summer ice motion relative to the average melt year of 2009. However, despite record summer melting, subsequent reduced winter ice motion resulted in 6% less net annual ice motion in 2012 than in 2009. Our findings suggest that surface melt-induced acceleration of land-terminating regions of the ice sheet will remain insignificant even under extreme melting scenarios.

Significance Statement

During summer, meltwater generated on the Greenland Ice Sheet (GrIS) surface accesses the ice sheet bed, lubricating basal motion and resulting in periods of faster ice flow. However, the net impact of varying meltwater volumes upon seasonal and annual ice flow, and thus sea level rise, remains unclear. In 2012, despite record ice sheet runoff including two extreme melt events, ice at a land-terminating margin flowed more slowly than in the ‘average’ melt year of 2009, due principally to slower winter flow following faster summer flow. Our findings suggest that annual motion of land-terminating margins of the ice sheet, and thus the projected dynamic contribution of these margins to sea level rise, is insensitive to melt volumes commensurate with temperature projections for 2100.

Surface melting and runoff from the Greenland Ice Sheet (GrIS) have increased during the last 30 years (Rignot et al., 2011; Shepherd et al., 2012; Sasgen et al., 2012) coincident with northern hemisphere warming (Hanna et al., 2011, 2012) resulting in unprecedented melt extents (Fettweis et al., 2011), and with widespread dynamic thinning which has penetrated up to 120 km into the ice sheet interior (Pritchard et al., 2009). One potential dynamic thinning mechanism is surface melt-induced acceleration of ice sheet motion (termed hydro-dynamic coupling) during summer (Zwally et al., 2002; Andersen et al., 2010; Bartholomew et al., 2011a; Sole et al., 2011). Observations of GrIS ice motion during the summer show considerable variability over a range of timescales (Bartholomew et al., 2012). Rapid variations in meltwater input from the ice sheet surface to the glacier bed result in periods when the subglacial drainage system is more highly pressurised, leading to an increase in basal sliding (Iken and Bindschadler, 1986; Bartholomew et al., 2010). This mechanism explains both multi-day increases in ice motion at the beginning of the melt season, analogous to the 'spring events' observed at alpine glaciers (Röthlisberger and Lang, 1987), and increases in velocity at other times when meltwater is delivered to the bed at a rate faster than the subglacial drainage system can expand to accommodate.

However, as the drainage system capacity gradually expands in response to increased melting, the subglacial water pressure falls and higher velocities can therefore only be caused by much larger meltwater pulses than earlier in the melt season (Cowton et al., 2013). This feedback mechanism has been invoked previously to suggest that net annual ice flow could be slower in warmer years, but observations have either been limited to close to the ice sheet margin (Sundal et al., 2011) or have been unable to resolve the seasonal behaviour responsible for the velocity variations (van de Wal et al., 2008). A recent study — incorporating seasonal ice flow and melt observations extending beyond the equilibrium line — showed that summer velocity enhancement is negated by subsequent reductions in winter flow rates (Sole et al., 2013), but the bounding conditions of the study have since been exceeded by the exceptional

melting observed in 2012 (Nghiem et al., 2012). Moreover, the current paucity of field observations is a significant impediment to modelling the impact of coupled hydro-dynamics on net ice mass loss (Shannon et al., 2013).

The recent trend of warmer summers in Greenland is related to an increase in the frequency of anticyclonic conditions (Fettweis et al., 2013). Persistent anticyclonic conditions during summer 2012 resulted in extreme runoff volumes from the Greenland Ice Sheet (Tedesco et al., 2013a), compounded by unprecedented melt extent in July 2012 associated with low-level liquid clouds (Bennartz et al., 2013), which led to flood damage such as the destruction of the Watson River bridge in Kangerlussuaq, west Greenland. These conditions resulted in a year during which ice-sheet-wide runoff set a new record at $\sim 3.9\sigma$ above the 1958–2011 mean (Tedesco et al., 2013a). NCEP/NCAR reanalysis 1000 mb temperature anomalies above Kangerlussuaq (25 km west of our site 1) relative to the 1981-2010 mean were $+2.2^{o}$C during May–August 2012, compared to $\pm 0.3^{o}$C during May–August 2009. The 2012 melt season is therefore a surrogate for potential future melting and forms a natural test for quantifying the effect of extreme meltwater supply on ice motion compared to the 'average' melt year of 2009.

We used Global Positioning System (GPS) records to observe ice motion during 2009 and 2012 at seven sites along a transect on a land-terminating margin of the GrIS, at $\sim 67^{o}$N (Figure 4.1). Air temperature and annual ablation were also measured at each site. The lowest three sites on the transect are located within Leverett Glacier's inferred hydrological catchment, from which we measured bulk runoff (Bartholomew et al., 2011b). Transect dynamics during 2012 (Figure 4.2) had similar characteristics to previous years (Bartholomew et al., 2011a; Sole et al., 2013): initiation of meltwater-induced acceleration during multi-day 'spring' speed-up events, followed by shorter duration spikes in velocity superimposed on gradually declining background seasonal velocities which fell below pre-melt season velocities by the end of summer.

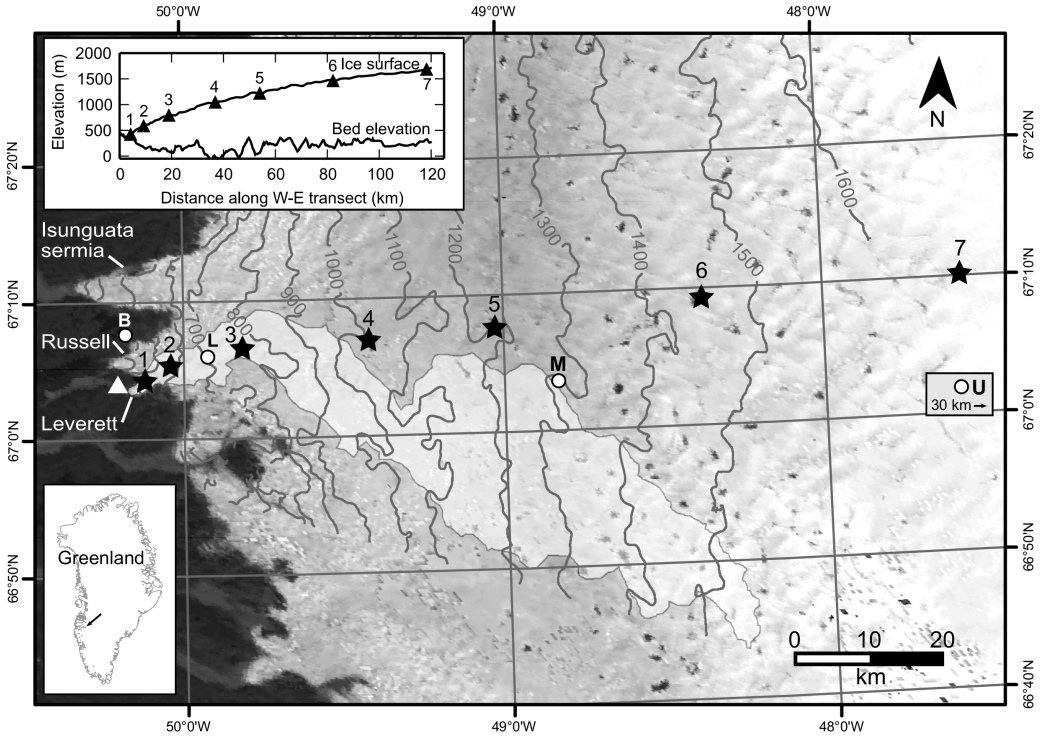

Figure 4.1: Location of the transect on the western margin of the GrIS. Stars indicate sites where ice motion, temperature and seasonal melting were measured. The triangle indicates where proglacial discharge was measured and the GPS base station located. Circles indicate locations of 'KAN' PROMICE/GAP weather stations along the K-transect. Contours (metres) are from a digital elevation model (DEM) of the ice sheet surface produced from interferometric synthetic aperture radar (Palmer et al., 2011). The inferred hydrological catchment of Leverett Glacier, delineated in light grey, was calculated from the ice sheet surface DEM. Inset plot shows surface and bed elevation along our transect as measured by IceBridge ATM (ILATM2) and MCoRDS (IRMCR2) respectively in 2010 and 2011 (Allen, 2011).

Here we concentrate on two specific aspects of hydro-dynamic coupling during 2012 to give insight into the likely dynamic behaviour of the ice sheet in a warming climate. We examine (1) the ice flow response to the extreme melt events of 12 July and 29 July (Nghiem et al., 2012), and (2) the impact of unprecedented melt volumes (Tedesco et al., 2013a) on total annual ice motion.

Enhanced ice flow lasting approximately 2 days was associated with both extreme melt events (shaded periods in Figures 4.2, 4.3 and 4.4), with several characteristics common to both events. Firstly, peak velocities occurred in advance of satellite-observed peak ice sheet melt extent (Nghiem et al., 2012), while proglacial discharge was still rising — 2 days in

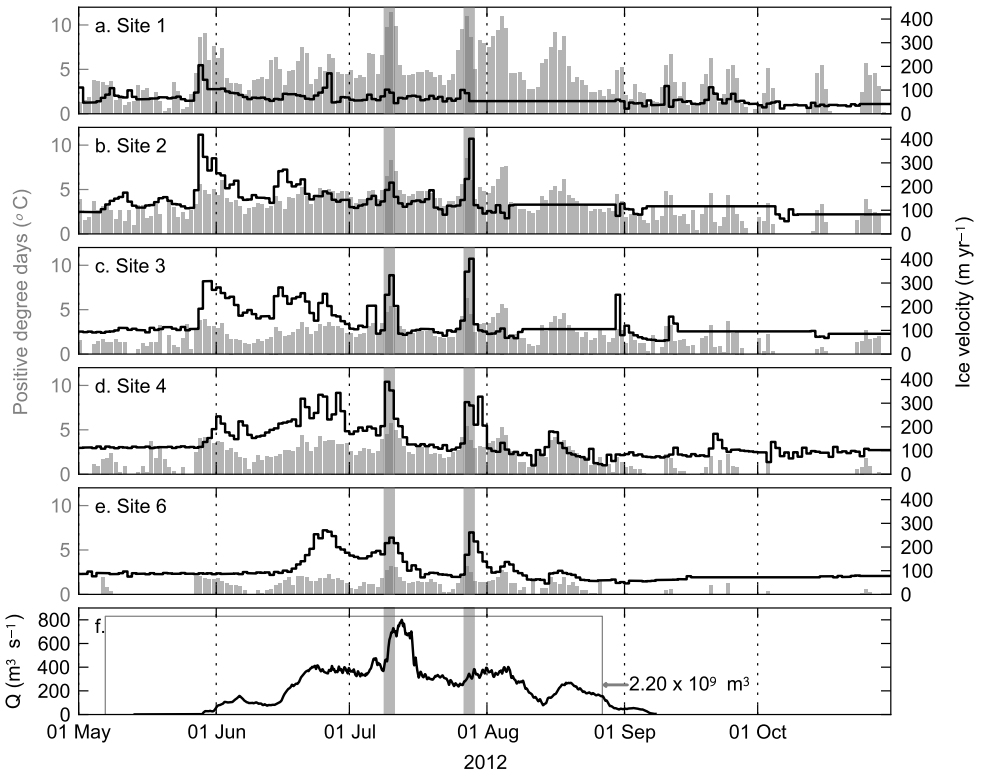

Figure 4.2: Transect observations during 2012. a–e. Daily (24-hour) along-track ice velocities (stepped black lines) and positive degree days (grey bars) for each transect site at which daily measurements were made. f. Discharge hydrograph for Leverett Glacier (m^3s^{-1}), with cumulative discharge between 7 May and 27 August (marked by grey box). The associated catchment is shown on Figure 1. a–f. Grey shading defines peak velocity response to 12 July and 29 July melt events (see text).

advance of 12 July, and 1 day in advance of 29 July. Secondly, velocities increased at every site at which daily observations were made along the transect during the enhanced ice flow period. Thirdly, at the majority of sites, velocities were lower after the enhanced ice flow period than before it (Figure 4.2).

Prior to the 12 July melt event, sites up to 1482 m a.s.l (site 6) experienced positive air temperatures every day from 10 June (Figure 4.2). Peak velocities during 9–10 July were coincident with a 2.3°C increase in mean air temperature at our transect sites and a 73% increase in mean wind speed at PROMICE/GAP K-transect sites (Figure 4.1) compared to the

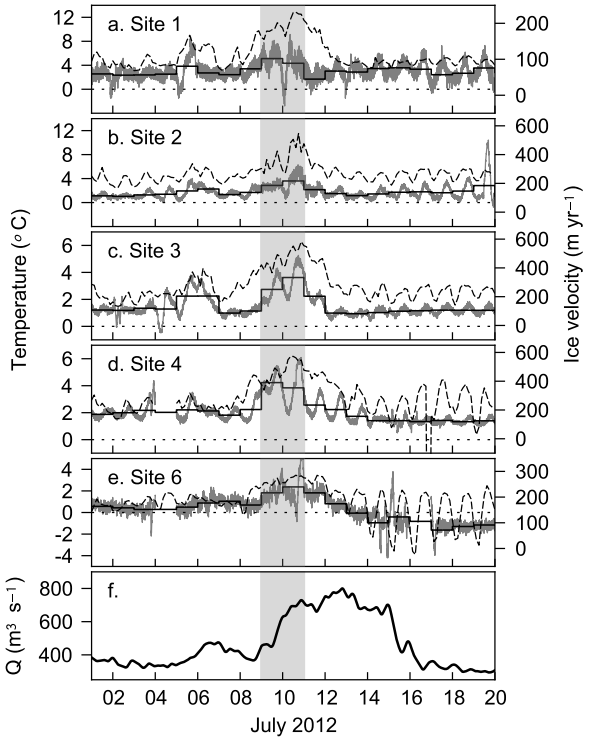

Figure 4.3: Observations around 12 July melt event. a–e. Near-surface air temperatures (dashed lines), daily (24-hour) along-track ice velocities (stepped black lines) and short-term along-track ice velocities (grey lines) for each site at which daily measurements were made. Periods with inadequate quality observations removed. f. Discharge hydrograph for Leverett Glacier ($m^3 s^{-1}$). a–f. Grey shading defines the peak velocity response to the melt event (see text).

previous 8 days. The mean daily transect velocity during 9–10 July was 61% greater than during the preceding 8 days, with sites 3 and 4 (794 m a.s.l and 1061 m a.s.l) experiencing the highest peak velocities of 103% and 77% greater respectively than the previous 8 days (Figure 4.3). By 12 July, ice velocities were falling despite peaks in both ice-sheet-wide melting and proglacial river discharge (∼800 $m^3 s^{-1}$; in excess of double that observed both at the start of the melt event and in previous years (Sole et al., 2013)). Sites 1 and 2 returned to daily velocities within 10 m yr^{-1} of 1–8 July mean velocities, and sites 3, 4 and 6 decreased to velocities at least 30 m yr^{-1} slower than 1–8 July mean velocities.

In contrast to the 12 July melt event, a period of falling air temperatures in the previous 15 days leading up to the 29 July melt event (as low as -7°C at site 6) resulted in falling discharge

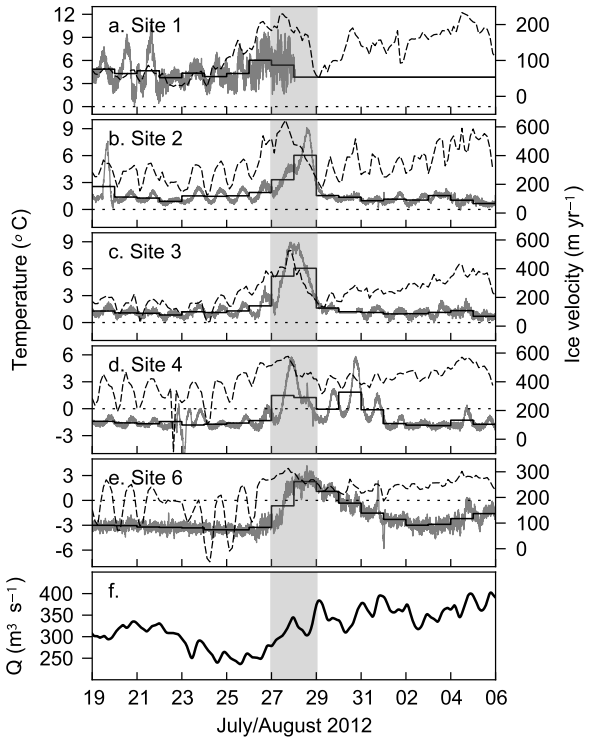

Figure 4.4: Observations around 29 July melt event. See A-F in Fig. 4.3 for details.

to a minimum of 240 m^3s^{-1} on 25 July, the lowest since 18 June (Figure 4.2). During 27–28 July the mean transect air temperature rose by 4.4°C compared to the previous 8 days, with associated — though lagged — increases in discharge and velocity (Figure 4.4). Mean transect ice velocity on 27–28 July was 116% greater than during the preceding 8 days. At sites 2, 3 and 4 the velocity perturbation was short-lived, lasting ∼2 days before an abrupt drop in velocities which returned to within 20 m yr^{-1} of pre-event velocities. Site 6 slowed down more gradually after the 28 July peak. Unlike the 12 July melt event, river discharge remained close to its event peak of ∼400 m^3s^{-1} for 8 days following the 29 July melt event (Figure 4.2f).

Increased ice velocities in the lead-up to the 12 and 29 July melt events were clearly caused by a rapid increase in the rate of meltwater supply to the ice sheet bed forced by changes in the rate of surface melting. While antecedent melt conditions and the absolute volumes

of meltwater associated with each event were different, the nature and style of meltwater forcing, overwhelming the capacity of the hydrological system and leading to ice acceleration, were very similar, replicating responses observed previously (Bartholomew et al., 2012; Cowton et al., 2013).

We estimated the potential contribution of each melt event to summer ice displacement by comparison to estimates of the projected ice displacement that would have occurred in the absence of the melt events. We used mean ice velocities at each site during the 8 days preceding each 2-day period of enhanced ice flow to estimate what the total displacement would likely have been through the 2-day enhanced ice flow period and the following 8 days in the absence of the enhanced ice flow period (see Materials and Methods for more information). Observations during the corresponding time periods are shown in Figures 4.3 and 4.4. On average the 12 July melt event forced only 7% more ice displacement over the 10-day period, while the 29 July melt event, which was preceded by lower melt rates than the 12 July event, forced 34% more ice displacement over the equivalent 10-day period. These findings reinforce the importance of antecedent melt rates (as opposed to simply meltwater volume) and thus drainage system efficiency in controlling the short-term dynamic response to variations in meltwater supply (Schoof, 2010).

The second exceptional characteristic of 2012 was ice-sheet-wide runoff of $\sim 3.9\sigma$ above the 1958–2011 mean (Tedesco et al., 2013a). For comparison, Figure 4.5 shows observations collected along our transect in the 'average' melt year of 2009. Exceptional melting during 2012 resulted in a mean of 117% more ablation relative to 2009 along our transect (Figure 4.5a) with bulk runoff from the local ice sheet margin (2.20×10^9 m^3) 113% greater than 2009 (Sole et al., 2013). Summer velocities (Figure 4.5b) at all but the lowest two sites were also higher in 2012 than in 2009. However, winter velocities at all sites were on average 11% lower in 2012 than 2009, resulting in 6% *less* net annual ice motion along the transect in 2012–2013 than in 2009–2010 (Figure 4.5). These observations support previous findings that stronger melting results in faster summers, but that faster summers

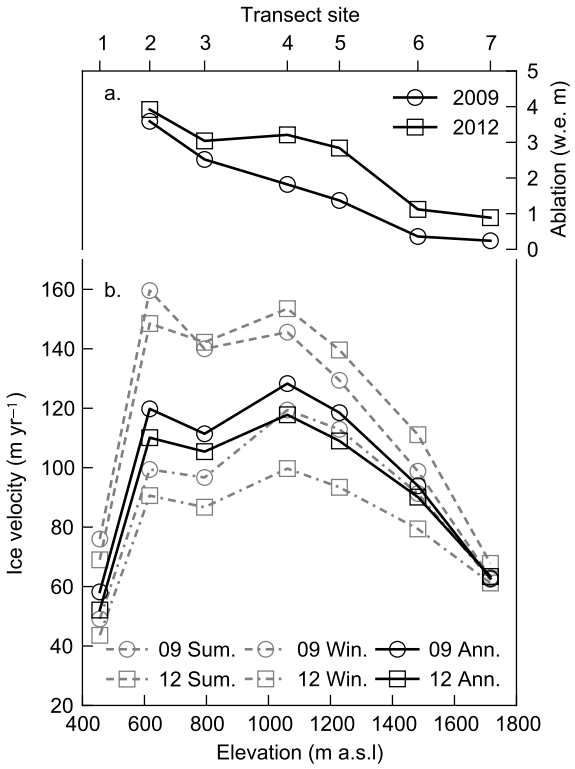

Figure 4.5: a. Annual (1 May–30 April) ablation in water equivalent metres for sites 2–7 in 2009 and 2012. b. Summer (Sum., 1 May–31 August), winter (Win., 1 September–30 April) and annual (Ann., 1 May–30 April) velocities for each site in 2009 and 2012.

are then offset by subsequent slower winter ice flow due to the evolution of a larger, more extensive subglacial drainage system which drains high basal water pressure regions (Sole et al., 2013). Our findings also support ice-sheet modelling results (Shannon et al., 2013) which suggest that enhanced basal lubrication will not cause substantial net mass loss from the ice sheet, and provide the observations which Shannon et al (Shannon et al., 2013) had stated were currently 'insufficient to determine whether changes in subglacial hydraulics will limit the potential for the speedup of flow'.

Our findings demonstrate that despite the exceptional melting observed in 2012, annual ice motion along our transect was not enhanced relative to an 'average' melt year (2009). These findings suggest that while hydrologically forced ice motion influences short-term and seasonal ice dynamics, land terminating margins of the Greenland Ice Sheet ice sheet are

insensitive dynamically over annual timescales to melt volumes that are commensurate with temperature projections for 2100 (Meehl et al., 2007). Furthermore, our data demonstrate that the importance of hydrologically forced ice motion over annual timescales can only be understood with reference both to summer and winter seasonal velocities due to their significant inter-annual variability. We also note that the effects of surface melt and oceanic forcing mechanisms on the dynamics of marine terminating glaciers in a warming climate remain unclear and should be a priority for future research.

4.1 Materials and Methods

Ice motion was recorded at seven sites, up to 1716 m a.s.l elevation and 113 km from the ice sheet margin (Figure 4.1). Dual-frequency GPS receivers mounted on poles frozen into the ice recorded position at 10 second intervals. Data were subsequently processed kinematically in overlapping 28-hour windows using Track 1.21 (Chen, 1999) utilising International GNSS (Global Navigation Satellite System) Service precise orbits relative to an off-ice base station (Figure 4.1), apart from 12–29 August 2012 when the Kellyville global GPS network station was used. Positions were filtered using a high-pass Gaussian filter to suppress high frequency noise without distorting the long-term signal and then differenced every 24 hours to calculate daily velocities (Sole et al., 2013). Short-term velocities were calculated at 1 minute intervals and smoothed with a 6-hour mean sliding window. Horizontal velocity uncertainties are approximately ± 1 cm at each epoch and 5.2 m yr^{-1} for daily velocities (Bartholomew et al., 2011a). Power failure prevented continuous recording of ice velocities at sites 5 and 7 during summer 2012 and at sites 1–3 in late summer. The absolute displacements during these periods of power failure were still obtained at each site.

The enhanced ice flow periods were defined in whole days for clarity and in order to make inter-comparisons between sites more objective. Each enhanced ice flow period started when most sites showed a substantial increase in velocity on the previous day and ended on the last day before velocities at all sites decreased. We chose 8-day baseline periods for examining

the ice displacement associated with each peak melt event as these represented the longest periods over which we could compare velocities without overlapping the periods associated with each melt event. The variability associated with choosing different lengths in baseline and enhanced ice flow period was insignificant in the context of the large differences in displacement exhibited by each event.

Air temperatures were measured at sites 1, 3 and 6 using shielded Campbell Scientific T107 temperature sensors connected to Campbell Scientific CR800 data loggers, and at sites 2 and 4 using shielded HOBO U21-004 temperature sensors, situated ∼2 m above the ice sheet surface. Sensors sampled once per minute and recorded a mean value every 15 minutes. Air temperatures were then converted to positive degree days (PDDs) by calculating the mean of all positive values each day. Snow depths were measured at sites 2–7 just prior to the onset of the melt season, and seasonal ablation water equivalent totals were determined from ablation stakes at sites 2–7. To compare measurements of ice velocities and ablation made in 2009 and 2012, we calculated the percentage difference between the years at each site and then took the mean of those values to derive a transect average.

The volume of meltwater draining from Leverett Glacier's inferred hydrological catchment (Figure 4.1) was measured using continuous water stage monitoring through a stable bedrock section. Stage was converted to discharge with a continuous stage-discharge curve obtained from repeat Rhodamine WT and Rhodamine B dye dilution injections undertaken throughout both melt seasons, following methods described previously (Bartholomew et al., 2011b). The normalised root mean squared deviation of the discharge record is estimated to be ±10%.

Chapter 5

Greenland Ice Sheet annual motion insensitive to spatial variations in subglacial hydraulic structure

In the previous chapter, coupled hydrology-dynamics during two contrasting melt years was examined. Rather than a positive feedback between melting and net annual ice motion as was initially hypothesised (Zwally et al., 2002; Parizek and Alley, 2004), the observations showed that, relative to an average melt year, extreme melting during summer results in faster summer motion but slower winter motion, resulting in slower annual ice motion overall. Together with previous observations (Sole et al., 2013) the chapter therefore supports the hypothesis that projected melting will not cause annual ice flow to speed up, and may even cause it to slow down.

The observations in the previous chapter only addressed spatial variability in annual ice motion along a longitudinal transect corresponding approximately to the glacier flowline (Palmer et al., 2011). Meanwhile, observations on alpine glaciers have revealed that over diurnal timescales, surface ice motion is greatest and most variable above inferred subglacial channels, and becomes less variable further away (e.g. Nienow et al., 2005). Sub-seasonal

observations of ice motion in south-west Greenland show substantial spatial variability, for instance during winter (Joughin et al., 2010) and summer (Sundal et al., 2011), with striking resemblance to patterns of supraglacial drainage features (Palmer et al., 2011; Joughin et al., 2013). However, it is unclear whether summer melting and hydro-dynamic coupling causes some areas to flow faster than others over the course of a full melt-year.

This chapter therefore examines whether spatial variability in subglacial drainage system structure has an impact on spatial variations in net annual ice motion across a $\sim$300 km^2 area of the ice sheet, using (1) detailed GPS measurements of ice motion collected above and transverse to an inferred subglacial channel, and (2) observations of seasonal and annual ice motion acquired by the TerraSAR-X/TanDEM-X radar satellites.

Published in **Geophysical Research Letters**, December 2014.

Authors: Andrew J. Tedstone[1], Peter W. Nienow[1], N. Gourmelen[1] and Andrew J. Sole[2].

1. School of GeoSciences, University of Edinburgh, Edinburgh, EH8 9XP, UK
2. Department of Geography, University of Sheffield, Sheffield, S10 2TN, UK

Citation: Tedstone, A. J., P. W. Nienow, N. Gourmelen and A. J. Sole (2014), Greenland Ice Sheet annual motion insensitive to spatial variations in subglacial hydraulic structure, *Geophys. Res. Lett.*, 41(24), 8910-8917. DOI: 10.1002/2014GL062386.

Author contributions: A.J.T. and P.W.N. designed research; A.J.T., P.W.N. and A.J.S. collected field observations; N.G. processed the radar data; A.J.T., N.G. and A.J.S contributed new analytic tools; A.J.T. and N.G. analyzed the data; and A.J.T. and P.W.N. wrote the paper.

Abstract

We present ice velocities observed with global positioning systems and TerraSAR-X/TanDEM-X in a land-terminating region of the south-west Greenland Ice Sheet (GrIS) during the melt-year 2012–2013, to examine the spatial pattern of seasonal and annual ice motion. We find that whilst spatial variability in the configuration of the subglacial drainage system controls ice motion at short timescales, this configuration has negligible impact on the spatial pattern of the proportion of annual motion which occurs during summer. Whilst absolute annual velocities vary substantially, the proportional contribution of summer motion to annual motion does not. These observations suggest that in land-terminating margins of the GrIS, subglacial hydrology does not significantly influence spatial variations in net summer speedup. Furthermore, our findings imply that not every feature of the subglacial drainage system needs to be resolved in ice sheet models.

5.1 Introduction

One potential dynamic thinning mechanism of the Greenland Ice Sheet (GrIS) is surface melt-induced acceleration of ice motion (Zwally et al., 2002; Parizek and Alley, 2004; Andersen et al., 2010). During summer, rapid increases in meltwater input from the ice sheet surface result in periods when the subglacial drainage system is more highly pressurized, leading to transient increases in basal sliding (Bartholomew et al., 2011a; Sole et al., 2011). However, drainage system capacity changes in response (Röthlisberger, 1972; Schoof, 2010; Hoffman and Price, 2014), introducing a negative feedback which acts to lower the water pressure of the drainage system and reduce basal sliding, such that subsequent increases in basal sliding require either (a) larger meltwater pulses or (b) reductions in drainage system capacity, decreasing the quantity of meltwater required to over-pressurize the system (Cowton et al., 2013).

Remotely sensed observations of ice motion of a land-terminating portion of the south-west

GrIS made on a single day in late summer have revealed spatially distinct flow enhancements of up to 300% relative to winter (Palmer et al., 2011). The spatial coincidence of faster flowing areas with surface drainage routing suggests that localised meltwater input to the ice bed, and the associated changes in subglacial water pressure, is the likely cause of the flow enhancement. However, point-based observations from the same region have shown that net annual ice motion is insensitive to these short-term variations in ice flow (van de Wal et al., 2008; Sole et al., 2013; Tedstone et al., 2013, Chapter 4), except possibly at high elevations well above the equilibrium line altitude (Doyle et al., 2014). Similarly, spatially extensive satellite observations at lower elevations have identified slower late summer flow in warmer summers, but were not able to capture ice motion over a full melt-year (Sundal et al., 2011; Fitzpatrick et al., 2013). No study to date has therefore combined the required spatial and temporal coverage and resolution to investigate whether the insensitivity of net annual ice motion to short-term variations in ice flow holds across broader spatial scales, so the impact of spatially variable subglacial drainage and potential related flow enhancement on net annual regional ice motion remains unquantified.

Two specific aspects of surface melt-induced ice acceleration of the GrIS remain unexplored. Firstly, whilst recent observations in south-west Greenland suggest that the subglacial drainage system is channelized to at least 40 km inland during summer (Chandler et al., 2013), the spatial extent of surface melt-induced velocity perturbations forced by water pressure variability in these subglacial channels (e.g. Nienow et al., 2005) is unknown. Secondly, over annual timescales it is unclear whether areas of ice close to surface meltwater input points and/or underlain by a channelized subglacial drainage system flow at a disproportionately faster rate than less hydrologically active areas. It is essential to identify whether surface-melt induced ice acceleration has an impact on annual regional ice motion because surface melting of the ice sheet is projected to increase during the next century (Stocker et al., 2013).

Here, we present measurements of ice motion made during 2012–13 at Leverett Glacier, a

land-terminating glacier in the south-west of the GrIS at $\sim 67^{o}$N (Figure 5.1). We measured ice motion continously by global positioning systems (GPS) at 5 survey sites to examine spatial variability in the hydrological forcing of ice motion, and by the TerraSAR-X/TanDEM-X (TSX/TDX) satellites over a ∼20 by ∼15 km area of the ice sheet margin to examine the spatial structure of seasonal and annual ice motion.

5.2 Data and Methods

5.2.1 Field measurements

We used GPS records to observe ice motion during 2012 at three sites along a longitudinal transect (S1, S2 and S3) and at two locations transverse to the longitudinal transect ∼18 km from the ice sheet margin, at ∼800 metres above sea level: S3M, 2.8 km and S3N, 4.7 km north of S3 respectively (Figure 5.1). Details of the GPS processing undertaken and longitudinal transect observations during 2012 have been described previously (Tedstone et al., 2013, (Chapter 4)). GPS receiver malfunction at S3N resulted in noisy pseudo-range data, preventing accurate determination of sub-weekly variability in ice motion, but seasonal displacements were recorded. Additionally, power failure prevented continuous recording of ice motion at S3M between 1 July 2012 and late August 2012, restricting detailed analysis of ice motion to early summer, but absolute summer displacement was obtained. Along-track velocity uncertainties are approximately ±1 cm at each epoch and 5.2 m y^{-1} for daily velocities (Bartholomew et al., 2011a). Seasonal trends in vertical and across-track displacement were removed by linear regression.

Air temperatures at S3 were logged every 15 minutes using a Campbell CR800 logger with a Campbell C107 shielded temperature probe. Discharge draining from the Leverett Glacier hydrological catchment was measured using continuous water stage monitoring through a stable bedrock section and converted to discharge by calibration with repeat Rhodamine

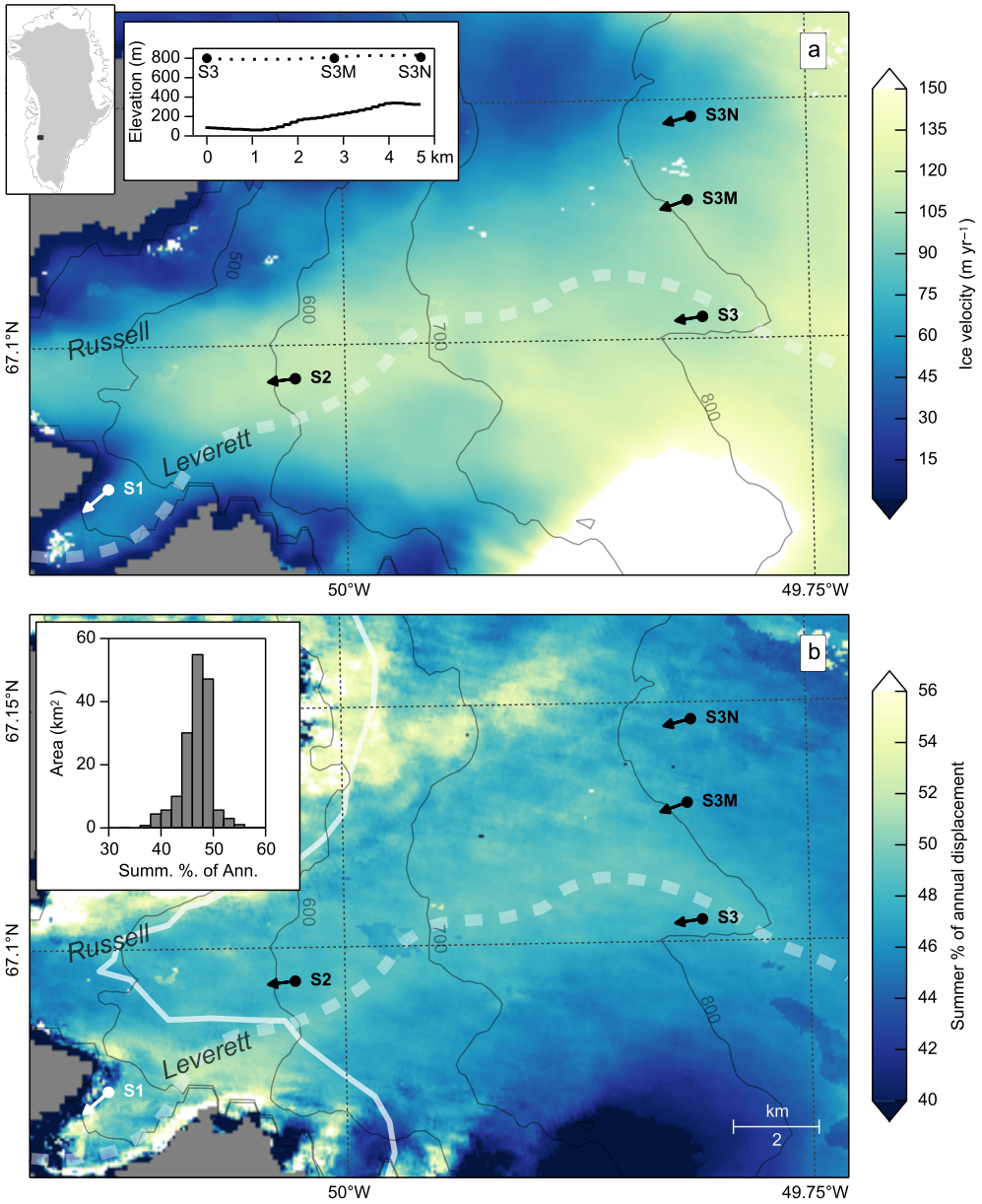

Figure 5.1: (a): Ice velocity (m yr^{-1}) measured by TSX/TDX during 1 May 2012 – 30 April 2013; inset: ice surface (dotted) and bed (solid) profiles through the GPS transect; outset: location of study area. (b): Summer (1 May 2012 – 31 August 2012) proportion of annual (1 May 2012 – 30 April 2013) displacement, with white line marking 2 km from the ice margin; inset: all observations further than 2 km from the ice margin as a histogram. (a,b): GPS sites denoted by circles, with arrows indicating along-track flow direction; contours (in metres) from a digital elevation model derived from Operation IceBridge altimetry data (Morlighem et al., 2013); thick dashed line indicates approximate location of main subglacial channel from hydraulic potential analysis (Figure 5.2).

dye dilution injections, following methods described previously (Bartholomew et al., 2011b, and Section 3.3).

5.2.2 Remote sensing of ice motion

We processed synthetic aperture radar (SAR) data acquired between 26 April 2012 and 11 May 2013 by TSX/TDX into 23 ice displacement maps by applying feature tracking (Paul et al., 2013) (Table S1). Our use of two tracks yields near-continuous temporal coverage but restricts spatial coverage to ∼20 km inland from the ice margin. The two gaps in temporal coverage of 17 and 28 days occurred during winter (Table S1) and were filled by calculating the mean displacement of the immediately preceding and subsequent displacement maps. Steady trends in winter GPS velocities, where available (e.g. Joughin et al., 2010) show that this limited averaging should not produce significant errors in ice motion estimates. Azimuth and range displacement maps were used to compute summer (1 May 2012 – 31 August 2012) and winter (1 September 2012 – 30 April 2013) displacements.

5.2.3 Hydraulic potential analysis

We used digital elevation models (DEMs) of the ice sheet surface and bed derived from Operation IceBridge altimetry and ice penetrating radar data (Morlighem et al., 2013) to produce a theoretical reconstruction of the subglacial drainage network (Shreve, 1972) to complement analyses of our ice motion data. The dense radar survey in this section of the ice sheet has an average flight spacing of ∼500 m and a nominal precision of 10 m for ice thickness (Morlighem et al., 2013). Calculations followed procedures outlined by Sharp et al. (1993). Field observations of proglacial discharge, dye and SF_6 tracer experiments show that most meltwater from our study area exits the ice sheet through the Leverett Glacier terminus rather than through Russell Glacier (Figure 5.1) (Bartholomew et al., 2011a; Chandler et al., 2013). Theoretical reconstructions suggest that meltwaters from the catchment will only drain through the correct Leverett outlet when subglacial water pressure P_w is equal to ice

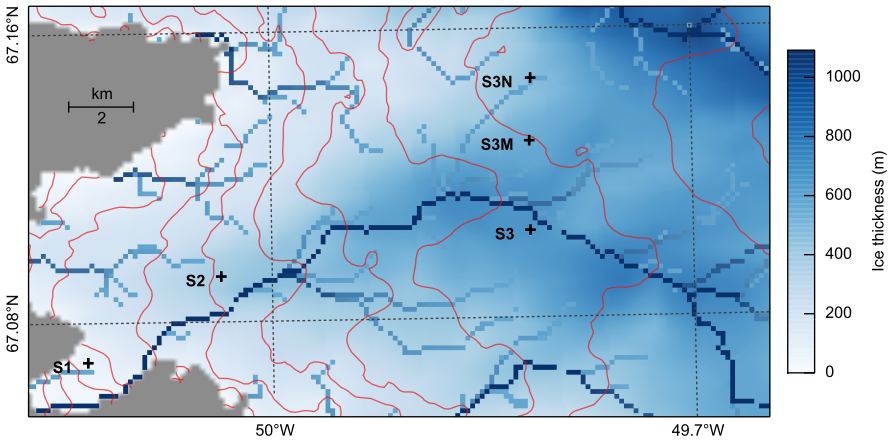

Figure 5.2: Ice thickness from Operation IceBridge (Morlighem et al., 2013). Subglacial hydraulic potential contours (red every 500 kPA) and major drainage pathways predicted by subglacial hydraulic potential analysis where water pressure equals ice overburden. Channel shading defined by the quantity of Upstream Contributing Cells (UCC) (values >50 UCC shown, with >1000 UCC in dark blue). Crosses denote GPS sites.

overburden pressure (P_i) (i.e., $P_w = P_i$) (Figure 5.2); at lower water pressures, the meltwater exits the catchment via Russell Glacier. Despite this sensitivity, all hydraulic reconstructions predict the presence of a major drainage pathway less than 200 m north of S3, an invariance controlled primarily by the ice surface topography (Figure 5.1).

5.3 Results

5.3.1 Diurnal motion at S3 and S3M

Detailed data from S3 and S3M enable us to examine the impact that spatial variability in the configuration of the subglacial drainage system has on ice motion. During the period of observation there were three clear speed-up events when ice motion increased by >100% compared to the previous two days (Figure 5.3, E1-3). These pronounced speed-ups coincided with increasing air temperatures and rising proglacial discharge as observed in

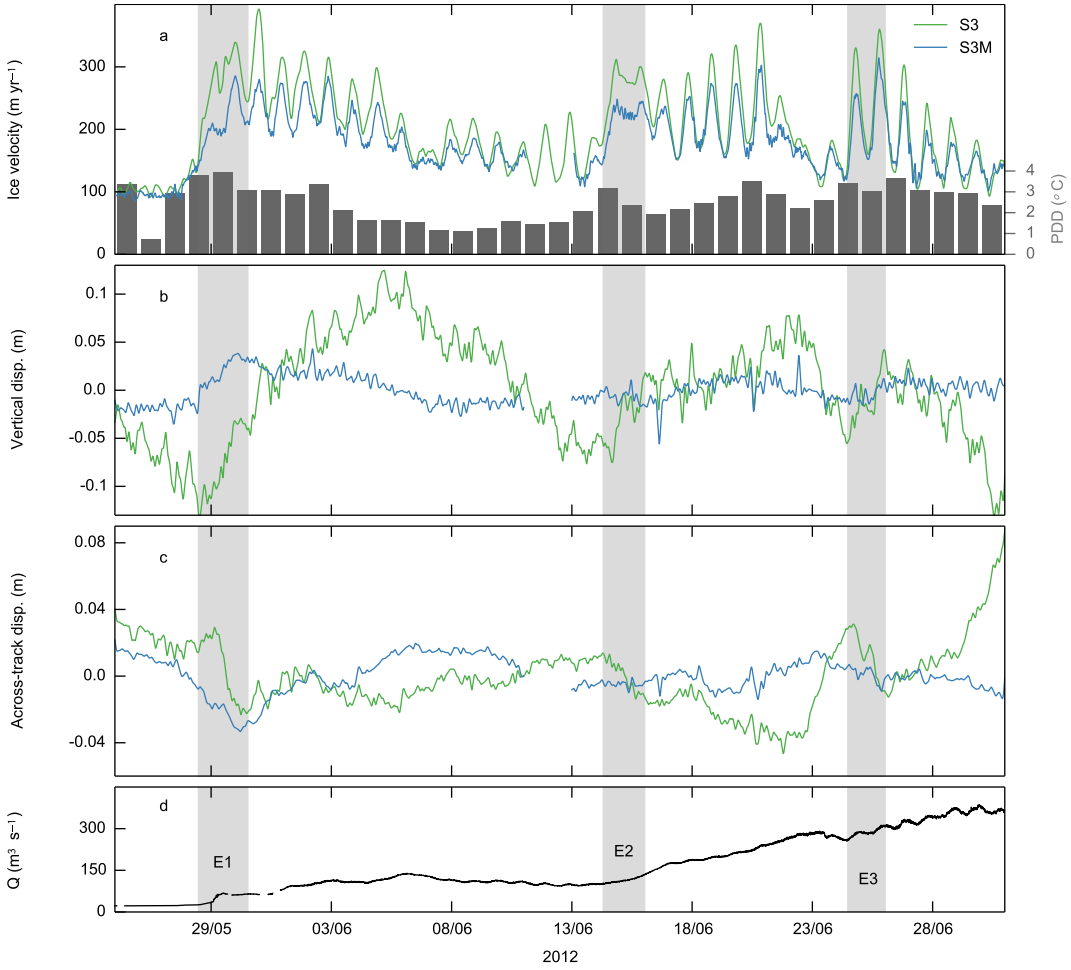

Figure 5.3: Time series at S3 and S3M of (a) along-track velocity, and positive degree days (PDD, ^{o}C) at S3, (b) de-trended vertical displacement and (c) detrended across-track displacement. (d): proglacial discharge hydrograph for Leverett Glacier (m^3s^{-1}.)

previous studies (e.g. Iken and Bindschadler, 1986; Mair et al., 2003; Bartholomew et al., 2011a).

During each event, along-track velocity at S3 increased rapidly (Figure 5.3a), accompanied by ice surface uplift of 5–10 cm (Figure 5.3b) and across-track displacement (perpendicular to the flow direction at each site shown in Figure 5.1) of 2–4 cm south-east (Figure 5.3c). While S3M's along-track velocity was 9% slower than S3 during the summer (Table 5.1), cross-correlation of their continuous velocity records (Figure 5.4) shows that during each event and over the full observation period, the sites were most highly correlated at zero

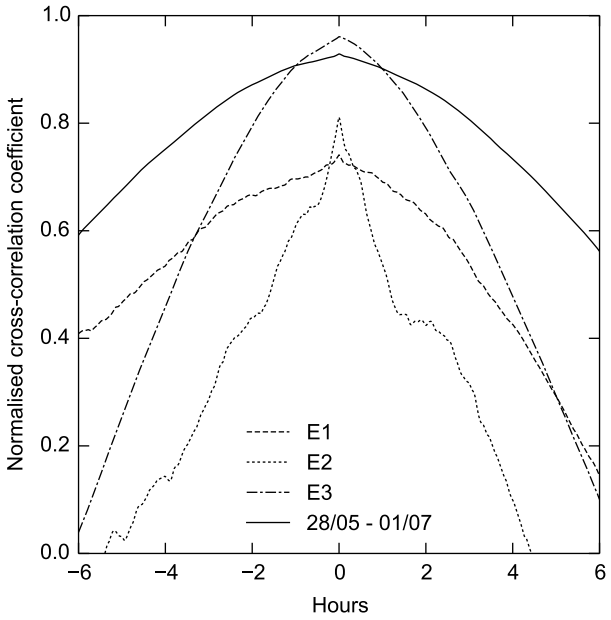

Figure 5.4: Cross-correlation functions between S3 and S3M during 28 May – 1 July and for events 1–3 (Figure 5.3), S3 as primary variable.

lag ($r > 0.8$). However, S3M only moved upward and across-flow during E1, subsequently showing no resolvable signals in vertical or cross-track displacement.

After E1, S3 continued to show clear uplift and subsidence of ∼2–5 cm over diurnal cycles for the remainder of the observation period, but without any corresponding variability in cross-track displacement except during E2 and E3. Meanwhile, S3M did not display any systematic variability in either vertical or across-track displacement (Figure 5.3b,c).

5.3.2 Seasonal and annual displacement

To identify whether spatially variable subglacial drainage during summer has an impact on ice motion over annual timescales, we examined net displacement at S3, S3M and S3N (Table 5.1) during summer (1 May – 31 August 2012) and over a full year (1 May 2012 – 30 April 2013). During summer, S3 flowed fastest, with S3M and S3N flowing at 91% and 64% of horizontal speed at S3 respectively. Similarly, during the full year, S3 flowed fastest,

with S3M and S3N displaced by 93% and 64% of S3 respectively. However, the *proportion* of annual displacement attributable to motion during summer varied by just 2% between the three sites. S1 and S2 (∼2 km and ∼8 km from the ice margin respectively) displayed equivalent behaviour (Table 5.1) such that summer motion at all sites accounted for 43.4% to 45.4% of annual motion.

Observations of ice motion from TSX/TDX complement the GPS observations, providing much greater spatial coverage of seasonal and annual ice displacement. Over the full year, absolute ice displacement observed by TSX/TDX varied by ±2% on average of the observations recorded at each GPS site, a close agreement which validates the observations made by TSX/TDX over the rest of the study area.

The ice motion observed by TSX/TDX over the melt-year (Figure 5.1a) reveals clear spatial variability both along and across flow, with areas of faster ice motion broadly co-located with thicker ice (Figure 5.2). However, there is very little variability in the proportion of annual ice displacement attributable to summer motion beyond ∼2 km from the ice sheet margin (Figure 5.1b). There is a ∼3 km wide flow zone of slightly faster (∼2%) summer motion between S3 and S3M, the location of which is coincident with the subglacial drainage channel predicted by hydraulic potential analysis (Figure 5.2).

The homogeneous behaviour of this area of the ice sheet in terms of the proportionality of summer speed-up, particularly away from the thin ice margin, is clear in Figure 5.1b (inset). Summer displacement of 43.9–49.7% of total annual displacement, corresponding to $\bar{x} \pm 1\sigma$, accounted for 81% of variability in the study area further than 2 km from the ice margin. Areas where ice flowed proportionally faster (white in Figure 1b) or slower (dark blue in Figure 1b) during summer are restricted to marginal ice thinner than ∼200 m in the former case and a steep ice fall (Sundal et al., 2011) in the latter case.

Table 5.1: Ice displacement at observation sites during 2012. Annual (Ann., metres, 1 May 2012 – 30 April 2013), Summer (Summ., metres, 1 May – 31 August), Summer % (Summ. %, proportion of annual motion attributable to Summer).

	Ice displacement, 2012		
	Ann. m	**Summ. m**	**Summ. %**
S1	52.1	23.3	44.7
S2	110.1	50	45.4
S3	105.4	47.9	45.4
S3M	98.2	43.6	44.4
S3N	70.5	30.6	43.4

5.4 Discussion

5.4.1 Drivers of diurnal ice motion

Observations of alpine glaciers have revealed Variable Pressure Axes (VPAs) tens of metres wide centered on a hydraulically efficient channel, in which subglacial water pressures (P_w) vary substantially over diurnal melt cycles, in constrast to adjacent areas of the bed where P_w becomes progressively higher and less variable as the influence of the VPA declines with distance (e.g. Hubbard et al., 1995; Harbor et al., 1997). At Haut Glacier d'Arolla (Swiss Alps), the highest diurnal ice surface velocities occur over the VPA. However, the wide area over which ice velocities increase in phase with VPA P_w can only be explained by reductions in basal shear traction over a much wider (∼560 m) area of the bed, requiring either an inefficient drainage system or a channelized system with many channels that hydraulically connect large areas of the bed (Nienow et al., 2005).

Previous studies at Leverett Glacier have inferred the presence of an efficient, channelized subglacial drainage system to at least 40 km into the ice sheet interior during summer (Bartholomew et al., 2011a; Chandler et al., 2013). The hydro-dynamical behaviour observed at S3 and S3M is explicable both by the alpine VPA framework and by hydrological modelling of the interaction between channelized and distributed subglacial drainage systems (Werder et al., 2013). S3, inferred to be in the vicinity of a major drainage pathway (Figure 5.2),

experiences large oscillations in diurnal along-track velocity and vertical displacement, consistent with oscillatory variability in P_w. Furthermore, Sugiyama et al. (2010) observe that vertical ice displacement over a basal perturbation can induce a cross-track displacement at some distance away from the basal perturbation; the south-easterly displacement of S3 during the speed-up periods E1–3 mimics this behaviour and places S3 to the south of the VPA, in agreement with the hydraulic potential analysis.

Without additional survey sites or coupled hydro-dynamic modeling (e.g. Hoffman and Price, 2014), it is not possible to identify whether the fluctuations in stress regime which force synchronous along-track motion at S3 and S3M, most likely through fluctuating P_w, originate from (a) local meltwater input points or (b) fluctuations in VPA P_w forced by upglacier surface meltwater inputs. As a result, it is not possible to elucidate the relative importance of transverse stresses or the coupling lengths over which local VPA ice-bed decoupling could propagate enhanced motion away from the VPA. Nevertheless, Werder et al. (2013) model pressure variations up to $\sim$ 2 km away from a subglacial channel, which would fit with our observations of a dynamic response at S3M driven by pressure variations within the inferred subglacial channel.

5.4.2 Seasonal and annual ice motion

Our continuous observations of ice motion at S3 and S3M during 2012 confirm that, as suggested by Palmer et al. (2011) at the broader catchment scale, surface melt-induced ice acceleration is spatially variable over diurnal timescales. At annual timescales there is also substantial spatial variability in absolute ice motion (Figure 5.1a). However, it is variability in driving stress caused primarily by differing ice thickness, rather than a spatially variable drainage system, which is the cause of this variability in our study area.

Despite clear evidence for distinct subglacial channels (both from the ice motion data presented here and previous tracer studies, e.g. Chandler et al. (2013)) which induce

complex diurnal flow patterns, the structure of the subglacial drainage system does not appear to have a significant impact on the overall extent to which summer motion contributes to annual motion. Instead, in 81% of the area further than 2 km from the ice margin, the contribution of summer motion to annual motion falls within the narrow range of ∼44–50%, irrespective of proximity to underlying subglacial channels. This suggests that the surrounding regions of distributed drainage readily connect to and interact with channelized drainage features, smoothing spatial variations in velocity forced by water pressure fluctuations in the channels. Thus, the existence of channels constitutes an important control on regional subglacial water pressure, but the precise location of each channel is less important because they interact readily with the surrounding distributed drainage system rather than acting in isolation.

Our finding, that an essentially spatially invariant proportion of annual motion occurs during the melt season, may be explicable both by recent field observations from the GrIS and modeling. Using observations of ice velocity, moulin water levels and borehole water pressures, Andrews et al. (2014) concluded that decreasing water pressures in the unchannelized (or 'distributed') regions of the subglacial drainage system, not the channelized areas, were responsible for their observed late summer slowdown in ice velocities. Such hydro-dynamic coupling in unchannelized regions, which underlie the majority of our study area, in contrast to narrow, discrete channelized drainage features (or VPAs), may therefore provide a plausible explanation for the spatial invariance in the proportion of annual motion which we observe during summer.

Furthermore, these observations qualitiatively agree with modeling results (Hoffman and Price, 2014) which suggest that upon the delivery of meltwater to the ice sheet bed, ice velocity transiently increases, but a negative feedback then dominates the subsequent velocity response whereby sliding over bedrock bumps increases cavity space, lowering water pressure and in turn sliding. This negative feedback occurs even in the absence of channelization, acting to limit the magnitude of any surface melt-driven velocity increase.

Thus, the coupled hydrology-dynamics of the spatially extensive unchannelized regions of the ice sheet bed may explain our observation that the summer proportion of annual ice motion is spatially invariant.

5.5 Conclusions

We have examined spatial variability in surface melt-induced ice motion in a land-terminating region of the south-west GrIS. We have shown that whilst spatial variability in the configuration of subglacial drainage controls ice motion at short timescales, these variations have negligible impact on the proportion of annual motion which occurs during summer as a result of surface meltwater inputs to the ice sheet bed. Whilst absolute annual velocities vary substantially across the study area (due to variations in driving stress), the proportional contribution of summer motion to annual ice motion does not.

This observation is important because it implies that, for land-terminating regions of the GrIS, (1) it may not be necessary to include complex representations of subglacial hydrology in ice sheet models for simulating ice flow and (2) the placement of GPS relative to subglacial channels should only affect the detailed pattern of ice velocities over short timescales and not the relative seasonal displacement resulting from hydraulic forcing. Nevertheless, additional research needs to determine the extent to which our findings are applicable to the wider ice sheet and in particular (1) whether the invariance of ice motion to the configuration of the subglacial drainage system over annual timescales extends further inland where the extent of channelization remains equivocal (Chandler et al., 2013; Meierbachtol et al., 2013) and (2) the applicability of our findings to other land-terminating margins of the ice sheet and to marine-terminating margins, where hydro-dynamic coupling remains poorly understood.

5.6 Supplementary Information

Table 5.2 For each TSX/TDX acquisition:

Column "Start date", date that TSX/TDX acquisition begins (year, month, day).

Column "End date", date that TSX/TDX acquisition ends (year, month, day).

Column "Time", Universal Time Coordinated (UTC) time of TSX/TDX overpass time on "Start date" and "End date" of each acquisition.

Column "Days", duration of acquisition in days.

Column "Relative orbit", relative orbit angle of TSX/TDX in degrees.

Column "Incidence", incidence angle of TSX/TDX in degrees.

Column "Heading", heading angle of TSX/TDX in degrees.

Start date	End date	Time	Days	Relative orbit	Incidence	Heading
20120426	20120518	09:57:27	22	96	37	193
20120518	20120529	09:57:27	11	96	37	193
20120529	20120609	09:57:27	11	96	37	193
20120609	20120620	09:57:27	11	96	37	193
20120620	20120701	09:57:27	11	96	37	193
20120701	20120723	09:57:27	22	96	37	193
20120723	20120803	09:57:27	11	96	37	193
20120803	20120814	09:57:27	11	96	37	193
20120814	20120825	09:57:27	11	96	37	193
20120825	20120905	09:57:27	11	96	37	193
20120905	20121008	09:57:27	33	96	37	193
20121008	20121030	09:57:27	22	96	37	193
20121030	20121110	09:57:27	11	96	37	193
20121110	20121121	09:57:27	11	96	37	193
20121121	20121202	09:57:27	11	96	37	193
20121202	20121213	09:57:27	11	96	37	193
20121213	20121224	09:57:27	11	96	37	193
20121224	20130104	09:57:27	11	96	37	193
20130104	20130115	09:57:27	11	96	37	193
20130228	20130311	09:57:27	11	96	37	193
20130311	20130322	09:57:27	11	96	37	193
20130419	20130511	20:40:57	22	27	35	346

Table 5.2: TerraSAR-X/TanDEM-X acquisitions utilised in study.

Chapter 6

Decadal slowdown of a land-terminating sector of the Greenland Ice Sheet despite warming

Chapter 4 demonstrated that 'extreme' melting can result in slower annual ice motion than 'average' melting, up to at least 70 km inland. Chapter 5 presented complementary evidence showing that over the course of a melt-year, the proportion of net annual motion which occurs during the melt season is spatially invariant. These chapters therefore paint an emerging picture in which coupled hydrology-dynamics is essentially self-regulating: temporally transient speedups are negated by subsequent slowdown due to increasing drainage system efficiency, and, despite the evolution of a subglacial drainage system with discrete efficient drainage features, there are no significant spatial variations in the proportion of annual motion which occurs during summer.

However, the importance of coupled hydrology-dynamics over inter-annual to decadal timescales remains unclear as very few observations of requisite duration exist. This chapter takes advantage of the recent release of unprecedented volumes of historical Landsat program satellite imagery by using feature tracking between successive images to extract

ice motion over an 8000 km^2 area (Figure 3.1) from 1985 to 2014, in order to assess the impact of surface meltwater production on ice motion over the last three decades.

Under review with **Nature**, July 2015.

Authors: Andrew J. Tedstone[1], Peter W. Nienow[1], N. Gourmelen[1], Amaury Dehecq[2,1], Daniel Goldberg[1] and Edward Hanna[3].

1. School of GeoSciences, University of Edinburgh, Edinburgh, EH8 9XP, UK
2. Université de Savoie, Polytech Annecy-Chambéry, LISTIC, BP 80439, 74944 Annecy-le-Vieux cedex, France
3. Department of Geography, University of Sheffield, Sheffield, S10 2TN, UK

Author contributions: A.J.T., P.W.N. and N.G. designed this study. A.D., N.G. and A.J.T. developed the processing chain used for feature tracking of Landsat imagery. A.J.T., A.D. and N.G. processed the Landsat imagery. A.J.T. and D.G. calculated the impact of changing ice geometry upon ice motion. E.H. processed the melt data. A.J.T., N.G. and P.W.N. analyzed the results. A.J.T., P.W.N. and N.G. wrote the manuscript. All authors discussed the results and edited the manuscript. A.J.T. was the lead author of this work.

Acknowledgements: N.G. acknowledges European Space Agency Dragon 3 grant 10302 and a fellowship from the Centre National d'Etudes Spatiales to A.D.. This work made use of the resources provided by the Edinburgh Compute and Data Facility (ECDF) (http://www.ecdf.ed.ac.uk/). P. Huybrechts worked on the runoff/retention model used in this study.

Ice flow along land-terminating margins of the Greenland Ice Sheet (GrIS) varies considerably in response to fluctuating surface meltwater inputs to the ice-sheet bed which lubricate the ice-bed interface, resulting in periods of faster ice motion (Zwally et al., 2002; Sole et al., 2013). Stronger melting results in faster ice motion during summer, but slower motion over the subsequent winter due to the evolution of a more extensive drainage system at the ice-sheet bed, which drains high-pressure regions more efficiently (Sole et al., 2013; Tedstone et al., 2013). However, the impact of hydro-dynamic coupling on ice motion over decadal timescales remains poorly constrained. Here we show that annual ice motion across an 8000 km^2 land-terminating region of the west GrIS margin extending to 1100 m asl was 12% slower in 2007–2014 compared to 1985–1994, despite a corresponding 50% increase in surface meltwater production. Our findings suggest that hydro-dynamic coupling in this section of the ablation zone resulted in net ice motion slowdown over decadal timescales — not speedup as previously postulated (Zwally et al., 2002). Increases in meltwater production from projected climate warming may therefore further reduce the motion of land-terminating margins of the GrIS, which suggests that these sectors of the ice sheet are more resilient to the dynamic impacts of enhanced meltwater production than previously thought.

The Greenland Ice Sheet (GrIS) is losing mass at an accelerating rate (Shepherd et al., 2012; Enderlin et al., 2014) as a result both of increased surface melting (Hanna et al., 2013) and enhanced ice discharge from accelerating marine-terminating glaciers (Enderlin et al., 2014). Enhanced melting accounts for ∼60% of GrIS mass loss since 2000 (Enderlin et al., 2014); summer air temperatures over the south-west GrIS warmed by 0.9^{o}C during 1994–2007 (Box et al., 2009) and meltwater production during the summers of 2007–2012 (except 2009) is without precedent in the last 50 years of reanalysis-forced reconstructions (Fettweis et al., 2013). During 1993–2012 the average annual melt doubled from that which occurred during 1961–1990 (Fettweis et al., 2013).

While the acceleration of marine-terminating glaciers is believed to be driven primarily by processes operating at the ice-ocean interface, atmospheric forcing can change ice motion at both land- and marine-terminating glaciers through the delivery of surface meltwater to the ice-sheet bed (Zwally et al., 2002; Howat et al., 2010). Surface meltwaters can drain rapidly to the ice-sheet bed via moulins and supraglacial lake drainage events which provide direct surface-to-bed connectivity and a mechanism by which surface meltwater can influence basal motion (Das et al., 2008; Chandler et al., 2013; Andrews et al., 2014). It was hypothesised that this mechanism could lead to a positive feedback between enhanced surface meltwater production and ice-sheet motion as ice would move more quickly to lower elevations where temperatures are warmer (Zwally et al., 2002; Parizek and Alley, 2004).

More recent studies have highlighted the importance of the subglacial drainage system in controlling the relationship between surface melting and ice motion through changes in system capacity and morphology (Schoof, 2010; Bartholomew et al., 2011a; Cowton et al., 2013). During summer, rapid increases in meltwater from the ice-sheet surface result in periods when the subglacial drainage system is more highly pressurised, leading to transient periods when water pressure exceeds ice overburden pressure, resulting in enhanced basal sliding (Bartholomew et al., 2011a). However, subglacial drainage system capacity increases in response (Röthlisberger, 1972; Schoof, 2010), introducing a negative feedback which lowers the water pressure and reduces basal sliding (Cowton et al., 2013; Hoffman and Price, 2014). By the end of summer, an efficient drainage system has evolved upglacier (Bartholomew et al., 2011a; Cowton et al., 2013) which drains surrounding regions of the ice-sheet bed that were previously hydraulically isolated. This reduces basal lubrication during the subsequent winter, counteracting summer speed-up and making net annual ice motion relatively insensitive to summer melting (Sole et al., 2013; Tedstone et al., 2013).

Despite these advances in understanding coupled hydro-dynamics, it remains unclear whether enhanced surface melting has a long-term impact on annual ice motion. Eight Global Positioning System (GPS) stations on a transect extending 130 km inland in the

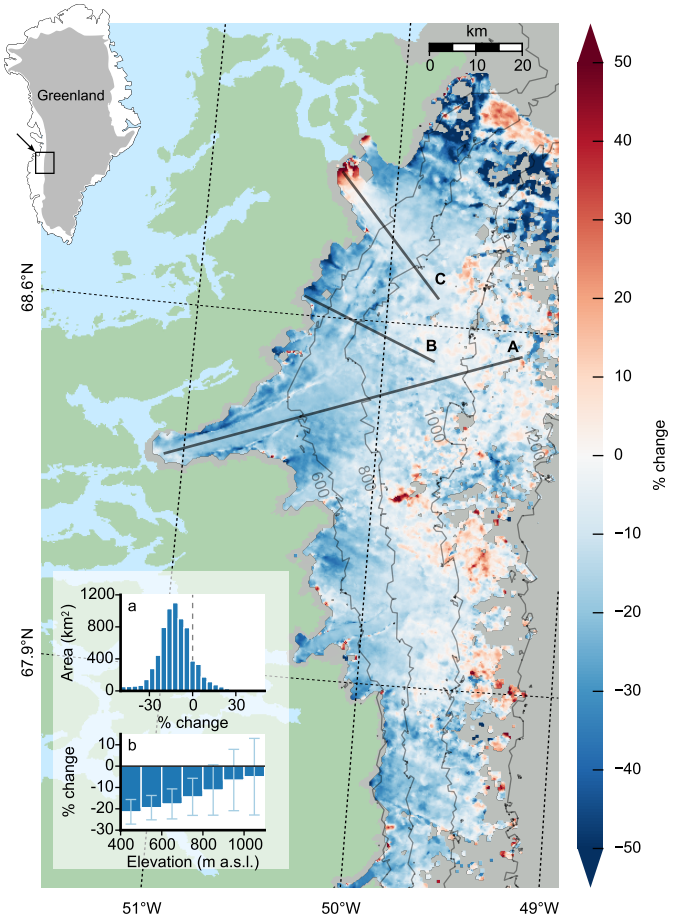

Figure 6.1: Study area in the ablation zone of the western GrIS. Colour shows percentage change of ice velocities in 2007–2014 reference period compared to 1985–1994 reference period (see main text). Transects correspond to Figure 6.3. Ice surface contours from Howat *et al.* (Howat et al., 2014). Grey denotes areas where ice velocities cannot be resolved; green denotes land areas; light blue denotes inland and coastal waters. Inset (a): percentage change of ice velocities in 4% bins. Inset (b): Median percentage change in each 100 m elevation band between 400–1100 m asl and associated uncertainties (see Methods).

south-west GrIS showed an average 10% decrease from 1991 to 2007, during a period when surface melt increased significantly, but with considerable spatial variability (van de Wal et al., 2008), and the slowdown trend at lower sites continued into 2012 (van de Wal et al., 2015). Meanwhile from 2009 to 2012 a small acceleration signal was observed above the ∼1500 m asl equilibrium line altitude (Doyle et al., 2014). The parametrization of basal lubrication in higher-order ice-sheet models, using observations from south-west Greenland, suggests that basal lubrication is unlikely to increase the contribution of the ice sheet to

sea level rise by more than 5% of the contribution expected from a negative surface mass budget alone, and could conceivably act as a negative feedback upon ice motion (Shannon et al., 2013).

Here we present observations of annual motion spanning three decades, which extend back to 1985. Our ∼8000 km^2 study area extends along ∼170 km of predominantly land-terminating margin of the west GrIS to ∼50 km inland and ∼1100 m asl (Figure 6.1). We apply feature tracking (see Methods) to 475 pairs of remotely-sensed optical Landsat imagery separated by approximately one year (Dehecq et al., 2015). Next, we derive robust ice motion and uncertainty estimates over ∼1–2 year periods from 1985 to 2014 (Figure 6.2b and Figure 6.8), and over multi-year reference periods spanning (a) 1985–1994, capturing the period before air temperatures began to warm (Box et al., 2009), and (b) 2007–2014, corresponding to the recent series of record melt summers (Fettweis et al., 2013).

Ice motion shows a clear regional slow down (Figure 6.1) with 84% of the study area flowing more slowly in 2007–2014 than in 1985–1994 (Figure 6.1a). On average ice motion slowed by 12% across the study area. Slowdown was strongest (∼15-20%) at elevations below ∼800 m asl (Figure 6.1b). Isolated areas experienced speedup in 2007–2014 compared to 1985–1994. In the far north-east, the speedup can likely be attributed to the dynamics of the neighbouring marine-terminating Jakobshavn Isbrae (Figure 3.1), which like many of Greenland's marine-terminating glaciers has accelerated since the mid 1990s (Enderlin et al., 2014).

The ice motion record can be divided into two statistically significant periods (see Methods). Segmented linear regression ($R^2 = 0.79$) shows that there was no significant trend in ice motion during 1985–2002 ($p = 0.85$). Ice motion slowdown likely began around 2002 and despite inter-annual variability, there was a robust overall trend of -1.5 m yr^{-2} during 2002–2014 ($p < 0.01$). Meanwhile, surface meltwater production (Figure 6.2a) can be divided into three statistically significant periods (see Methods): sustained 'low' melt of 2.1 water equivalent (w.e.) m yr^{-1} during 1985–1993, rising melt during 1993–2002, and

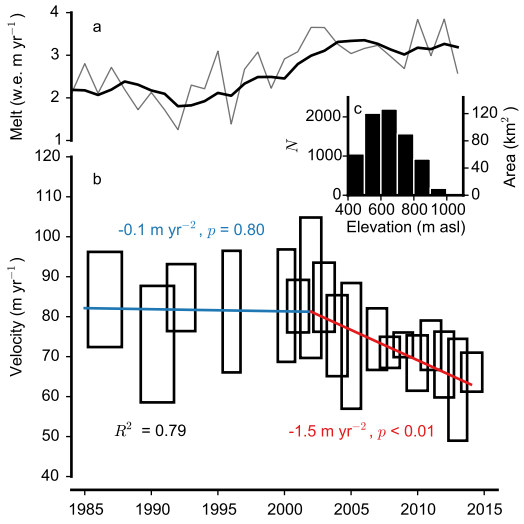

Figure 6.2: Surface melting and ice motion averaged over the study area. (a) Annual mean modelled surface melt (grey), smoothed with a 5-year moving mean (black), both in water equivalent (w.e.) m per year (see Methods). (b) Median ice velocities during each period (black boxes) calculated using the common sampling pixels across the time series, ± 1σ_p. The width of each box corresponds to the total timespan of the pairs of Landsat images acquired during each period. The height of each box corresponds to ± σ_p (see Methods). Blue and red lines illustrate the trends in ice velocity computed by segmented linear regression weighted by σ_p. (c) The altitudinal distribution of the common sampling pixels used to compute the velocities in (b).

sustained high melt of 3.2 w.e. m yr^{-1} during 2002–2014 coincident with when ice motion began to slow down. Overall there was a 49.8% rise in surface meltwater production across our study area between 1985–1994 and 2007–2014.

We explored temporal variability in ice motion along three transects (Figure 6.1) selected to represent different ice-marginal conditions. Transect A (Figure 6.3a) extends 80 km inland from Nordenskjöld glacier, which has a lacustrine-terminating margin; transect B (Figure 6.3b) extends ∼30 km inland from a land-terminating margin; and transect C (Figure 6.3c) extends ∼30 km inland from the marine-terminating Alangordliup sermia. Transects A and B slowed down during 2000–2014 to attain velocities averaged along the transect 19% and 18% lower in 2013/14 than during the 1985–1994 reference period respectively. Ice motion characteristics at the marine-terminating transect C were more complex. The transect slowed on average from the mid 2000s to 2014 although ice motion within 10 km of the margin sped up in the late 2000s following earlier slowdown and by

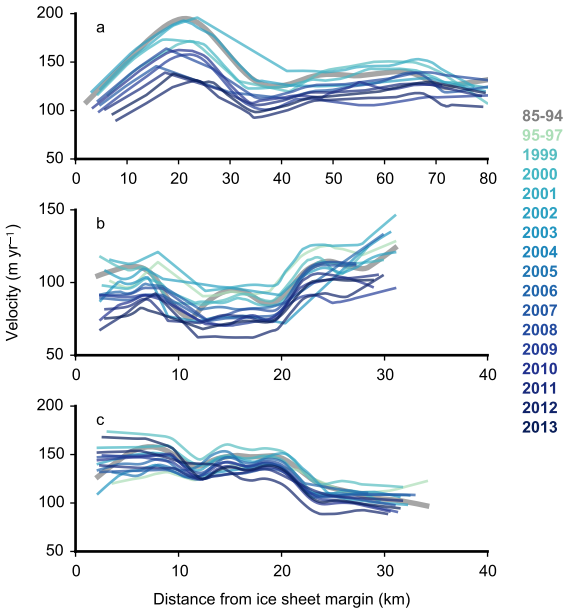

Figure 6.3: Ice velocities along three transects in the study area. The transects correspond to those shown in Figure 6.1. Only periods in which ice velocities are observed along at least 60% of each transect are shown. Velocities during the 1985-1994 reference period are also shown. (a) Transect A, (b) Transect B, (c) Transect C.

2013–2014 was flowing up to ∼ 50 m yr^{-1} faster than during the 1985–1994 reference period. Such behaviour is in line with other tidewater glaciers that have recently accelerated (Enderlin et al., 2014).

The slowdown signal across our predominantly land-terminating region extends up to ∼1100 m asl (Figure 6.1) where the mean ice thickness is ∼850 m (Morlighem et al., 2014). The clear deceleration in ice motion requires a decrease in rates of either internal ice deformation, basal motion or a combination of both mechanisms. Melting has caused marginal thinning of the GrIS (Sole et al., 2008; Pritchard et al., 2009; Helm et al., 2014). During 1993–1998 land-terminating glaciers on the west GrIS margin thinned by 0.02-0.23 m yr^{-1} below 1000 m asl (Sole et al., 2008). Our study area thinned by ∼0.2 m yr^{-1} during 2003–2007 (Pritchard et al., 2009) and this rate increased to 1–1.5 m yr^{-1} during 2011–2014 (Helm et al., 2014). We modelled the velocity change that would be caused by 10–20 m of ice thinning (and the associated gradient changes) along transect A over the 1985–2014 study period (see

Methods), corresponding to a maximum thinning rate of ∼0.6 m yr^{-1}. The resulting change in driving stress can explain only ∼17-33% of the observed overall 12% slowdown signal beyond 10 km from the ice sheet margin and can explain none of the slowdown beyond 50 km from the margin (Figure 6.7c). Thus, while a component of the observed slowdown can be explained by changes in driving stress through ice thinning, the majority of the slowdown (i.e. the remaining 67–83%) must be the result of processes operating at the ice-bed interface causing a reduction in basal motion.

Previous studies have suggested that the coupling between surface melting and basal motion is self-regulating, such that there is no significant relationship between melting and ice motion over annual timescales (Sole et al., 2013; van de Wal et al., 2015). In agreement with these studies we find no relationship between annual melt volume and annual ice motion ($R^2 = 0.08$). There is however a strong relationship between antecedent melt volumes and ice motion (Table 6.1). The mean melt volume from each observation period and previous year combined explain 23% of observed ice motion ($p < 0.05$), increasing to 44% when the previous four years of melt are included. Moreover, melt volumes explain 50% of observed ice motion when the mean melt volume is calculated using only the previous three years ($p < 0.01$).

We therefore hypothesise that sustained high surface meltwater production (Figure 6.2a) is responsible for the observed slowdown. Observations from the GrIS show that during the melt season, the large cumulative increase in the rate of meltwater supply to the ice-sheet bed results in the expansion of a channelized subglacial drainage system (Cowton et al., 2013), even beneath ice ∼1 km thick (Chandler et al., 2013). As air temperatures warm, more meltwater at higher elevations allows an efficient drainage system to evolve which extends further into the ice sheet. Summers of extreme melt result in a higher-capacity, more extensive channelized drainage system which stays open at atmospheric pressure for longer after cessation of melt (Sole et al., 2013; Tedstone et al., 2013). Dye tracing of alpine glaciers (Richards et al., 1996) indicates that transit speeds through unchannelized

drainage systems are ∼0.01 m s^{-1} (∼850 m d^{-1}). Thus, while channels at atmospheric pressure beneath ∼1 km thick ice close within hours to days (Chandler et al., 2013), channels which stay open, for example for just two days as opposed to one, have the capacity to evacuate significantly more water from surrounding unchannelized regions of the ice-sheet bed, causing more widespread dewatering of the ice-bed interface. Sources of meltwater, including frictional melting by basal slip and geothermal heat, will enable water pressure (P_w) to recover gradually through the subsequent winter, but may be insufficient to replace the stored waters evacuated during the previous melt season.

Previous observations have illustrated the importance of changing connectivity between channelized and unchannelized regions of the ice-sheet bed in controlling ice velocities late in the melt season (Andrews et al., 2014). We postulate that these unchannelized drainage regions and their connectivity to the channelized drainage system govern ice motion not only late in the melt season but also during the following winter and spring. We hypothesise that if increases in drainage efficiency occur year-on-year, gradual net drainage of water stored in unchannelized regions of the ice-sheet bed will result in reduced basal lubrication and net ice slowdown. Additional field observations, such as borehole arrays transverse to subglacial channels recording water pressure gradients (e.g. Hubbard et al., 1995), in conjunction with hydrological modelling (e.g. Schoof, 2010) are required to test the robustness of our hypothesis. Furthermore, while melt-driven seasonal evolution in subglacial drainage can impact the flow of tidewater glaciers (Howat et al., 2010), their ongoing acceleration (Enderlin et al., 2014) during a period of warming, in contrast to our observations, suggests that other processes are controlling their dynamics.

Our observations of GrIS ice motion made over three decades provide conclusive evidence that a 50% rise in meltwater production has not led to ice speedup along a land-terminating margin; instead average annual ice motion at elevations below 800 m asl slowed by >15% and likely by at least 5% up to 1100 m asl. Only ∼17-33% of the slowdown can be explained by reduced internal deformation caused by ice thinning, and we therefore hypothesise that

since 2002, increases in subglacial drainage efficiency associated with sustained larger melt volumes have reduced basal lubrication, resulting in slower ice flow. It remains unclear whether the observed slowdown occurs at elevations above 1100 m asl and whether the slowdown will migrate inland as enhanced melting extends to higher elevations and allows a more extensive efficient subglacial drainage system to evolve. Furthermore, while our findings relate to land-terminating margins, the forcing mechanisms which have driven the recent speedup of many tidewater glaciers remain poorly understood (Enderlin et al., 2014; Pritchard et al., 2009) and require a similar examination of annual ice motion over decadal timescales.

6.1 Methods

6.1.1 Remote sensing of ice motion

We applied feature tracking techniques to extract ice motion from Landsat Program imagery. Landsat images were obtained from the U.S. Geological Survey (via the earthexplorer.usgs.gov catalogue) and the European Space Agency (via the EOLI-SA catalogue). Here we provide an outline of the processing strategy and the specific parameters used in this study. A detailed description of the processing strategy is available elsewhere (Dehecq et al., 2015). Our approach builds individual annual velocity fields from feature tracking of Landsat pairs, overlapping in time and space. These velocity fields are then combined over inter-annual time periods in order to increase the robustness of the velocity estimates and to enable statistical determination of uncertainties.

We used images from the Landsat 5, 7 and 8 missions; the quality and quantity of images from Landsat missions 1–3 were insufficient to permit their inclusion in this study. We identified 475 image pairs with temporal baselines between 352–400 days acquired during April–October over the 1985–2014 study period (see pair list in Supplementary Information). The temporal baseline of $\sim$1 year was chosen to minimize the impact of seasonal flow variability upon inter-annual trends in ice velocity, as we are specifically interested in long-term changes in ice motion.

To enhance the images prior to feature tracking we used Principal Component Analysis to combine the optimum spectral bands, identified during testing as bands 2 and 3 for each satellite mission. A high pass filter (utilising Sobel kernels) was used to compute the intensity gradients of each image, enhancing surface features such as crevasses and reducing the impact of basal topography related features which by definition are temporally stable. We then used the gradients as features to be tracked. The tracking (used to extract ice displacement) was performed on matching windows of 44 pixels (1320 m) and a grid

spacing of 8 pixels (240 m), whilst the search window was set automatically to correspond to the maximum expected displacement over the baseline duration between the two images based on previous velocity observations (Joughin et al., 2010).

The processing strategy exploits the redundancy offered by multiple, spatio-temporally overlapping pairs to efficiently remove velocity outliers and produce robust velocity fields. Firstly, we filter low quality velocity estimates by applying a threshold to the signal-to-noise ratio returned during the feature tracking. The threshold value was determined by examining all velocity pairs to identify the value beyond which the Median Absolute Deviation (MAD) of stable area velocities became asymptotic. We use a median based approach to minimize the impact of outliers and because the distribution of velocity tends not to follow a normal distribution (Dehecq et al., 2015). Next, for the period 2000–2014, velocities were grouped into 1-year time periods, while for the period 1985–2000, velocities were grouped into 2-year time periods due to the lower number of Landsat pairs available. This provides spatio-temporal redundancy in the velocity estimates at each pixel and enables us to quantify uncertainties. To produce the final velocity field for each period we compute the median of all the available velocity estimates at each pixel. Lists of the Landsat pairs which contribute to each period are available in the Supplementary Information. Finally we compute the 1σ uncertainty of the velocity estimate at each pixel in each period. To do so we fit a law of the form

$$\sigma = \frac{k}{2}\frac{MAD}{N^{\alpha}}, \tag{6.1}$$

where N is the number of velocities used to compute the median velocity, σ is the 1-σ confidence interval and k and α are the parameters to be determined. k and α were determined for each time period from the velocity estimates made over stable land areas whose true value is known and equal to 0. Uncertainty of the final ice velocity of each pixel at each time period is then obtained by extrapolating this relationship to on-ice areas with

the appropriate values of *MAD* and N for a given pixel. Considering N and *MAD* at the pixel level allows the surface characteristics at the location of the pixel considered (e.g. surface conditions, variability of velocity during the time period considered) to be taken into account. Pixels with σ >60 m yr^{-1} are discarded in the subsequent analysis.

We computed the percentage change in ice velocities between 1985–1994 and 2007–2014 at all of the pixels which are common to both periods (Fig 6.1) and then computed the median percentage change, both over the whole study area and in 100 m asl elevation bands. For each elevation band in Figure 6.1b we calculated the uncertainty of the percentage change by firstly estimating the uncertainty of the 1985–1994 (e_1) and 2007–2014 (e_2) velocities separately as $\sqrt{\sum_{i=1}^{N} \sigma_i^2/N}$, and then computing $\sqrt{{e_1}^2 + {e_2}^2}$. Residual striping patterns in Figure 6.1 are caused by lines of missing data in the Landsat 5 imagery.

To compute inter-annual median velocities (Figure 6.2b), firstly periods in which less than 30% of the study area have observations were discarded. Then, the pixels common to all the retained periods (shown in Figure 6.8) were selected so as to avoid temporal variation caused by spatial bias. For each period we calculated the median of the 8025 temporally common pixels and the associated uncertainty, estimated as $\sigma_p = \sqrt{\sum_{i=1}^{N} \sigma_i^2/N}$. The altitudinal distribution of the common sampling pixels is shown in Fig 6.2c.

The decision to discard periods in which less than 30% of the study area has observations is a compromise between calculating the median velocity of each period using the greatest possible number of pixels common to all periods, versus retaining the maximum possible temporal resolution. We examined the sensitivity of the ice motion time series (Figure 6.2b) to 40% and 50% thresholds. At 40%, there are 5970 more common sampling pixels than at 30%, but temporal resolution decreases as ice velocities observed in 2003–2006 are no longer retained. The R^2 of the two-trend model decreases to 0.65. The rate of slowdown during 2002–2014 increases from 1.5 m yr^{-2} to 1.9 m yr^{-2} ($p < 0.01$). At 50%, there are 8397 more common sampling pixels than at 30%. Velocities observed during the 1995–1997 period are also discarded. The R^2 of the two-trend model is 0.63. The rate of slowdown during

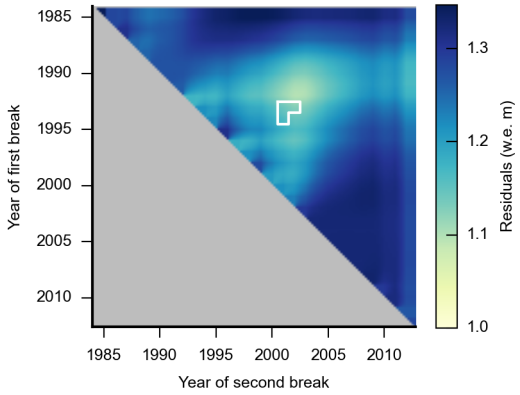

Figure 6.4: Statistical significance of three different periods of surface meltwater production. Hypothesis test of the Wilcoxon rank sum test at 95% confidence, showing that three periods of surface melt separated by the specified dates have statistically different medians (outlined white region). The shading shows the residuals of a 3-trend linear segmented regression model fitted to melting at each possible combination of break dates, expressed as the root-mean-square error.

2002–2014 remains the same as at 40% ($p < 0.01$). There is no statistically significant trend in ice motion from 1985 to 2002 ($p > 0.05$) at either of the tested thresholds. From this sensitivity analysis we conclude that our 30% threshold case yields the highest temporal resolution and also the most conservative trend in ice motion during 2002–2014.

6.1.2 Identification of trends in melting and ice motion

For both time series we test whether they can be divided into temporally distinct populations separated by break dates. We therefore apply the Mann-Whitney-Wilcoxon (MWW) rank sum test in order to investigate the effect of prescribing different break dates. We chose the MWW test over the t-test as we do not know whether the dataset follows a normal distribution. The test computes the probability that the populations, separated by prescribed break dates, are similar.

The melt time series (Figure 6.2a) consists of several years of sustained low melt, followed

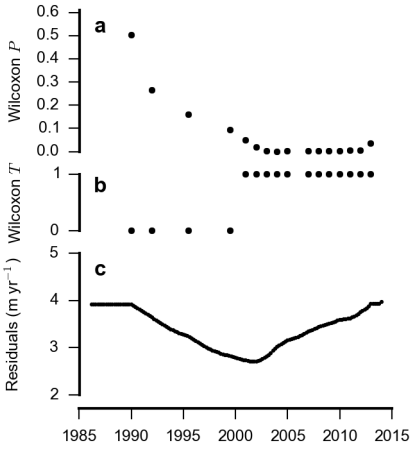

Figure 6.5: Statistical significance of two different periods of ice motion. (a) Wilcoxon rank sum test for equal medians, showing the probability of the two populations separated by the specified date to be similar. (b) Hypothesis test of the Wilcoxon rank sum test at the 0.05 significance level. 0 signifies that the hypothesis of equal medians cannot be rejected and 1 signifies that the hypothesis of equal medians can be rejected. (c) Residuals shown as the sum-of-squares (m yr^{-1})^2 of a 2-trend model fitted to velocities at each possible break date.

by a period of rising melt and then several years of sustained higher melt. We therefore test whether the melt time series can be split into three statistically different populations, with two break dates separating the periods of sustained low, rising and sustained high melt. We find that the break date combinations of (i) 1992 and 2001, (ii) 1993 and 2001, and (ii) 1993 and 2002 are all significant with 95% confidence (Figure6.4). To find the best possible combination of break dates, we then compute the root-mean-squared error, or residuals, of the best fitting 3-trend segmented linear regression model (Figure 6.4). We observe the lowest residuals for break dates of 1991–1993 and 2001–2004. The combination of break dates which satisfy the MWW test and have the lowest residuals is 1993 and 2002. With this chosen combination of break dates, the probability that (i) 1985–1993 is similar to 2002–2013 is 0.02%, (ii) 1985–1993 is similar to 1994–2001 is 2%, and (iii) 1994–2001 is similar to 2002–2013 is 3%.

For the ice motion time series, we first test whether it can be divided into two temporally distinct populations, in order to justify the use of segmented linear regression (Figure 6.2). We apply the MWW test as previously. We find that for break dates beyond mid 2001, the

Table 6.1: Statistical relationship between melting and ice motion. The results of linear regression analysis carried out between all periods of ice motion in Fig 6.2b and different estimates of temporally coincident(1) and antecedent meltwater production (see Methods).

Years preceding period (N)	Period and preceding N years		Preceding N years only	
	R^2	p	R^2	p
0	0.08(1)	0.23	-	-
1	0.23	0.04	0.28	0.02
2	0.35	< 0.01	0.48	< 0.01
3	0.41	< 0.01	0.5	< 0.01
4	0.44	< 0.01	0.5	< 0.01

null hypothesis (equal median) can be statistically rejected (Figure 6.5b), meaning that the pre- and post- 2001 populations are statistically different with 95% confidence. To test the ability of two distinct periods separated by a given break date to represent the velocity time series we then compute the residuals of the best fitting 2-trend segmented linear regression model for a set of break dates spanning the time period of the dataset (Figure 6.5c). We observe a minimum for a break date in 2002 but with a region of low residuals spanning the period 1998 to 2004. We conclude from these tests that there are two distinct temporal populations of ice motion in our dataset and that the break point occurs during 1998–2004. For our analysis (Figure 6.2) we select a break date of 2002, which corresponds both with the lowest residuals and the MWW test suggesting that the pre- and post-2002 populations are statistically different.

We then examine whether there is a statistically significant relationship between meltwater production and ice motion by applying linear regression analysis to investigate the extent to which variability in ice motion can be explained by (a) temporally coincident and (b) antecedent meltwater production (Table 6.1). In (b) we quantify antecedent meltwater production in two different ways. In one scenario we calculate the mean during the period of observed ice motion and the preceding N years. In the other scenario we calculate the mean of only the preceding N years.

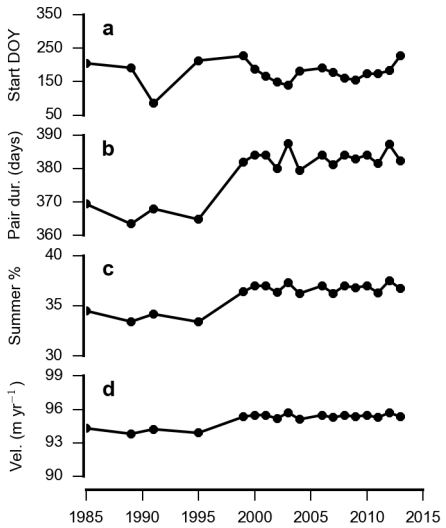

Figure 6.6: Sensitivity of extracted ice motion to variations in baseline duration. For each period (a) the average start Day-Of-Year of all pairs used in the period; (b) the average baseline duration of all pairs used in the period; (c) the proportion of the baseline duration attributable to summer, which is defined as 1 May to 31 August; and (d) the annual velocity which would be expected in the ablation zone of the Leverett glacier catchment based on the average proportion of summer versus winter and the average baseline duration for each year.

6.1.3 Impact of varying baseline durations on annual velocity

Images separated by baseline durations of 352–400 days duration were paired together for feature tracking. Here we examine the impact that the variable baseline duration has on the velocity field of each period.

The average start day-of-year of the pairs which comprise each period are shown in Figure 6.6a. The start day becomes less variable once imagery from Landsat 7 comes online in 1999. The average baseline duration increases by ∼15 days after 1999 (Figure 6.6b), increasing the proportion of the baseline attributable to summer motion (defined as 1 May to 31 August in common with previous studies (Sole et al., 2013; Tedstone et al., 2013)) by ∼ 2% (Figure 6.6c).

We use mean summer and winter velocities from Leverett Glacier sites S1 to S4 during 2009 to 2012 (Sole et al., 2013; Tedstone et al., 2013) to test the sensitivity of annual velocities

to the varying baseline duration. Winter days in each period are ascribed velocities of 81.6 m yr^{-1} and summer days are ascribed velocities of 127.6 m yr^{-1}. We then estimate the mean annual velocity that would be expected for each period (Figure 6.6d). Variations in the baseline duration between periods are estimated to impact extracted annual ice motion by <2 m yr^{-1}. Furthermore, according to this analysis, increased baseline durations during the 2000s leads to an small artificial increase in ice motion caused by the feature tracking method. This is in the opposite direction to the inter-annual slowdown signal which we observe in our study area and leads us to conclude that our slowdown trend is robust to varying baseline durations.

6.1.4 Impact of changing ice geometry on velocity

During the last 30 years, the Greenland ice sheet (GrIS) has thinned along its margins (Krabill et al., 2000; Pritchard et al., 2009; Helm et al., 2014), changing the geometry of the ice mass. It is likely that these changes will have affected ice velocity by modifying driving stress. Here we evaluate the impact that thinning may have had on velocity along transect A (see Figure 6.1), in order to bound the extent to which our observed slowdown could be the result of geometric changes.

We characterize the surface velocity u_s as a sum of a basal sliding (u_b) and vertical shear deformation (u_d) contributions (Cuffey and Paterson, 2010):

$$\begin{aligned} u_s =& u_b + u_d \\ =& C_b(\rho_i g S H)^m + \frac{A}{4}(\rho_i g S)^3 H^4, \end{aligned} \tag{6.2}$$

where A is a temperature-dependent Glen's flow parameter, ρ_i is the density of ice, g is

gravitational acceleration, S is the surface slope (positive where the surface lowers toward the margin), H is the ice thickness, and C_b and m are parameters related to basal sliding. A, C_b and m are in general poorly-constrained, and are likely to vary spatially; however, the only assumptions we make in our analysis regarding these parameters are that they do not change significantly over the time interval of interest, and further that m is less than or equal to 3. Note that our model allows for either the power-law rheological model of Weertman (1957) (Weertman, 1957) or the Newtonian till model of Alley (1987) (Alley et al., 1987). Thus the maximum deceleration predicted by the above model bounds the slowdown that can be explained by geometric changes alone. Below, we estimate this maximum deceleration to first order.

We introduce the variable λ, which represents the fraction of surface velocity explained by vertical shear, i.e.

$$u_d = \lambda u_s, \quad u_b = (1-\lambda)u_s.$$

If we consider a small change δS in slope ($\delta S \ll S$), and a small change δH in ice thickness ($\delta H \ll H$), Eqn. 6.2 leads to the following change in u_s:

$$\begin{aligned}\frac{\delta u_s}{u_s} =& \left(\frac{m u_b + 3u_d}{u_s}\right)\frac{\delta S}{S} + \left(\frac{m u_b + 4u_d}{u_s}\right)\frac{\delta H}{H} + \mathcal{O}(\delta H^2, \delta S^2) \\ =& (m(1-\lambda)+3\lambda)\frac{\delta S}{S} + (m(1-\lambda)+4\lambda)\frac{\delta H}{H} + \mathcal{O}(\delta H^2, \delta S^2), \end{aligned} \tag{6.3}$$

where the $\mathcal{O}$-notation is employed to signify terms which are of order δH^2 and δS^2 or higher and thus negligibly small. Again, we make no assumption regarding the spatial variability

of λ other than the fact that it is between 0 and 1, as our aim is to find the conditions under which velocity is most sensitive to thinning. With $\left(\frac{\delta S}{S}\right)$ positive and $\left(\frac{\delta H}{H}\right)$ negative in Eqn. 6.3, then at any point along the transect, and for any $m \leq 3$, the change to u_s cannot be more negative than when the flow is due to vertical shear, i.e. when λ is equal to 1. The first-order relative change in surface velocity, $\frac{\delta u_s}{u_s}$, is thus bounded by

$$3\frac{\delta S}{S} + 4\frac{\delta H}{H}. \tag{6.4}$$

We use Expression 6.4 to estimate the maximal impact of these thinning scenarios on ice velocity, solving every 240 m along transect A. To estimate the total ice thinning during 1985–2014, $\delta H = 10, 20$ are prescribed at the ice sheet margin and linearly interpolated along the transect to $\delta H = 0$ m at 100 km inland (equivalent to the equilibrium line altitude, ∼1500 m asl (van de Wal et al., 2012)) (Figure 6.7a). We add δH to current ice thickness along the transect (Morlighem et al., 2014) to set H to values appropriate for 1985. We prescribe the initial slope S as the mean slope in our study area, 0.02 m/m. The change in slope, δS, is calculated from the prescribed linear change in ice thickness over distance inland.

In Figure 6.7b we plot Expression (6.4) corresponding to the two thinning scenarios described above. These profiles represent the largest (i.e. most negative) percentage changes in velocity associated with the prescribed geometric change. We then convert these profiles to the predicted reductions in velocity and remove them from the observed 1985–1994 velocities (Figure 6.7c), generating a lower bound for the 2007–2014 velocities under the assumption that the observed slowdown was geometrically induced. Between ∼0-5 km from the ice margin for the $\delta H = 20$m scenario, the observed slowdown is within the range predicted by Expression 6.4, and we cannot reject the possibility that the thinning here was responsible for the slowdown. However, between 10–50 km inland, at most 17–33% of the observed slowdown can be attributed to changing ice sheet geometry depending on the

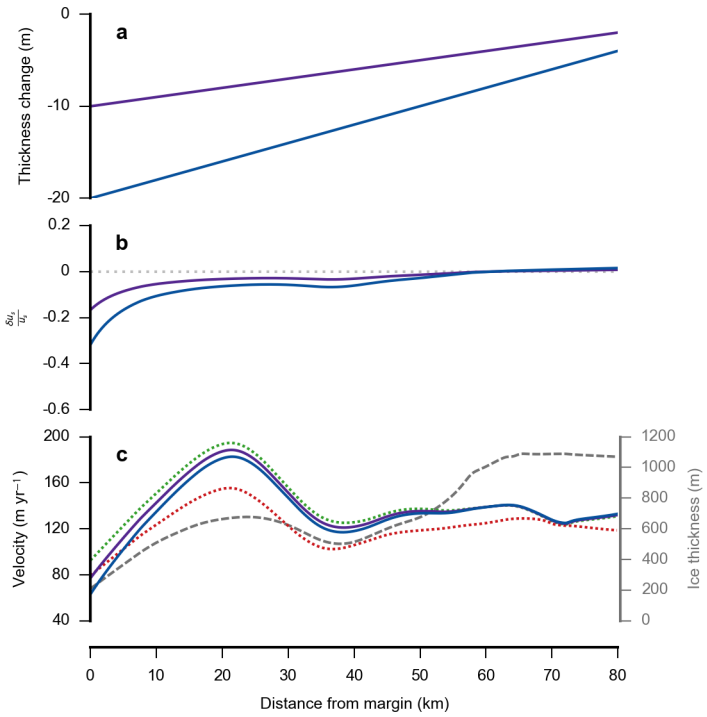

Figure 6.7: Impact of changing ice geometry on ice motion. Ice thinning of 10 m (purple) and 20 m (blue) at the ice margin through to 0 m at 100 km inland were applied to Transect A. (a) Prescribed change in ice thickness over transect length. (b) The ratio of velocity change calculated by Eqn. 6.4. (c) Left axis: Observed ice velocity during 1985–1994 (dotted green) and 2007–2014 (dotted red). Modelled velocities in 2014 (solid lines) for the prescribed ice thicknesses. Right axis: ice thickness (dashed grey) (Morlighem et al., 2014).

prescribed δH. By 60 km inland, there is essentially no net change in ice velocity attributable to geometrical changes.

It remains to consider our assumption that the Glen's law parameter A can be treated as constant in time. Phillips et al (Phillips et al., 2010) demonstrated that latent heat transferred to the ice from surface melt could warm glacial ice at depth, thereby leading to an increase in A. However, this process would result in acceleration rather than deceleration. Thus our decision not to consider temporal changes in A in our analysis of maximal geometrically-induced slowdown is justified. We conclude that the slowdown which we have observed during 1985–2014 is not explicable by geometrical changes to the ice sheet alone and instead

must be dominated, at distances greater than ∼5 km from the margin, by other processes impacting basal motion.

6.1.5 Surface melting

GrIS annual melting was output from a runoff/retention model applied to downscaled ERA-I data on an equal-area 5x5 km polar stereographic grid for the Greenland region (Hanna et al., 2011). We calculated mean annual melt rates for the study area (67.45^{o}N, 51.5^{o}W to 69.2^{o}N, 49.2^{o}W). Inter-annual fluctuations and trends from several independent melt models show good agreement (Vernon et al., 2013), including with the methodology used in this study.

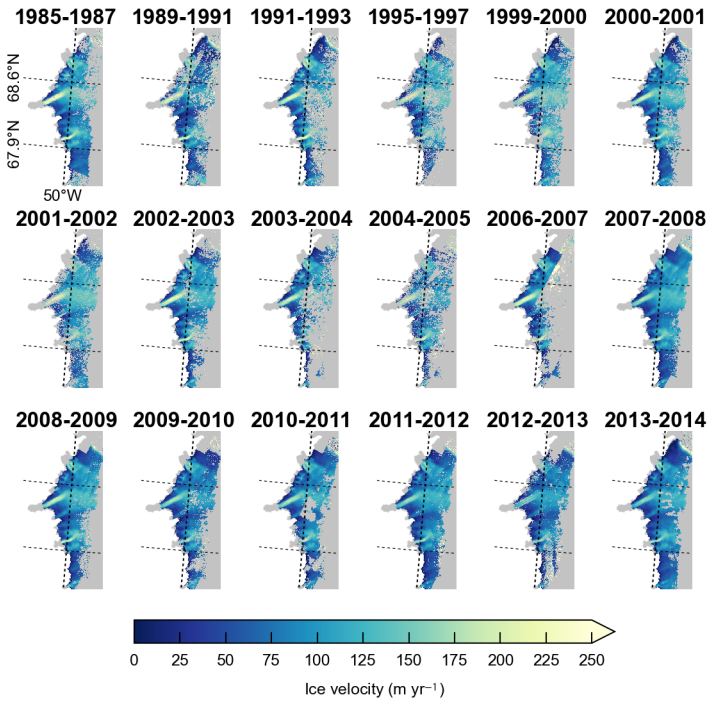

Figure 6.8: Ice velocities during each period. The velocities have uncertainties < 60 m yr^{-1} and were observed across at least 30% of the study area in each period (see Methods).

Chapter 7

Conclusions

The overall aim of this thesis has been to improve our understanding of one of the processes controlling the motion of the Greenland Ice Sheet: coupled hydrology-dynamics. This has been motivated by the need to determine more accurately the response of the ice sheet to projected climate change (Meehl et al., 2007). Under projected climate scenarios, surface melting of the Greenland Ice Sheet is expected to increase. Studies prior to this thesis have already shown that meltwater produced on the ice sheet surface can penetrate to the ice sheet bed and cause ice motion to speed up transiently through enhanced basal sliding (e.g. Zwally et al., 2002; Alley et al., 2005b; Das et al., 2008; Catania et al., 2008; Shepherd et al., 2009; Bartholomew et al., 2010, 2011a). The importance however of coupled hydrology-dynamics both to current ice sheet motion and to the stability of the Greenland Ice Sheet over the coming century has been unclear.

The first section of these conclusions summarises the main findings of this thesis. The second highlights the recurring themes of this thesis in comparison to other studies. The final section identifies some of the areas which should form priorities for future research.

7.1 Summary of findings

A key shortcoming of many previous studies has been their concentration upon sub-seasonal measurements of ice motion (see Section 2.3.2), rather than over full melt-years when the net impact of coupled hydro-dynamics upon ice motion begins to emerge. Across three complementary studies this thesis has elucidated, at unprecedented spatial and temporal resolution, the net impact of coupled hydrology-dynamics over a section of the south-western Greenland Ice Sheet. It has used a suite of high temporal resolution *in situ* measurements of ice motion and associated records of air temperatures and proglacial discharge, combined with spatially extensive observations of ice motion made by satellite remote sensing. These records have enabled this thesis to examine the net effect of coupled hydrology-dynamics over temporal intervals ranging from diurnal transient ice speedup, to seasonal, annual and decadal variability in ice motion. Furthermore, rapidly changing climate conditions over the last three decades have resulted in contrasting melt-years which are analogues for the climate changes projected by the end of the 21st century: (a) extreme melting during 2012 (Nghiem et al., 2012), and (b) the 50% rise in surface meltwater production from 1985–1994 to 2007–2014 (Chapter 6). These analogues were used in this thesis to examine the likely future hydro-dynamic sensitivity of the Greenland Ice Sheet in a world which continues to warm.

The research presented in Chapters 4 and 5 of this thesis drew on field observations of coupled hydrology-dynamics made at Leverett Glacier, a land-terminating outlet glacier situated at ~67^{o}N on the western margin of the Greenland Ice Sheet. These field observations enabled detailed examinations of the relationship between surface melting, the subglacial drainage system structure and ice motion to be made.

Chapter 4 (Tedstone et al., 2013) explored the importance of meltwater volume versus supply rate in generating ice motion. The impact of meltwater supply rates on ice motion was assessed using in-situ GPS records of ice motion obtained during the two extreme melt

events which occurred during July 2012, one of which was the most significant melt event since 1889 (Nghiem et al., 2012). During the 10-day periods centred over the melt events, the July 12 event forced 7% additional ice displacement, whilst the less extreme July 29 event forced 34% more ice displacement relative to the displacement estimated to have occurred in the absence of the melt events. Nevertheless, the additional contribution of each melt event to net summer motion was <2.1 m at all transect sites, equivalent to at most ∼2% of net annual ice motion.

To examine the impact of varying meltwater volumes, Chapter 4 compared GPS records of ice motion made during two contrasting melt-years: the 'average' melt-year of 2009, versus the 'extreme' melt-year of 2012. ice-sheet-wide runoff during summer 2012 was 3.9σ above the 1958-2011 mean (Tedesco et al., 2013a). Relative to the 1981–2010 mean, the 2012 May-August 1000 mb temperature anomalies 25 km west of field Site 1 were +2.2°C, corresponding approximately to the rise in air temperatures projected for the end of the century (Stocker et al., 2013), compared to ±0.3°C during May-August 2009. 2012 is therefore a surrogate for addressing the potential role of future melt volumes on ice motion. The warmer summer led to stronger melting, resulting in faster summer ice motion in 2012 than during 2009 at all sites except the two lowest within 7 km of the ice margin. However, on average all sites moved 11% slower during winter 2012–2013 than winter 2009–2010, negating the summer speedup caused by the individual melt events and record meltwater volumes. On average, net ice motion across all transect sites was 6% less during 2012–2013 compared to 2009–2010.

These observations of coupled hydrology-dynamics reinforce conclusions reached previously at Leverett Glacier based on observations from 2009 to 2011: that in warmer summers the ice generally flows faster but then flows more slowly during the subsequent winter (Sole et al., 2013). During warmer summers, a more efficient and extensive subglacial drainage system is expected to evolve that drains more high basal water pressure regions for longer at the end of summer. This will increase net basal traction and result in slower winter ice

motion. The observations in Chapter 4, in conjunction with Sole et al. (2013), suggest that hydro-dynamic coupling at land-terminating margins is largely insensitive to the projected rises in melt volumes during the rest of this century, up to at least the equilibrium line altitude estimated by van de Wal et al. (2015).

Chapter 5 (Tedstone et al., 2014) built on the findings reached in Chapter 4 by investigating whether the insensitivity of net annual ice motion to short-term variations in ice flow holds across broader spatial scales. Specifically, it examined the dynamic response to meltwater inputs in the vicinity of, and distal to a major subglacial drainage axis. The presence of this axis was inferred from hydraulic potential analysis (Chapter 5) and previous drainage system tracing campaigns (Cowton et al., 2013; Chandler et al., 2013).

Detailed in-situ observations of ice motion indicated the seasonal presence of a variable pressure axis (VPA) within 14 km of the margin of Leverett Glacier. Site S3, inferred to be located above or very near to the VPA, experienced large oscillations in diurnal ice motion and vertical displacement, consistent with oscillatory variability in P_w in a VPA (Hubbard et al., 1995). Meanwhile, a site (S3M) located 2.5 km away from S3 transverse to ice flow experienced damped diurnal ice motion oscillations and minimal vertical ice displacement, consistent with less variable P_w in the increasingly inefficient, unchannelized regions of bed further away from a VPA (e.g. Nienow et al., 2005). Secondly, observations made by TerraSAR-X satellite radar of total summer and winter ice motion over a 300 km^2 region of the lower ablation zone showed that whilst annual ice motion is spatially variable, this is attributable primarily to differing ice thickness, rather than a spatially variable drainage system. During 2012–2013, across 81% of the area further than 2 km from the ice margin, the contribution of summer motion to annual motion was within the range 44-50%, irrespective of proximity to the inferred underlying subglacial drainage axis. It is plausible that declining P_w in the widespread hydraulically isolated and inefficient regions of the ice sheet over the course of the melt season, as observed by Andrews et al. (2014), may provide an explanation

for the spatial invariance in the proportion of annual motion which we observe during summer.

The results from Chapters 4 and 5 therefore suggest that across land-terminating sections of the Greenland Ice Sheet, hydro-dynamic coupling controls transient spatial variability in ice motion over diurnal to weekly timescales, but that over annual timescales this coupling has only a minimal impact on net ice motion. However, other observations, whilst being spatially limited, indicate inter-annual slow-down of this region of the ice sheet since 1991 (van de Wal et al., 2008). The observations in Chapter 6 were therefore used to investigate the evidence for hydro-dynamic coupling over decadal timescales and the impact of long term temperature changes on ice motion. The findings in Chapter 6 utilised the recent release of unprecedented volumes of satellite optical imagery from the Landsat Program to observe annual ice motion from 1985 to 2014, across an 8000 km^2 area of the land-terminating margin to the north of Leverett Glacier, extending up to 1100 m asl and ∼50 km inland.

Between 1985–1994 and 2007–2014, meltwater production in the region increased by 50%, yet on average the annual ice motion during 2007–2014 was 12% slower than during 1985–1994, substantially (∼70%) more than can be attributed to velocity changes caused by changes in ice geometry alone. These findings indicate that hydro-dynamic coupling has resulted in spatially extensive net slowdown of ice motion over decadal timescales at a time of substantial climate warming. This represents perhaps the clearest illustration yet that it is essential to capture ice motion over annual timescales, not just seasonal and sub-seasonal, in order to reveal the full relationship between hydrology and dynamics in response to projected climate change. Through doing so, this thesis has conclusively shown that, in the study region in south-west Greenland, more melt has not generated more ice motion over decadal timescales. Thus, the 'Zwally effect' (Zwally et al., 2002) proposed previously, in which larger surface meltwater volumes lead to ice acceleration, appears not to hold for land-terminating margins of the south-west Greenland Ice Sheet, up to at least the approximate equilibrium line.

7.2 Synthesis of findings

The findings presented in this thesis build upon the conceptual framework of coupled hydrology-dynamics which has emerged from other studies, both at alpine glaciers and land-terminating margins of the Greenland Ice Sheet. Prior to this thesis it was already clear that surface meltwaters could gain access to the bed of the Greenland Ice Sheet (Alley et al., 2005b; Das et al., 2008; Catania et al., 2008) and force transient speedups in ice motion of up to ∼300% over diurnal timescales (Joughin et al., 1998; Zwally et al., 2002; Shepherd et al., 2009). High-velocity 'spring events', as meltwater first gains access to the glacier bed, occur progressively further inland with increasing melt extent, and an efficient subglacial drainage system expands upglacier over the course of the melt season, such that late summer velocities tend to be substantially less than during early summer (Bartholomew et al., 2010; Sundal et al., 2011; Bartholomew et al., 2011b,a; Hoffman et al., 2011; Bartholomew et al., 2012; Cowton et al., 2013; Chandler et al., 2013; van de Wal et al., 2015). After the cessation of surface meltwater inputs, early winter velocities are typically lower than immediately before the start of the melt season but gradually rise in the absence of surface meltwater inputs, until melting re-starts the following spring.

This thesis has endeavoured to enhance the clarity of a number of aspects of the foregoing conceptual framework, in order to identify whether land-terminating margins of the Greenland Ice Sheet will speed up or slow down in a warming world. These aspects include the net impact on annual and decadal ice motion of (a) transient periods of exceptionally high rates of meltwater supply to the ice sheet bed; (b) a spatially hetereogeneous subglacial drainage system; and (c) melt volumes commensurate with expected meltwater production by the end of the 21st century. The following discussion is limited to the ablation zone. Dynamics above the equilibrium line are discussed later.

7.2.1 Rate of meltwater supply

Field observations made during 2012 captured the velocity response to two extreme melt events which supplied very large quantities of meltwater to the ice sheet bed (Chapter 4). However, the transient velocity response did not scale with the absolute volume of meltwater delivered. Instead, the velocity responses to each melt event were at least partly a function of meltwater supply rates to the ice sheet bed over the preceding weeks. The smaller of the two melt events, on 29 July 2012, forced a larger dynamic response than the event on 12 July 2012 because it had been preceded by around two weeks of freezing temperatures at higher elevations, presumably causing the morphology of the subglacial drainage system to adapt to smaller meltwater fluxes. A smaller rate of meltwater supply entering a relatively inefficient subglacial drainage system was therefore able to force a larger transient peak in P_w and thus ice velocity compared with the larger rate of meltwater supply entering a relatively efficient high-capacity drainage system during the 12 July melt event.

Transient peaks in P_w are not just a function of surface melt rates against drainage system capacity. The nature of the englacial pathways that route surface meltwater to the ice sheet bed determines the rate at which water is delivered. Tedesco et al. (2013b) observed 'fast' and 'slow' lake drainage events, corresponding to water delivery by hydro-fracture and lake overspill to a nearby moulin, respectively. 'Fast' drainage forced a larger transient velocity response than 'slow' drainage, but 'fast' drainage only caused faster ice motion for a few hours. On the other hand, meltwater delivery to the ice sheet bed via persistent moulins may continue all summer if surface meltwater is generated quickly enough to keep the moulin open in the absence of supraglacial lake overspill. This suggests that P_w fluctuations associated with meltwater supplied via moulins dominate the net seasonal dynamic response to surface melting, as moulins deliver meltwater to the glacier bed over timescales of weeks to months, and not just over hours, as is the case for 'fast' lake drainage by hydro-fracture.

The consideration of coupled hydrology-dynamics in terms of the rate of meltwater supply

is not new to this thesis (e.g. Mair et al., 2002; Bingham et al., 2006; Schoof, 2010; Bartholomew et al., 2012). However, the observations presented here highlight some shortcomings in recent subglacial hydrology models. For example, models do not agree on the net impact of meltwater supply rates upon ice motion. As introduced in Section 2.3.2, Mayaud et al. (2014) used the SWMM EXTRAN model previously deployed at Haut Glacier d'Arolla, Switzerland (Arnold et al., 1998) to model subglacial hydrology in the Paakitsoq region, just to the north of Jakobshavn Isbrae, over the 21st century using runoff forcing based on The IPCC 5th Assessment Report's Representative Concentration Pathways (RCPs). They scaled up the total volume of sample proglacial hydrographs collected during the 2000s, which had the implicit effect of also increasing the meltwater supply rate on the rising limbs. They found that there would be an earlier transition to efficient subglacial drainage as bulk seasonal runoff increases through the 21st century, and therefore suggested that correspondingly lower P_w will lead to *slower* summer, and therefore annual, ice motion — despite observations in Chapter 4 and Sole et al. (2013) which show that summer ice motion is faster in warmer years because the drainage system remains pressurised for longer. In contrast, coupled hydro-dynamic modelling (Bougamont et al., 2014) which represented ice flow over a soft bed of porous deformable sediment linked to a laminar distributed water film suggested that projected increases in melting will result in a greater number of high magnitude (or 'extreme') melt events, leading to *faster* annual ice motion. However, Bougamont et al. (2014) did not explicitly treat efficient modes of water drainage, so in the model larger volumes of meltwater may not be routed quickly enough to the margin, causing higher P_w to persist and forcing faster ice motion for longer than may be physically realistic.

A key issue to be resolved amongst subglacial hydrology models — which may be responsible for the conflicting findings outlined above — is the temporal response of the subglacial drainage system morphology in response to varying meltwater supply rates. Chapter 4 showed that even in the presence of an efficient subglacial drainage system, if the rate of meltwater supply is sufficiently large to raise P_w, it will cause a transient increase in ice

velocity regardless. Moreover, if meltwater supply falls substantially over days to weeks, any subsequent increase in meltwater supply will not need to be as large to produce a transient velocity response as it will enter a drainage system that has adapted its morphology to drain smaller volumes of water.

Whilst the latest subglacial hydrology modelling captures the physics of cavity growth and their transition to conduits (Schoof, 2010), the timescales of evolution in models remain slow compared to observations of hydrology and dynamics. For instance, Werder et al. (2013) qualitatively reproduced many of the features observed in study areas such as Leverett Glacier, but the evolution of an efficient drainage system occurred over the order of months, not days as indicated by tracer observations (Cowton et al., 2013; Chandler et al., 2013). There could be several reasons why present models of channel/conduit growth evolve at different rates to those expected by observations. Firstly, the physics of channel initiation, when channel growth occurs very slowly unlike at larger channel sizes, remains debatable (Hewitt, 2013). The spatial extent, and magnitude of, hydraulic jacking could be important here in determining the size of cavities which then evolve into channels, along with pre-existing basal topographic lows. Secondly, Glen's flow law parameter A varies significantly between studies. The larger the value of A, the more quickly the overlying ice will deform and close the channel, therefore making it more difficult to maintain an open channel. However, it is unclear how determination of A could be improved, particularly as it could vary on the scale of several metres.

The temporal response of the subglacial drainage system may not be adequately represented until models couple hydrology and ice motion together. Ice motion is able to change the capacity of the subglacial drainage system. Hoffman and Price (2014) found that the dominant feedback of ice motion on the subglacial drainage system is negative: sliding opens cavity space which lowers water pressure and in turn sliding. However, the choice of sliding law strongly affects the speed of ice motion, which in turn determines the rate of cavity opening and therefore the rate at which transient peaks in P_w are reduced via

increasing the capacity of the subglacial drainage system (Hewitt, 2013). Thus, to improve physical models of subglacial hydrology, the timescales over which the system evolves in response to short-term variability in the rate of meltwater supply need to be considered in more detail, along with the impact that ice motion makes upon the capacity of the subglacial drainage system.

7.2.2 Spatial heterogeneity in subglacial drainage

Here we are concerned with spatial variations in ice motion driven by the subglacial drainage system. Chapter 5 focussed on observations collected in the ablation zone transverse to longitudinal ice flow. The key question is whether the morphology and structure of the subglacial drainage system is manifest in patterns of ice motion at the surface.

Studies of alpine glaciers have revealed variable pressure axes (VPAs) in which P_w oscillates rapidly over diurnal timescales in response to surface meltwater inputs. Large increases in the rate of meltwater supply to the ice sheet bed can over-pressurise the VPA, causing local reductions in basal traction and transient ice motion speedup. At increasing distance from the VPA, it is inferred that drainage through the slow, inefficient unchannelized system attenuates variability in P_w, resulting in more diurnally stable ice velocities (Hubbard et al., 1995; Nienow et al., 2005). With such a system one might expect there to be inset units of faster ice flow associated with the position of VPAs. The detailed GPS observations made in Chapter 5 showed that ice motion in the immediate vicinity of an inferred subglacial drainage axis (site S3) was faster and more variable over diurnal timescales when forced with surface meltwater inputs compared to a site (S3M) located 2.5 km away transverse to ice flow. Moreover, remotely sensed observations from a single day in late summer show spatially distinct flow enhancements of up to 300% relative to winter, including in the vicinity of S3 (Palmer et al., 2011). In conjunction with Chapter 5, the results of Palmer et al. (2011) suggest that several VPAs together form an arborescent drainage system beneath this region of the ice sheet (Figure 2.8).

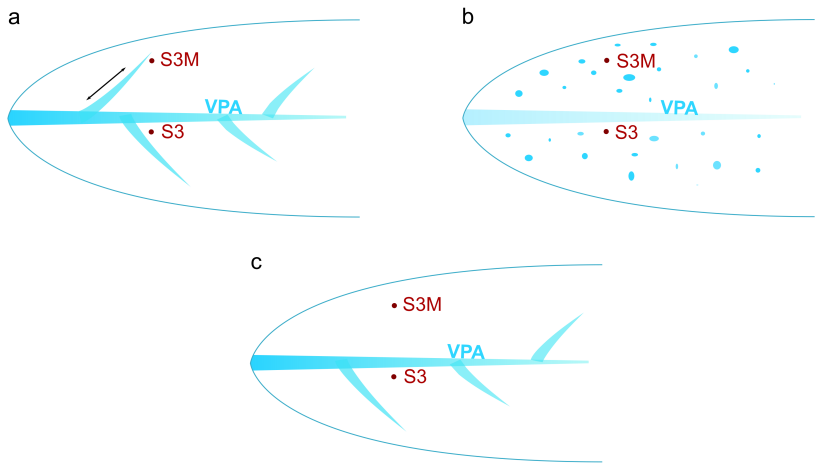

Figure 7.1: Schematic of potential drivers of synchronous ice motion at S3 and S3M (see Figure 5.1). In all three scenarios a VPA is inferred to be immediately adjacent to S3. (a) An efficient subglacial drainage system rapidly transmits P_w variations to/from the VPA. (b) P_w variations and thus basal motion are driven by local meltwater input points. (c) Synchronous motion between S3 and S3M is driven by transverse coupling through the ice.

Despite faster peak diurnal ice velocities at S3 during the observation period, the proportion of annual motion which occurred during summer was essentially the same at both S3 and S3M. This may be explicable by variations in diurnal ice motion beyond the end of the observation period, as during the final few days of observations in late June, diurnal velocity minima at S3 were lower than at S3M. If this pattern continued through July and August the larger diurnal velocity maxima experienced by S3 earlier in the melt season would be cancelled out by correspondingly lower minima. In contrast, further upglacier, where there are fewer meltwater input points (Chu, 2013) and melt rates are lower (Bartholomew et al., 2011b), ice velocity responses to surface meltwater inputs may be more localised and able to cause significant spatial variability in ice motion. However, this thesis lacks the observations to investigate this possibility further. Thus, whilst the satellite observations in Chapter 5 make it clear that the significant diurnal spatial variability in ice motion identified by Palmer et al. (2011) is not manifested at lower elevations over annual timescales, it is unclear whether this is also the case at higher elevations.

Similar findings have been made at alpine glaciers. At Haut Glacier d'Arolla, Switzerland, the

enhanced diurnal motion which occurred over the VPA during summer was barely discernible in the spatial pattern of annual velocity. It was therefore proposed that transverse coupling to adjacent ice suppressed the basal motion discontinuity (Harbor et al., 1997). Observations in Chapter 5 showed that over diurnal timescales, ice motion at S3 was synchronous with ice motion at S3M. However, it is not possible to identify the mechanism(s) responsible. Figure 7.1 illustrates three possible mechanisms. In scenario (a), an efficient drainage system underlies both S3 and S3M and is able to rapidly transmit P_w fluctuations, in turn causing synchronous velocity responses at both sites, even if fluctuating P_w originates from upglacier surface meltwater inputs. In scenario (b), multiple surface input points enable the rapid local delivery of meltwater to the ice sheet bed, causing widespread synchronous increases in P_w even in the absence of an efficient subglacial drainage system. Finally, in scenario (c), ice motion forced by P_w fluctuations in the VPA adjacent to S3 is transmitted to S3M via transverse coupling through the ice. However, without additional observations or modelling is it not possible to elucidate the relative importance of transverse stresses or the coupling lengths over which local VPA ice-bed decoupling could propagate enhanced ice motion away from the VPA.

Regardless of the mechanism responsible for synchronous ice motion between S3 and S3M, drawing on hydraulic potential analysis (Chapter 5), observations of ice motion (Chapter 5) and tracer evidence (Cowton et al., 2013) in conjunction with existing remote sensing observations (Palmer et al., 2011) provide strong evidence that a major subglacial drainage axis exhibiting VPA characteristics underlies the lower Leverett Glacier catchment. However, in the lower ablation zone at least, the presence of this axis makes little difference to spatial variability in hydrologically-forced ice motion over the course of a melt-year.

The drilling of boreholes enables more direct observations of P_w to be made. Borehole campaigns on the south-west Greenland Ice Sheet have not generally been able to intersect with VPAs and/or other efficient drainage elements beyond a few kilometres from the margin. Meierbachtol et al. (2013) drilled a total of 23 boreholes at four sites up to 34 km into the

interior where ice is >800 m thick, both above and adjacent to an inferred subglacial trough. However, unlike nearer the margin, their boreholes beyond 17 km inland remained at high water pressures throughout the summer melt season and did not experience large diurnal fluctuations, which led them to suggest that water pressures further into the ice sheet interior beneath deep ice are likely to be unfavourable to the development of efficient subglacial drainage.

The data on which Meierbachtol et al. (2013) based their conclusions may not be fully representative of the subglacial drainage system. Firstly, previous borehole campaigns (e.g. Hubbard et al., 1995) showed that pressure fluctuations originating from the efficient drainage system are spatially discrete and attenuate by a few hundred metres away from the VPA. The boreholes which Meierbachtol et al. (2013) drilled on the tongue of the outlet glacier Isunguata Sermia were inferred to connect to efficient drainage elements. This is relatively unsurprising as all the water from higher in the catchment is routed beneath the relatively narrow (∼7 km) outlet glacier. However, further inland, boreholes are much more likely to sample elements of distributed inefficient drainage simply because efficient drainage elements are narrow. Boreholes are therefore much less likely to connect to efficient drainage features further inland, even if drilled above a bedrock trough. Secondly, tracer evidence shows that water entering the ice sheet up to 40 km inland can exit the ice sheet within ∼12 hours, which can only be explained by recourse to efficient drainage (Cowton et al., 2013; Chandler et al., 2013). Thus, on borehole evidence alone, one cannot confidently conclude that subglacial conditions further inland prevent the evolution of efficient drainage features.

Recent simultaneous observations of ice motion, borehole and moulin water levels (Andrews et al., 2014) go a significant way towards reconciling the foregoing inconsistencies and are complementary to the findings of Chapter 5. Andrews et al. (2014) measured hydraulic head in moulins and boreholes located hundreds of metres apart where ice was ∼600 m thick, ∼22 km from the ice sheet margin in south-west Greenland. Water pressure records from

moulins displayed diurnal oscillatory behaviour coincident with diurnal velocity maxima, reminiscent of VPA behaviour on alpine glaciers (e.g. Hubbard et al., 1995). Meanwhile, the water pressure of adjacent boreholes was less variable and was anti-correlated with local diurnal velocity maxima. However, over seasonal timescales, neither the maximum nor minimum daily moulin water head was observed to decrease as would be expected with increasing drainage efficiency. This led Andrews et al. (2014) to suggest that slower ice velocities observed later in the melt season were driven not by pressure decreases in the efficient drainage system but instead by gradually declining water pressures in isolated, hydraulically inefficient regions of the ice sheet bed.

The findings of Andrews et al. (2014) go some way to supporting the observations made in Chapters 4 and 5 and by Sole et al. (2013). Andrews et al. (2014) suggested that over-pressurisation of hydrologically connected areas of the ice sheet bed would cause ice motion that would be transferred laterally through the ice to hydraulically isolated areas, causing cavities to open, reducing P_w and resulting in ice motion slowdown as summer progresses. They proposed that this mechanism could explain winter mediation of summer acceleration. However, it is unclear how P_w in hydraulically isolated areas of the bed will remain low if the volume of water present in the cavities does not change, as according to cavitation theory (e.g. Iken, 1981), one would expect cavities beneath thick ice to rapidly collapse until ice overburden pressure is balanced by P_w, meaning that cavities will rapidly return to high P_w and their previous extent once sliding slows down.

These considerations suggest that increasing connectivity and drainage of previously hydraulically isolated, inefficient regions to the efficient drainage system are required in order that P_w is reduced sufficiently to decrease the extent of cavities present at the ice sheet bed, thereby raising basal traction over wide areas by the start of winter. Following Sole et al. (2013), I postulate that during a warmer summer, more meltwater will drain through the efficient subglacial drainage system, which will lead to more times when the system is over-pressurised. During these times, pressure fluctuations will be transmitted laterally

away from the efficient drainage system, resulting in progressively greater connectivity of previously isolated inefficient regions of drainage and their consequent drainage as summer progresses. This will more substantially increase basal traction, which in turn explains slower winter ice motion after summers of stronger melting.

If spatial variability in the structure of the subglacial drainage system is important for spatial variability in ice motion over annual and longer timescales, the surface expression of major subglacial drainage pathways ought to be apparent in decadal records of annual ice motion (Chapter 6). Over these timescales, much as over a single melt-year (Chapter 5), most spatial variability in ice motion appears to be controlled by surface and basal topography (Morlighem et al., 2014). There does not appear to be any surface velocity manifestation of arborescent subglacial drainage (e.g. Figure 2.3) such as that predicted by models (e.g. Werder et al., 2013).

Observations thus indicate a scale discontinuity between the strong spatial variability in hydrologically-forced ice motion observed over diurnal timescales, versus the suppression of the surface expression of this variability over seasonal and annual timescales (Chapter 5). One perhaps provocative conclusion which could be drawn from Chapter 5 is that the representation of hydrology in ice sheet models may be simplified through higher order parameterisations (e.g. Shannon et al., 2013), as it appears that detailed treatment of spatial variability in coupled hydrology-dynamics (e.g. Schoof, 2010; Hewitt, 2013) is not critical to the ice motion variability of land-terminating margins over annual timescales. However, observations of decadal ice motion slowdown (Chapter 6) suggest that very small changes in subglacial hydrology over annual timescales aggregate to drive longer-term changes in ice motion. Thus, to *understand* observed variability, theoretical developments are still required in order to evaluate the role of the subglacial drainage system in driving the observed slowdown.

The slowdown mechanism proposed by Sole et al. (2013) and in this thesis postulates that stronger melt years lead to the evolution of a more widespread efficient channelized

drainage system, which hydraulically connects a greater proportion of the remaining inefficient unchannelized drainage system. This leads to widespread net P_w reduction by the end of summer and consequently slower winter ice motion. Modelling may support such a mechanism: Hewitt (2013) found that with certain parameter choices, water in the unchannelized ('sheet') regions of the bed may be drained by the growth of channels, thereby containing less water by the end of summer than if the melt season had not occurred. However, under different parameter choices, Hewitt (2013) found that sheet regions could instead retain summer meltwater, becoming *more* pressurized and resulting in higher ice velocities for longer following the cessation of melt. Thus, it is clear that the value of parameters used in subglacial hydrology models requires further attention.

Following on from previous studies (Röthlisberger, 1972; Nienow et al., 1998; Bartholomew et al., 2012; Cowton et al., 2013; Chandler et al., 2013) this thesis has tended to implicitly assume subglacial drainage over a hard bed in order to explain observed variability in ice motion. However, it is unlikely that the whole study region is underlain by a hard bed. A seismic reflection line acquired 13 km inland on Russell Glacier was interpreted as indicative of weak sediments of ∼30% porosity (Dow et al., 2013). These observations led Bougamont et al. (2014) to investigate the sensitivity of ice motion to surface melt drainage assuming a spatially uniform soft, hydro-mechanically deformable bed of sediment (study introduced previously in Section 7.2.1). While the study by Bougamont et al. (2014) represents a valuable effort to examine the importance of previously neglected mechanisms linking hydrology and dynamics, in doing so the authors disregarded physical representation of efficient subglacial drainage. Given that field evidence indicates the existence of efficient subglacial drainage (Cowton et al., 2013; Chandler et al., 2013), and that these efficient drainage pathways strongly influence ice velocity over diurnal timescales (Chapter 5), an ideal study would consider the combined influence both of efficient drainage pathways and deformable sediments upon ice motion.

Finally, in recent years a number of studies have investigated the role of supraglacial

lake (SGL) drainage in forming a spatial control on hydrologically-forced ice motion. The observations presented in Chapter 5 did not extend far enough inland (20 km, ~800 m asl) for it to be possible to consider the impact that SGL drainage has on spatial variability in annual ice motion. Transient speed-ups have been observed locally within hundreds of metres of SGLs in the hours and days during and after SGL drainage (Das et al., 2008; Bartholomew et al., 2011a; Doyle et al., 2013; Joughin et al., 2013), but do not appear in ice motion records collected further away (Hoffman et al., 2011) which instead reflect bulk variations in meltwater input to the ice sheet bed (Bartholomew et al., 2011a). Moreover, Joughin et al. (2013) found that after regional lake drainage during early summer, ice velocities gradually declined over the remainder of summer. However, from the observations of Joughin et al. (2013) it is not clear (a) whether the subsequently lower velocities 'cancel out' the initial transient speedups, or (b) whether the proportion of annual motion which occurs during summer is spatially invariant where lakes are present, as has been observed lower in the ablation zone where lakes are absent (Chapter 5). The observations made by Joughin et al. (2013) did not span the full annual melt cycle. Thus, although SGL drainage clearly controls where hydro-fracture is able to occur and deliver meltwater to the bed, it is unclear whether SGL drainage has an impact on spatial variability in hydrologically-forced ice motion in the ablation zone over longer timescales. Seasonal and annual measurements of ice motion higher in the ablation zone would be required to clarify these uncertainties.

7.2.3 Dynamic impact of increasing meltwater volumes

Enhanced surface melting of the ice sheet is projected to occur under climate warming (Vaughan et al., 2013). However, understanding the impact of projected climate warming upon coupled hydrology-dynamics remains one of the greatest remaining challenges, even at land-terminating margins which experience a much smaller range of external forcings than their marine-terminating counterparts. The primary difficulty has been the collection of observational evidence over sufficiently long periods to draw conclusions that are commensurate with climate change timescales.

Sole et al. (2013) and Chapter 4 provided snapshots of how annual ice motion might be expected to change under enhanced melting. They concluded that increased summer melting preconditions the ice-bed interface for reduced winter motion resulting in limited dynamic sensitivity to inter-annual variations in surface melting, and that annual ice flow in the exceptional melt-year of 2012 was not enhanced relative to the average melt-year of 2009. Thus, there is no significant correlation between annual meltwater volume and annual ice flow (Sole et al., 2013), a conclusion supported by 20 years of complementary observations made by van de Wal et al. (2015).

The synthesis of four consecutive years of observations of melting and ice flow at Leverett Glacier enhances these conclusions. This is presented in Figure 7.2 and captures contrasting melt-years. The focus here is on sites S1–S6; dynamics at S7 are discussed separately in Section 7.3. There is no inter-annual trend in net surface ablation (Figure 7.2a). Most sites flowed further during summers of more melting (Figure 7.2b), as already established for the 2009–2011 period by Sole et al. (2013). However, net annual ice flow at sites S1–S6 was lower in 2012 than in 2009 and, moreover, at sites S4–S6 ice flow decreased in each successive melt-year. The slow-down observed from 2009 to 2012 is attributable to declining winter flow (Figure 7.2), which at sites S4–S6 decreased in each successive melt-year despite the large inter-annual variability in surface melting. This suggests that falling annual ice flow observed over the study period is forced by more complex coupled hydrology-dynamics as opposed to just annual meltwater volumes.

The relationship between meltwater supply *rate* and *volume* is likely to lie in the capacity of efficient features of the subglacial drainage system. Whilst rapid increases in the rate of meltwater supply cause transient velocity responses in the ablation zone even during late summer (e.g. Bartholomew et al., 2012, and Chapter 4), observations indicate that surface mass balance and ice velocity are negatively correlated during late summer, compared to positively correlated during early summer (van de Wal et al., 2015), even though the net summer relationship is positive (Sole et al., 2013; van de Wal et al., 2015). Some

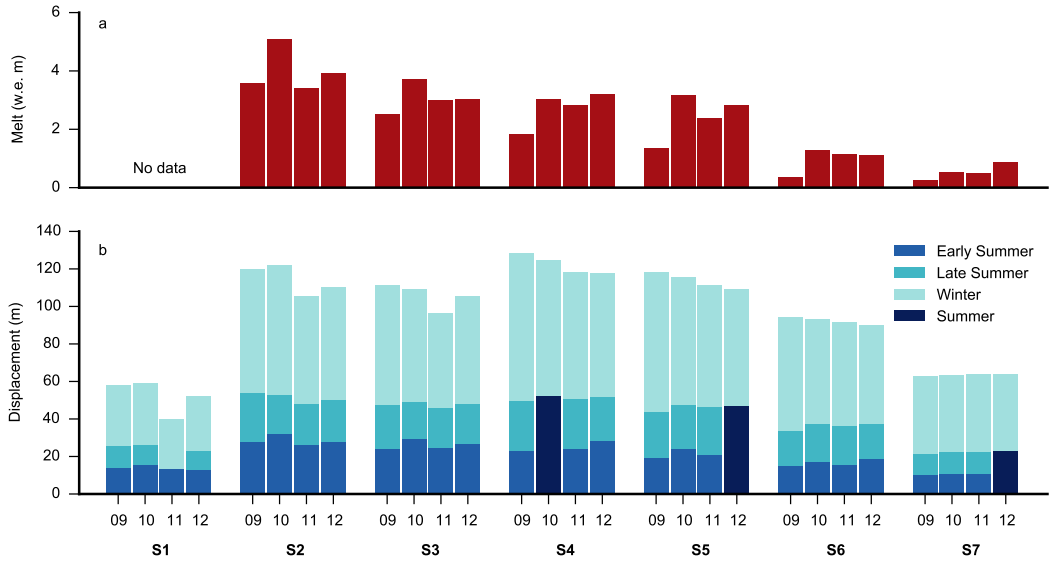

Figure 7.2: Surface melting and seasonal ice flow on Leverett Glacier from 2009 to 2012. (a) Total annual ablation (melting) in metres water equivalent (w.e. m) at each site. (b) Displacement at each site for early summer (1 May–30 June) and late summer (1 July–31 August) or summer (1 May–31 August), and winter (1 September–30 April). Missing late summer and annual data at S1 in 2011, and early and late summer data for S4 in 2010 and S5 and S7 in 2012, are due to several power failures.

have suggested that larger meltwater volumes will cause an earlier transition to efficient drainage during warmer summers (e.g. Sundal et al., 2011; Mayaud et al., 2014). However, observations show that the system becomes efficient very early in the season (Cowton et al., 2013), so the difference in ice motion between early and late summer is not explicable by some 'binary' transition to efficient drainage. Rather, the increasing capacity of the efficient drainage system in response to increasing meltwater volumes makes it increasingly difficult to over-pressurise the system over durations long enough to cause significant increases in ice motion during high melt years (Bartholomew et al., 2012), hence late summer is slower than early summer, but net summer ice motion is still greater in higher melt-years (Sole et al., 2013).

It is only over inter-annual to decadal timescales that the importance of meltwater volume in modulating ice motion begins to emerge. Observations presented in Chapter 6 represent the

first known study to examine decadal variability in annual ice motion of a land-terminating margin across such an extensive spatial area, and show that ice motion slowed down by 12% from 1985–1994 to 2007–2014. Unlike the field observations made at Leverett Glacier, in these complementary satellite-based observations it is not possible to resolve seasonal variability in ice flow. However, declining annual ice flow observed at just a few locations over four years at Leverett Glacier is replicated in the observations made in Chapter 6, which suggests that the detailed hydro-dynamic processes identified in the Leverett Glacier catchment are applicable over wider areas. Although in neither Figure 7.2 nor Chapter 6 is there evidence of a significant relationship of ∼annual ice motion with annual melt volumes, there is a significant relationship of ∼annual ice motion with *antecdent* melt volumes. This suggests that the slowdown observed during 2002–2014 occurred in response to several years of high sustained meltwater volumes. I hypothesise that this is because, as outlined above, summers of higher melting result in a higher-capacity, more extensive efficient subglacial drainage system which stays open for longer after the cessation of melting, enabling the drainage of stored meltwater. Several consecutive years of sustained high meltwater volumes are thus likely to enable the gradual net drainage of water stored in surrounding inefficient regions of the bed, resulting in reduced basal lubrication, greater basal traction and a net slowdown in ice motion.

The ice motion slowdown observed over the last twenty years occurred during a 50% increase in surface meltwater production. It is therefore difficult to envisage how further increases in runoff volumes could result in future speedup of land-terminating margins. As discussed in Section 7.2.1, Mayaud et al. (2014) applied IPCC representative concentration pathways to sample hydrographs from the last decade in order to model the impact of projected runoff volumes on effective pressure. They found that P_w is likely to decline in response to rising meltwater volumes and therefore postulate that ice motion along land-terminating margins will likely decrease. Whilst it is a little simplistic to assume that the temporal distribution of melting over the course of the melt season will remain the same as during the last decade, there is currently no evidence to suggest that climate change will bring episodic periods of

warming and cooling which would be needed to force enhanced transient dynamic responses similar to that observed in response to the 29 July 2012 melt event (Chapter 4). Rather, in light of the slowdown observed during 2002–2014 which occurred in response to sustained high meltwater volumes (Chapter 6), it appears that theoretical developments should now seek to determine the *lowest* annual ice velocities which could occur in response to the high sustained meltwater volumes projected for rest of the 21st century.

7.3 Future research

A number of challenges remain if we are to fully understand the response of the Greenland Ice Sheet to projected warming. In the context of the research presented in this thesis, these challenges range from improving the representation of subglacial hydrology in ice sheet models, to elucidating the likely response of ice motion at higher elevations to increased melting, and identifying the role of coupled hydrology-dynamics in controlling the flow of marine-terminating catchments.

The primary limitation of the research presented in this thesis only S7 (1700 m asl), presented in Chapter 4, provided observations of ice motion in the accumulation zone of the ice sheet. Observations from S7 during 2009–2011 have been discussed elsewhere (Sole et al., 2013) and during 2012–13 in Chapter 5. Observations from the full study period are summarised in Figure 7.3 together with the only other known annual record of ice motion at higher elevations, made by Doyle et al. (2014) at their S10 site at 1840 m asl. Comparison of the two records serves to illustrate that the trend in annual ice flow in the accumulation zone is currently difficult to interpret. Net annual motion at S10 increased by 2.2% over the period 2009–2012, flowing slightly faster year-on-year by $\sim$0.05 $\pm$0.03 m yr^{-2}, whilst S7 was slower in 2012–2013 than in 2011–2012. These sites are located 30 km away from one another ($\sim$20 km in the along-flow direction) and less than 100 m asl apart, where surface slopes are relatively constant (e.g. Howat et al., 2014).

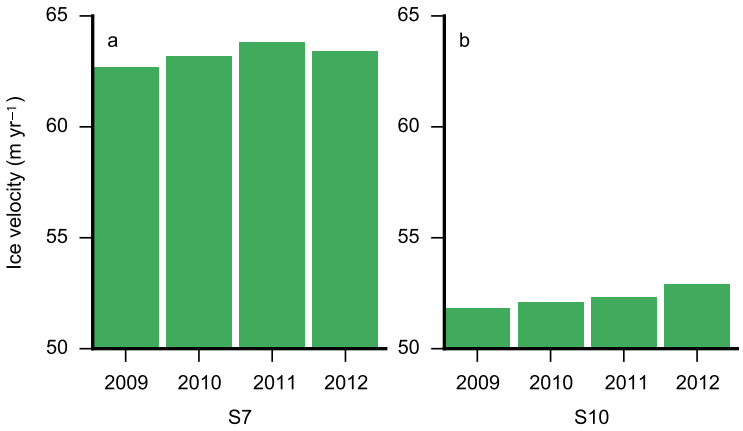

Figure 7.3: Comparison of ice motion records in the accumulation zone. a: Annual ice motion at transect site S7, 1715 m asl. b: Annual ice motion at S10 (1840 m asl, 30 km south-west of S7) (Doyle et al., 2014)

.

There are thus two major challenges at higher elevations. The first is to identify the overall long-term trend in annual ice motion above the ELA, which is difficult because the current generation of remote sensing technology is unable to track ice motion in these areas due to lack of coherence between images with few discernible surface features (e.g. Joughin et al., 2010). The second is to understand the mechanisms causing the annual variability observed during 2009–2013 as reported by Doyle et al. (2013). For instance, evolution of efficient drainage might limit annual motion at S7 but not at S10. Ice thickness at S7 is estimated to be 1390 ±114 m (Morlighem et al., 2014), and at S10 is 1590 ± 17 m (Doyle et al., 2014). It is plausible, if unlikely, that these relatively small differences in ice thickness could be sufficient to hinder the development of sufficiently efficient drainage at S10 in order to cause year-on-year speedup but not at S7, as higher overburden pressure forces channels to close more rapidly (e.g. Hooke et al., 1990; Chandler et al., 2013). In this scenario, higher P_w and lower basal traction would therefore be maintained at S10, leading to faster sliding.

Longitudinal coupling (Price et al., 2008) has previously been invoked to explain acceleration at higher elevations even in the absence of local surface meltwater inputs (Bartholomew et al., 2012; Hewitt, 2013), but this would require lower elevations to show signals of speedup,

not slowdown as observed (Sole et al., 2013). In addition, the propagation of melting further into the ice sheet interior may cause cryo-hydrologic warming of the inland ice mass, which over decadal timescales might result in ice flow acceleration owing to the dependency of ice deformation on ice mass temperature (Phillips et al., 2010).

Supraglacial Lakes (SGLs) have expanded inland to higher elevations since 2000, and in the south-west of Greenland now regularly form and drain above 2000 m asl (Howat et al., 2013), enabling meltwater to reach the ice sheet bed further inland. In a warming climate, if SGLs form and drain further inland, they could accelerate ice flow at higher elevations by delivering water to previously frozen areas of the ice sheet bed (Howat et al., 2013) or through afore-mentioned cryo-hydrologic warming (Phillips et al., 2010). Some SGLs at higher elevations have been observed to fill and drain multiple times in one melt season, suggesting that either englacial and/or subglacial drainage pathways do not remain open for long (Fitzpatrick et al., 2014). However, there may be physical limits on the inland extent of supraglacial lakes in south-west Greenland. Poinar et al. (2015) examined surface strain rates. They found that crevasses (and therefore moulins) are unlikely to form above 1600 m asl, which is also roughly the elevation above which lakes do not drain completely, and lower than the wet-frozen basal transition inferred to lie at ∼2000 m asl. If future melting extends to higher elevations, meltwater is more likely to flow via supraglacial streams into SGLs and moulins further down-glacier, which is in turn likely to have a limiting effect on the inland expansion of melt-induced ice acceleration (Poinar et al., 2015).

Further uncertainties remain about how the subglacial drainage system evolves under ice >1000 m thick in order to route the meltwater away towards the ice sheet margin. Towards the interior of the ice sheet, the surface and bed gradients are shallower and the ice thicker. Some numerical simulations of low-pressure R-channels (Röthlisberger, 1972) suggest that they do not grow significantly in response to SGL drainage, and subsequently grow only if P_w is sustained above overburden, otherwise closing rapidly at lower pressures (Dow et al., 2014). Similarly, Meierbachtol et al. (2013) used observational constraints from boreholes

drilled up to 35 km inland and which were inferred to access distributed regions of drainage in order to model R-channels, and found that shallow hydraulic gradients further away from the ice sheet margin are the chief limitation on the evolution of persistent channels, rather than rapid closure by creep. By contrast, a separate study which combined tracer evidence and R-channel creep closure modelling concluded that the drainage system can sustain low-pressure channels as far as 40 km inland beneath ice $\sim$1 km thick but that beyond this channels remain at high pressure (Chandler et al., 2013). As Hewitt (2013) notes, the physics of how small channels initiate remains debatable. Furthermore, meltwater flowing along the ice sheet bed is likely to erode, mobilise and re-work the substrate, which could lead to preferred flow paths through, for instance, highly sorted till (Gulley et al., 2012) which persist inter-annually. These issues, together with widely varying choices of overburden pressures, may provide more reasons to explain why studies modelling the evolution of R-channels do not tend to agree on timescales of channel growth, persistence and closure, nor indeed the hydraulic conditions under which they can exist.

It may be that inconsistencies in nomenclature have stymied agreement between studies. Some recent studies have examined whether R-channels are able to evolve beneath thick ice (e.g. Meierbachtol et al., 2013; Dow et al., 2014). Their conclusions, based on borehole observations and modelling, suggest that channelized drainage morphologies cannot be sustained beneath the thick ice that characterises the interior of the Greenland Ice Sheet. Conversely, observations made at Leverett Glacier all point to the rapid evolution of an *efficient* subglacial drainage system. Tracer evidence indicates that shortly after surface-bed drainage pathways are established, meltwater transits to the glacier margin within several hours (Cowton et al., 2013; Chandler et al., 2013), even 40 km inland below 1 km thick ice (D. Chandler, tracer injections during 2012, *pers. comm.*). Moreover, after the first spring event, most speed-up events caused by greater rates of meltwater supply are transient and short-lived, tending to cessate within hours to two days (e.g. Bartholomew et al., 2012). Thus, the observed speed of meltwater routing dictates that, if channelized drainage morphologies

cannot evolve beneath km-thick ice, some other efficient drainage morphology must exist instead to route meltwater rapidly to the glacier margin.

In common with the findings made at alpine glaciers, the efficient drainage system inferred to underlie Leverett Glacier has primarily been attributed to channelized drainage morphologies (e.g. Chapters 4 and 5, Cowton et al., 2013; Chandler et al., 2013; Sole et al., 2013). If, as other studies suggest, this is not the case, then progress needs to be made in defining the physics of alternative drainage morphologies. For instance, Meierbachtol et al. (2013) surmise that *'towards the interior a network of efficient distributed pathways develops in contrast to large melt channels'* (p. 779). A key test for the physics behind this proposed morphology is whether it is efficient enough to route large meltwater fluxes to the ice sheet margin over timescales which agree with observations. Moreover, the development of these physics needs to capture the coupled hydrology-dynamics which explain the observed winter ice flow. At Leverett Glacier slower winter velocities following a warmer summer have been explained through the evacuation of surrounding inefficient (unchannelized) regions of the bed by efficient (channelized) drainage pathways. Dow et al. (2014) propose a similar mechanism that could explain the observations made at Leverett Glacier: *'the cessation of surface water input at the end of the melt season would cause a local paucity of water along drainage pathways that would be recharged slowly by the more distant distributed system'* (p. 1050). This mechanism invokes 'drainage pathways', which one could further imply as being efficient, but this then brings one back around to the question of, if not an R-channel, then what alternative morphology of efficient drainage pathway is realistic within the initial constraints already provided by field evidence.

A full understanding of the role of the subglacial drainage system beyond 1700 m asl, where ice thickness and elevation may be important constraints upon system evolution, remains out of reach. The observations in this thesis (Chapter 4 and Figure 7.3) do not preclude the evolution of efficient subglacial drainage further inland. However, the few observations already available from contrasting melt-years (Figure 7.3) suggest that,

realistically, significant changes in ice motion at these elevations in response to projected warming are unlikely.

More broadly, the community understanding of coupled hydrology-dynamics at marine-terminating margins is extremely poor. Observations of sediment plumes rising from tidewater termini have been observed in remote sensing imagery (Chu et al., 2009; Tedstone and Arnold, 2012) and with time-lapse cameras (Sole et al., 2011), and indicate the likely presence of large subglacial channels delivering water originating from up-glacier into the fjord. However, marine-terminating margins present a number of extra and considerable challenges to the elucidation of subglacial drainage. Firstly, surface crevassing makes it difficult to deploy instrumentation on the ice sheet surface, iceberg calving makes it dangerous to approach the glacier terminus, and mélange in the fjord limits the deployment of oceanographic sensors. Secondly, it is not possible to observe bulk proglacial runoff, as meltwater discharges from the subglacial drainage system directly into the ocean. Thirdly, marine-terminating margins are subject also to oceanic forcing mechanisms (e.g. Straneo et al., 2013), which makes it difficult to disentangle the precise dynamic response to a specific external perturbation.

Despite the challenges which tidewater margins present, the continuing acceleration of major tidewater termini such as Jakobshavn Isbrae (Joughin et al., 2014) means that it is essential to identify the key mechanisms which control tidewater glacier dynamics. The IPCC 5th Assessment Report (Stocker et al., 2013) concluded that there is *high confidence* that basal lubrication does not explain recent dramatic speed ups that have resulted in rapid increases in ice loss from calving glaciers. However, observations show that beyond 35 km from the calving margin, surface melting is able to control diurnal to seasonal variability in ice motion (Sole et al., 2011), so hydro-dynamic coupling may yet play an important role in determining decadal scale ice flow variability inland from marine-terminating margins.

Subglacial hydrology may have other impacts at marine-terminating margins besides basal lubrication. Delivery of surface runoff to the glacier grounding line enhances submarine

melting along the ice front (Jenkins, 2011). Modelled submarine melt rates are much stronger if the subglacial drainage system delivers water to the terminus via a distributed system discharging along the length of the calving front as opposed to a few channels which only result in melt over a localised area (Slater et al., 2015). Thus, it is important to constrain the morphology of the subglacial drainage system near the terminus of tidewater glaciers in order to identify the rate at which mass is lost by submarine melting. Furthermore, the distribution of melt rate across the calving front may have ramifications for the style and quantity of calving (Chauché et al., 2014; Slater et al., 2015).

Lastly, there is clearly a wider need to continue the monitoring and analysis of melting, surface mass balance and ice motion as projected climate changes unfold. The impact of future extreme melt events on long-term surface mass balance and on hydro-dynamic coupling may require attention, as warming temperatures coupled with increasing quantities of black carbon from higher frequency forest fires (reducing ice albedo) are likely to result in near-annual extreme melt events by the end of the 21st century (Keegan et al., 2014). Moreover, whilst the evidence presented in Chapter 6 makes it clear that flow of land-terminating margins of the ice sheet has slowed in response to warming over the last 20 years, the melting which has occurred is nevertheless a very significant mass loss, which requires continued attention in order to quantify projected future mass losses from the ice sheet.

7.4 Concluding remarks

The research presented in this thesis has contributed to a rapidly emerging picture of coupled hydrology-dynamics along land-terminating margins of the Greenland Ice Sheet. It has shown that substantial transient ice motion variability occurs both due to temporally varying meltwater inputs (Chapter 4) and the configuration of the subglacial drainage system (Chapter 5), but that over the course of full melt-years the impact of coupled hydrology-dynamics on net annual ice motion, even during extreme melt-years, is minimal (Chapters 4

and 5). These findings are placed in longer-term context by examination of decadal trends in ice motion (Chapter 6), which show that even though surface melt production has increased by 50% in the last twenty years, hydro-dynamic coupling has led to an overall slowdown in ice flow up to at least 1100 m asl. These findings substantiate the overall conclusion of the IPCC's 5th Assessment Report and Shannon et al. (2013) that surface meltwater, although abundant, does not seem to be driving significant changes in basal lubrication that impact on annual ice sheet flow, and further suggest that ice motion might continue to slow down in response to the rising meltwater volumes projected for the 21st century.

There are now two major challenges. Firstly, at marine-terminating margins our understanding of all dynamic mechanisms — including coupled hydrology-dynamics — remains exceptionally poor. Secondly, at both land- and marine- terminating margins we need to identify whether coupled hydrology-dynamics may become an important mechanism at higher elevations in a warming climate. Observations of ice motion over decadal timescales, coupled with further improvements in hydrology and ice sheet models, are likely to be critical to improving our understanding of these areas in the context of projected climate change.

Bibliography

Allen, C., 2011. IceBridge MCoRDS L2 Ice Thickness 2010 and 2011, Digital media.

Alley, R., 2000. The Two-Mile Time Machine: Ice Cores, Abrupt Climate Change, and Our Future, Princeton University Press.

Alley, R. B., D. D. Blankenship, S. T. Rooney and C. R. Bentley, 1987. Till beneath ice stream B: 4. A coupled ice-till flow model, *Journal of Geophysical Research: Solid Earth*, **92**(B9), 8931–8940.

Alley, R. B., P. U. Clark, P. Huybrechts and I. Joughin, 2005a. Ice-sheet and sea-level changes, *Science*, **310**, 456–60.

Alley, R. B., T. K. Dupont, B. R. Parizek and S. Anandakrishnan, 2005b. Access of surface meltwater to beds of sub-freezing glaciers: preliminary insights, *Annals of Glaciology*, **40**, 8–14.

Andersen, M. L., T. B. Larsen, M. Nettles, P. Elosegui, D. van As, G. S. Hamilton, L. A. Stearns, J. L. Davis, A. P. Ahlstrom, J. de Juan, G. Ekström, L. Stenseng, S. A. Khan, R. Forsberg and D. Dahl-Jensen, 2010. Spatial and temporal melt variability at Helheim Glacier, East Greenland, and its effect on ice dynamics, *J. Geophys. Res.*, **115**, F04041.

Andrews, L. C., G. A. Catania, M. J. Hoffman, J. Gulley, M. Luthi, C. Ryser, R. L. Hawley and T. A. Neumann, 2014. Direct observations of evolving subglacial drainage beneath the Greenland Ice Sheet, *Nature*, **514**, 80–83.

Arnold, N., K. Richards, I. Willis and M. Sharp, 1998. Initial results from a distributed, physically based model of glacier hydrology, *Hydrological Processes*, **12**(2), 191–219.

Balise, M. J. and C. F. Raymond, 1985. Transfer of basal sliding variations to the surface of a linarly viscous glacier, *Journal of Glaciology*, **31**, 308–318.

Bamber, J. L., R. B. Alley and I. Joughin, 2007. Rapid response of modern day ice sheets to external forcing, *Earth and Planetary Science Letters*, **257**(1-2), 1–13.

Bamber, J. L., J. A. Griggs, R. T. W. L. Hurkmans, J. A. Dowdeswell, S. P. Gogineni, I. Howat, J. Mouginot, J. Paden, S. Palmer, E. Rignot and D. Steinhage, 2013. A new bed elevation dataset for Greenland, *The Cryosphere*, **7**(2), 499–510.

Banwell, A. F., I. Willis and N. Arnold, 2013. Modelling subglacial water routing at Paakitsoq, W Greenland, *Journal of Geophysical Research: Earth Surface*, **118**, 1282–1295.

Bartholomaus, T. C., R. S. Anderson and S. P. Anderson, 2008. Response of glacier basal motion to transient water storage, *Nature Geosci.*, **1**(1), 33–37.

Bartholomew, I., P. Nienow, D. Mair, A. Hubbard, M. King and A. Sole, 2010. Seasonal evolution of subglacial drainage and acceleration in a Greenland outlet glacier, *Nature Geosci.*, **3**(6), 408–411.

Bartholomew, I., P. Nienow, A. Sole, D. Mair, T. Cowton, M. King and S. Palmer, 2011a. Seasonal variations in Greenland Ice Sheet motion: Inland extent and behaviour at higher elevations, *Earth Planet. Sci. Lett.*, **307**, 271–278.

Bartholomew, I., P. Nienow, A. Sole, D. Mair, T. Cowton and M. A. King, 2012. Short-term variability in Greenland Ice Sheet motion forced by time-varying meltwater drainage: Implications for the relationship between subglacial drainage system behavior and ice velocity, *J. Geophys. Res.*, **117**, F03002.

Bartholomew, I., P. Nienow, A. Sole, D. Mair, T. Cowton, S. Palmer and J. Wadham, 2011b. Supraglacial forcing of subglacial drainage in the ablation zone of the Greenland ice sheet, *Geophys. Res. Lett.*, **38**, L08502.

Benn, D. and D. Evans, 2010. Glaciers and Glaciation, 2nd edition, Hodder Arnold/Routledge.

Benn, D. I., C. R. Warren and R. H. Mottram, 2007. Calving processes and the dynamics of calving glaciers, *Earth-Science Reviews*, **82**, 143 – 179.

Bennartz, R., M. D. Shupe, D. D. Turner, V. P. Walden, K. Steffen, C. J. Cox, M. S. Kulie, N. B. Miller and C. Pettersen, 2013. July 2012 Greenland melt extent enhanced by low-level liquid clouds, *Nature*, **496**(7443), 83–86.

Bingham, R. G., A. L. Hubbard, P. W. Nienow and M. J. Sharp, 2008. An investigation into the mechanisms controlling seasonal speedup events at a High Arctic glacier, *J. Geophys. Res.*, **113**, F02006.

Bingham, R. G., P. Nienow and M. J. Sharp, 2003. Intra-annual and intra-seasonal flow dynamics of a High Arctic polythermal valley glacier, *Annals Of Glaciology*, **37**, 181–188.

Bingham, R. G., P. W. Nienow, M. J. Sharp and L. Copland, 2006. Hydrology and dynamics of a polythermal (mostly cold) High Arctic glacier, *Earth Surface Processes and Landforms*, **31**, 1463–1479.

Boon, S. and M. Sharp, 2003. The role of hydrologically-driven ice fracture in drainage system evolution on an Arctic glacier, *Geophys. Res. Lett.*, **30**(18), 1916.

Bougamont, M., P. Christoffersen, A. L. Hubbard, A. Fitzpatrick, S. H. Doyle and S. P. Carter, 2014. Sensitive response of the Greenland ice sheet to surface melt drainage over a soft bed, *Nature Communications*, **5**, 5052.

Boulton, G. S. and A. S. Jones, 1979. Stability of temperate ice caps and ice sheets resting on beds of deformable sediment, *J. Glaciol.*, **24**(90), 29–43.

Box, J. E. and K. Ski, 2007. Remote sounding of Greenland supraglacial melt lakes : implications for subglacial hydraulics, *J. Glaciol.*, **53**(181), 257–265.

Box, J. E., L. Yang, D. H. Bromwich and L.-S. Bai, 2009. Greenland Ice Sheet Surface Air Temperature Variability: 1840âĂŞ2007, *Journal of Climate*, **22**, 4029–4049.

van den Broeke, M., J. Bamber, J. Ettema, E. Rignot, E. Schrama, W. J. van de Berg, E. van Meijgaard, I. Velicogna and B. Wouters, 2009. Partitioning recent Greenland mass loss, *Science*, **326**(5955), 984–986.

Campbell, F. M., P. W. Nienow and R. S. Purves, 2006. Role of the supraglacial snowpack in mediating meltwater delivery to the glacier system as inferred from dye tracer investigations, *Hydrological Processes*, **20**(4), 969–985.

Catania, G. A. and T. A. Neumann, 2010. Persistent englacial drainage features in the Greenland Ice Sheet, *Geophys. Res. Lett.*, **37**(2), L02501.

Catania, G. A., T. A. Neumann and S. F. Price, 2008. Characterizing englacial drainage in the ablation zone of the Greenland ice sheet, *J. Glaciol.*, **54**(187), 567–578.

Chandler, D. M., J. L. Wadham, G. P. Lis, T. Cowton, A. Sole, I. Bartholomew, J. Telling, P. Nienow, E. B. Bagshaw, D. Mair, S. Vinen and A. Hubbard, 2013. Evolution of the subglacial drainage system beneath the Greenland Ice Sheet revealed by tracers, *Nature Geosci.*, **6**(3), 195–198.

Chauché, N., A. Hubbard, J.-C. Gascard, J. E. Box, R. Bates, M. Koppes, A. Sole, P. Christoffersen and H. Patton, 2014. Ice-ocean interaction and calving front morphology at two west Greenland tidewater outlet glaciers, *The Cryosphere*, **8**(4), 1457–1468.

Chen, G., 1999. GPS kinematic poisitioning for the airborne laser altimetry at Long Valley, California., (PhD thesis), Massachusetts Institute of Technology.

Christoffersen, P., R. I. Mugford, K. J. Heywood, I. Joughin, J. A. Dowdeswell, J. P. M. Syvitski, A. Luckman and T. J. Benham, 2011. Warming of waters in an East Greenland fjord prior to glacier retreat: mechanisms and connection to large-scale atmospheric conditions, *Cryosphere*, **5**(3), 701–714.

Chu, V. W., 2013. Greenland ice sheet hydrology: a review, *Progress in Physical Geography*, **38**(1), 19–54.

Chu, V. W., L. C. Smith, A. K. Rennermalm, R. R. Forster, J. E. Box and N. Reehy, 2009. Sediment plume response to surface melting and supraglacial lake drainages on the Greenland ice sheet, *J. Glaciol.*, **55**(194), 1072–1082.

Clarke, G. K., 2005. Subglacial Processes, *Annu. Rev. Earth Planet. Sci.*, **33**(1), 247–276.

Colgan, W., K. Steffen, W. S. McLamb, W. Abdalati, H. Rajaram, R. Motyka, T. Phillips and R. Anderson, 2011. An increase in crevasse extent, West Greenland: Hydrologic implications, *Geophys. Res. Lett.*, **38**(18), 1–7.

Copland, L., M. J. Sharp and P. Nienow, 2003. Links between short-term velocity variations and the subglacial hydrology of a predominantly cold polythermal glacier, *J. Glaciol.*, **49**(166), 337–348.

Cowton, T., 2013. The hydrology of a land-terminating Greenlandic outlet glacier, (PhD thesis), The University of Edinburgh.

Cowton, T., P. Nienow, I. Bartholomew, A. Sole and D. Mair, 2012. Rapid erosion beneath the Greenland ice sheet, *Geology*, **40**(4), 343 – 346.

Cowton, T., P. Nienow, A. Sole, J. Wadham, G. Lis, I. Bartholomew, W. F. Mair and D. M. Chandler, 2013. Evolution of drainage system morphology at a land-terminating Greenland outlet glacier, *J. Geophys. Res.*, **118**, 29–41.

Cuffey, K. and W. S. B. Paterson, 2010. The Physics of Glaciers, Butterworth-Heinemann, 3rd ed.

Das, S. B., I. Joughin, M. D. Behn, I. M. Howat, M. A. King, D. Lizarralde and M. P. Bhatia, 2008. Fracture propagation to the base of the Greenland Ice Sheet during supraglacial lake drainage., *Science*, **320**(5877), 778–81.

Dehecq, A., N. Gourmelen and E. Trouvé, 2015. Deriving large scale glacier velocities from a complete satellite archive: application to the Pamir-Karakoram-Himalaya, *Remote Sensing of Environment*, **162**, 55–66.

Dow, C., A. Hubbard, A. D. Booth, S. Doyle, A. Gusmeroli and B. Kulessa, 2013. Seismic evidence of mechanically weak sediments underunder Russell Glacier, West Greenland, *Annals of Glaciology*, **54**(64), 135–141.

Dow, C. F., B. Kulessa, I. Rutt, S. Doyle and A. Hubbard, 2014. Upper bounds on subglacial channel development for interior regions of the Greenland ice sheet, *Journal of Glaciology*, **60**, 1044.

Doyle, S. H., A. Hubbard, A. A. W. Fitzpatrick, D. van As, A. B. Mikkelsen, R. Pettersson and B. Hubbard, 2014. Persistent flow acceleration within the interior of the Greenland ice sheet, *Geophysical Research Letters*, **41**(3), 899–905.

Doyle, S. H., A. L. Hubbard, C. F. Dow, G. A. Jones, A. Fitzpatrick, A. Gusmeroli, B. Kulessa, K. Lindback, R. Pettersson and J. E. Box, 2013. Ice tectonic deformation during the rapid in situ drainage of a supraglacial lake on the Greenland Ice Sheet, *The Cryosphere*, **7**(1), 129–140.

Enderlin, E. M., I. M. Howat, S. Jeong, M.-J. Noh, J. H. van Angelen and M. R. van den Broeke, 2014. An improved mass budget for the Greenland ice sheet, *Geophysical Research Letters*, **41**(3), 866–872.

Estey, L. H. and C. M. Meertens, 1999. TEQC: The Multi-Purpose Toolkit for GPS/GLONASS Data, *GPS Solutions*, **3**, 42–49.

Ferguson, R. I., 1973. Sinuosity of Supraglacial streams, *Geological Society of America Bulletin*, **84**, 251–256.

Fettweis, X., E. Hanna, C. Lang, A. Belleflamme, M. Erpicum and H. Gallée, 2013. Brief communication "Important role of the mid-tropospheric atmospheric circulation in the recent surface melt increase over the Greenland ice sheet", *Cryosphere*, **7**(1), 241–248.

Fettweis, X., M. Tedesco, M. van den Broeke and J. Ettema, 2011. Melting trends over the Greenland ice sheet (1958-2009) from spaceborne microwave data and regional climate models, *Cryosphere*, **5**(2), 359–375.

Fischer, U. H. and G. K. C. Clarke, 1997. Stick-slip sliding behaviour at the base of a glacier, *J. Glaciol.*, **24**, 390–396.

Fitzpatrick, A. A. W., A. Hubbard, I. Joughin, D. J. Quincey, D. Van As, A. P. Mikkelsen, S. H. Doyle, B. Hasholt and G. A. Jones, 2013. Ice flow dynamics and surface meltwater flux at a land-terminating sector of the Greenland ice sheet, *J. Glaciol.*, **59**, 687–696.

Fitzpatrick, A. A. W., A. L. Hubbard, J. E. Box, D. J. Quincey, D. van As, A. P. B. Mikkelsen, S. H. Doyle, C. F. Dow, B. Hasholt and G. A. Jones, 2014. A decade (2002-2012) of supraglacial lake volume estimates across Russell Glacier, West Greenland, *The Cryosphere*, **8**(1), 107–121.

Flowers, G. E., 2015. Modelling water flow under glaciers and ice sheets, *Proceedings of the Royal Society of London A: Mathematical, Physical and Engineering Sciences*, **471**(2176).

Fountain, A. G., 1994. Borehole water-level variations and implications for the subglacial hydraulics of South Cascade Glacier, Washington State, U.S.A., *Journal of Glaciology*, **40**(135), 293–304.

Fountain, A. G., 1996. Effect of Snow and Firn Hydrology on the Physical and Chemical Characteristics of Glacial Runoff, *Hydrological Processes*, **10**(4), 509–521.

Fountain, A. G. and S. Walder, 1998. Water flow through temperate glaciers, *Rev. Geophys.*, **36**(3), 299–328.

Fowler, A. C., 1987. Sliding with cavity formation, *J. Glaciol.*, **33**(115), 255–267.

Fowler, A. C., 2003. On the rheology of till, *Annals of Glaciology*, **37**(1), 55–59.

Fox, A. M., I. C. Willis and N. S. Arnold, 2008. Modification and testing of a one-dimensional energy and mass balance model for supraglacial snowpacks, *Hydrological Processes*, **22**, 3194– 3209.

Gordon, S., M. Sharp, B. Hubbard, C. Smart, B. Ketterling and I. C. Willis, 1998. Seasonal reorganisation of subglacial drainage inferred from borehole measurements, *Hydrological Processes*, **12**, 105–133.

Gregory, J. M., 2004. Threatened loss of the Greenland ice-sheet, *Nature*, **428**(l), 2513–2513.

Gulley, J., M. Grabiec, J. Martin, J. Jania, G. Catania and P. Glowacki, 2012. The effect of discrete recharge by moulins and heterogeneity in flow-path efficiency at glacier beds on subglacial hydrology, *Journal of Glaciology*, **58**(211), 926–940.

Hanna, E., P. Huybrechts, J. Cappelen, K. Steffen, R. C. Bales, E. Burgess, J. R. McConnell, J. Peder Steffensen, M. Van den Broeke, L. Wake, G. Bigg, M. Griffiths and D. Savas, 2011. Greenland Ice Sheet surface mass balance 1870 to 2010 based on Twentieth Century Reanalysis, and links with global climate forcing, *J. Geophys. Res.*, **116**(D24).

Hanna, E., P. Huybrechts, I. Janssens, J. Cappelen, K. Steffen and A. Stephens, 2005. Runoff and mass balance of the Greenland ice sheet: 1958-2003, *J. Geophys. Res.*, **110**, D13108.

Hanna, E., P. Huybrechts, K. Steffen, J. Cappelen, R. Huff, C. Shuman, T. Irvine-Fynn, S. Wise and M. Griffiths, 2008. Increased Runoff from Melt from the Greenland Ice Sheet: A Response to Global Warming, *J. Climate*, **21**(2), 331–341.

Hanna, E., S. H. Mernild, J. Cappelen and K. Steffen, 2012. Recent warming in Greenland in a long-term instrumental (1881-2012) climatic context: I. Evaluation of surface air temperature records, *Environ. Res. Lett.*, **7**(4), 045404.

Hanna, E., F. J. Navarro, F. Pattyn, C. M. Domingues, X. Fettweis, E. R. Ivins, R. J. Nicholls, C. Ritz, B. Smith, S. Tulaczyk, P. L. Whitehouse and H. J. Zwally, 2013. Ice sheet mass balance and climate change, *Nature*, **498**, 51–59.

Hansen, J., M. Sato, P. Kharecha, D. Beerling, R. Berner, V. Masson-Delmotte, M. Pagani, M. Raymo, D. L. Royer and J. C. Zachos, 2008. Target atmospheric CO2: where should humanity aim?, *The Open Atmospheric Science Journal*, **2**, 217–231.

Harbor, J., M. Sharp, L. Copland, B. Hubbard, P. Nienow and D. Mair, 1997. Influence of subglacial drainage conditions on the velocity distribution within a glacier cross section, *Geology*, **25**, 739–742.

Hawkings, J. R., J. L. Wadham, M. Tranter, R. Raiswell, L. G. Benning, P. J. Statham, A. J. Tedstone, P. Nienow, K. Lee and J. Telling, 2014. Ice sheets as a significant source of highly reactive nanoparticulate iron to the oceans, *Nature Communications*, **5**, 3929.

Helm, V., A. Humbert and H. Miller, 2014. Elevation and elevation change of Greenland and Antarctica derived from CryoSat-2, *The Cryosphere*, **8**(4), 1539–1559.

Hewitt, I., 2013. Seasonal changes in ice sheet motion due to melt water lubrication, *Earth and Planetary Science Letters*, **371**, 16 – 25.

Hock, R., 2005. Glacier melt: a review of processes and their modelling, *Progress in Physical Geography*, **29**(3), 362–391.

Hoffman, M. and S. Price, 2014. Feedbacks between coupled subglacial hydrology and glacier dynamics, *Journal of Geophysical Research: Earth Surface*, **119**(3), 414–436.

Hoffman, M. J., G. A. Catania, T. A. Neumann, L. C. Andrews and J. A. Rumrill, 2011. Links between acceleration, melting and supraglacial lake driainage of the western Greenland ice sheet, *J. Geophys. Res.*, **116**, F04035.

Hooke, R. L., P. Calla, P. Holmlund, M. Nilsson and A. Stroeven, 1989. A 3 year record of seasonal variations in surface velocity, Storglaciäaren, Sweden, *Journal of Glaciology*, **35**, 235–247.

Hooke, R. L., T. Laumann and J. Kohler, 1990. Subglacial water pressures and the shape of subglacial conduits, *J. Glaciol.*, **36**(122), 67–71.

Howat, I. M., J. E. Box, Y. Ahn, A. Herrington and E. M. Mcfadden, 2010. Seasonal variability in the dynamics of marine-terminating outlet glaciers in Greenland, *Journal of Glaciology*, **56**(198), 601–613.

Howat, I. M., A. Negrete and B. E. Smith, 2014. The Greenland Ice Mapping Project (GIMP) land classification and surface elevation data sets, *The Cryosphere*, **8**(4), 1509–1518.

Howat, I. M., S. de la Peña, J. H. van Angelen, J. Lenaerts and M. van den Broeke, 2013. Brief Communication: "Expansion of meltwater lakes on the Greenland Ice Sheet", *The Cryosphere*, **7**, 201–204.

Hubbard, B. and P. Nienow, 1997. Alpine subglacial hydrology, *Quaternary Science Reviews*, **16**(9), 939–955.

Hubbard, B., M. Sharp, I. Willis, M. Nielsen and C. Smart, 1995. Borehole water-level variations and the structure of the subglacial hydrological system of Haut Glacier d'Arolla, Valais, Switzerland, *J. Glaciol.*, **41**(139), 572–583.

Iken, A., 1981. The effect of the subglacial water pressure on the sliding velocity of a glacier in an idealized numerical model, *J. Glaciol.*, **27**(97), 407–421.

Iken, A. and R. A. Bindschadler, 1986. Combined measurements of subglacial water pressure and surface velocity of Findelengletscher, Switzerland: conclusions about drainage system and sliding mechanism, *J. Glaciol.*, **32**(110), 101–119.

Iken, A. and M. Truffer, 1997. The relationship between subglacial water pressure and velocity of Findelengletscher, Switzerland, during its advance and retreat, *Journal of Glaciology*, **43**, 328–338.

Isenko, E., R. Naruse and B. Mavlyudov, 2005. Water temperature in englacial and supraglacial channels: Change along the flow and contribution to ice melting on the channel wall, *Cold Regions Science and Technology*, **42**(1), 53–62.

Iverson, N. R., B. Hanson, R. L. Hooke and P. Jansson, 1995. Flow mechanism of glaciers on soft beds, *Science*, **267**(5194), 80–81.

Janssens, I. and P. Huybrechts, 2000. The treatment of meltwater retention in mass-balance parameterizations of the Greenland ice sheet, *Annals of Glaciology*, **31**(1), 133–140.

Jenkins, A., 2011. Convection-Driven Melting near the Grounding Lines of Ice Shelves and Tidewater Glaciers, *Journal of Physical Oceanography*, **41**(12), 2279–2294.

Jezek, C., P. Gogineni and M. Shanableth, 1994. Radar measurements of melt zones on the Greenland Ice Sheet, *Geophys. Res. Lett.*, **21**(1), 33–36.

Joughin, I., S. B. Das, G. E. Flowers, M. D. Behn, R. B. Alley, M. A. King, B. E. Smith, J. Bamber, M. R. van den Broeke and J. H. van Angelen, 2013. Influence of supraglacial lakes and ice-sheet geometry on seasonal ice-flow variability, *Cryosphere Discuss.*, **7**(2), 1101–1118.

Joughin, I., S. B. Das, M. A. King, B. E. Smith, I. M. Howat and T. Moon, 2008. Seasonal speedup along the western flank of the Greenland Ice Sheet, *Science*, **320**(5877), 781–3.

Joughin, I., B. E. Smith, I. M. Howat, T. Scambos and T. Moon, 2010. Greenland flow variability from ice-sheet-wide velocity mapping, *Journal of Glaciology*, **56**(197), 415–430.

Joughin, I., B. E. Smith, D. E. Shean and D. Floricioiu, 2014. Brief Communication: Further summer speedup of Jakobshavn Isbrae, *The Cryosphere*, **8**(1), 209–214.

Joughin, I., S. Tulaczyk, M. Fahnestock and R. Kwok, 1998. A mini-surge on the Ryder Glacier, Greenland, observed by satellite radar interferometry, *Science*, **274**, 228–230.

Kamb, B., 1987. Glacier surge mechanism based on linked cavity configuration of the basal water conduit system, *Journal of Geophysical Research*, **92**, 9083–9100.

Kavanaugh, J. L. and G. K. C. Clarke, 2001. Abrupt glacier motion and reorganisation of basal shear stress following the establishment of a connected drainage system, *J. Glaciol.*, **47**(158), 472–480.

Keegan, K. M., M. R. Albert, J. R. McConnell and I. Baker, 2014. Climate change and forest fires synergistically drive widespread melt events of the Greenland Ice Sheet, *Proceedings of the National Academy of Sciences*, **111**(22), 7964–7967.

King, M., 2004. Rigorous GPS data-processing strategies for glaciological applications, *J. Glaciol.*, **50**(171), 601–607.

Klobuchar, J. A., 1991. Ionospheric effects on GPS, *GPS World*, **04**.

Krabill, W., W. Abdalati, E. Frederick, S. Manizade, C. Martin, J. Sonntag, R. Swift, R. Thomas, W. Wright and J. Yungel, 2000. Greenland Ice Sheet: High-Elevation Balance and Peripheral Thinning, *Science*, **289**(5478), 428–430.

Krawczynski, M. J., M. D. Behn, S. B. Das and I. Joughin, 2009. Constraints on the lake volume required for hydro-fracture through ice sheets, *Geophys. Res. Lett.*, **36**(10), 1–5.

Lawson, E. C., J. L. Wadham, M. Tranter, M. Stibal, G. P. Lis, C. E. H. Butler, J. Laybourn-Parry, P. Nienow, D. Chandler and P. Dewsbury, 2014. Greenland Ice Sheet exports labile organic carbon to the Arctic oceans, *Biogeosciences*, **11**(14), 4015–4028.

Liang, Y.-L., W. Colgan, Q. Lv, K. Steffen, W. Abdalati, J. Stroeve, D. Gallaher and N. Bayou, 2012. A decadal investigation of supraglacial lakes in West Greenland using a fully automatic detection and tracking algorithm, *Remote Sensing of Environment*, **123**(0), 127 – 138.

Lliboutry, L., 1968. General theory of subglacial cavitation and sliding of temperate glaciers, *Journal of Glaciology*, **7**(49), 21–58.

Lliboutry, L., 1979. Local friction laws for glaciers: a critical review and new openings, *J. Glaciol.*, **23**(89), 67–95.

Lüthje, M., L. Pedersen, N. Reeh and W. Greuell, 2006. Modelling the evolution of supraglacial lakes on the West Greenland ice-sheet margin, *J. Glaciol.*, **52**(179), 608–618.

Mair, D., P. Nienow, M. Sharp, T. Wohlleben and I. Willis, 2002. Influence of subglacial drainage system evolution on glacier surface motion: Haut Glacier d'Arolla, Switzerland, *J. Geophys. Res.*, **107**, 2175, 13pp.

Mair, D., P. Nienow, I. Willis and M. Sharp, 2001. Spatial patterns of glacier motion during a high-velocity event: Haut Glacier d'Arolla, Switzerland, *J. Glaciol.*, **47**(156), 9–20.

Mair, D., I. Willis, U. H. Fischer, B. Hubbard, P. Nienow and A. Hubbard, 2003. Hydrological controls on patterns of surface, internal and basal motion during three "spring events": Haut Glacier d'Arolla, Switzerland, *J. Glaciol.*, **49**(167), 555–567.

Mayaud, J. R., A. F. Banwell, N. S. Arnold and I. C. Willis, 2014. Modeling the response of subglacial drainage at Paakitsoq, west Greenland, to 21st century climate change, *Journal of Geophysical Research: Earth Surface*, **119**(12), 2619–2634.

McMillan, M., P. Nienow, A. Shepherd, T. Benham and A. Sole, 2007. Seasonal evolution of supra-glacial lakes on the Greenland Ice Sheet, *Earth Planet. Sci. Lett.*, **262**(3-4), 484–492.

Meehl, G., T. Stocker, W. Collins, P. Friedlingstein, A. Gaye, J. Gregory, A. Kitoh, R. Knutti, J. Murphy, A. Noda, S. Raper, I. Watterson, A. Weaver and Z.-C. Zhao, 2007. Global Climate Projections, Solomon, S., D. Qin, M. Manning, Z. Chen, M. Marquis, K. Averyt, M. Tignor and H. Miller, eds., Climate Change 2007: The Physical Science Basis. Contribution of Working Group I to the Fourth Assessment Report of the Intergovernmental Panel on Climate Change, Cambridge University Press.

Meierbachtol, T., J. Harper and N. Humphrey, 2013. Basal Drainage System Response to Increasing Surface Melt on the Greenland Ice Sheet, *Science*, **341**(6147), 777–779.

Mernild, S. H., E. Hanna, J. R. McConnell, M. Sigl, A. P. Beckerman, J. C. Yde, J. Cappelen, J. K. Malmros and K. Steffen, 2014. Greenland precipitation trends in a long-term instrumental climate context (1890âĂŞ2012): evaluation of coastal and ice core records, *International Journal of Climatology*.

Mernild, S. H., G. E. Liston, C. A. Hiemstra, K. Steffen, E. Hanna and J. H. Christensen, 2009. Greenland Ice Sheet surface mass-balance modelling and freshwater flux for 2007, and in a 1995-2007 perspective, *Hydrological Processes*, **23**, 2470– 2484.

Mernild, S. H., G. E. Liston, K. Steffen, M. van den Broeke and B. Hasholt, 2010. Runoff and mass-balance simulations from the Greenland Ice Sheet at Kangerlussuaq (Søndre Strømfjord) in a 30-year perspective, 1979-2008, *Cryosphere*, **4**(2), 231–242.

Moon, T., I. Joughin, B. Smith and I. M. Howat, 2012. 21st-century evolution of Greenland outlet glacier velocities, *Science*, **336**, 576–578.

Morlighem, M., E. Rignot, J. Mouginot, H. Seroussi and E. Larour, 2014. Deeply incised submarine glacial valleys beneath the Greenland ice sheet, *Nature Geoscience*, **7**, 418–422.

Morlighem, M., E. Rignot, J. Mouginot, X. Wu, H. Seroussi, E. Larour and J. Paden, 2013. High-resolution bed topography mapping of Russell Glacier, Greenland, inferred from Operation IceBridge data, *Journal of Glaciology*, **59**(218), 1015–1023.

Mote, T. L., 2007. Greenland surface melt trends 1973-2007: Evidence of a large increase in 2007, *Geophys. Res. Lett.*, **34**(22), 1–5.

Murray, T. and G. K. C. Clarke, 1995. Black-box modeling of the subglacial water system, *Journal of Geophysical Research: Solid Earth*, **100**(B6), 10231–10245.

Murray, T., K. Scharrer, T. D. James, S. R. Dye, E. Hanna, A. D. Booth, N. Selmes, A. Luckman, A. L. C. Hughes, S. Cook and P. Huybrechts, 2010. Ocean regulation hypothesis for glacier dynamics in southeast Greenland and implications for ice sheet mass changes, *J. Geophys. Res.*, **115**, F03026.

Nghiem, S. V., D. K. Hall, T. L. Mote, M. Tedesco, M. R. Albert, K. Keegan, C. A. Shuman, D. N. E and G. Neumann, 2012. The extreme melt across the Greenland ice sheet in 2012, *Geophys. Res. Lett.*, **39**, L20502.

Nick, F. M., A. Vieli, M. Andersen, I. Joughin, A. J. Payne, T. L. Edwards, F. Pattyn and R. S. W. van de Wal, 2013. Future sea-level rise from Greenland's main outlet glaciers in a warming climate, *Nature*, **497**, 235–238.

Nienow, P., M. Sharp and I. Willis, 1998. Seasonal changes in the morphology of the subglacial drainage system, Haut Glacier d'Arolla, Switzerland, *Earth Surface Processes and Landforms*, **23**, 825–843.

Nienow, P. W., A. L. Hubbard, B. P. Hubbard, D. M. Chandler, D. W. F. Mair, M. J. Sharp and I. C. Willis, 2005. Hydrological controls on diurnal ice flow variability in valley glaciers, *J. Geophys. Res.*, **110**(F4), F04002.

Nye, J. F., 1965. The flow of a glacier in a channel of rectangular, elliptic or parabolic cross-section, *J. Glaciol.*, **5**, 661–690.

Ohmura, A. and N. Reeh, 1991. New precipitation and accumulation maps for Greenland, *Journal of Glaciology*, **37**, 140–148.

Palmer, S., A. Shepherd, P. Nienow and I. Joughin, 2011. Seasonal speedup of the Greenland Ice Sheet linked to routing of surface water, *Earth Planet. Sci. Lett.*, **302**, 423–428.

Parizek, B. R. and R. B. Alley, 2004. Implications of increased Greenland surface melt under global-warming scenarios: ice-sheet simulations, *Quaternary Science Reviews*, **23**(9-10), 1013–1027.

Paul, F., T. Bolch, A. Kääb, T. Nagler, C. Nuth, K. Scharrer, A. Shepherd, T. Strozzi, F. Ticconi, R. Bhambri, E. Berthier, S. Bevan, N. Gourmelen, T. Heid, S. Jeong, M. Kunz, T. R. Lauknes, A. Luckman, J. P. M. Boncori, G. Moholdt, A. Muir, J. Neelmeijer, M. Rankl, J. VanLooy and T. V. Niel, 2013. The glaciers climate change initiative: Methods for creating glacier area, elevation change and velocity products, *Remote Sensing of Environment*.

Phillips, T., S. Leyk, H. Rajaram, W. Colgan, W. Abdalati, D. McGrath and K. Steffen, 2011. Modeling moulin distribution on Sermeq Avannarleq glacier using ASTER and WorldView imagery and fuzzy set theory, *Remote Sensing of Environment*, **115**(9), 2292–2301.

Phillips, T., H. Rajaram and K. Steffen, 2010. Cryo-hydrologic warming: A potential mechanism for rapid thermal response of ice sheets, *Geophysical Research Letters*, **37**(20), L20503.

Pimentel, S. and G. E. Flowers, 2011. A numerical study of hydrologically driven glacier dynamics and subglacial flooding, *Proceedings of the Royal Society A*, **467**(2126), 537–558.

Piotrowski, J. A., D. M. Mickelson, S. Tulaczyk, D. Krzyszkowski and F. W. Junge, 2001. Were deforming subglacial beds beneath past ice sheets really widespread?, *Quaternary International*, **86**(1), 139 – 150.

Poinar, K., I. Joughin, S. B. Das, M. D. Behn, J. T. M. Lenaerts and M. R. van den Broeke, 2015. Limits to future expansion of surface-melt-enhanced ice flow into the interior of western Greenland, *Geophysical Research Letters*, n/a–n/a.

Price, S. F., A. J. Payne, G. A. Catania and T. A. Neumann, 2008. Seasonal acceleration of inland ice via longitudinal coupling to marginal ice, *J. Glaciol.*, **54**(185), 213–219.

Pritchard, H. D., R. J. Arthern, D. G. Vaughan and L. A. Edwards, 2009. Extensive dynamic thinning on the margins of the Greenland and Antarctic ice sheets, *Nature*, **461**(7266), 971–5.

Raymond, C. F., 1971. Flow in a transverse section of Athabasca Glacier, Alberta, Canada, *J. Glaciol.*, **10**, 55–84.

Reyes, A. V., A. E. Carlson, B. L. Beard, R. G. Hatfield, J. S. Stoner, K. Winsor, B. Welke and D. J. Ullman, 2014. South Greenland ice-sheet collapse during Marine Isotope Stage 11, *Nature*, **510**, 525–528.

Richards, K., M. Sharp, N. Arnold, A. Gurnell, M. Clark, M. Tranter, Nienow, G. Brown, I. Willis and W. Lawson, 1996. An integrated approach to modelling hydrology and water quality in glacierized catchments, *Hydrological Processes*, **10**(4), 479–508.

Rignot, E. and P. Kanagaratnam, 2006. Changes in the velocity structure of the Greenland Ice Sheet, *Science*, **311**(5763), 986–90.

Rignot, E., I. Velicogna, M. R. van den Broeke, A. Monaghan and J. Lenaerts, 2011. Acceleration of the contribution of the Greenland and Antarctic ice sheets to sea level rise, *Geophys. Res. Lett.*, **38**(5), 1–5.

Rippin, D. M., I. C. Willis, N. S. Arnold, A. J. Hodson and M. Brinkhaus, 2005. Spatial and temporal variations in surface velocity and basal drag across the tongue of the polythermal glacier Midre Lovénbreen, Svalbard, *J. Glaciol.*, **175**, 588–600.

Röthlisberger, H., 1972. Water pressure in intra- and subglacial channels, *J. Glaciol.*, **11**(62), 177–203.

Röthlisberger, H. and H. Lang, 1987. Glacio-Fluvial Sediment Transfer: An Alpine Perspective, John Wiley and Sons, chap. Glacial Hydrology, 207–284.

Sasgen, I., M. van den Broeke, J. L. Bamber, E. Rignot, L. S. Sorensen, B. Wouters, Z. Martinec, I. Velicogna and S. B. Simonsen, 2012. Timing and origin of recent regional ice-mass loss in Greenland, *Earth Planet. Sci. Lett.*, **333**(0), 293 – 303.

Scambos, T. A., M. J. Dutkiewicz, J. C. Wilson and R. A. Bindschadler, 1992. Application of image cross-correlation to the measurement of glacier velocity using satellite image data, *Remote Sensing of Environment*, **42**(3), 177 – 186.

Schoof, C., 2010. Ice-sheet acceleration driven by melt supply variability, *Nature*, **468**(7325), 803–806.

Selmes, N., T. Murray and T. D. James, 2011. Fast draining lakes on the Greenland Ice Sheet, *Geophys. Res. Lett.*, **38**(15), 1–5.

Shannon, S. R., A. J. Payne, I. D. Bartholomew, M. R. van den Broeke, T. L. Edwards, X. Fettweis, O. Gagliardini, F. Gillet-Chaulet, H. Goelzer, M. J. Hoffman, P. Huybrechts, D. W. F. Mair, P. W. Nienow, M. Perego, S. F. Price, C. J. P. P. Smeets, A. J. Sole, R. S. W. van de Wal and T. Zwinger, 2013. Enhanced basal lubrication and the contribution of the Greenland ice sheet to future sea-level rise, *Proceedings of the National Academy of Sciences*, **110**(35), 14156–14161.

Sharp, M., K. Richards, I. Willis, N. Arnold, P. Nienow, W. Lawson and J.-L. Tison, 1993. Geometry, bed topography and drainage system structure of the haut glacier d'Arolla, Switzerland, *Earth Surface Processes and Landforms*, **18**(6), 557–571.

Shepherd, A., A. Hubbard, P. Nienow, M. King, M. McMillan and I. Joughin, 2009. Greenland ice sheet motion coupled with daily melting in late summer, *Geophys. Res. Lett.*, **36**(1), 2–5.

Shepherd, A., E. R. Ivins, G. A, V. R. Barletta, M. J. Bentley, S. Bettadpur, K. H. Briggs, D. H. Bromwich, R. Forsberg, N. Galin, M. Horwath, S. Jacobs, I. Joughin, M. A. King, J. T. M. Lenaerts, J. Li, S. R. M. Ligtenberg, A. Luckman, S. B. Luthcke, M. McMillan, R. Meister, G. Milne, J. Mouginot, A. Muir, J. P. Nicolas, J. Paden, A. J. Payne, H. Pritchard, E. Rignot, H. Rott, L. S. Sohn, H.-G.rensen, T. A. Scambos, B. Scheuchl, E. J. O. Schrama, B. Smith, A. V. Sundal, J. H. van Angelen, W. J. van de Berg, M. R. van den Broeke, D. G. Vaughan, I. Velicogna, J. Wahr, P. L. Whitehouse, D. J. Wingham, D. Yi, D. Young and H. J. Zwally, 2012. A Reconciled Estimate of Ice-Sheet Mass Balance, *Science*, **338**(6111), 1183–1189.

Shreve, R., 1972. Movement of water in glaciers, *J. Glaciol.*, **11**(62), 205–214.

Slater, D. A., P. W. Nienow, T. R. Cowton, D. N. Goldberg and A. J. Sole, 2015. Effect of near-terminus subglacial hydrology on tidewater glacier submarine melt rates, *Geophysical Research Letters*, advance online publication.

Sneed, W. A. and G. S. Hamilton, 2007. Evolution of melt pond volume on the surface of the Greenland Ice Sheet, *Geophys. Res. Lett.*, **34**, L03501.

Sole, A., P. Nienow, I. Bartholomew, D. Mair, T. Cowton, A. Tedstone and M. King, 2013. Winter motion mediates dynamic response of the Greenland ice sheet to warmer summers, *Geophys. Res. Lett.*, **40**, 3940–3944.

Sole, A., P. W. Nienow, I. D. Bartholomew, D. Mair, T. Cowton, M. King and M. Burke, 2010. Seasonal acceleration of the Greenland Ice Sheet in contrasting melt-seasons, *AGU Fall Meeting Abstracts*, A2.

Sole, A., T. Payne, J. Bamber, P. Nienow and W. Krabill, 2008. Testing hypotheses of the cause of peripheral thinning of the Greenland Ice Sheet: is land-terminating ice thinning at anomalously high rates?, *Cryosphere*, **2**, 205–218.

Sole, A. J., D. W. F. Mair, P. W. Nienow, I. D. Bartholomew, M. A. King, M. J. Burke and I. Joughin, 2011. Seasonal speedup of a Greenland marine-terminating outlet glacier forced by surface melt-induced changes in subglacial hydrology, *J. Geophys. Res.*, **116**(F3), 1–11.

Stocker, T., D. Qin, G.-K. Plattner, L. Alexander, S. Allen, N. Bindoff, F.-M. BrÃl'on, J. Church, U. Cubasch, S. Emori, P. Forster, P. Friedlingstein, N. Gillett, J. Gregory, D. Hartmann, E. Jansen, B. Kirtman, R. Knutti, K. Krishna Kumar, P. Lemke, J. Marotzke, V. Masson-Delmotte, G. Meehl, I. Mokhov, S. Piao, V. Ramaswamy, D. Randall, M. Rhein, M. Rojas, C. Sabine, D. Shindell, L. Talley, V. D.G. and S.-P. Xie, 2013. Climate Change 2013: The Physical Science Basis. Contribution of Working Group I to the Fifth Assessment Report of the Intergovernmental Panel on Climate Change, Cambridge University Press, Cambridge, United Kingdom and New York, NY, USA., chap. Technical Summary.

Straneo, F., R. G. Curry, D. A. Sutherland, G. S. Hamilton, C. Cenedese, K. Våge and L. A. Stearns, 2011. Impact of fjord dynamics and glacial runoff on the circulation near Helheim Glacier, *Nature Geosci.*, **4**(5), 322–327.

Straneo, F., P. Heimbach, O. Sergienko, G. S. Hamilton, G. A. Catania, S. Griffies, R. Hallberg, A. Jenkins, I. Joughin, R. J. Motyka, W. T. Pfeffer, S. F. Price, E. Rignot, T. Scambos, M. Truffer and A. Vieli, 2013. Challenges to understanding the dynamic response of greenland's marine terminating glaciers to oceanic and atmospheric forcing, *Bulletin of the American Meteorological Society*, **94**, 1131–1144.

Strozzi, T., A. Luckman, T. Murray, U. Wegmuller and C. L. Werner, 2002. Glacier motion estimation using SAR offset-tracking procedures, *Geoscience and Remote Sensing, IEEE Transactions*, **40**, 2384–2391.

Sugiyama, S., A. Bauder, P. Riesen and M. Funk, 2010. Surface ice motion deviating toward the margins during speed-up events at Gornergletscher, Switzerland, *Journal of Geophysical Research*, **115**, F03010.

Sundal, A. V., A. Shepherd, P. Nienow, E. Hanna, S. Palmer and P. Huybrechts, 2009. Evolution of supra-glacial lakes across the Greenland Ice Sheet, *Remote Sensing of Environment*, **113**(10), 2164–2171.

Sundal, A. V., A. Shepherd, P. Nienow, E. Hanna, S. Palmer and P. Huybrechts, 2011. Melt-induced speed-up of Greenland ice sheet offset by efficient subglacial drainage., *Nature*, **469**(7331), 521–524.

Tedesco, M., X. Fettweis, T. Mote, J. Wahr, P. Alexander, J. E. Box and B. Wouters, 2013a. Evidence and analysis of 2012 Greenland records from spaceborne observations, a regional climate model and reanalysis data, *Cryosphere*, **7**(2), 615–630.

Tedesco, M., I. C. Willis, M. J. Hoffman, A. F. Banwell, P. Alexander and N. S. Arnold, 2013b. Ice dynamic response to two modes of surface lake drainage on the Greenland ice sheet, *Environmental Research Letters*, **8**(3), 034007.

Tedstone, A. J. and N. S. Arnold, 2012. Automated remote sensing of sediment plumes for identification of runoff from the Greenland ice sheet, *J. Glaciol.*, **58**(210), 699–712.

Tedstone, A. J., P. W. Nienow, N. Gourmelen and A. J. Sole, 2014. Greenland ice sheet annual motion insensitive to spatial variations in subglacial hydraulic structure, *Geophysical Research Letters*, **41**(24), 8910–8917.

Tedstone, A. J., P. W. Nienow, A. J. Sole, D. W. Mair, T. R. Cowton, I. D. Bartholomew and M. A. King, 2013. Greenland ice sheet motion insensitive to exceptional meltwater forcing, *Proceedings of the National Academy of Sciences*, **110**(49), 19719–19724.

Telling, J., M. Stibal, A. M. Anesio, M. Tranter, I. Nias, J. Cook, C. Bellas, G. Lis, J. Wadham, A. Sole, P. Nienow and A. Hodson, 2012. Microbial nitrogen fixing on the Greenland ice sheet, *Biogeosciences*, **9**, 2431–2442.

Thomas, R., E. Frederick, W. Krabill, S. Manizade and C. Martin, 2009. Recent changes on Greenland outlet glaciers, *J. Glaciol.*, **55**(189), 147–162.

Vaughan, D., J. C. Comiso, I. Allison, J. Carrasco, G. Kaser, R. Kwok, P. Mote, T. Murray, F. Paul, J. Ren, E. Rignot, O. Solomina, K. Steffen and T. Zhang, 2013. Climate Change 2013: The Physical Science Basis. Contribution of Working Group I to the Fifth Assessment Report of the Intergovernmental Panel on Climate Change, Cambridge University Press, chap. Observations: Cryosphere, 317–382.

van der Veen, C. J., 2007. Fracture propagation as means of rapidly transferring surface meltwater to the base of glaciers, *Geophys. Res. Lett.*, **34**(1), 1–5.

Velicogna, I. and J. Wahr, 2006. Acceleration of Greenland ice mass loss in spring 2004, *Nature*, **443**(7109), 329–31.

Vernon, C. L., J. L. Bamber, J. E. Box, M. R. van den Broeke, X. Fettweis, E. Hanna and P. Huybrechts, 2013. Surface mass balance model intercomparison for the Greenland ice sheet, *The Cryosphere*, **7**(2), 599–614.

van de Wal, R. S. W., W. Boot, M. R. van den Broeke, C. J. P. P. Smeets, C. H. Reijmer, J. J. A. Donker and J. Oerlemans, 2008. Large and rapid melt-induced velocity changes in the ablation zone of the Greenland Ice Sheet, *Science*, **321**(5885), 111–3.

van de Wal, R. S. W., W. Boot, C. J. P. P. Smeets, H. Snellen, M. R. van den Broeke and J. Oerlemans, 2012. Twenty-one years of mass balance observations along the K-transect, West Greenland, *Earth System Science Data*, **4**(1), 31–35.

van de Wal, R. S. W., C. J. P. P. Smeets, W. Boot, M. Stoffelen, R. van Kampen, S. H. Doyle, F. Wilhelms, M. R. van den Broeke, C. H. Reijmer, J. Oerlemans and A. Hubbard, 2015. Self-regulation of ice flow varies across the ablation area in south-west Greenland, *The Cryosphere*, **9**(2), 603–611.

Weertman, J., 1957. On the sliding of glaciers, *J. Glaciol.*, **3**(21), 33–38.

Werder, M. A., I. J. Hewitt, C. G. Schoof and G. E. Flowers, 2013. Modeling channelized and distributed subglacial drainage in two dimensions, *Journal of Geophysical Research: Earth Surface*, **118**(4), 2140–2158.

Willis, I. C., 1995. Intra-annual variations in glacier motion: a review, *Progress in Physical Geography*, **19**(1), 61–106.

Zwally, H. J., W. Abdalati and T. Herring, 2002. Surface melt-induced acceleration of Greenland Ice-Sheet flow, *Science*, **297**, 218–222.

Appendices

Appendix A

Sole *et al.*, 2013 (Geophys. Res. Lett.)

GEOPHYSICAL RESEARCH LETTERS, VOL. 40, 3940–3944, doi:10.1002/grl.50764, 2013

Winter motion mediates dynamic response of the Greenland Ice Sheet to warmer summers

Andrew Sole,[1,2] Peter Nienow,[2] Ian Bartholomew,[2] Douglas Mair,[3] Thomas Cowton,[2] Andrew Tedstone,[2] and Matt A. King[4,5]

Received 30 May 2013; revised 12 July 2013; accepted 15 July 2013; published 6 August 2013.

[1] We present ice velocities from a land-terminating transect extending >115 km into the western Greenland Ice Sheet during three contrasting melt years (2009–2011) to determine whether enhanced melting accelerates dynamic mass loss. We find no significant correlation between surface melt and annual ice flow. There is however a positive correlation between melt and summer ice displacement, but a negative correlation with winter displacement. This response is consistent with hydro-dynamic coupling; enhanced summer ice flow results from longer periods of increasing surface melting and greater duration ice surface to bed connections, while reduced winter motion is explicable by drainage of high basal water pressure regions by larger more extensive subglacial channels. Despite mean interannual surface melt variability of up to 70%, mean annual ice velocities changed by <7.5%. Increased summer melting thereby preconditions the ice-bed interface for reduced winter motion resulting in limited dynamic sensitivity to interannual variations in surface melting. **Citation:** Sole, A., P. Nienow, I. Bartholomew, D. Mair, T. Cowton, A. Tedstone, and M. A. King (2013), Winter motion mediates dynamic response of the Greenland Ice Sheet to warmer summers, *Geophys. Res. Lett.*, *40*, 3940–3944, doi:10.1002/grl.50764.

1. Introduction

[2] Meltwater generated at the surface of the Greenland Ice Sheet (GrIS) drains through the ice into the subglacial hydraulic system and influences rates of basal motion by altering effective pressure at the ice-bed interface, defined as ice overburden minus subglacial water pressure. Lower effective pressure (i.e., higher water pressure) encourages faster sliding by reducing friction between the ice and its bed [*Iken and Bindschadler*, 1986]. Ice velocities in marginal areas of the GrIS are consequently greater in summer than winter [*Bartholomew et al.*, 2010, 2012; *Joughin et al.*, 2008; *Sundal et al.*, 2011; *Van de Wal et al.*, 2008; *Zwally et al.*, 2002], and if the long-term relationship between meltwater production and ice motion is positive [*Zwally et al.*, 2002], this mechanism could increase significantly GrIS mass loss under climate warming [*Parizek and Alley*, 2004].

[3] In response to sustained inputs of surface meltwater, however, theory and data suggest that subglacial drainage systems develop from hydraulically inefficient structures into efficient channels, which operate at lower pressures for a given discharge [*Kamb*, 1987; *Röthlisberger*, 1972; *Schoof*, 2010, *Cowton et al.*, 2013], thereby reducing the lubrication effect of further meltwater inputs. This reasoning can explain why GrIS ice velocities in late summer are lower than those in early summer [*Bartholomew et al.*, 2010; *Sundal et al.*, 2011]. Recent theoretical [*Pimentel and Flowers*, 2011; *Schoof*, 2010], remote sensing, and field [*Sundal et al.*, 2011; *Van de Wal et al.*, 2008] studies have proposed that marginal ice will flow *more slowly* in higher melt years since subglacial channelization will occur more quickly in response to increased inputs of meltwater, thereby reducing the dynamic sensitivity of the GrIS to climate warming. However, these studies have been limited to areas close to the ice sheet margin [*Sundal et al.*, 2011] or utilize measurements which cannot resolve the seasonal behavior that determines the observed interannual velocity variations [*Van de Wal et al.*, 2008]. The dynamic behavior of the whole ablation zone in different melt seasons and the resulting impact on annual ice motion therefore remain uncertain.

2. Data and Methods

[4] We present data between May 2009 and May 2012 from seven sites along a land-terminating transect in west Greenland at ~67°N that extends 115 km from the ice margin to 1715 m elevation (Figure 1). At each site, we measured continuous site position and air temperature and annual ablation (see supporting information for details). Meltwater discharge was recorded from the Leverett Glacier hydrological catchment, incorporating our lowest three sites [*Bartholomew et al.*, 2011b] (Figure 1). In the following analysis, mean winter velocities (MWV) for each site represent its average displacement over the 2009–2010, 2010–2011, and 2011–2012 winters (1 September–30 April).

3. Results and Discussion

[5] Mean summer (May–August) temperatures measured at our sites in 2010 and 2011 were 2.3°C and 1.1°C warmer, respectively, than in 2009. Catchment runoff was 92% and 19% greater in 2010 and 2011, respectively, than 2009, while mean surface melt increased by 70% and 34%, respectively (Figure 2b). National Centers for Environmental Prediction/National Center for Atmospheric Research reanalysis data show that May–August 1000 mb temperature anomalies in

Additional supporting information may be found in the online version of this article.

[1]Department of Geography, University of Sheffield, Sheffield, UK.
[2]School of GeoSciences, University of Edinburgh, Edinburgh, UK.
[3]School of Geosciences, University of Aberdeen, Aberdeen, UK.
[4]School of Civil Engineering and Geosciences, Newcastle University, Newcastle upon Tyne, NE1 7RU, United Kingdom.
[5]School of Geography and Environmental Studies, University of Tasmania, Tasmania, Australia.

Corresponding author: A. Sole, Department of Geography, University of Sheffield, Winter Street, Sheffield S10 2TN, UK. (A.Sole@sheffield.ac.uk)

0094-8276/13/10.1002/grl.50764

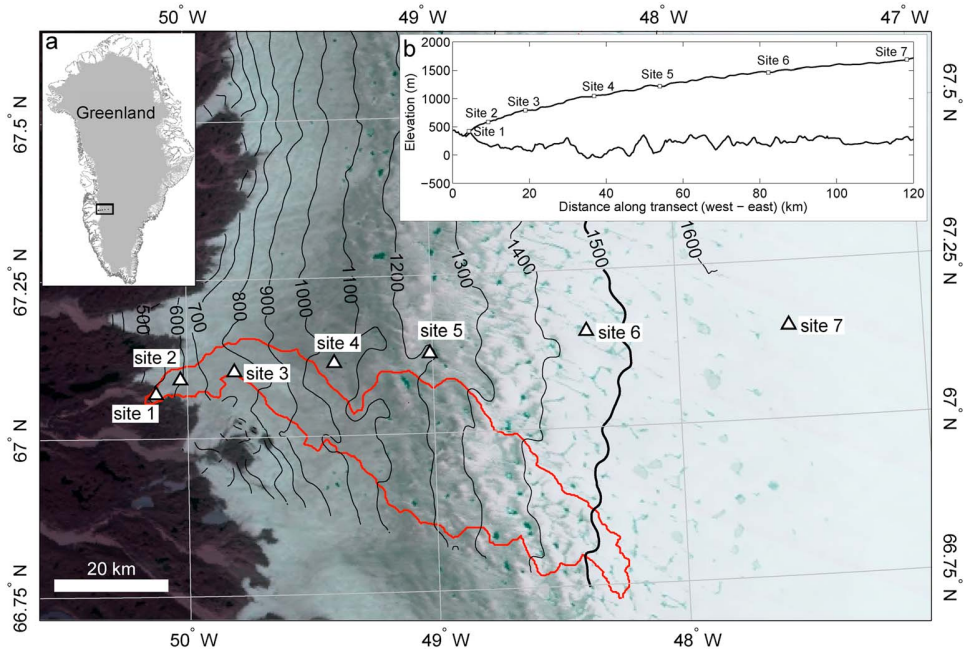

Figure 1. (a) Location of the study region on the western margin of the GrIS. (b) Ice surface and bed elevation along our transect as measured by IceBridge ATM (ILATM2) and MCoRDS (IRMCR2), respectively, in 2010 and 2011 [*Allen*, 2011]; main panel, location of GPS sites. Contours (100 m intervals) from a digital elevation model are derived from InSAR [*Palmer et al.*, 2011]. The bold contour (1500 m) represents the approximate equilibrium line altitude [*van de Wal et al.*, 2008]. The Leverett Glacier hydrological catchment is shown in red [*Bartholomew et al.*, 2011b].

west Greenland near to Kangerlussuaq (approximately 25 km west of site 1) were between −0.3 and +0.3°C in 2009 and 2011, and +2.4°C in 2010 (relative to the 1981–2010 mean). These contrasting melt characteristics provide an opportunity to evaluate the effect that increased summer temperatures, commensurate with predictions for climate warming over the next century [*Meehl et al.*, 2007], will have on GrIS ice motion.

[6] Along our transect, we measured daily summer velocities up to 300% above MWV. In each year, ice accelerated first near the ice sheet margin and then at progressively higher elevations (Figures 2c–2i) [*Bartholomew et al.*, 2010, 2011a; *Sundal et al.*, 2011]. We also observed end-of-melt-season slow-downs below MWV at sites 2 and 4 in 2009, 1–7 in 2010 and 1–6 in 2011 when daily velocities were up to 44% below MWV. While such minima have been observed in this region previously [*Bartholomew et al.*, 2010] and elsewhere in Greenland [*Colgan et al.*, 2011, 2012; *Joughin et al.*, 2008; *Zwally et al.*, 2002], their effect on interannual ice displacement variations has not been quantified.

[7] Mean annual ice velocity for sites 2–7 was 105.8 my^{-1} in 2009, 104.7 my^{-1} in 2010 (−1.0% cf. 2009), and 97.8 my^{-1} in 2011 (−7.5% cf. 2009) (Table S2). Site 1 is not included in this comparison because power failure in 2011 disrupted data collection. We found no statistically significant relationship ($r = 0.1$, $p = 0.9$) between annual ice displacement and surface melt at individual sites (Figure S1). In order to explain both the limited interannual ice flow variability and lack of a statistically significant relationship between annual ice flow and surface melt, we divided each year into "seasons." Summer is defined as 1 May to 31 August subdivided into early and late summer on 1 July; winter as 1 September to 30 April; and annual as 1 May to 30 April.

[8] Our summer data describe a significant positive correlation between normalized ice motion (see supporting information for details of normalization method) and surface melt ($r = 0.79$, $p < 0.05$) with most sites flowing faster in the warmer summers (Figure 3b). While additional sources of water, such as rainfall and geothermal and basal melting also contribute to the basal hydraulic system, they are typically small relative to surface melting, so we do not incorporate them into our analysis. There was however an exceptional rainfall event in 2011 which we discuss later. Each summer, the lowest sites showed the greatest speed-up above MWV with the effect attenuating inland (Figures 2c–2i, 3a and 3f). Sites 1–3, below 1000 m, recorded mean summer velocities 45.9 to 65.7% above MWV, while sites 5–7, above 1200 m, displayed mean increases of <34% (Figure 3f). The summer speed-up at our lowest sites started 20 and 35 days earlier in 2010 (2 May) than 2009 and 2011, respectively (Figures 2c–2i). Comparisons between the Leverett Glacier hydrographs and ice velocities at sites 1–3 (Figures 2b–2e) reveal that ice velocities were greatest while catchment discharge was rising, between 2 June and 17 July (45 days) in 2009, 8 May and 1 July (54 days) in 2010, and 9 June and 15 July (36 days) in 2011, and became subdued once discharge stabilized or declined. While meltwater inputs are consistently rising, our data suggest that steady state hydrological conditions do not apply, even once the subglacial drainage system has become channelized [*Bartholomew et* al., 2012, *Röthlisberger*, 1972]. Instead, enhanced ice velocities are sustained by constantly challenging the drainage system to accommodate larger volumes of water [*Bartholomaus et al.*, 2008; *Bartholomew et al.*, 2012].

[9] In summer 2009, site 7 did not speed-up appreciably above MWV (1.6%) and delimited approximately the

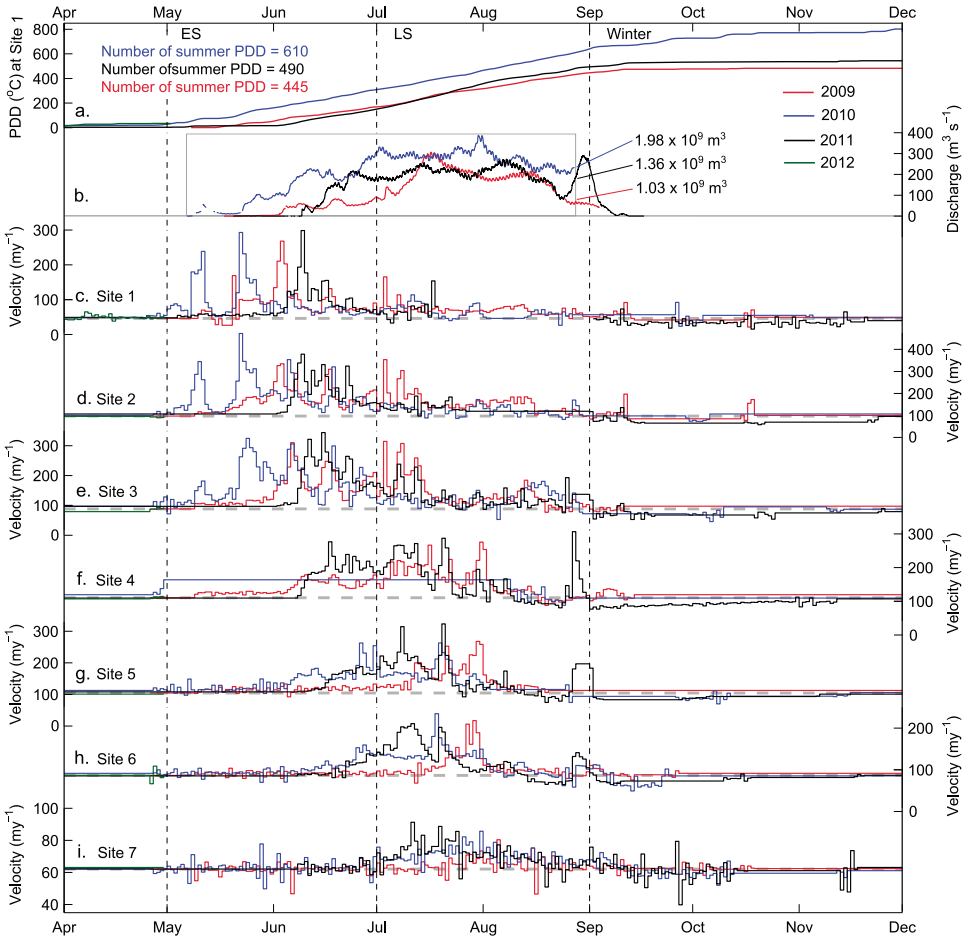

Figure 2. (a) Cumulative PDD at site 1 showing summer PDD sums (PDD calculated as described in the supporting information). (b) Discharge hydrograph for Leverett Glacier catchment with the cumulative discharge between 7 May and 27 August (delimited by the hollow grey box) for each year. (c–i) 24 h horizontal velocity at sites 1–7 for 2009, 2010, 2011, and the early part of 2012. Mean 2009–2010, 2010–2011, and 2011–2012 winter velocities for each site (MWV = grey dashed line) are also shown.

inland extent of hydrologically forced velocity variations [*Bartholomew et al.*, 2011a]. In 2010 and 2011, when the May–August mean temperatures at site 7 were 2.9°C and 2.7°C warmer than in 2009, increases in summer motion relative to MWV were 7.2% and 6.9%, respectively, indicating that ice flow variations propagate further into the ice sheet in warmer years (Figure 3a).

[10] The summer flow enhancement does not however typically result in increased annual ice displacement (Figure 3d) because warmer summers are generally followed by reduced winter ice flow. This is demonstrated by a significant negative correlation ($r = -0.55$, $p < 0.05$; Figure 3c) between normalized winter ice velocity and late summer melt (as characterized by Positive Degree Days (PDD)). Ice velocity typically reaches a minimum in early winter before recovering to within a few percent of MWV by the start of the next melt season (e.g., Figure 2f, 2011). This pattern of ice motion can also be explained by hydrodynamic coupling. The reduced sensitivity of ice flow to variations in meltwater input toward the end of each melt season, shown by our data and observed previously [e.g., *Bartholomew et al.*, 2011a], indicates that efficient channels extended beneath much of our transect during the late summer of each year. Such channels are however likely to be spatially limited to areas downstream from surface meltwater sources, with inefficient drainage elsewhere [*Hewitt*, 2011]. Once surface melting ceases at the end of the summer, the subglacial channels will operate at low pressure. We postulate that the resulting hydraulic gradient will drain water from adjacent areas of higher water pressure to the low pressure subglacial channels as observed over diurnal timescales at Alpine glaciers [*Hubbard et al.*, 1995], leading to a net reduction in basal water pressure and consequent decline in ice velocity [*Hewitt*, 2011]. By the end of each winter, measured ice velocities return to within a few percent of MWV at all our sites, presumably due to gradual repressurization of the subglacial hydraulic system from basal melting and channel creep closure [*Zwally et al.*, 2002]. We suggest that enhanced surface melting associated with warmer conditions in late summer is able to sustain larger and more widespread low-pressure subglacial channels. This in turn promotes more extensive and prolonged drainage of high pressure water from adjacent regions resulting in a greater drop in net basal water pressure and reduced displacement over the subsequent winter (Figure 3c).

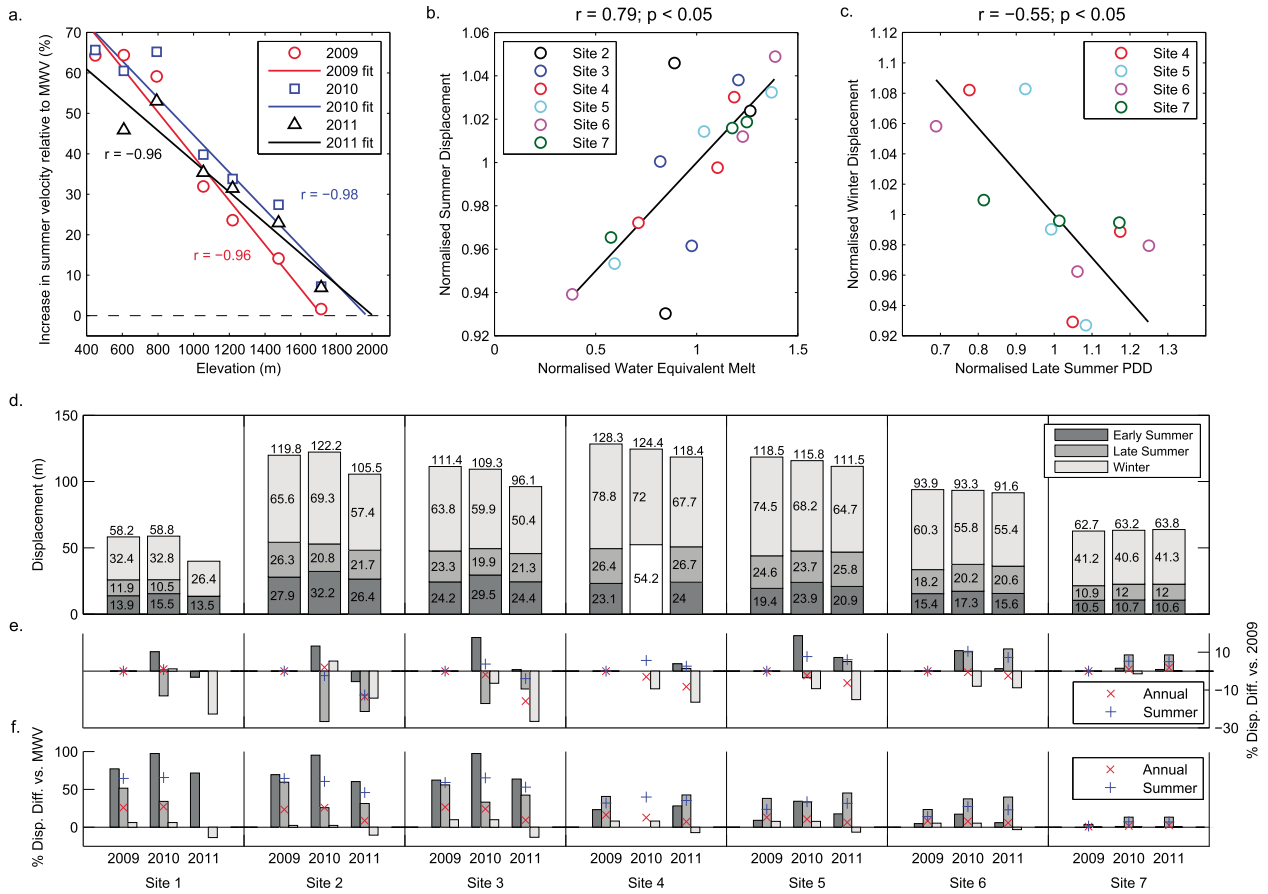

Figure 3. (a) Increase in summer ice velocity relative to MWV for all sites in 2009, 2010, and sites 2–7 in 2011. The extrapolated intercepts of zero percent (i.e., no difference with respect to MWV) and the respective best-fit lines represent estimates of the inland extent of summer ice flow variations. (b) Relationship between normalized water equivalent melt and normalized summer ice displacement. (c) Relationship between normalized late summer PDD and normalized winter ice displacement. Not all sites could be included in these statistical analyses due to GPS power failure in 2011 at site 1 and missing temperature data at sites 2 and 3. (d) Displacement at each site in 2009, 2010, and 2011 for early summer (dark grey), late summer (medium grey), and winter (light grey). (e) Difference in early summer, late summer, summer, winter, and annual ice displacement between 2009, 2010, and 2011 as a percentage of the 2009 value (same color scheme as above). (f) Difference between measured early summer, late summer, summer, winter, and annual ice displacement in 2009, 2010, and 2011 as a percentage of equivalent MWV (same color scheme as above). Missing late summer and annual data at site 1 in 2011, and early and late summer data for site 4 in 2010 (shown by the white bar) are due to several power failures as described in supporting information. Data contributing to this figure are included in Tables S1, S2, and S3.

[11] The net response is a general pattern of *faster* summer but *slower* winter ice flow in warmer years relative to cooler years (Figures 3d and 3e) with the opposing effects of *enhanced* summer and *reduced* winter velocity in warmer years acting to limit the effect of hydrodynamic forcing on annual ice motion. That ice displacements were further reduced in 2011, despite less extreme surface melt rates than in 2010 can be explained by the timing of runoff variations, and specifically a late summer event when annual discharge reached its maximum (Figure 2b). Sites 3–6 display a sharp increase in ice flow rate at the end of August, concurrent with the increase in runoff, indicating that the effect on the subglacial drainage system was widespread and not limited to the Leverett Glacier catchment. This unseasonal late summer runoff event was driven by exceptional rainfall (cumulative precipitation of 29.4 mm from 23 August to 2 September measured at the Danish Meteorological Institute meteorological station at Kangerlussuaq airport http://www.dmi.dk/dmi/tr13-11.zip) which is why it is not evident in the PDD record (Figure 2a). The rainfall-derived runoff would have reopened or enlarged existing subglacial channels leading to slower overwinter repressurization of the subglacial drainage system (e.g., Figure 2f) resulting in 2011 winter velocities across all sites that were on average 12.5% lower than in 2009. Interannual variations in winter velocity are thus as important as those in summer for determining annual ice displacement, and the prescription of a mean winter velocity based on combining several years' data precludes accurate comparison of ice displacement from one year to the next.

4. Conclusions

[12] We find no statistically significant correlation between normalized surface melt and annual ice flow. Splitting the data into "summer" and "winter" periods reveals that, while in warmer years, the ice generally flows faster in summer, it

also moves slower the following winter. Our results do not therefore support the hypothesis that increased surface melting will reduce summer ice flow due to earlier channelization of the subglacial drainage system [*Pimentel and Flowers*, 2011; *Sundal et al*., 2011; *Van de Wal et al*., 2008]. Instead, our data suggest that summer velocities will *increase* due to both longer melt-seasons and more prevalent unsteady conditions in subglacial channels. This annual pattern of ice motion is consistent with coupling to glacier hydrology; enhanced summer ice motion is caused by longer periods of consistently increasing surface melting and greater duration ice surface to bed connections, while reduced winter motion is induced via drainage of high basal water pressure regions by larger and more extensive subglacial channels.

[13] The net result is that despite interannual variations in mean surface melt of up to 70%, mean annual ice velocities changed by less than 7.5%. Increased summer melting may therefore precondition the ice-bed interface for reduced winter velocity limiting the ice sheet's dynamic sensitivity to interannual variations in surface temperature and melt. This self-regulating behavior can explain previous, apparently contradictory observations which show that (a) summer velocity enhancement scales with summer temperatures [*Bartholomew et al*., 2011a; *Zwally et al*., 2002]; while (b) over longer time periods, ice velocities decrease slightly, despite generally increasing surface melt [*Van de Wal et al*., 2008].

[14] **Acknowledgments.** We thank the following for financial support: UK Natural Environment Research Council (NERC, through grants to P.N./D.M., studentships to I.B./A.T.), Edinburgh University Moss Scholarships (I.B./T.C/A.T.), and a Research Councils UK Academic Fellowship and an Australian Research Council Future Fellowship (project number FT110100207) (M.A.K.). GPS equipment and training were provided by the NERC Geophysical Equipment Facility.

[15] The Editor thanks an anonymous reviewer and Stephen Price for their assistance in evaluating this paper.

References

Allen C. (2011), IceBridge MCoRDS L2 Ice Thickness 2010 and 2011, Boulder, Colorado USA: National Snow and Ice Data Center. Digital media.

Bartholomaus, T. C., R. S. Anderson, and S. P. Anderson (2008), Response of glacier basal motion to transient water storage, *Nat. Geosci.*, *1*(1), 33–37, doi:10.1038/ngeo.2007.52.

Bartholomew, I., P. Nienow, D. Mair, A. Hubbard, M. A. King, and A. Sole (2010), Seasonal evolution of subglacial drainage and acceleration in a Greenland outlet glacier, *Nat. Geosci.*, *3*, 408–411, doi:10.1038/NGEO863.

Bartholomew, I., P. Nienow, A. Sole, D. Mair, T. Cowton, M. A. King, and S. Palmer (2011a), Seasonal variations in Greenland Ice Sheet motion: Inland extent and behaviour at higher elevations, *Earth Planet. Sci. Lett.*, *307*, 271–278, doi:10.1016/j.epsl.2011.04.014.

Bartholomew I., P. Nienow, A. Sole, D. Mair, T. Cowton, S. Palmer, and J. Wadham (2011b), Supraglacial forcing of subglacial hydrology in the ablation zone of the Greenland Ice Sheet, *Geophys. Res. Lett.*, *38*, L08502, doi:10.1029/2011GL047063.

Bartholomew, I., P. Nienow, A. Sole, D. Mair, T. Cowton, and M. A. King (2012), Short-term variability in Greenland Ice Sheet motion forced by time-varying meltwater drainage: Implications for the relationship between subglacial drainage system behavior and ice velocity, *J. Geophys. Res.*, *117*, F03002, doi:10.1029/2011JF002220.

Colgan, W., H. Rajaram, R. Anderson, K. Steffen, T. Phillips, I. Joughin, and W. Abdalati (2011), The annual glaciohydrology cycle in the ablation zone of the Greenland ice sheet: Part 1. Hydrology model, *J. Glaciol.*, *57*(204), 697–709.

Colgan, W., H. Rajaram, R. Anderson, K. Steffen, T. Phillips, I. Joughin, and W. Abdalati (2012), The annual glaciohydrology cycle in the ablation zone of the Greenland ice sheet: Part 2. Observed and modeled ice flow, *J. Glaciol.*, *58*(207), 51–64, doi:10.3189/2012JoG11J081.

Hewitt, I. (2011), Modelling distributed and channelized subglacial drainage: The spacing of channels, *J. Glaciol.*, *57*(202), 302–314.

Hubbard, B. P., M. Sharp, I. C. Willis, M. K. Nielsen, and C. C. Smart (1995), Borehole water-level variations and the structure of the subglacial hydrological system of Haut Glacier d' Arolla, Valais, Switzerland, *J. Glaciol.*, *41*(139), 572–583.

Iken, A., and R. Bindschadler (1986), Combined measurements of subglacial water pressure and surface velocity of Findelengletscher, Switzerland: Conclusions about drainage system and sliding mechanism, *J. Glaciol.*, *32*(110), 101–119.

Joughin, I., S. Das, M. A. King, B. Smith, I. Howat, and T. Moon (2008), Seasonal speedup along the Western Flank of the Greenland Ice Sheet, *Science*, *320*(5877), 781–783, doi:10.1126/science.1153288.

Kamb, B. (1987), Glacier surge mechanism based on linked cavity configuration of the basal water conduit system, *J. Geophys. Res.*, *92*, 9083–9100.

Meehl G. A., et al. (2007), In climate change 2007: The physical science basis. Contribution of Working Group I to the Fourth Assessment Report of the Intergovernmental Panel on Climate Change (eds Solomon, S. et al.) 747–846, Cambridge University Press, Cambridge.

Palmer, S., A. Shepherd, P. Nienow, and I. Joughin (2011), Seasonal speedup of the Greenland Ice Sheet linked to routing of surface water, *Earth Planet. Sci. Lett.*, *302*, 423–428, doi:10.1016/j.epsl.2010.12.037.

Parizek, B. R., and R. B. Alley (2004), Implications of increased Greenland surface melt under global warming scenarios: Ice-sheet simulations, *Quat. Sci. Rev.*, *23*, 1013–1027.

Pimentel, S., and G. E. Flowers (2011), A numerical study of hydrologically driven glacier dynamics and subglacial flooding, *Proc. R. Soc. London, Ser. A*, *467*, 537–558, doi:10.1098/rspa.2010.0211.

Röthlisberger, H. (1972), Water pressure in intra- and subglacial channels, *J. Glaciol.*, *11*, 177–203.

Schoof, C. (2010), Ice-sheet acceleration driven by melt supply variability, *Nature*, *468*, 803–806, doi:10.1038/nature09618.

Sundal, A. V., A. Shepherd, P. Nienow, E. Hanna, S. Palmer, and P. Huybrechts (2011), Melt-induced speed-up of Greenland Ice Sheet offset by efficient subglacial drainage, *Nature*, *469*(7331), 521–524, doi:10.1038/nature09740.

Van de Wal, R. S. W., W. Boot, M. R. Van den Broeke, C. Smeets, C. H. Reijmer, J. J. A. Donker, and J. Oerlemans (2008), Large and rapid melt-induced velocity changes in the ablation zone of the Greenland Ice Sheet, *Science*, *321*(5885), 111–113, doi:10.1126/science.1158540.

Zwally, H. J., W. Abdalati, T. Herring, K. Larson, J. Saba, and K. Steffen (2002), Surface melt-induced acceleration of Greenland ice-sheet flow, *Science*, *297*(5579), 218–222.

Appendix B

Tedstone *et al.*, 2013 (Proc. Nat. Acad. Sci. USA)

Greenland ice sheet motion insensitive to exceptional meltwater forcing

Andrew J. Tedstone[a,1], Peter W. Nienow[a], Andrew J. Sole[a,b], Douglas W. F. Mair[c], Thomas R. Cowton[a,b], Ian D. Bartholomew[a], and Matt A. King[d,e]

[a]School of Geosciences, University of Edinburgh, Edinburgh EH8 9XP, Scotland; [b]Department of Geography, University of Sheffield, Sheffield S10 2TN, United Kingdom; [c]School of Geosciences, University of Aberdeen, Aberdeen AB24 3UE, Scotland; [d]School of Geography and Environmental Studies, University of Tasmania, Hobart, TAS 7001, Australia; and [e]School of Civil Engineering and Geosciences, Newcastle University, Newcastle upon Tyne NE1 7RU, United Kingdom

Edited by Mark H. Thiemens, University of California at San Diego, La Jolla, CA, and approved October 23, 2013 (received for review August 24, 2013)

Changes to the dynamics of the Greenland ice sheet can be forced by various mechanisms including surface-melt–induced ice acceleration and oceanic forcing of marine-terminating glaciers. We use observations of ice motion to examine the surface melt–induced dynamic response of a land-terminating outlet glacier in southwest Greenland to the exceptional melting observed in 2012. During summer, meltwater generated on the Greenland ice sheet surface accesses the ice sheet bed, lubricating basal motion and resulting in periods of faster ice flow. However, the net impact of varying meltwater volumes upon seasonal and annual ice flow, and thus sea level rise, remains unclear. We show that two extreme melt events (98.6% of the Greenland ice sheet surface experienced melting on July 12, the most significant melt event since 1889, and 79.2% on July 29) and summer ice sheet runoff ∼3.9σ above the 1958–2011 mean resulted in enhanced summer ice motion relative to the average melt year of 2009. However, despite record summer melting, subsequent reduced winter ice motion resulted in 6% less net annual ice motion in 2012 than in 2009. Our findings suggest that surface melt–induced acceleration of land-terminating regions of the ice sheet will remain insignificant even under extreme melting scenarios.

ice sheet dynamics | ice sheet hydrology | ice sheet melt | global positioning systems

Surface melting and runoff from the Greenland ice sheet (GrIS) has increased during the last 30 y (1–3) coincident with Northern Hemisphere warming (4, 5) resulting in unprecedented melt extents (6) and widespread dynamic thinning, which has penetrated up to 120 km into the ice sheet interior (7). One potential dynamic thinning mechanism is surface melt–induced acceleration of ice sheet motion (termed hydrodynamic coupling) during summer (8–11). Observations of GrIS ice motion during the summer show considerable variability over a range of timescales (12). Rapid variations in meltwater input from the ice sheet surface to the glacier bed result in periods when the subglacial drainage system is more highly pressurized, leading to an increase in basal sliding (13, 14). This mechanism explains both multiday increases in ice motion at the beginning of the melt season, analogous to the "spring events" observed at alpine glaciers (15), and increases in velocity at other times when meltwater is delivered to the bed at a rate faster than the subglacial drainage system can expand to accommodate.

However, as the drainage-system capacity gradually expands in response to increased melting, the subglacial water pressure falls and higher velocities can therefore only be caused by much larger meltwater pulses than earlier in the melt season (16). This feedback mechanism has been invoked previously to suggest that the ice sheet could flow more slowly in a warmer year, but observations have either been limited to close to the ice sheet margin (17) or have been unable to resolve the seasonal behavior responsible for the velocity variations (18). A recent study, which incorporated seasonal ice flow and melt observations extending beyond the equilibrium line, showed that summer velocity enhancement is negated by subsequent reductions in winter flow rates (19), but the bounding conditions of the study have since been exceeded by the exceptional melting observed in 2012 (20). Moreover, the current paucity of field observations is a significant impediment to modeling the impact of coupled hydrodynamics on net ice-mass loss (21).

The recent trend of warmer summers in Greenland is related to an increase in the frequency of anticyclonic conditions (22). Persistent anticyclonic conditions during summer 2012 resulted in extreme runoff volumes from the Greenland ice sheet (23), compounded by unprecedented melt extent in July 2012 associated with low-level liquid clouds (24), which led to flood damage such as the destruction of the Watson River bridge in Kangerlussuaq, west Greenland. These conditions resulted in a year during which ice sheet–wide runoff set a new record at ∼3.9σ above the 1958–2011 mean (23). National Centers for Environmental Prediction/National Center for Atmospheric Research reanalysis 1,000-mb temperature anomalies above Kangerlussuaq (25 km west of our site 1) relative to the 1981–2010 mean were +2.2 °C during May–August 2012, compared with ±0.3 °C during May–August 2009. The 2012 melt season is therefore a surrogate for potential future melting and forms a natural test for quantifying the effect of extreme meltwater supply on ice motion compared with the "average" melt year of 2009.

We used global positioning system (GPS) records to observe ice motion during 2009 and 2012 at seven sites along a transect on a land-terminating margin of the GrIS, at ∼67°N (Fig. 1). Air temperature and annual ablation were also measured at each site. The lowest three sites on the transect are located within

Significance

During summer, meltwater generated on the Greenland ice sheet surface accesses the ice sheet bed, lubricating basal motion and resulting in periods of faster ice flow. However, the net impact of varying meltwater volumes upon seasonal and annual ice flow, and thus sea level rise, remains unclear. In 2012, despite record ice sheet runoff, including two extreme melt events, ice at a land-terminating margin flowed more slowly than in the average melt year of 2009, due principally to slower winter flow following faster summer flow. Our findings suggest that annual motion of land-terminating margins of the ice sheet, and thus the projected dynamic contribution of these margins to sea level rise, is insensitive to melt volumes commensurate with temperature projections for 2100.

Author contributions: P.W.N. and D.W.F.M. designed research; A.J.T., P.W.N., A.J.S., D.W.F.M., T.R.C., and I.D.B. performed research; A.J.T., A.J.S., I.D.B., and M.A.K. contributed new reagents/analytic tools; A.J.T., A.J.S., T.R.C., I.D.B., and M.A.K. analyzed data; and A.J.T. and P.W.N. wrote the paper.

The authors declare no conflict of interest.

This article is a PNAS Direct Submission.

[1]To whom correspondence should be addressed. E-mail: a.j.tedstone@ed.ac.uk.

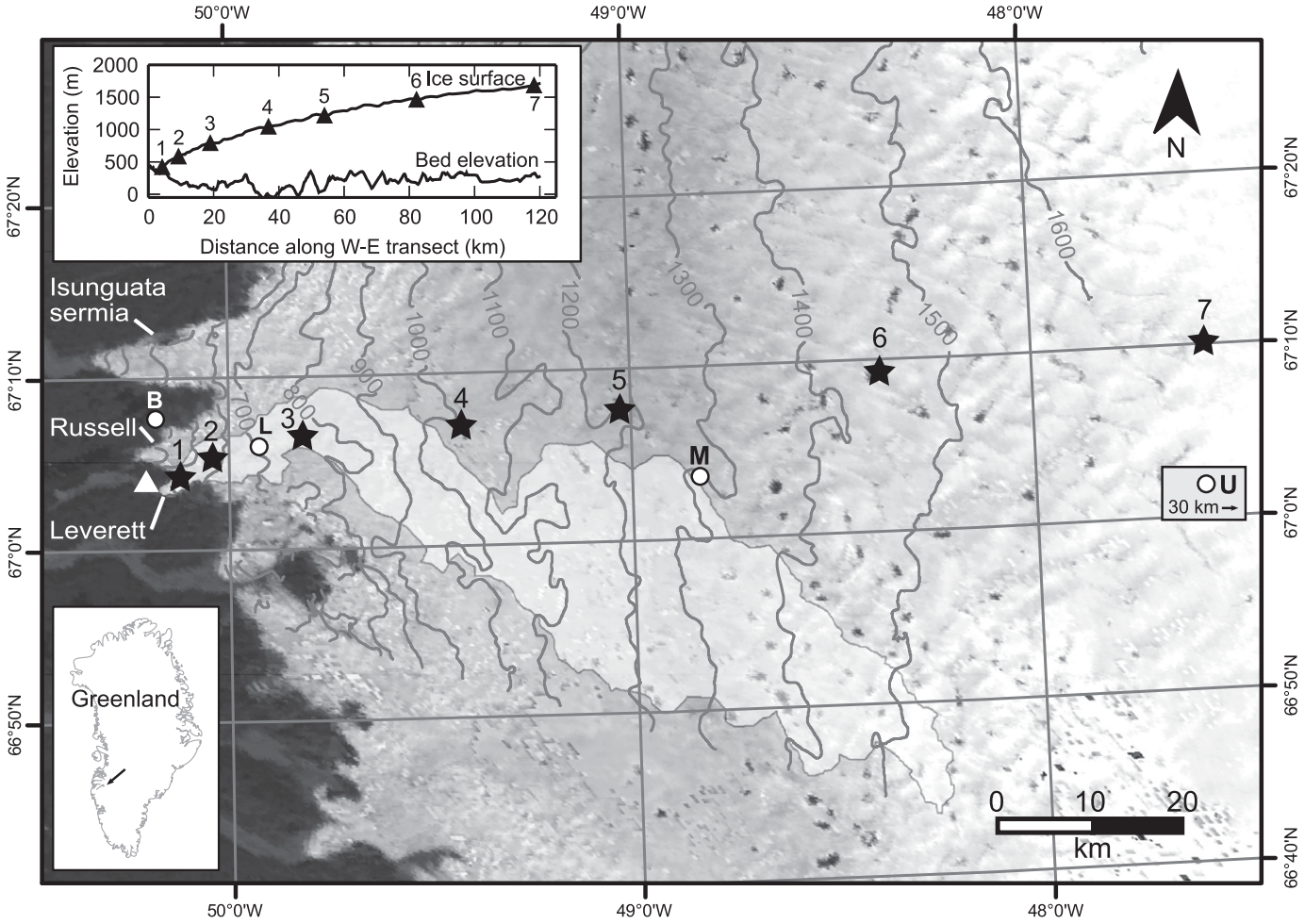

Fig. 1. Location of the transect on the western margin of the GrIS. Stars indicate sites where ice motion, temperature, and seasonal melting were measured. The triangle indicates where proglacial discharge was measured and the GPS base station located. Circles indicate locations of 'KAN' PROMICE/GAP weather stations along the K transect. Contours (in meters) are from a digital elevation model (DEM) of the ice sheet surface produced from interferometric synthetic aperture radar (InSAR) (29). The inferred hydrological catchment of Leverett Glacier, delineated in light gray, was calculated from the ice sheet surface DEM. *Inset* shows surface and bed elevation along our transect as measured by IceBridge ATM (ILATM2) and MCoRDS (IRMCR2) in 2010 and 2011, respectively (30).

Leverett Glacier's inferred hydrological catchment, from which we measured bulk runoff (25). Transect dynamics during 2012 (Fig. 2) had similar characteristics to previous years (10, 19): initiation of meltwater-induced acceleration during multiday "spring" speed-up events, followed by shorter duration spikes in velocity superimposed on gradually declining background seasonal velocities, which fell below premelt season velocities by the end of summer.

Here we concentrate on two specific aspects of hydrodynamic coupling during 2012 to give insight into the likely dynamic behavior of the ice sheet in a warming climate. We examine (*i*) the ice flow response to the extreme melt events of July 12 and July 29 (20), and (*ii*) the impact of unprecedented melt volumes (23) on total annual ice motion.

Enhanced ice flow lasting ∼2 d was associated with both extreme melt events (shaded periods in Figs. 2–4), with several characteristics common to both events. First, peak velocities occurred in advance of satellite-observed peak ice sheet melt extent (20), while proglacial discharge was still rising—2 d in advance of July 12, and 1 d in advance of July 29. Second, velocities increased at every site along the transect during the enhanced ice flow period. Third, at the majority of sites, velocities were lower after the enhanced ice flow period than before it (Fig. 2).

Before the July 12 melt event, sites up to 1,482 m above sea level (site 6) experienced positive air temperatures every day from June 10 (Fig. 2). Peak velocities during July 9–10 were coincident with a 2.3 °C increase in mean air temperature at our transect sites and a 73% increase in mean wind speed at Programme for Monitoring the Greenland Ice Sheet (PROMICE)/Greenland Analogue Project (GAP) K-transect sites (Fig. 1) compared with the previous 8 d. The mean daily transect velocity during July 9–10 was 61% greater than during the preceding 8 d, with sites 3 and 4 (794 and 1,061 m a.s.l, respectively) experiencing the highest peak velocities of 103 and 77% greater, respectively, than the previous 8 d (Fig. 3). By July 12, ice velocities were falling despite peaks in both ice sheet–wide melting and proglacial river discharge (∼800 $m^3\ s^{-1}$; in excess of double that observed both at the start of the melt event and in previous years; ref. 19). Sites 1 and 2 returned to daily velocities within 10 m y^{-1} of July 1–8 mean velocities; and sites 3, 4, and 6 decreased to velocities at least 30 m y^{-1} slower than July 1–8 mean velocities.

In contrast to the July 12 melt event, a period of falling air temperatures in the previous 15 d leading up to the July 29 melt event (as low as −7 °C at site 6) resulted in falling discharge to a minimum of 240 $m^3\ s^{-1}$ on July 25, the lowest since June 18 (Fig. 2). During July 27–28, the mean transect air temperature rose by 4.4 °C compared with the previous 8 d, with associated, although lagged, increases in discharge and velocity (Fig. 4).

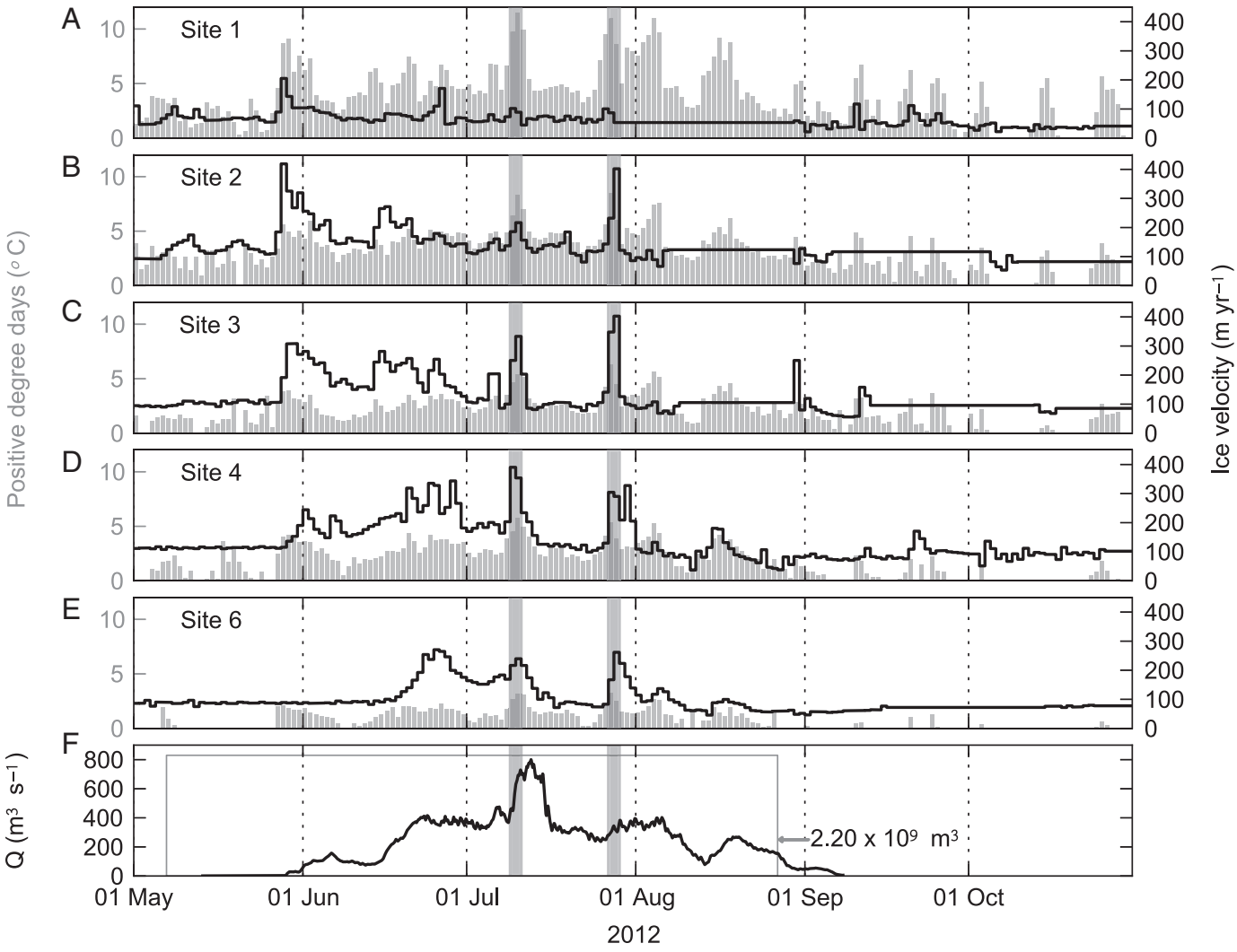

Fig. 2. Transect observations during 2012. (*A–E*). Daily (24 h) along-track ice velocities (stepped black lines) and positive degree days (gray bars) for each transect site at which daily measurements were made. (*F*) Discharge hydrograph for Leverett Glacier (in cubic meters per second), with cumulative discharge between May 7 and August 27 (marked by gray box). The associated catchment is shown on Fig. 1. (*A–F*) Gray shading defines peak velocity response to July 12 and July 29 melt events (see text).

Mean transect ice velocity on July 27–28 was 116% greater than during the preceding 8 d. At sites 2, 3, and 4, the velocity perturbation was short-lived, lasting ∼2 d before an abrupt drop in velocities that returned to within 20 m y^{-1} of preevent velocities. Site 6 slowed down more gradually after the July 28 peak. Unlike the July 12 melt event, river discharge remained close to its event peak of ∼400 m^3 s^{-1} for 8 d following the July 29 melt event (Fig. 2*F*).

Increased ice velocities in the lead up to the July 12 and 29 melt events were clearly caused by a rapid increase in the rate of meltwater supply to the ice sheet bed forced by changes in the rate of surface melting. Although antecedent melt conditions and the absolute volumes of meltwater associated with each event were different, the nature and style of meltwater forcing, overwhelming the capacity of the hydrological system and leading to ice acceleration, were very similar, replicating responses observed previously (12, 16).

We estimated the potential contribution of each melt event to summer ice displacement by comparison with estimates of the projected ice displacement that would have occurred in the absence of the melt events. We used mean ice velocities at each site during the 8 d preceding each 2-d period of enhanced ice flow to estimate what the total displacement would likely have been through the 2-d enhanced ice flow period and the following 8 d in the absence of the enhanced ice flow period (see *Materials and Methods* for more information). Observations during the corresponding time periods are shown in Figs. 3 and 4. On average, the July 12 melt event forced only 7% more ice displacement over the 10-d period, and the July 29 melt event, which was preceded by lower melt rates than the July 12 event, forced 34% more ice displacement over the equivalent 10-d period. These findings reinforce the importance of antecedent melt rates (as opposed to simply meltwater volume) and thus drainage system efficiency in controlling the short-term dynamic response to variations in meltwater supply (26).

The second exceptional characteristic of 2012 was ice sheet–wide runoff of ∼3.9σ above the 1958–2011 mean (23). For comparison, Fig. 5 shows observations collected along our transect in the average melt year of 2009. Exceptional melting during 2012 resulted in a mean of 117% more ablation relative to 2009 along our transect (Fig. 5*A*) with bulk runoff from the local ice sheet margin (2.20×10^9 m^3) 113% greater than 2009 (19). Summer velocities (Fig. 5*B*) at all but the lowest two sites were also higher in 2012 than in 2009. However, winter velocities at all sites were on average 11% lower in 2012 than in 2009, resulting in 6% less net annual ice motion along the

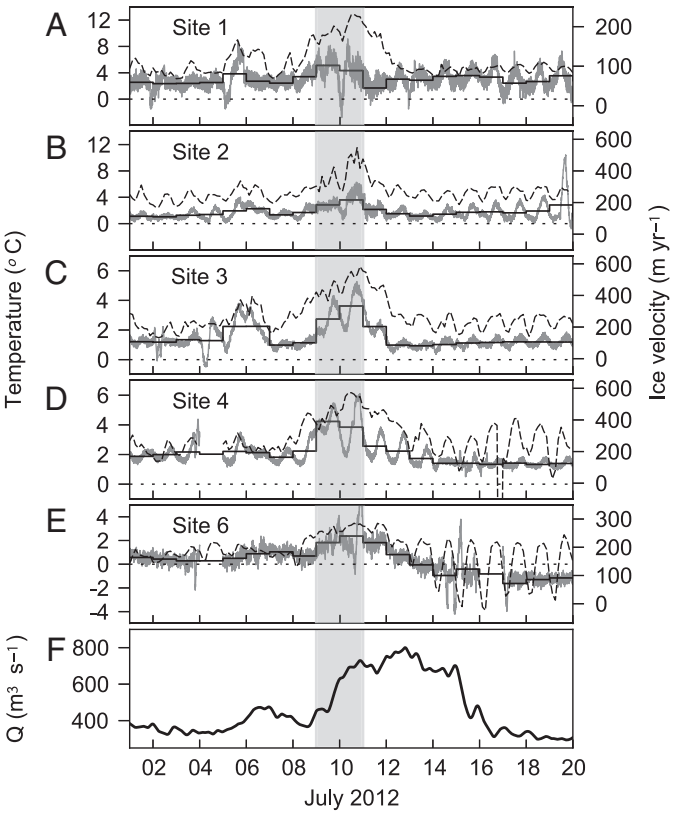

Fig. 3. Observations around July 12 melt event. (*A–E*) Near-surface air temperatures (dashed lines), daily (24 h) along-track ice velocities (stepped black lines) and short-term along-track ice velocities (gray lines) for each site at which daily measurements were made. Periods with inadequate quality observations removed. (*F*) Discharge hydrograph for Leverett Glacier (in cubic meters per second).(*A–F*) Gray shading defines the peak velocity response to the melt event (see text).

transect in 2012–2013 than in 2009–2010 (Fig. 5). These observations support previous findings that stronger melting results in faster summers, but that faster summers are then offset by subsequent slower winter ice flow due to the evolution of a larger, more extensive subglacial drainage system that drains high basal water pressure regions (19). Our findings also support ice sheet modeling results (21), which suggest that enhanced basal lubrication will not cause substantial net mass loss from the ice sheet, and provide the observations which Shannon et al. (21) had stated were currently "insufficient to determine whether changes in subglacial hydraulics will limit the potential for the speedup of flow."

Our findings demonstrate that despite the exceptional melting observed in 2012, annual ice motion along our transect was not enhanced relative to an average melt year (2009). These findings suggest that although hydrologically forced ice motion influences short-term and seasonal ice dynamics, land-terminating margins of the Greenland ice sheet are insensitive dynamically over annual timescales to melt volumes that are commensurate with temperature projections for 2100 (27). Furthermore, our data demonstrate that the importance of hydrologically forced ice motion over annual timescales can only be understood with reference to both summer and winter seasonal velocities due to their significant interannual variability. We also note that the effects of surface melt and oceanic forcing mechanisms on the dynamics of marine terminating glaciers in a warming climate remain unclear and should be a priority for future research.

Materials and Methods

Ice motion was recorded at seven sites, up to 1,716 m a.s.l elevation and 113 km from the ice sheet margin (Fig. 1). Dual-frequency GPS receivers mounted on poles frozen into the ice recorded position at 10-s intervals. Data were subsequently processed kinematically in overlapping 28-h windows using Track 1.21 (28) using International GNSS (Global Navigation Satellite System) Service precise orbits relative to an off-ice base station (Fig. 1), apart from August 12 to 29, 2012, when the Kellyville global GPS network station was used. Positions were filtered using a high-pass Gaussian filter to suppress high-frequency noise without distorting the long-term signal and then differenced every 24 h to calculate daily velocities (19). Short-term velocities were calculated at 1-min intervals and smoothed with a 6-h mean sliding window. Horizontal velocity uncertainties are approximately ±1 cm at each epoch and 5.2 m y^{-1} for daily velocities (10). Power failure prevented continuous recording of ice velocities at sites 5 and 7 during summer 2012 and at sites 1–3 in late summer (Fig. 1). The absolute displacements during these periods of power failure were still obtained at each site. The enhanced ice flow periods were defined in whole days for clarity and to make intercomparisons between sites more objective. Each enhanced ice flow period started when most sites showed a substantial increase in velocity on the previous day and ended on the last day before velocities at all sites decreased. We chose 8-d baseline periods for examining the ice displacement associated with each peak melt event as these represented the longest periods over which we could compare velocities without overlapping the periods associated with each melt event. The variability associated with choosing different lengths in baseline and enhanced ice flow period was insignificant in the context of the large differences in displacement exhibited by each event. Air temperatures were measured at sites 1, 3, and 6 using shielded Campbell Scientific T107 temperature sensors connected to Campbell Scientific CR800 data loggers, and at sites 2 and 4 using shielded HOBO U21-004 temperature sensors, situated ~2 m above the ice sheet surface. Sensors sampled once per minute and recorded a mean value every 15 min. Air temperatures were then converted to positive degree days by calculating the mean of all positive values each day. Snow depths were measured at sites 2–7 just before the onset of the melt season, and seasonal ablation water equivalent totals were determined from ablation stakes at sites 2–7. To compare measurements of

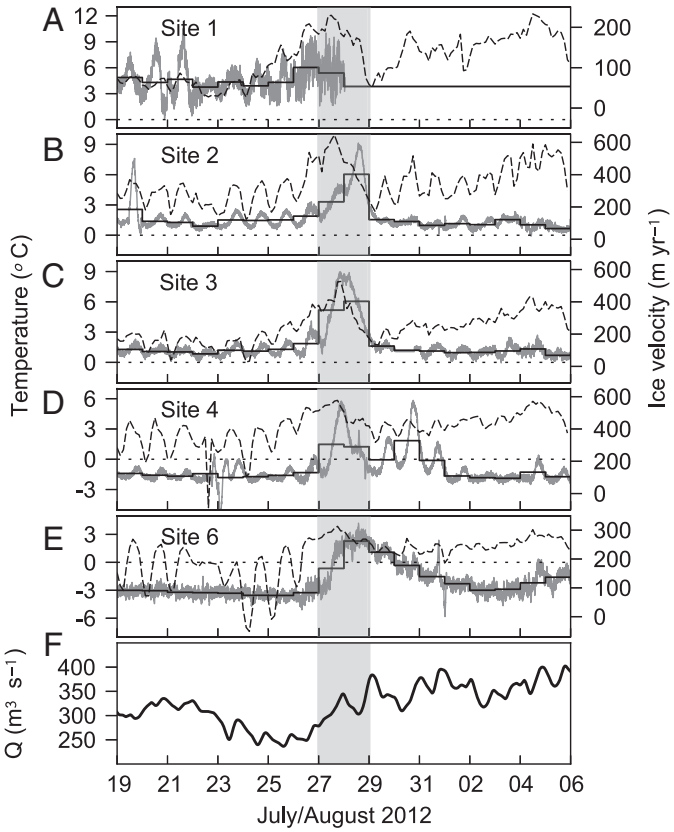

Fig. 4. Observations around July 29 melt event. See *A–F* in Fig. 3 for details.

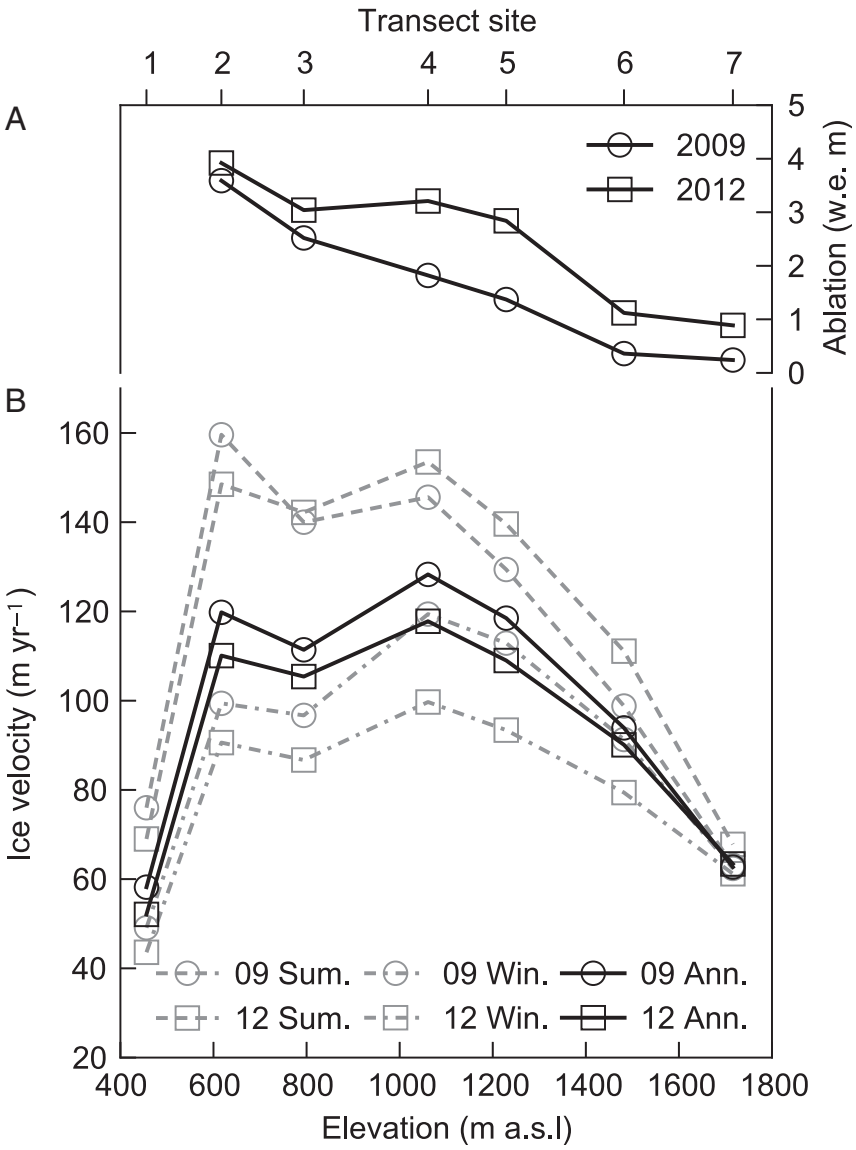

Fig. 5. (*A*) Annual (May 1–April 30) ablation in water equivalent meters for sites 2–7 in 2009 and 2012. (*B*) Summer (Sum, May 1–August 31), winter (Win, September 1–April 30), and annual (Ann, May 1–April 30) velocities for each site in 2009 and 2012.

ice velocities and ablation made in 2009 and 2012, we calculated the percentage difference between the years at each site and then took the mean of those values to derive a transect average. The volume of meltwater draining from Leverett Glacier's inferred hydrological catchment (Fig. 1) was measured using continuous water stage monitoring through a stable bedrock section. Stage was converted to discharge with a continuous stage–discharge curve obtained from repeat Rhodamine WT and Rhodamine B dye dilution injections undertaken throughout both melt seasons, following methods described previously (25). The normalized root mean squared deviation of the discharge record is estimated to be ±10%.

ACKNOWLEDGMENTS. We thank the Leverett field camp members who helped with data acquisition. We acknowledge UK Natural Environment Research Council (NERC) Grants NE/F021399/1 (to P.W.N.) and NE/H024964/1 (to D.W.F.M.); NERC studentships NE/152830X/1 and NE/J500021/1 (to A.J.T.) and NE/H526794/1 (to I.D.B.); Edinburgh University Moss Scholarships (to A.J.T., T.R.C., and I.D.B.) and Development Trust; The Carnegie Trust (P.W.N.); Mackay Greenland Fund (A.J.T.); Research Councils Academic Fellowship (to M.A.K.); and Australian Research Council Future Fellowship FT110100207 (to M.A.K.). GPS equipment and training were provided by the NERC Geophysical Equipment Facility loan 868. Wind speed data from PROMICE and the GAP were provided by the Geological Survey of Greenland on www.promice.dk.

1. Rignot E, Velicogna I, van den Broeke MR, Monaghan A, Lenaerts J (2011) Acceleration of the contribution of the Greenland and Antarctic ice sheets to sea level rise. *Geophys Res Lett* 38:1–5.
2. Shepherd A, et al. (2012) A reconciled estimate of ice-sheet mass balance. *Science* 338(6111):1183–1189.
3. Sasgen I, et al. (2012) Timing and origin of recent regional ice-mass loss in Greenland. *Earth Planet Sci Lett* 333:293–303.
4. Hanna E, et al. (2011) Greenland ice sheet surface mass balance 1870 to 2010 based on twentieth century reanalysis, and links with global climate forcing. *J Geophys Res* 116:D24121.
5. Hanna E, Mernild SH, Cappelen J, Steffen K (2012) Recent warming in Greenland in a long-term instrumental (18812012) climatic context: I. Evaluation of surface air temperature records. *Environ Res Lett* 7:045404.
6. Fettweis X, Tedesco M, van den Broeke M, Ettema J (2011) Melting trends over the Greenland ice sheet (1958-2009) from spaceborne microwave data and regional climate models. *Cryosphere* 5:359–375.
7. Pritchard HD, Arthern RJ, Vaughan DG, Edwards LA (2009) Extensive dynamic thinning on the margins of the Greenland and Antarctic ice sheets. *Nature* 461(7266): 971–975.
8. Zwally HJ, et al. (2002) Surface melt-induced acceleration of Greenland ice-sheet flow. *Science* 297(5579):218–222.
9. Andersen ML, et al. (2010) Spatial and temporal melt variability at Helheim Glacier, East Greenland, and its effect on ice dynamics. *J Geophys Res* 115:F04041.
10. Bartholomew I, et al. (2011) Seasonal variations in Greenland Ice Sheet motion: Inland extent and behaviour at higher elevations. *Earth Planet Sci Lett* 307:271–278.
11. Sole AJ, et al. (2011) Seasonal speedup of a Greenland marine-terminating outlet glacier forced by surface melt-induced changes in subglacial hydrology. *J Geophys Res* 116:1–11.
12. Bartholomew I, et al. (2012) Short-term variability in Greenland ice sheet motion forced by time-varying meltwater drainage: Implications for the relationship between subglacial drainage system behavior and ice velocity. *J Geophys Res* 117: F03002.

13. Iken A, Bindschadler RA (1986) Combined measurements of subglacial water pressure and surface velocity of Findelengletscher, Switzerland: Conclusions about drainage system and sliding mechanism. *J Glaciol* 32:101–119.
14. Bartholomew I, et al. (2010) Seasonal evolution of subglacial drainage and acceleration in a Greenland outlet glacier. *Nat Geosci* 3:408–411.
15. Röthlisberger H, Lang H (1987) Glacial Hydrology. *Glacio-Fluvial Sediment Transfer: An Alpine Perspective*, eds Gurnell A, Clark M (John Wiley and Sons, Chichester, UK), pp 207–284.
16. Cowton T, et al. (2013) Evolution of drainage system morphology at a land-terminating Greenland outlet glacier. *J Geophys Res* 118:29–41.
17. Sundal AV, et al. (2011) Melt-induced speed-up of Greenland ice sheet offset by efficient subglacial drainage. *Nature* 469(7331):521–524.
18. van de Wal RSW, et al. (2008) Large and rapid melt-induced velocity changes in the ablation zone of the Greenland Ice Sheet. *Science* 321(5885):111–113.
19. Sole A, et al. (2013) Winter motion mediates dynamic response of the Greenland ice sheet to warmer summers. *Geophys Res Lett* 40:3940–3944.
20. Nghiem SV, et al. (2012) The extreme melt across the Greenland ice sheet in 2012. *Geophys Res Lett* 39:L20502.
21. Shannon SR, et al. (2013) Enhanced basal lubrication and the contribution of the Greenland ice sheet to future sea-level rise. *Proc Natl Acad Sci USA*, doi: 10.1073/pnas.1212647110.
22. Fettweis X, et al. (2013) Brief communication "Important role of the mid-tropospheric atmospheric circulation in the recent surface melt increase over the Greenland ice sheet". *Cryosphere* 7:241–248.
23. Tedesco M, et al. (2013) Evidence and analysis of 2012 Greenland records from spaceborne observations, a regional climate model and reanalysis data. *Cryosphere* 7:615–630.
24. Bennartz R, et al. (2013) July 2012 Greenland melt extent enhanced by low-level liquid clouds. *Nature* 496(7443):83–86.
25. Bartholomew I, et al. (2011) Supraglacial forcing of subglacial drainage in the ablation zone of the Greenland ice sheet. *Geophys Res Lett* 38:L08502.
26. Schoof C (2010) Ice-sheet acceleration driven by melt supply variability. *Nature* 468(7325):803–806.
27. Meehl G, et al. (2007) Global Climate Projections. *Climate Change 2007: The Physical Science Basis. Contribution of Working Group I to the Fourth Assessment Report of the Intergovernmental Panel on Climate Change*, eds Solomon S, et al. (Cambridge University Press).
28. Chen G (1999) GPS kinematic positioning for the airborne laser altimetry at Long Valley, California. Ph.D. thesis (Massachusetts Institute of Technology).
29. Palmer S, Shepherd A, Nienow P, Joughin I (2011) Seasonal speedup of the Greenland Ice Sheet linked to routing of surface water. *Earth Planet Sci Lett* 302:423–428.
30. Allen C (2011) IceBridge MCoRDS L2 ice thickness 2010 and 2011. Digital media http://nsidc.org/data/irmcr2.html.

Appendix C

Tedstone *et al.*, 2014 (Geophys. Res. Lett.)

AGU PUBLICATIONS

Geophysical Research Letters

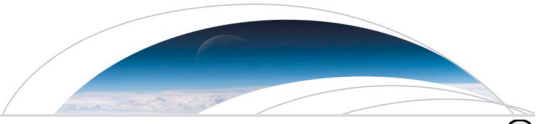

RESEARCH LETTER
10.1002/2014GL062386

Key Points:
- Spatial variability in ice sheet motion is compared with subglacial hydrology
- The proportion of annual motion that occurs in summer is spatially homogeneous
- Representation of complex hydrology in ice sheet models may be simplified

Supporting Information:
- Readme
- Table S1

Correspondence to:
A. J. Tedstone,
a.j.tedstone@ed.ac.uk

Citation:
Tedstone, A. J., P. W. Nienow, N. Gourmelen, and A. J. Sole (2014), Greenland ice sheet annual motion insensitive to spatial variations in subglacial hydraulic structure, *Geophys. Res. Lett.*, *41*, 8910–8917, doi:10.1002/2014GL062386.

Received 31 OCT 2014
Accepted 7 DEC 2014
Accepted article online 11 DEC 2014
Published online 23 DEC 2014

Greenland ice sheet annual motion insensitive to spatial variations in subglacial hydraulic structure

A. J. Tedstone[1], P. W. Nienow[1], N. Gourmelen[1], and A. J. Sole[2]

[1]School of Geosciences, University of Edinburgh, Edinburgh, UK, [2]Department of Geography, University of Sheffield, Sheffield, UK

Abstract We present ice velocities observed with global positioning systems and TerraSAR-X/TanDEM-X in a land-terminating region of the southwest Greenland ice sheet (GrIS) during the melt year 2012–2013, to examine the spatial pattern of seasonal and annual ice motion. We find that while spatial variability in the configuration of the subglacial drainage system controls ice motion at short timescales, this configuration has negligible impact on the spatial pattern of the proportion of annual motion which occurs during summer. While absolute annual velocities vary substantially, the proportional contribution of summer motion to annual motion does not. These observations suggest that in land-terminating margins of the GrIS, subglacial hydrology does not significantly influence spatial variations in net summer speedup. Furthermore, our findings imply that not every feature of the subglacial drainage system needs to be resolved in ice sheet models.

1. Introduction

One potential dynamic thinning mechanism of the Greenland ice sheet (GrIS) is surface melt-induced acceleration of ice motion [*Zwally et al.*, 2002; *Parizek and Alley*, 2004; *Andersen et al.*, 2010]. During summer, rapid increases in meltwater input from the ice sheet surface result in periods when the subglacial drainage system is more highly pressurized, leading to transient increases in basal sliding [*Bartholomew et al.*, 2011a; *Sole et al.*, 2011]. However, drainage system capacity changes in response [*Röthlisberger*, 1972; *Schoof*, 2010; *Hoffman and Price*, 2014], introducing a negative feedback which acts to lower the water pressure of the drainage system and reduce basal sliding, such that subsequent increases in basal sliding require either (a) larger meltwater pulses or (b) reductions in drainage system capacity, decreasing the quantity of meltwater required to overpressurize the system [*Cowton et al.*, 2013].

Remotely sensed observations of ice motion of a land-terminating portion of the southwest GrIS made on a single day in late summer have revealed spatially distinct flow enhancements of up to 300% relative to winter [*Palmer et al.*, 2011]. The spatial coincidence of faster flowing areas with surface drainage routing suggests that localized meltwater input to the ice bed, and the associated changes in subglacial water pressure, is the likely cause of the flow enhancement. However, point-based observations from the same region have shown that net annual ice motion is insensitive to these short-term variations in ice flow [*van de Wal et al.*, 2008; *Sole et al.*, 2013; *Tedstone et al.*, 2013], except possibly at high elevations well above the equilibrium line altitude [*Doyle et al.*, 2014]. Similarly, spatially extensive satellite observations at lower elevations have identified slower late summer flow in warmer summers but were not able to capture ice motion over a full melt year [*Sundal et al.*, 2011; *Fitzpatrick et al.*, 2013]. No study to date has therefore combined the required spatial and temporal coverage and resolution to investigate whether the insensitivity of net annual ice motion to short-term variations in ice flow holds across broader spatial scales, so the impact of spatially variable subglacial drainage and potential related flow enhancement on net annual regional ice motion remains unquantified.

Two specific aspects of surface melt-induced ice acceleration of the GrIS remain unexplored. First, while recent observations in southwest Greenland suggest that the subglacial drainage system is channelized to at least 40 km inland during summer [*Chandler et al.*, 2013], the spatial extent of surface melt-induced velocity perturbations forced by water pressure variability in these subglacial channels [e.g., *Nienow et al.*, 2005] is unknown. Second, over annual timescales it is unclear whether areas of ice close to surface meltwater input points and/or underlain by a channelized subglacial drainage system flow at a disproportionately faster rate than less hydrologically active areas. It is essential to identify whether surface

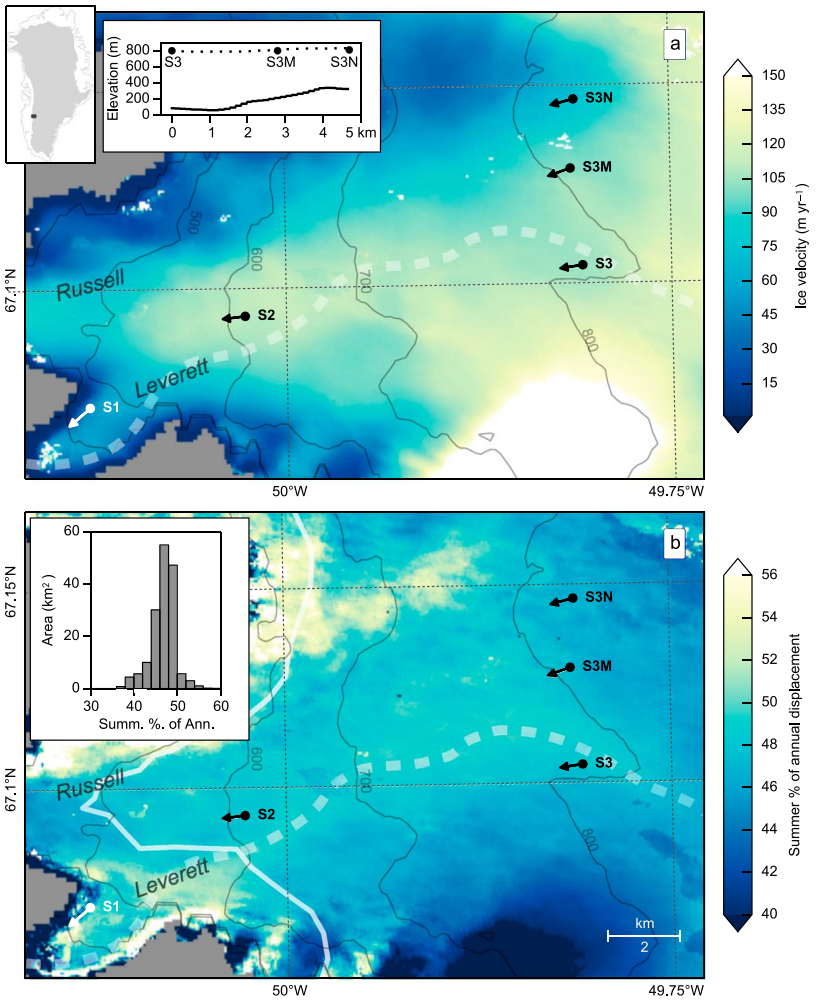

Figure 1. (a) Ice velocity (m yr^{-1}) measured by TSX/TDX during 1 May 2012 to 30 April 2013; inset: ice surface (dotted) and bed (solid) profiles through the GPS transect; outset: location of study area. (b) Summer (1 May 2012 to 31 August 2012) proportion of annual (1 May 2012 to 30 April 2013) displacement, with white line marking 2 km from the ice margin; inset: all observations further than 2 km from the ice margin as a histogram. GPS sites denoted by circles, with arrows indicating along-track flow direction; contours (in meters) from a digital elevation model derived from Operation IceBridge altimetry data [*Morlighem et al.*, 2013]; thick dashed line indicates approximate location of main subglacial channel from hydraulic potential analysis (Figure 2).

melt-induced ice acceleration has an impact on annual regional ice motion because surface melting of the ice sheet is projected to increase during the next century [*Stocker et al.*, 2013].

Here we present measurements of ice motion made during 2012–2013 at Leverett Glacier, a land-terminating glacier in the southwest of the GrIS at ~67°N (Figure 1). We measured ice motion continuously by global positioning systems (GPS) at five survey sites to examine spatial variability in the hydrological forcing of ice motion and by the TerraSAR-X/TanDEM-X (TSX/TDX) satellites over a ~20 by ~15 km area of the ice sheet margin to examine the spatial structure of seasonal and annual ice motion.

2. Data and Methods

2.1. Field Measurements

We used GPS records to observe ice motion during 2012 at three sites along a longitudinal transect (S1, S2, and S3) and at two locations transverse to the longitudinal transect ~18 km from the ice sheet margin, at ~800 m above sea level: S3M, 2.8 km and S3N, 4.7 km north of S3, respectively (Figure 1). Details of the GPS processing undertaken and longitudinal transect observations during 2012 have been described

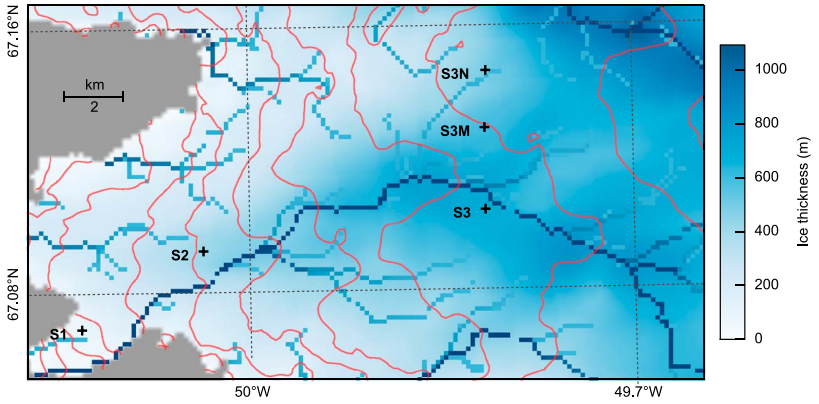

Figure 2. Ice thickness from Operation IceBridge [*Morlighem et al.*, 2013]. Subglacial hydraulic potential contours (red every 500 kPA) and major drainage pathways predicted by subglacial hydraulic potential analysis where water pressure equals ice overburden. Channel shading defined by the quantity of Upstream Contributing Cells (UCC) (values >50 UCC shown, with >1000 UCC in dark blue). Crosses denote GPS sites.

previously [*Tedstone et al.*, 2013]. GPS receiver malfunction at S3N resulted in noisy pseudo-range data, preventing accurate determination of subweekly variability in ice motion, but seasonal displacements were recorded. Additionally, power failure prevented continuous recording of ice motion at S3M between 1 July 2012 and late August 2012, restricting detailed analysis of ice motion to early summer, but absolute summer displacement was obtained. Along-track velocity uncertainties are approximately ±1 cm at each epoch and 5.2 m yr^{-1} for daily velocities [*Bartholomew et al.*, 2011a]. Seasonal trends in vertical and across-track displacement were removed by linear regression.

Air temperatures at S3 were logged every 15 min using a Campbell CR800 logger with a Campbell C107 shielded temperature probe. Discharge draining from the Leverett glacier hydrological catchment was measured using continuous water stage monitoring through a stable bedrock section and converted to discharge by calibration with repeat Rhodamine dye dilution injections, following methods described previously [*Bartholomew et al.*, 2011b].

2.2. Remote Sensing of Ice Motion

We processed synthetic aperture radar (SAR) data acquired between 26 April 2012 and 11 May 2013 by TSX/TDX into 23 ice displacement maps by applying feature tracking [*Paul et al.*, 2013] (Table S1). Our use of two tracks yields near-continuous temporal coverage but restricts spatial coverage to ~20 km inland from the ice margin. The two gaps in temporal coverage of 17 and 28 days occurred during winter (Table S1) and were filled by calculating the mean displacement of the immediately preceding and subsequent displacement maps. Steady trends in winter GPS velocities, where available [e.g., *Joughin et al.*, 2010], show that this limited averaging should not produce significant errors in ice motion estimates. Azimuth and range displacement maps were used to compute summer (1 May 2012 to 31 August 2012) and winter (1 September 2012 to 30 April 2013) displacements.

2.3. Hydraulic Potential Analysis

We used digital elevation models of the ice sheet surface and bed derived from Operation IceBridge altimetry and ice penetrating radar data [*Morlighem et al.*, 2013] to produce a theoretical reconstruction of the subglacial drainage network [*Shreve*, 1972] to complement analyses of our ice motion data. The dense radar survey in this section of the ice sheet has an average flight spacing of ~500 m and a nominal precision of 10 m for ice thickness [*Morlighem et al.*, 2013]. Calculations followed procedures outlined by *Sharp et al.* [1993]. Field observations of proglacial discharge, dye, and SF_6 tracer experiments show that most meltwater from our study area exits the ice sheet through the Leverett Glacier terminus rather than through Russell Glacier (Figure 1) [*Bartholomew et al.*, 2011a; *Chandler et al.*, 2013]. Theoretical reconstructions suggest that meltwaters from the catchment will only drain through the correct Leverett outlet when subglacial water pressure P_w is equal to ice overburden pressure (P_i) (i.e., $P_w = P_i$) (Figure 2); at lower water pressures, the meltwater exits the catchment via Russell Glacier. Despite this sensitivity, all

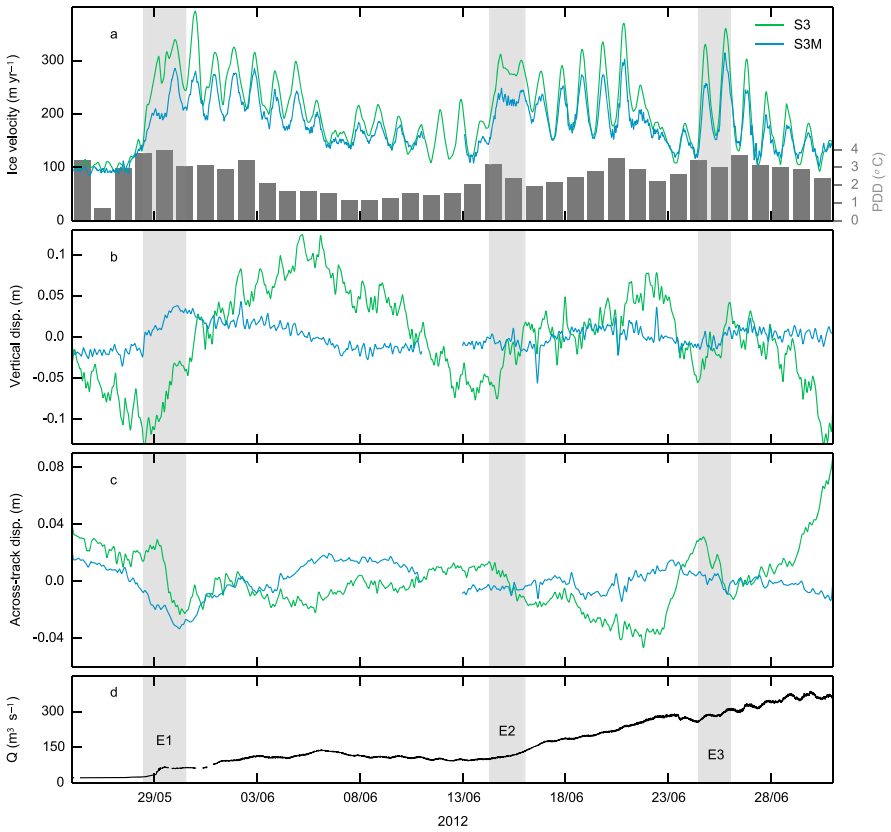

Figure 3. Time series at S3 and S3M of (a) along-track velocity and positive degree days (PDD, °C) at S3, (b) detrended vertical displacement, and (c) detrended across-track displacement. (d) Proglacial discharge hydrograph for Leverett Glacier ($m^3\ s^{-1}$).

hydraulic reconstructions predict the presence of a major drainage pathway less than 200 m north of S3, an invariance controlled primarily by the ice surface topography (Figure 1).

3. Results

3.1. Diurnal Motion at S3 and S3M

Detailed data from S3 and S3M enable us to examine the impact that spatial variability in the configuration of the subglacial drainage system has on ice motion. During the period of observation there were three clear speedup events when ice motion increased by >100% compared to the previous 2 days (Figure 3, E1–3). These pronounced speedups coincided with increasing air temperatures and rising proglacial discharge as observed in previous studies [e.g., *Iken and Bindschadler*, 1986; *Mair et al.*, 2003; *Bartholomew et al.*, 2011a].

During each event, along-track velocity at S3 increased rapidly (Figure 3a), accompanied by ice surface uplift of 5–10 cm (Figure 3b) and across-track displacement (perpendicular to the flow direction at each site shown in Figure 1) of 2–4 cm southeast (Figure 3c). While S3M's along-track velocity was 9% slower than S3 during the summer (Table 1), cross correlation of their continuous velocity records (Figure 4) shows that during each event and over the full observation period, the sites were most highly correlated at zero lag ($r > 0.8$). However, S3M only moved upward and across flow during E1, subsequently showing no resolvable signals in vertical or cross-track displacement.

After E1, S3 continued to show clear uplift and subsidence of ~2–5 cm over diurnal cycles for the remainder of the observation period but without any corresponding variability in cross-track displacement except during E2 and E3. Meanwhile, S3M did not display any systematic variability in either vertical or across-track displacement (Figures 3b and 3c).

Table 1. Ice Displacement at Observation Sites During 2012[a]

	Ice Displacement, 2012		
	Ann. (m)	Summ. (m)	Summ. %
S1	52.1	23.3	44.7
S2	110.1	50	45.4
S3	105.4	47.9	45.4
S3M	98.2	43.6	44.4
S3N	70.5	30.6	43.4

[a]Annual (Ann., meters, 1 May 2012 to 30 April 2013), Summer (Summ., meters, 1 May to 31 August), and Summer % (Summ. %, proportion of annual motion attributable to summer).

3.2. Seasonal and Annual Displacement

To identify whether spatially variable subglacial drainage during summer has an impact on ice motion over annual timescales, we examined net displacement at S3, S3M, and S3N (Table 1) during summer (1 May to 31 August 2012) and over a full year (1 May 2012 to 30 April 2013). During summer, S3 flowed fastest, with S3M and S3N flowing at 91% and 64% of motion at S3, respectively. Similarly, during the full year, S3 flowed fastest, with S3M and S3N displaced by 93% and 64% of S3, respectively. However, the *proportion* of annual displacement attributable to motion during summer varied by just 2% between the three sites. S1 and S2 (~2 km and ~8 km from the ice margin respectively) displayed equivalent behavior (Table 1) such that summer motion at all sites accounted for 43.4% to 45.4% of annual motion.

Observations of ice motion from TSX/TDX complement the GPS observations, providing much greater spatial coverage of seasonal and annual ice displacement. Over the full year, absolute ice displacement observed by TSX/TDX varied by ±2% on average of the observations recorded at each GPS site, a close agreement which validates the observations made by TSX/TDX over the rest of the study area.

The ice motion observed by TSX/TDX over the melt year (Figure 1a) reveals clear spatial variability both along and across flow, with areas of faster ice motion broadly colocated with thicker ice (Figure 2). However, there is very little variability in the proportion of annual ice displacement attributable to summer motion beyond ~2 km from the ice sheet margin (Figure 1b). There is a ~3 km wide flow zone of slightly faster (~2%) summer motion between S3 and S3M, the location of which is coincident with the subglacial drainage channel predicted by hydraulic potential analysis (Figure 2).

The homogeneous behavior of this area of the ice sheet in terms of the proportionality of summer speedup, particularly away from the thin ice margin, is clear in Figure 1b (inset). Summer displacement of 43.9–49.7% of total annual displacement, corresponding to $\bar{x} \pm 1\sigma$, accounted for 81% of variability in the study area further than 2 km from the ice margin. Areas where ice flowed proportionally faster (white in Figure 1b) or slower (dark blue in Figure 1b) during summer are restricted to marginal ice thinner than ~200 m in the former case and a steep ice fall [*Sundal et al.*, 2011] in the latter case.

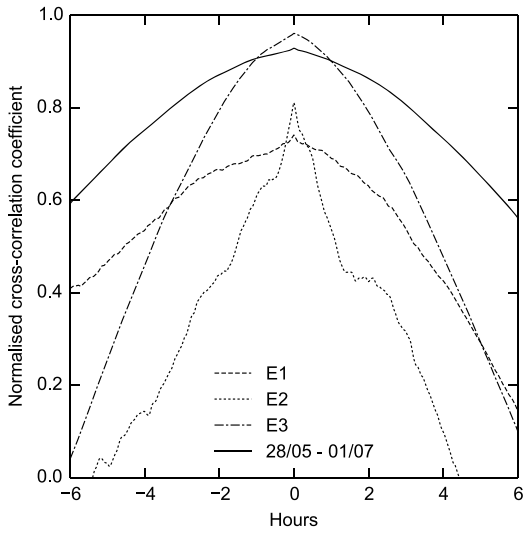

Figure 4. Cross-correlation functions between S3 and S3M during 28 May to 1 July and for events 1–3 (Figure 3), S3 as primary variable.

4. Discussion

4.1. Drivers of Diurnal Ice Motion

Observations of alpine glaciers have revealed variable pressure axes (VPAs) tens of meters wide centered on a hydraulically efficient channel, in which subglacial water pressures (P_w) vary substantially over diurnal melt cycles, in constrast to adjacent areas of the bed where P_w becomes progressively higher and less variable as the influence of the VPA declines with distance [e.g., *Hubbard et al.*, 1995; *Harbor et al.*, 1997]. At Haut Glacier d'Arolla (Swiss Alps), the highest diurnal ice surface velocities occur over the

VPA. However, the wide area over which ice velocities increase in phase with VPA P_w can only be explained by reductions in basal shear traction over a much wider (~560 m) area of the bed, requiring either an inefficient drainage system or a channelized system with many channels that hydraulically connect large areas of the bed [*Nienow et al.*, 2005].

Previous studies at Leverett Glacier have inferred the presence of an efficient, channelized subglacial drainage system to at least 40 km into the ice sheet interior during summer [*Bartholomew et al.*, 2011a; *Chandler et al.*, 2013]. The hydro-dynamical behavior observed at S3 and S3M is explicable both by the Alpine VPA framework and by hydrological modeling of the interaction between channelized and distributed subglacial drainage systems [*Werder et al.*, 2013]. S3, inferred to be in the vicinity of a major drainage pathway (Figure 2), experiences large oscillations in diurnal along-track velocity and vertical displacement, consistent with oscillatory variability in P_w. Furthermore, *Sugiyama et al.* [2010] observe that vertical ice displacement over a basal perturbation can induce a cross-track displacement at some distance away from the basal perturbation; the southeasterly displacement of S3 during the speedup periods E1–3 mimics this behavior and places S3 to the south of the VPA, in agreement with the hydraulic potential analysis.

Without additional survey sites or coupled hydro-dynamic modeling [e.g., *Hoffman and Price*, 2014], it is not possible to identify whether the fluctuations in stress regime which force synchronous along-track motion at S3 and S3M, most likely through fluctuating P_w, originate from (a) local meltwater input points or (b) fluctuations in VPA P_w forced by upglacier surface meltwater inputs. As a result, it is not possible to elucidate the relative importance of transverse stresses or the coupling lengths over which local VPA ice-bed decoupling could propagate enhanced motion away from the VPA. Nevertheless, *Werder et al.* [2013] model pressure variations up to ~ 2 km away from a subglacial channel, which would fit with our observations of a dynamic response at S3M driven by pressure variations within the inferred subglacial channel.

4.2. Seasonal and Annual Ice Motion

Our continuous observations of ice motion at S3 and S3M during 2012 confirm that, as suggested by *Palmer et al.* [2011] at the broader catchment scale, surface melt-induced ice acceleration is spatially variable over diurnal timescales. At annual timescales there is also substantial spatial variability in absolute ice motion (Figure 1a). However, it is variability in driving stress caused primarily by differing ice thickness, rather than a spatially variable drainage system, which is the cause of this variability in our study area.

Despite clear evidence for distinct subglacial channels (both from the ice motion data presented here and previous tracer studies, e.g., *Chandler et al.* [2013]) which induce complex diurnal flow patterns, the structure of the subglacial drainage system does not appear to have a significant impact on the overall extent to which summer motion contributes to annual motion. Instead, in 81% of the area further than 2 km from the ice margin, the contribution of summer motion to annual motion falls within the narrow range of ~44–50%, irrespective of proximity to underlying subglacial channels. This suggests that the surrounding regions of distributed drainage readily connect to and interact with channelized drainage features, smoothing spatial variations in velocity forced by water pressure fluctuations in the channels. Thus, the existence of channels constitutes an important control on regional subglacial water pressure, but the precise location of each channel is less important because they interact readily with the surrounding distributed drainage system rather than acting in isolation.

Our finding that an essentially spatially invariant proportion of annual motion occurs during the melt season may be explicable by both recent field observations from the GrIS and modeling. Using observations of ice velocity, moulin water levels, and borehole water pressures, *Andrews et al.* [2014] concluded that decreasing water pressures in the unchannelized (or "distributed") regions of the subglacial drainage system, not the channelized areas, were responsible for their observed late summer slowdown in ice velocities. Such hydro-dynamic coupling in unchannelized regions which underlie the majority of our study area, in contrast to narrow, discrete channelized drainage features (or VPAs), may therefore provide a plausible explanation for the spatial invariance in the proportion of annual motion which we observe during summer.

Furthermore, these observations qualitatively agree with modeling results [*Hoffman and Price*, 2014] which suggest that upon the delivery of meltwater to the ice sheet bed, ice velocity transiently increases, but a negative feedback then dominates the subsequent velocity response whereby sliding over bedrock bumps increases cavity space, lowering water pressure and in turn sliding. This negative feedback occurs even in

the absence of channelization, acting to limit the magnitude of any surface melt-driven velocity increase. Thus, the coupled hydrology dynamics of the spatially extensive unchannelized regions of the ice sheet bed may explain our observation that the summer proportion of annual ice motion is spatially invariant.

5. Conclusions

We have examined spatial variability in surface melt-induced ice motion in a land-terminating region of the southwest GrIS. We have shown that while spatial variability in the configuration of subglacial drainage controls ice motion at short timescales, these variations have negligible impact on the proportion of annual motion which occurs during summer as a result of surface meltwater inputs to the ice sheet bed. While absolute annual velocities vary substantially across the study area (due to variations in driving stress), the proportional contribution of summer motion to annual ice motion does not.

This observation is important because it implies that, for land-terminating regions of the GrIS, (1) it may not be necessary to include complex representations of subglacial hydrology in ice sheet models for simulating ice flow and (2) the placement of GPS relative to subglacial channels should only affect the detailed pattern of ice velocities over short timescales and not the relative seasonal displacement resulting from hydraulic forcing. Nevertheless, additional research needs to determine the extent to which our findings are applicable to the wider ice sheet and in particular (1) whether the invariance of ice motion to the configuration of the subglacial drainage system over annual timescales extends further inland where the extent of channelization remains equivocal [*Chandler et al.*, 2013; *Meierbachtol et al.*, 2013] and (2) the applicability of our findings to other land-terminating margins of the ice sheet and to marine-terminating margins, where hydro-dynamic coupling remains poorly understood.

Acknowledgments

We acknowledge UK Natural Environment Research Council (NERC) studentships NE/152830X/1 and NE/J500021/1 (to A.J.T.); the Carnegie Trust (P.W.N.); and from Edinburgh University, a Moss Scholarship (to A.J.T.), the Mackay Greenland Fund (A.J.T.), and the Development Trust. GPS equipment and training were provided by the NERC Geophysical Equipment Facility loan 868. Field observations are archived with the United Kingdom Polar Data Centre. The TerraSAR-X/TanDEM-X data were obtained from the German Aerospace Center (DLR) under proposal XTI_GLAC0296. M. Morlighem provided bed topography and ice thickness data. We thank the Leverett field camp members who helped with data acquisition.

The Editor thanks two anonymous reviewers for their assistance in evaluating this paper.

References

Andersen, M. L., et al. (2010), Spatial and temporal melt variability at Helheim Glacier, east Greenland, and its effect on ice dynamics, *J. Geophys. Res.*, *115*, F04041, doi:10.1029/2010JF001760.

Andrews, L. C., G. A. Catania, M. J. Hoffman, J. Gulley, M. Luthi, C. Ryser, R. L. Hawley, and T. A. Neumann (2014), Direct observations of evolving subglacial drainage beneath the Greenland ice sheet, *Nature*, *514*, 80–83, doi:10.1038/nature13796.

Bartholomew, I., P. Nienow, A. Sole, D. Mair, T. Cowton, M. King, and S. Palmer (2011a), Seasonal variations in Greenland ice sheet motion: Inland extent and behaviour at higher elevations, *Earth Planet. Sci. Lett.*, *307*, 271–278, doi:10.1016/j.epsl.2011.04.014.

Bartholomew, I., P. Nienow, A. Sole, D. Mair, T. Cowton, S. Palmer, and J. Wadham (2011b), Supraglacial forcing of subglacial drainage in the ablation zone of the Greenland ice sheet, *Geophys. Res. Lett.*, *38*, L08502, doi:10.1029/2011GL047063.

Chandler, D. M., et al. (2013), Evolution of the subglacial drainage system beneath the Greenland ice sheet revealed by tracers, *Nat. Geosci.*, *6*(3), 195–198.

Cowton, T., P. Nienow, A. Sole, J. Wadham, G. Lis, I. Bartholomew, W. F. Mair, and D. M. Chandler (2013), Evolution of drainage system morphology at a land-terminating Greenlandic outlet glacier, *J. Geophys. Res. Earth Surf.*, *118*, 29–41, doi:10.1029/2012JF002540.

Doyle, S. H., A. Hubbard, A. A. W. Fitzpatrick, D. van As, A. B. Mikkelsen, R. Pettersson, and B. Hubbard (2014), Persistent flow acceleration within the interior of the Greenland ice sheet, *Geophys. Res. Lett.*, *41*, 899–905, doi:10.1002/2013GL058933.

Fitzpatrick, A. A. W., A. Hubbard, I. Joughin, D. J. Quincey, D. Van As, A. P. Mikkelsen, S. H. Doyle, B. Hasholt, and G. A. Jones (2013), Ice flow dynamics and surface meltwater flux at a land-terminating sector of the Greenland ice sheet, *J. Glaciol.*, *59*, 687–696.

Harbor, J., M. Sharp, L. Copland, B. Hubbard, P. Nienow, and D. Mair (1997), Influence of subglacial drainage conditions on the velocity distribution within a glacier cross section, *Geology*, *25*, 739–742.

Hoffman, M., and S. Price (2014), Feedbacks between coupled subglacial hydrology and glacier dynamics, *J. Geophys. Res. Earth Surf.*, *119*, 414–436, doi:10.1002/2013JF002943.

Hubbard, B., M. Sharp, I. Willis, M. Nielsen, and C. Smart (1995), Borehole water-level variations and the structure of the subglacial hydrological system of Haut Glacier d'Arolla, Valais, Switzerland, *J. Glaciol.*, *41*(139), 572–583.

Iken, A., and R. A. Bindschadler (1986), Combined measurements of subglacial water pressure and surface velocity of Findelengletscher, Switzerland: Conclusions about drainage system and sliding mechanism, *J. Glaciol.*, *32*(110), 101–119.

Joughin, I., B. E. Smith, I. M. Howat, T. Scambos, and T. Moon (2010), Greenland flow variability from ice-sheet-wide velocity mapping, *J. Glaciol.*, *56*(197), 415–430, doi:10.3189/002214310792447734.

Mair, D., I. Willis, U. H. Fischer, B. Hubbard, P. Nienow, and A. Hubbard (2003), Hydrological controls on patterns of surface, internal and basal motion during three "spring events": Haut Glacier d'Arolla, Switzerland, *J. Glaciol.*, *49*(167), 555–567, doi:10.3189/172756503781830467.

Meierbachtol, T., J. Harper, and N. Humphrey (2013), Basal drainage system response to increasing surface melt on the Greenland ice sheet, *Science*, *341*(6147), 777–779, doi:10.1126/science.1235905.

Morlighem, M., E. Rignot, J. Mouginot, X. Wu, H. Seroussi, E. Larour, and J. Paden (2013), High-resolution bed topography mapping of Russell Glacier, Greenland, inferred from operation icebridge data, *J. Glaciol.*, *59*(218), 1015–1023, doi:10.3189/2013JoG12J235.

Nienow, P. W., A. L. Hubbard, B. P. Hubbard, D. M. Chandler, D. W. F. Mair, M. J. Sharp, and I. C. Willis (2005), Hydrological controls on diurnal ice flow variability in valley glaciers, *J. Geophys. Res.*, *110*, F04002, doi:10.1029/2003JF000112.

Palmer, S., A. Shepherd, P. Nienow, and I. Joughin (2011), Seasonal speedup of the Greenland ice sheet linked to routing of surface water, *Earth Planet. Sci. Lett.*, *302*, 423–428, doi:10.1016/j.epsl.2010.12.037.

Parizek, B. R., and R. B. Alley (2004), Implications of increased Greenland surface melt under global-warming scenarios: Ice-sheet simulations, *Quat. Sci. Rev.*, *23*(9-10), 1013–1027, doi:10.1016/j.quascirev.2003.12.024.

Paul, F., et al. (2013), The glaciers climate change initiative: Methods for creating glacier area, elevation change and velocity products, *Remote Sens. Environ.*, doi:10.1016/j.rse.2013.07.043, in press.

Röthlisberger, H. (1972), Water pressure in intra- and subglacial channels, *J. Glaciol.*, *11*(62), 177–203.
Schoof, C. (2010), Ice-sheet acceleration driven by melt supply variability, *Nature*, *468*(7325), 803–806, doi:10.1038/nature09618.
Sharp, M., K. Richards, I. Willis, N. Arnold, P. Nienow, W. Lawson, and J.-L. Tison (1993), Geometry, bed topography and drainage system structure of the Haut Glacier d'Arolla, Switzerland, *Earth Surf. Processes Landforms*, *18*(6), 557–571, doi:10.1002/esp.3290180608.
Shreve, R. (1972), Movement of water in glaciers, *J. Glaciol.*, *11*(62), 205–214.
Sole, A., P. Nienow, I. Bartholomew, D. Mair, T. Cowton, A. Tedstone, and M. King (2013), Winter motion mediates dynamic response of the Greenland ice sheet to warmer summers, *Geophys. Res. Lett.*, *40*, 3940–3944, doi:10.1002/grl.50764.
Sole, A. J., D. W. F. Mair, P. W. Nienow, I. D. Bartholomew, M. A. King, M. J. Burke, and I. Joughin (2011), Seasonal speedup of a Greenland marine-terminating outlet glacier forced by surface melt-induced changes in subglacial hydrology, *J. Geophys. Res.*, *116*, F03014, doi:10.1029/2010JF001948.
Stocker, T., et al. (2013), *Climate Change 2013: The Physical Science Basis. Contribution of Working Group I to the Fifth Assessment Report of the Intergovernmental Panel on Climate Change, Chap. Technical Summary*, Cambridge Univ. Press, Cambridge, U. K., and New York.
Sugiyama, S., A. Bauder, P. Riesen, and M. Funk (2010), Surface ice motion deviating toward the margins during speed-up events at Gornergletscher, Switzerland, *J. Geophys. Res.*, *115*, F03010, doi:10.1029/2009JF001509.
Sundal, A. V., A. Shepherd, P. Nienow, E. Hanna, S. Palmer, and P. Huybrechts (2011), Melt-induced speed-up of Greenland ice sheet offset by efficient subglacial drainage., *Nature*, *469*(7331), 521–524, doi:10.1038/nature09740.
Tedstone, A. J., P. W. Nienow, A. J. Sole, D. W. Mair, T. R. Cowton, I. D. Bartholomew, and M. A. King (2013), Greenland ice sheet motion insensitive to exceptional meltwater forcing, *Proc. Natl. Acad. Sci.*, *110*(49), 19,719–19,724.
van de Wal, R. S. W., W. Boot, M. R. van den Broeke, C. J. P. P. Smeets, C. H. Reijmer, J. J. A. Donker, and J. Oerlemans (2008), Large and rapid melt-induced velocity changes in the ablation zone of the Greenland ice sheet, *Science*, *321*(5885), 111–113, doi:10.1126/science.1158540.
Werder, M. A., I. J. Hewitt, C. G. Schoof, and G. E. Flowers (2013), Modeling channelized and distributed subglacial drainage in two dimensions, *J. Geophys. Res. Earth Surf.*, *118*, 2140–2158, doi:10.1002/jgrf.20146.
Zwally, H. J., W. Abdalati, and T. Herring (2002), Surface melt-induced acceleration of Greenland ice-sheet flow, *Science*, *297*, 218–222, doi:10.1126/science.1072708.

Appendix D

Hawkings *et al.*, 2014 (Nat. Commun.)

nature COMMUNICATIONS

ARTICLE

Received 26 Aug 2013 | Accepted 22 Apr 2014 | Published 21 May 2014

DOI: 10.1038/ncomms4929 OPEN

Ice sheets as a significant source of highly reactive nanoparticulate iron to the oceans

Jon R. Hawkings[1], Jemma L. Wadham[1], Martyn Tranter[1], Rob Raiswell[2], Liane G. Benning[2], Peter J. Statham[3], Andrew Tedstone[4], Peter Nienow[4], Katherine Lee[1] & Jon Telling[1]

The Greenland and Antarctic Ice Sheets cover ~10% of global land surface, but are rarely considered as active components of the global iron cycle. The ocean waters around both ice sheets harbour highly productive coastal ecosystems, many of which are iron limited. Measurements of iron concentrations in subglacial runoff from a large Greenland Ice Sheet catchment reveal the potential for globally significant export of labile iron fractions to the near-coastal euphotic zone. We estimate that the flux of bioavailable iron associated with glacial runoff is 0.40–2.54 Tg per year in Greenland and 0.06–0.17 Tg per year in Antarctica. Iron fluxes are dominated by a highly reactive and potentially bioavailable nanoparticulate suspended sediment fraction, similar to that identified in Antarctic icebergs. Estimates of labile iron fluxes in meltwater are comparable with aeolian dust fluxes to the oceans surrounding Greenland and Antarctica, and are similarly expected to increase in a warming climate with enhanced melting.

[1] Bristol Glaciology Centre, School of Geographical Sciences, University of Bristol, University Road, Bristol BS8 1SS, UK. [2] Cohen Biogeochemistry Laboratory, School of Earth and Environment, University of Leeds, Leeds LS2 9JT, UK. [3] School of Ocean and Earth Science, National Oceanography Centre, University of Southampton, Southampton SO14 3ZH, UK. [4] School of Geoscience, University of Edinburgh, Edinburgh EH8 9XP, UK. Correspondence and requests for materials should be addressed to J.L.W. (email: j.l.wadham@bristol.ac.uk).

Iron limitation of primary producers is prevalent in large sectors of the world's oceans, most notably the Southern Ocean (SO), the Pacific Northwest and minor parts of the North Atlantic (NA), all areas proximal to significant glacial activity[1,2]. These iron (Fe) limited oceans are believed to have an impact on the global climate as they play a role in regulating concentrations of atmospheric CO_2 via their influence upon the strength of the biological pump[3,4]. Past studies of oceanic Fe inputs have focussed upon aeolian dust[5,6], riverine discharge[7], benthic recycling[7] and sea ice[8]. Each source delivers Fe in a variety of phases, the solubilities (and bioavailabilities) of which are currently poorly understood, as are their transformations to more bioavailable forms[7]. More recently, ice sheets have also been hypothesized as contributors of iron to the oceans via icebergs[9,10] and subglacial meltwaters[11,12]. Icebergs have been relatively well-studied in terms of their fertilization potential of the SO[9,10,13], but both Fe concentrations and phase speciation in glacial runoff remain poorly constrained[14]. Glacial runoff accounts for around half of the freshwater exported from the Greenland Ice Sheet (GrIS) and recent observational evidence suggests that subglacial meltwaters are exported from the Antarctic Ice Sheet (AntIS) via channels beneath the margins of major ice streams[15]. We contend that a consideration of meltwater Fe fluxes, which supplements iron from icebergs, is critical for understanding oceanic iron cycling and primary productivity in polar waters[14].

While there have been a few studies of Fe export in runoff from small valley glaciers in the Arctic[11,12,16], there are currently no representive data on fluxes from large ice sheet catchments. There may be fundamental differences in subglacial chemical weathering between large ice sheet catchments and valley glaciers as a result of prolonged water residence times, greater anoxia and elevated physical erosion rates under the former[17–19]. Subglacial meltwater from the AntIS exits via ice streams, which terminate in large ice shelves, hindering direct sampling owing to logistical difficulties. The GrIS provides a more accessible ice sheet system, with large, land-terminating glaciers allowing direct sampling of subglacial waters at the ice margin. Additionally, meltwater stored over-winter at the bed is released episodically in summer via outburst events[20]. These present an opportunity to improve understanding of potential iron release during similar outbursts events observed around the continental margins in Antarctica[21], linked to subglacial lake drainage events[22,23], which may discharge large volumes of meltwater[24].

Here we present the first dataset of iron fluxes from a large land-terminating catchment on the GrIS over a full-melt season, incorporating the release of long residence time waters from both early season runoff and subglacial outburst events. The underlying debris and morphology of the catchment is representative of >75% of the West Greenland ice margin[25], and bedrock geology is predominantly Neoproterozoic gneiss/granitic, which is typical of large areas of the crystalline rocks that dominate the Precambrian Shield on which Greenland lies[26]. These data provide the most comprehensive, and therefore, most useful dataset to enable estimates of Fe input to polar waters. We propose that ice sheets provide a large and previously unconsidered source of highly reactive and potentially bioavailable subglacially derived iron to the Polar oceans, likely to sustain oceanic primary production.

Results

Iron phase speciation. Fe is known to exist in a spectrum of labile phases[7], including 'truly dissolved' Fe (DFe), colloidal/nanoparticulate Fe (CNFe) and sediment-bound nanoparticulate Fe (SSFe), which fundamentally impact its subsequent transport and bioavailability. Hence, we measure two filterable phases in addition to the labile suspended sediment phase. Of the filterable phases, DFe is defined as Fe that passed through a 0.02 µm membrane, and CNFe is interpreted as that which passes through a 0.45 µm membrane minus DFe. SSFe is that extractable in an ascorbate solution, which preferentially dissolves labile ('highly reactive' ferrihydrite) iron, the most bioavailable form of iron oxyhydroxides[27]. These phases allow direct comparison with previous studies, by Statham *et al.*[11] for DFe/CNFe, and the study by Raiswell *et al.*[10] for SSFe.

Samples were collected at least once a day during the 2012 Greenland melt season from the subglacial channel draining Leverett Glacier (LG), South-West Greenland (Fig. 1). The glacier is ~85 km long, has a catchment of >600 km^2 and mean summer discharge of >200 $m^3 s^{-1}$. It overlies predominantly Precambrian crystalline rocks, typical of large areas of Greenland. Over a melt season, the subglacial drainage system beneath LG evolves from a slow-inefficient drainage system to a fast-efficient channelized system[28]. Seasonal drainage evolution is accompanied by a number of substantial 'outburst' events ('P' events; Fig. 2), believed to be triggered by supra-glacial lake drainage events which force out solute enriched, long-term stored meltwater from the glacier bed[20]. Previous research indicates that these outburst events occur annually[19,20].

By far the most significant source of labile Fe in meltwaters was SSFe. Mean ascorbate-extractable Fe was 0.15% (dry weight; Table 1), equating to 29.0 µM of potentially bioavailable Fe. TEM microphotographs, spectral elemental analyses and nanodiffraction measurements of sediments confirmed that nanoparticulates were a mixture of clays and poorly ordered ferrihydrite around 5–10 nm diameter (Fig. 3). Ferrihydrite, a labile Fe nanoparticle, is indicative of recent Fe weathering and forms by the rapid oxidation of Fe^{2+} in solution. Fe^{2+} is expected to be generated in anoxic subglacial environments by microbially mediated sulphide oxidation[17,29], and potentially via microbial Fe reduction[30], although the latter is yet to be demonstrated.

The second most significant Fe phase is CNFe (Fig. 2b, middle). Discharge-weighted CNFe concentrations (mean Fe weighted for discharge at the time the sample was taken) were two orders of magnitude higher than DFe (699 nM; Table 1). Our CNFe concentrations spanned an order of magnitude, with a maximum concentration of 4,701 nM and a minimum concentration of 232 nM. The four highest measured CNFe concentrations were all closely associated with outburst events (Fig. 2; P1, P4, P5 and P6). High-suspended sediment loads were often associated with elevated CNFe concentrations (Fig. 2), as has been observed in riverine environments[31].

In contrast to SSFe and CNFe, mean DFe concentrations in the bulk runoff were low (7 nM; Table 1), and comparable with studies of smaller catchments[11]. DFe concentrations generally decreased throughout the season as pH rose from ~7 to >9, and supra-glacial meltwater input increased (Fig. 2a). Higher early season concentrations of DFe are indicative of the release of concentrated meltwaters from distributed drainage systems, when supra-glacial input was low, as were suspended sediment concentrations.

Ice sheet iron fluxes. To estimate an Fe budget for the entire GrIS we scale up our LG data (Fig. 2; Table 1). We use mean modelled runoff (418 $km^3 a^{-1}$) from 2000–2011 (ref. 32) as our representative runoff water flux, and modelled runoff (665 $km^3 a^{-1}$) for 2012[32] as an indicator of possible future water fluxes in a warmer climate (2012 was a record melt year; Table 2)[32,33]. Based on 2000–2011 mean discharge, this generates a mean flux of 0.71 Tg Fe a^{-1} (0.40–2.54), of which 0.70 Tg (0.40–2.43) is SSFe, and 0.01 Tg (0.01–0.11) is DFe/CNFe (Table 2).

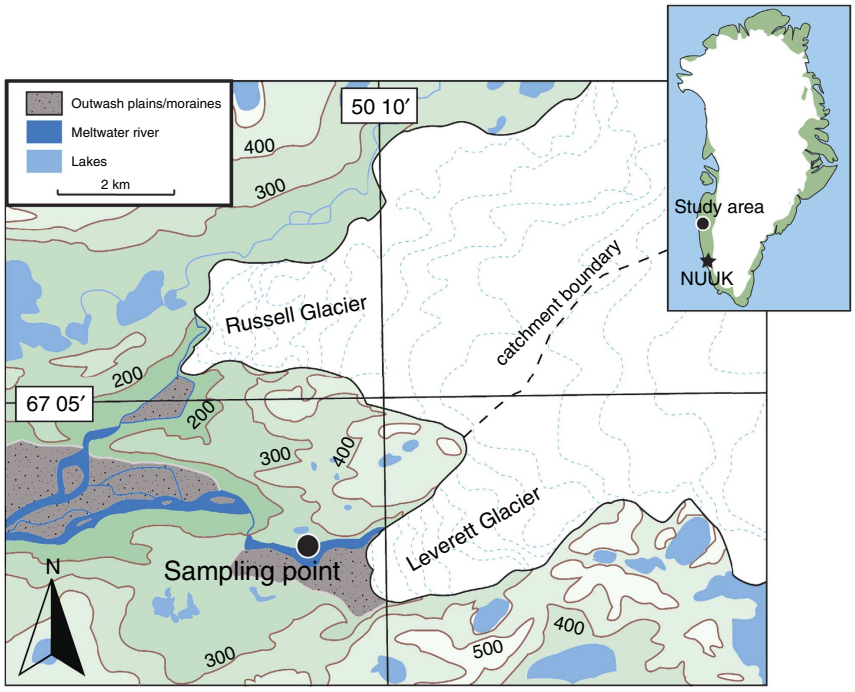

Figure 1 | Location of Leverett catchment. A catchment boundary is shown, deduced from data published in Cowton et al.[19] The glacier drains an area ~600 km^2 of the Greenland Ice Sheet. Adapated from 1:100,000 map. The approximate sampling location is marked with a black dot in the main image.

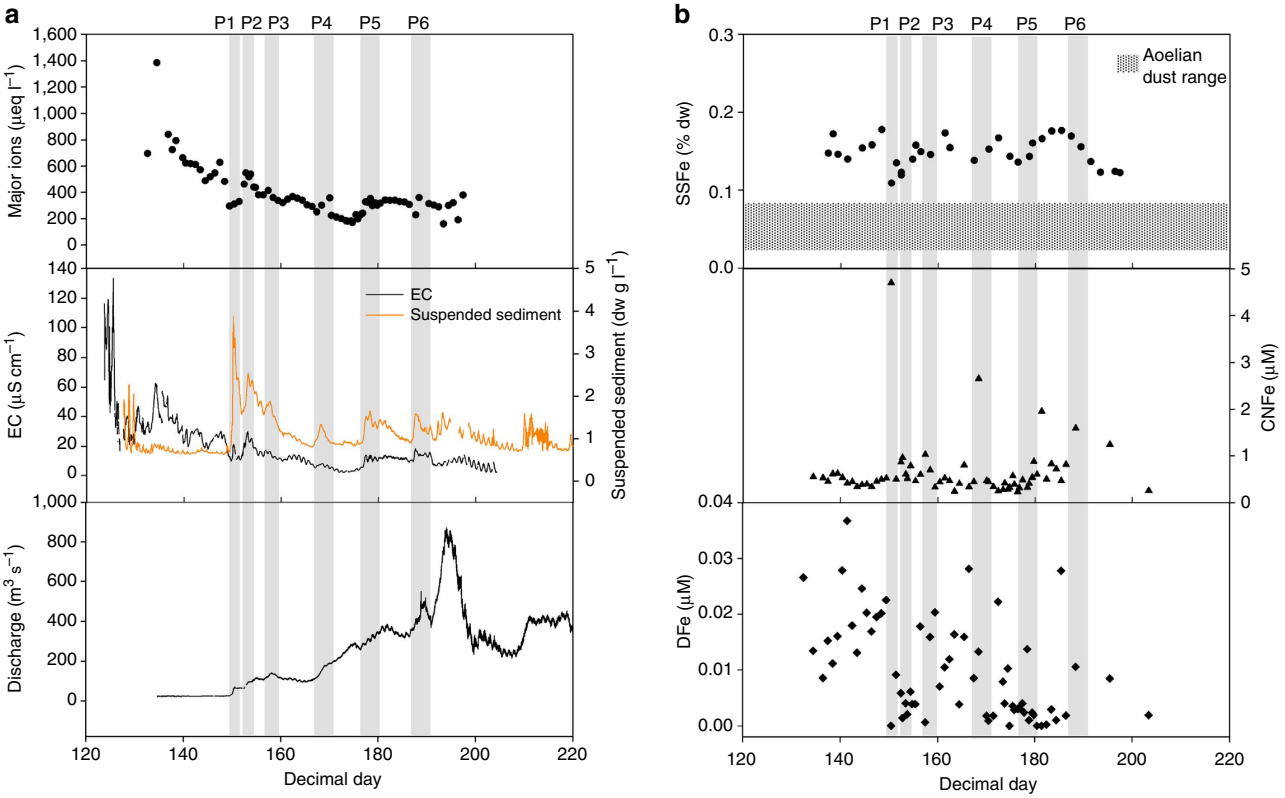

Figure 2 | Time series from LG proglacial river. (**a**) Summed major ion concentration (K^+, Na^+,Ca^{2+},Mg^{2+}, $SO4^{2-}$, Cl^-, HCO_3^-), Electrical conductivity (EC), suspended sediment concentrations and bulk discharge, and (**b**) of Fe fractions – SSFe, CNFe and DFe. The approximate timing of outburst events (P) is marked on **a** and **b** by shading. The range of ascorbate-extractable Fe concentrations found in aeolian dust is horizontally shaded in **b** for comparison.

Table 1 | Meltwater and suspended sediment Fe concentrations from Leverett Glacier and comparative studies.

Fe source	Mean Fe concentrations	s.d.	Fe range	n	Source
Filtered iron source (nM)					
Greenland					
<0.02 μm	7	9	<d1–37	66	DFe—this study
0.02–0.45 μm	699	650	232–4,701	63	CNFe—this study
<0.03 μm—GrIS	22		6–59	15	[11]
0.03–0.4 μm—GrIS	30.8		2–117	15	[11]
<0.2 μm—GrIS	3,700		2,200–9,310	13	[12]
Antarctica					
<0.2 μm—Blood Falls, AntIS	4×10^6			1	[41]
<0.45 μm—Dry Valleys, AntIS	335		82–1,146	11	[58]
Ascorbate-extractable sediments (% dw)					
Glacial meltwater—GrIS	0.15	0.02	0.11–0.18	33	SSFe—this study
Icebergs—AntIS	0.15	0.12	0.06–0.36	10	[10]
Icebergs—AntIS	0.19	0.18	0.04–0.49	4	[13]
Aoelian dust—East Med.	0.03			1	[37]
Aoelian dust—West Med.	0.08			1	[37]
Aoelian dust—Sahara	0.02			2	[37]
Aoelian dust—Sahel	0.02			2	[37]
Aoelian dust—Beijing	0.06			1	[37]

AntIS, Antarctic ice sheet; CNFe, colloidal/nanoparticulate Fe; DFe, dissolved Fe; GrIS, Greenland ice sheet.
Filtered concentrations are discharge weighted and presented in nanomolar. Values below the detection limit are indicated by <d1. Ascorbate-extractable concentrations are presented as % dry weight (% dw).

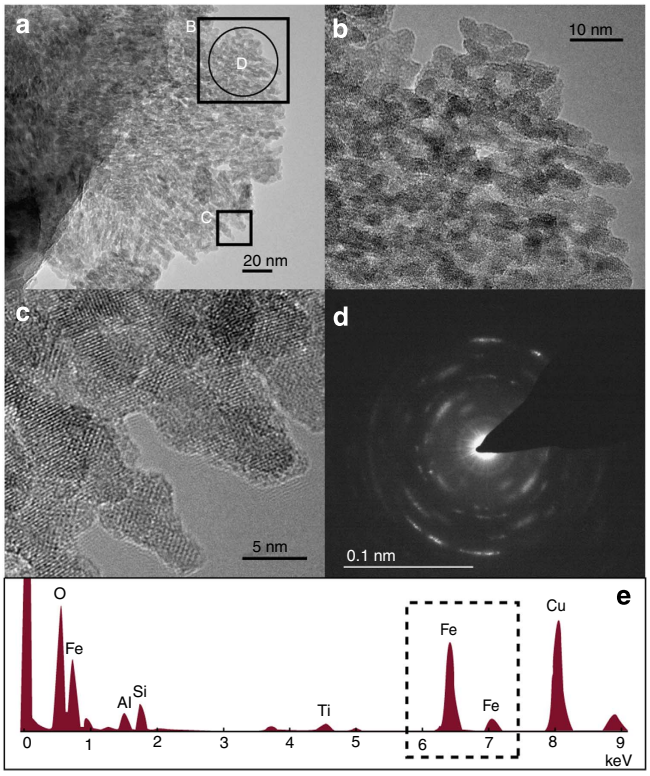

Figure 3 | Photomicrographs of LG subglacial suspended sediment. Nanoparticulate ferrihyrite ~5–10 nm in diameter has been identified. Images (**b**) and (**c**) are enlargements of (**a**), as indicated. The diffraction signal (**d**) shows some crystalline structure owing to possible impact of nano-clay particles, and potentially nano-hematite, but also the characteristic diffuse ferrihydrite rings are identifiable. EDS (**e**) analysis of the area further confirms Fe-dominated material.

Antarctic subglacial waters are not diluted by supra-glacial meltwater. They may be anoxic, with rock: water contact times likely an order of magnitude greater than in Greenland[18]. As a result, solute concentrations have been measured in the millimolar range, compared with a micromolar range from the GrIS[18,34]. We therefore postulate that our Fe concentrations might be conservative estimates for the AntIS. Hence, we employ the maximum concentrations of DFe (0.04 μM) and CNFe (4.70 μM) from our dataset to calculate Antarctic fluxes (Table 2). This produces a filterable phase meltwater flux range of 8.6–25.8 Gg a^{-1}, assuming a meltwater discharge of 32.5–97.5 km^3 a^{-1} (ref. 35). Although little is known of suspended sediment concentrations in Antarctic subglacial meltwater, evidence exists in sub-marine core records[36] for the release of sediment-rich meltwater plumes, and from first hand observations[21]. Using a lower order estimate of suspended sediment concentrations from Arctic glaciers (1 g l^{-1})[20] and assuming an ascorbate-extractable fraction of 0.15%, the AntIS SSFe flux is 48.8–146.3 Gg a^{-1}, which is of a similar order of magnitude to previous estimates[18].

Discussion

The data presented indicates that the potential for glacial iron export is large, driven primarily through SSFe and to a lesser extent CNFe. There appears to be no discernible trend in the SSFe concentrations through time (Fig. 2b, top: ± 12.4%), suggesting subglacial sediment exported from the catchment is largely compositionally uniform. Ascorbate-extractable SSFe is significantly higher than values reported from aeolian dust (0.02–0.09%)[37], and is close to those reported in Antarctic icebergs from Seymour Island (0.09–0.12%)[10], and the Weddell Sea (0.04–0.4%; Table 1)[13], indicating that glacial material is likely more bioavailable than aeolian dust. Culturing studies have already demonstrated the bioavailability of glacially derived

Table 2 | Fe fluxes from Leverett Glacier and scaled up estimates for the Greenland Ice Sheet and Antarctic Ice Sheet.

Source	Mass flux	Fe flux a^{-1}		
		Minimum	Mean	Maximum
Leverett catchment (Mg)				
DFe*	2.20 km^3 a^{-1}	0.0	0.9	4.5
CNFe*	2.20 km^3 a^{-1}	28.5	85.8	578
SSFe†	2.31 Tg a^{-1}	2,540	3,470	4,160
Total labile Fe		2,570	3,560	4,740
Greenland Ice Sheet (Gg)				
2000–2011 mean Q				
DFe‡	418 km^3 a^{-1}	0.0	0.2	0.9
CNFe‡	418 km^3 a^{-1}	5.4	16.3	110
SSFe§	0.3–1.6 Pg a^{-1}	403	695	2,430
Total labile Fe		409	712	2,540
2012 Q (Gg)				
DFe‡	665 km^3 a^{-1}	0.0	0.3	1.4
CNFe‡	665 km^3 a^{-1}	8.6	26.0	175
SSFe§	0.4–2.6 Pg a^{-1}	642	1,110	3,870
Total labile Fe		651	1,140	4,050
Antarctic Ice Sheet (Gg)				
DFe‖	32.5–97.5 km^3 a^{-1}	0.1	0.1	0.2
CNFe‖	32.5–97.5 km^3 a^{-1}	8.5	17.1	25.6
SSFe¶	0.03–0.10 Pg a^{-1}	48.8	97.5	146
Iceberg Fe#	1.25 Pg a^{-1}	600	900	1,200
Total labile Fe		657	1,010	1,370

CNFe, colloidal/nanoparticulate Fe; DFe, dissolved Fe; SSFe, sediment-bound nanoparticulate Fe.
Results presented to three significant figures.
Q indicates meltwater discharge.
*Calculated from minimum discharge-weighted mean and maximum Fe concentrations multiplied by the Leverett meltwater flux.
†Calculated using minimum (0.11%) discharge-weighted mean (0.15%) and maximum (0.18%) FeA concentrations, multiplied by the suspended sediment flux.
‡Calculated from minimum discharge-weighted mean and maximum recorded concentrations from Leverett catchment, multiplied by the Greenland meltwater flux.
§Calculated using minimum (0.643 g l^{-1}), discharge-weighted mean (1.109 g l^{-1}) and maximum (3.876 g l^{-1}) suspended sediment concentrations recorded from Leverett catchment, and the discharge weight mean Leverett FeA of 0.15%. We decided to use this method of calculation owing to the uncertainty surrounding mean suspended sediment concentrations in Greenlandic meltwaters, compared with the low standard deviation of FeA in samples.
‖Estimated using minimum (50% of mean), mean and maximum (150% of mean) meltwater fluxes from the study by Pattyn[35] coupled with maximum DFe and CNFe concentrations recorded from Leverett catchment.
¶Estimated using minimum (50% of mean), mean and maximum (150% of mean) meltwater fluxes from the study by Pattyn[35], a suspended sediment load of 1 g l^{-1} and mean Leverett FeA of 0.15%.
#From the study by Raiswell *et al.*[10]

sediment, with the addition of only 10 mg l^{-1} sediment increasing phytoplankton productivity in trace metal depleted waters[9].

Despite being of less importance than SSFe, CNFe concentrations are more than an order of magnitude greater than those previously reported from a smaller Greenlandic catchment (~10 km in length), located ~30 km to the north in a catchment with a similar bedrock type[11]. This suggests that catchment size, and hence meltwater residence times, are important in determining CNFe concentrations where geology remains relatively uniform[17]. In comparison, a smaller catchment in Greenland, of different lithology, yielded mean CNFe values nearly an order of magnitude higher than those reported here[12], indicating bedrock composition may be important in determining filterable iron concentrations. The periodic increase in the concentration of CNFe with outburst events (Fig. 2) is significant and suggests that the mode of subglacial meltwater release influences CNFe concentrations in meltwaters. It is hypothesized that dissolved (DFe) Fe(II) is formed *in situ* in isolated distributed systems within the subglacial environment, either in anoxic microcosms, or in more widespread anoxic systems[29,38]. Furthermore, observational evidence exists to suggest Fe(II) reservoirs may exist under the GrIS[39,40]. During outburst events (with elevated CNFe concentrations) Fe(II) from these more isolated parts of the drainage bed (long-term stored waters) may be oxidized *in situ* by injected O_2 saturated supra-glacial waters. The exported CNFe may therefore partly reflect oxidation of a large-subglacial Fe(II) pool. This has implications when considering Antarctic subglacial Fe discharge, as there are no oxygenated supra-glacial inputs to the subglacial system[18] and the ice sheet bed is thought to be anoxic[41,42], suggesting that Fe released in meltwater may be predominantly as Fe(II). One recent study has demonstrated that particulate Fe in marine waters around the Antarctic coastline, near the Jutulstarmen ice stream, has distinctive Fe(II) dominated mineralogy[43], which may suggest a subglacial source for the Fe(II). Hence, our data from outburst events at LG have clear relevance for Antarctica, where a substantial proportion of subglacial meltwater may be exported via subglacial lake drainage events[21–24]. Based upon these findings, we would anticipate Antarctic subglacial outbursts associated with lake drainage to also yield high concentrations of filterable Fe (CNFe + DFe).

DFe appears to be the least important component of glacial Fe export in bulk runoff. Although DFe concentrations rose during outburst events P5 and P6 (Fig. 2b), elevated levels were not consistent during all outburst events. Modification of DFe to CNFe fractions via oxidation and subsequent coagulation is likely to have occurred along the subglacial flowpath. Oxidation of DFe to CNFe (see discussion above) and eventual SSFe attachment, means that in Greenlandic catchments, DFe is likely less important than in Antarctica, where suboxic subglacial meltwater may directly enter oceanic waters[18].

The glacial impact on ocean productivity in iron-limited areas will depend on the magnitude of the glacial flux and the bioavailability of the exported Fe. High rates of physical erosion beneath ice sheets[19], combined with a suite of biogeochemical weathering processes that include sulphide oxidation[18,29], indicates that ice sheets are a globally significant source of labile Fe nanoparticles. Given the representative bedrock type and large catchment size, we believe our values are typical of the large outlet glaciers, which dominate water fluxes from the GrIS[44]. Leverett catchment is more than an order of magnitude larger than previously studied Greenlandic catchments, with a mean discharge of $212\,m^3\,s^{-1}$ (2009–2012) compared with $\sim 15\,m^3\,s^{-1}$ in the study by Statham *et al.*[11] and $<2\,m^3\,s^{-1}$ in the study by Bhatia *et al.*[12]

The global significance of subglacial Fe depends not only on the mass delivered but also on its behaviour following deposition in seawater. This is true for all sources of Fe. Behaviour is complex; iron may be dissolved (inorganically, photochemically and/or by complexation) and can be precipitated or lost by aggregation, sinking and scavenging[7]. A detailed consideration of these effects is beyond the scope of the present paper and we therefore present only a simple flux comparison between potentially bioavailable Fe from subglacial sources, icebergs and aeolian dust.

The iron flux calculated for the GrIS is significant. It is greater than the estimated input of labile Fe nanoparticles into the NA by icebergs ($0.25\,Tg\ SSFe\ a^{-1}$, assuming similar reactivity and sediment content to AntIS icebergs)[7], and comparable with aeolian dust input into the NA ($0.04–0.16\,Tg\ a^{-1}$, assuming Fe ascorbate solubility ranging from 0.02–0.085%)[5,37], but with more localized input, and less efficient transport to the open ocean[45]. If we consider that only ~10% of Fe may reach the open ocean (that is, ~90% is removed in the estuarine zone and coastal waters)[7], a conservative estimate of the GrIS meltwater Fe flux would be $0.07\,Tg\ Fe\ a^{-1}$ (0.04–0.25), similar to aeolian dust input. We believe that the data presented here is a truly conservative estimate of the labile Fe flux from the GrIS to the surrounding ocean owing to a number of reasons: Leverett suspended sediment load has been reported to be higher in previous years, and as high as $10\,g\,l^{-1}$ in other glacial catchments[19]; this does not include iron fluxes from Greenlandic icebergs (mean $497 \pm 50\,km^3\ a^{-1}$ from 1958 to 2010)[44], which have the potential for off-shelf fertilization; meltwater flux is predicted to increase in a warming climate (~60% higher based on preliminary 2012 GrIS meltwater flux; Table 1); and lastly, a number of Greenlandic glaciers discharge directly into the ocean[44], avoiding estuarine processing[7]. There is also an increasing body of evidence for medium to long-range transport (~100–900 km) of Fe bearing particles away from shelf/terrestrial sources to HNLC waters, with subsequent interactions with biota[46–48]. However, unlike aeolian dust, medium to long-range transport may require the additional process of recycling from shelf sediments, and its effect is currently poorly understood. Although Fe limitation is not commonly observed in oceans around Greenland (potentially owing to subglacial and aeolian dust inputs) parts of the south-western coastal margin are postulated to be iron limited[49–51], with large-annual blooms observed in this region strongly correlated to ice sheet meltwater input[52].

Our estimated AntIS iron flux is significantly higher than the estimated flux of labile Fe from dust to the SO ($5.3–23.0\,Gg\ a^{-1}$, assuming Fe ascorbate solubility of 0.02–0.085%)[5,37], although the input of meltwater-derived Fe will likely have a more localized impact than that of aeolian dust and iceberg-rafted Fe. Although meltwater fluxes of iron are an order of magnitude lower than the iceberg flux ($600–1{,}200\,Gg\ Fe\ a^{-1}$), recent work has demonstrated that subglacially derived Fe from ice streams may be able to travel up to 150 km offshore, fuelling productive phytoplankton blooms in the Amundsen Sea[46]. Significant lateral export of Fe, fuelling plankton blooms, has also been observed off other coastal areas of Antarctica[53,54], and meltwater input has been correlated to large-annual phytoplankton blooms off the Antarctic Peninsula, located both locally to the source location and over 100 km offshore[55]. Furthermore, a recent study found a unique Fe(II) signature downstream of the Jutulstraumen Ice Stream in Antarctica[43]. However, the source and mechanism of delivery wasn't known and the link to glacial input of bioavailable Fe is yet to be firmly established.

We conclude that ice sheets are likely to play a more significant role in the global iron cycle than previously recognized, via fresh subglacial weathering of Fe bearing minerals. SSFe and CNFe fluxes from the Antarctic and Greenland Ice Sheets are comparable, if not larger, than aeolian dust input to their respective regions (NA and SO), but may have a more localized impact owing to point source input. Our iron flux estimates for the AntIS demonstrate that meltwater discharge may supplement bioavailable Fe delivery to the SO from icebergs and aeolian dust, and thus, should be considered in future climate models. The impact of global warming on these iron budgets is unknown. However, it is likely that ice sheets will provide a greater flux of bioavailable Fe to coastal regions as larger quantities of meltwater are exported to the oceans in a warmer climate.

Methods

Water sample collection and filtration. Bulk meltwater samples were taken throughout main melt period (May June and July 2012) around ~1 km downstream from the glacier terminus (Fig. 1). For the majority of the sampling period, samples were collected at least once a day, always at 10:00 h, and on occasion at 18:00 h to observe diurnal variation. We know these waters were representative of bulk discharge as LG drains from a single portal on the northern side of the terminus[20], and point samples taken at the portal were of similar concentration to those taken downstream. Suspended sediment samples (SSFe) were collected by filtering ~200 ml of meltwater onto a 0.45 µm cellulose nitrate filter (Whatman). In accordance with studies of iron (oxy)hydroxide stability[7,27,56] samples were stored damp on the filter papers in a refrigerated 25 ml polypropylene bottle until analysis at the University of Leeds, ~3–4 months after collection. Little aging of freshly precipitated (oxy)hydroxides was therefore expected as the half life of transformation to more crystalline forms is >500 days at this temperature.

DFe and CNFe were collected according to trace metal procedures adopted by Schroth *et al.*[16], from methods developed by Shiller[31], and by using the trace metal sampling practices of Howard and Statham[57], with subsequent improvements for glacial meltwaters (Statham, personal communication). Briefly, all sampling equipment was sequentially soaked in a 6 M HCl acid bath (24 h), washed ×3 with ultrapure 18.2 MΩ cm Milli-Q water (Millipore), soaked in a 6 M HNO_3 acid bath (24 h), with a final ×6 wash with Milli-Q water before drying in a laminar flow hood. All sampling bottles were trace metal grade Nalgene LDPE (Thermo Scientific). Filters were cleaned with trace metal grade HCl in accordance with the study by Shiller[31]. CNFe was defined by using a 0.45 µm Whatman GD/XP syringe filter with polypropylene pre-filters and a polyethersulfone final filter (designed for trace metal analysis, high-particulate load samples). DFe was defined by using Whatman Anotop 0.02 µm syringe filters. Samples filtered for 0.02 µm used a 0.45 µm GD/XP filter as a pre-filter. Filtration was always conducted in a designated 'clean' lab tent, within a labmade box (low-density polyethylene sheet plastic covering a polycarbonate piping frame), thus minimizing any contamination with dust. Samples were preserved in the field by acidifying with Optima HNO_3 (Fisher) to a pH<2. Field procedural blanks were taken using transported Milli-Q water, using the same procedures that had been applied to glacial samples.

SSFe extractions. Sediment extractions were carried out according to the study by Raiswell *et al.*[27], with sequential extractions for amorphous ferrihydrite (ascorbate), and crystalline Fe (oxy)hydroxides (dithionite–data not presented in this study). Total Fe was analyzed by atomic absorption spectroscopy using an Analytik Jena High-Resolution Continuum Source, ContrAA 700 instrument at the School of Earth and Environment, University of Leeds. A procedural blank was below the detection limit of the instrument, while replicates showed a standard deviation of ±1.5%.

DFe and CNFe determination. DFe and CNFe were determined at the National Oceanography Centre (Southampton) Mass Spectrometer Lab, using a Thermo

Scientific XSERIES 2 quadrupole ICP-MS, with Be, In and Re as internal standards. CNFe blanks were 1.2 ± 0.7% of the lowest recorded concentration. DFe blanks were at or below the machine's detection limit of ~1 nM—sample values lower than this were recorded as <d1.

Microspectroscopic and nanodiffraction analyses. The morphology, structure and crystallinity of all phases but with particular focus on Fe (oxy)hydroxides were determined using Field Emission Gun Transmission Electron Microscopy (FEG-TEM; Tecnai) operating at 200 kV. Samples were dispersed in ethanol using an ultrasonic bath for ~1 min, and then a drop was pipetted onto an Agar standard holey carbon support films. Low fluency and high-resolution images of nano-particles were complemented by energy dispersive spectra (acquired with an Oxford Instrument EDS analyses system) and selected area electron diffraction patterns that were recorded to determine elemental characteristics of identified Fe nanophases.

Mass flux for leverett catchment. Total-meltwater flux from Leverett catchment was calculated from a season long record of meltwater discharge as in the study by Cowton *et al.*[19] (Fig. 2). Briefly, the meltwater river was monitored in a stable bedrock section ~2.2 km downstream of the terminus. Stage was logged every 5 min until July, when it was logged every 10 min. This was converted to discharge using a rating curve of rhodamine dye-dilution experiments.

Suspended sediment flux was calculated from suspended sediment concentrations[19], which were multiplied by discharge at each logged time point. Suspended sediment concentration was derived from a season long logged turbidity sensor. The turbidity sensor was calibrated using manual sediment collections. Briefly, 300 ml of meltwater was filtered through a 0.45 µm cellulose nitrate filter, oven dried overnight at 40 °C and weighed. Suspended sediment flux was calculated from the combined discharge and suspended sediment concentration time series.

Mass fluxes for the greenland and AntISs. Mean modelled GrIS runoff from the study by Tedesco *et al.*[32] for the period 2000–2011 is used, alongside the modelled 2012 runoff, a record melt year that may provide an indication of future meltwater flux. Suspended sediment flux was calculated from minimum (0.643 $g\,l^{-1}$) discharge-weighted mean (1.109 $g\,l^{-1}$) and maximum (3.876 $g\,l^{-1}$) recorded concentrations from Leverett catchment, multiplied by the Greenland meltwater flux.

For Antarctic meltwater flux, modelled basal melt rates from the study by Pattyn[35], of 65 km^3, with a standard deviation of ± 50% for minimum and maximum estimates were used to calculate meltwater flux from the Ice Sheet. Suspended sediment flux was estimated using a 1 $g\,l^{-1}$ suspended sediment concentration, as in the study by Wadham *et al.*[18]

References

1. Martin, J. H., Fitzwater, S. E. & Gordon, R. M. Iron deficiency limits phytoplankton growth in Antarctic waters. *Glob. Biogeochem. Cycles* **4,** 5–12 (1990).
2. Nielsdottir, M. C., Moore, C. M., Sanders, R., Hinz, D. J. & Achterberg, E. P. Iron limitation of the postbloom phytoplankton communities in the Iceland Basin. *Glob. Biogeochem. Cycles* **23,** GB3001 (2009).
3. de Baar, H. J. W., Gerringa, L. J. A., Laan, P. & Timmermans, K. R. Efficiency of carbon removal per added iron in ocean iron fertilization. *Mar. Ecol. Prog. Ser.* **364,** 269–282 (2008).
4. Laws, E. A., Falkowski, P. G., Smith, W. O., Ducklow, H. & McCarthy, J. J. Temperature effects on export production in the open ocean. *Glob. Biogeochem. Cycles* **14,** 1231–1246 (2000).
5. Jickells, T. D. *et al.* Global iron connections between desert dust, ocean biogeochemistry, and climate. *Science* **308,** 67–71 (2005).
6. Fan, S. M., Moxim, W. J. & Levy, H. Aeolian input of bioavailable iron to the ocean. *Geophys. Res. Lett.* **33,** L07602 (2006).
7. Raiswell, R. & Canfield, D. E. The iron biogeochemical cycle past and present. *Geochem. Perspect.* **1,** 1–220 (2012).
8. Lannuzel, D., Schoemann, V., de Jong, J., Tison, J. L. & Chou, L. Distribution and biogeochemical behaviour of iron in the East Antarctic sea ice. *Mar. Chem.* **106,** 18–32 (2007).
9. Smith, K. L. *et al.* Free-drifting icebergs: Hot spots of chemical and biological enrichment in the Weddell Sea. *Science* **317,** 478–482 (2007).
10. Raiswell, R., Benning, L. G., Tranter, M. & Tulaczyk, S. Bioavailable iron in the Southern Ocean: the significance of the iceberg conveyor belt. *Geochem. Trans.* **9,** 7 (2008).
11. Statham, P. J., Skidmore, M. & Tranter, M. Inputs of glacially derived dissolved and colloidal iron to the coastal ocean and implications for primary productivity. *Glob. Biogeochem. Cycles* **22,** GB3013 (2008).
12. Bhatia, M. P. *et al.* Greenland meltwater as a significant and potentially bioavailable source of iron to the ocean. *Nat. Geosci.* **6,** 274–278 (2013).
13. Shaw, T. J. *et al.* Input, composition, and potential impact of terrigenous material from free-drifting icebergs in the Weddell Sea. *Deep-Sea Res. II* **58,** 1376–1383 (2011).
14. Death, R. *et al.* Antarctic Ice Sheet fertilises the Southern Ocean. *Biogeosciences Discuss.* **10,** 12551–12570 (2013).
15. Le Brocq, A. *et al.* Evidence from ice shelves for channelized meltwater flow beneath the Antarctic Ice Sheet. *Nat. Geosci.* **6,** 945–948 (2013).
16. Schroth, A. W., Crusius, J., Chever, F., Bostick, B. C. & Rouxel, O. J. Glacial influence on the geochemistry of riverine iron fluxes to the Gulf of Alaska and effects of deglaciation. *Geophys. Res. Lett.* **38,** L16605 (2011).
17. Wadham, J. L. *et al.* Biogeochemical weathering under ice: size matters. *Glob. Biogeochem. Cycles* **24,** GB3025 (2010).
18. Wadham, J. *et al.* The potential role of the Antarctic Ice Sheet in global biogeochemical cycles. *Earth Environ. Sci. Trans. R. Soc. Edinb.* **104,** 55–67 (2013).
19. Cowton, T., Nienow, P., Bartholomew, I., Sole, A. & Mair, D. Rapid erosion beneath the Greenland ice sheet. *Geology* **40,** 343–346 (2012).
20. Bartholomew, I. *et al.* Supraglacial forcing of subglacial drainage in the ablation zone of the Greenland ice sheet. *Geophys. Res. Lett.* **38,** L08502 (2011).
21. Goodwin, L. The nature and origin of a jokulhlaup near Casey Station, Antarctica. *J. Glaciol.* **34,** 95–101 (1988).
22. Wingham, D. J., Siegert, M. J., Shepherd, A. & Muir, A. S. Rapid discharge connects Antarctic subglacial lakes. *Nature* **440,** 1033–1036 (2006).
23. Fricker, H. A., Scambos, T., Bindschadler, R. & Padman, L. An active subglacial water system in West Antarctica mapped from space. *Science* **315,** 1544–1548 (2007).
24. McMillan, M. *et al.* Three-dimensional mapping by CryoSat-2 of subglacial lake volume changes. *Geophys. Res. Lett.* **40,** 4321–4327 (2013).
25. Knight, P. G., Waller, R. I., Patterson, C. J., Jones, A. P. & Robinson, Z. P. Discharge of debris from ice at the margin of the Greenland ice sheet. *J. Glaciol.* **48,** 192–198 (2002).
26. Kalsbeek, F. The evolution of the Precambrian Shield of Greenland. *Geol. Rundsch.* **71,** 38–60 (1982).
27. Raiswell, R., Vu, H. P., Brinza, L. & Benning, L. G. The determination of labile Fe in ferrihydrite by ascorbic acid extraction: methodology, dissolution kinetics and loss of solubility with age and de-watering. *Chem. Geol.* **278,** 70–79 (2010).
28. Chandler, D. M. *et al.* Evolution of the subglacial drainage system beneath the Greenland Ice Sheet revealed by tracers. *Nat. Geosci.* **6,** 195–198 (2013).
29. Tranter, M., Sharp, M., Lamb, H., Brown, G., Hubbard, B. & Willis, I. Geochemical weathering at the bed of Haut Glacier d'Arolla, Switzerland, a new model. *Hydrol. Process.* **16,** 959–993 (2002).
30. Lovley, D. R. Dissimilatory Fe(III) and Mn(IV) reduction. *Microbiol. Rev.* **55,** 259–287 (1991).
31. Shiller, A. M. Syringe filtration methods for examining dissolved and colloidal trace element distributions in remote field locations. *Environ. Sci. Technol.* **37,** 3953–3957 (2003).
32. Tedesco, M. *et al.* Evidence and analysis of 2012 Greenland records from spaceborne observations, a regional climate model and reanalysis data. *Cryosphere* **7,** 615–630 (2013).
33. Nghiem, S. V. *et al.* The extreme melt across the Greenland ice sheet in 2012. *Geophys. Res. Lett.* **39,** L20502 (2012).
34. Skidmore, M., Tranter, M., Tulaczyk, S. & Lanoil, B. Hydrochemistry of ice stream beds - evaporitic or microbial effects? *Hydrol. Process.* **24,** 517–523 (2010).
35. Pattyn, F. Antarctic subglacial conditions inferred from a hybrid ice sheet/ice stream model. *Earth Planet. Sci. Lett.* **295,** 451–461 (2010).
36. Lowe, A. L. & Anderson, J. B. Reconstruction of the West Antarctic Ice Sheet in Pine Island Bay during the last glacial maximum and its subsequent retreat history. *Quat. Sci. Rev.* **21,** 1879–1897 (2002).
37. Shi, Z. B. *et al.* Impacts on iron solubility in the mineral dust by processes in the source region and the atmosphere: A review. *Aeolian Res.* **5,** 21–42 (2012).
38. Bottrell, S. H. & Tranter, M. Sulphide oxidation under partially anoxic conditions at the bed of the Haut Glacier d'Arolla, Switzerland. *Hydrol. Process.* **16,** 2363–2368 (2002).
39. Yde, J. C. *et al.* Basal ice microbiology at the margin of the Greenland ice sheet. *Ann. Glaciol.* **51,** 71–79 (2010).
40. Christner, B. C., Montross, G. G. & Priscu, J. C. Dissolved gases in frozen basal water from the NGRIP borehole: implications for biogeochemical processes beneath the Greenland Ice Sheet. *Polar Biol.* **35,** 1735–1741 (2012).
41. Mikucki, J. A. *et al.* A contemporary microbially maintained subglacial ferrous 'ocean'. *Science* **324,** 397–400 (2009).
42. Wadham, J. L. *et al.* Potential methane reservoirs beneath Antarctica. *Nature* **488,** 633–637 (2012).

43. von der Heyden, B. P., Roychoudhury, A. N., Mtshali, T. N., Tyliszczak, T. & Myneni, S. C. B. Chemically and geographically distinct solid-phase iron pools in the Southern Ocean. *Science* **338,** 1199–1201 (2012).
44. Bamber, J., van den Broeke, M., Ettema, J., Lenaerts, J. & Rignot, E. Recent large increases in freshwater fluxes from Greenland into the North Atlantic. *Geophys. Res. Lett.* **39,** L19501 (2012).
45. Li, F., Ginoux, P. & Ramaswamy, V. Distribution, transport, and deposition of mineral dust in the Southern Ocean and Antarctica: contribution of major sources. *J. Geophys. Res. Atmos.* **113,** D10207 (2008).
46. Gerringa, L. J. A. *et al.* Iron from melting glaciers fuels the phytoplankton blooms in Amundsen Sea (Southern Ocean): iron biogeochemistry. *Deep-Sea Res. II* **71-76,** 16–31 (2012).
47. Lam, P. J. *et al.* Wintertime phytoplankton bloom in the subarctic Pacific supported by continental margin iron. *Glob. Biogeochem. Cycles* **20,** GB1006 (2006).
48. Planquette, H., Sanders, R. R., Statham, P. J., Morris, P. J. & Fones, G. R. Fluxes of particulate iron from the upper ocean around the Crozet Islands: A naturally iron-fertilized environment in the Southern Ocean. *Glob. Biogeochem. Cycles* **25,** GB2011 (2011).
49. Tagliabue, A., Bopp, L. & Aumont, O. Ocean biogeochemistry exhibits contrasting responses to a large scale reduction in dust deposition. *Biogeosciences* **5,** 11–24 (2008).
50. Moore, J. K., Doney, S. C., Glover, D. M. & Fung, I. Y. Iron cycling and nutrient-limitation patterns in surface waters of the World Ocean. *Deep-Sea Res. II* **49,** 463–507 (2002).
51. Saba, V. S. *et al.* An evaluation of ocean color model estimates of marine primary productivity in coastal and pelagic regions across the globe. *Biogeosciences* **8,** 489–503 (2011).
52. Frajka-Williams, E. & Rhines, P. B. Physical controls and interannual variability of the Labrador Sea spring phytoplankton bloom in distinct regions. *Deep-Sea Res. II* **57,** 541–552 (2010).
53. Charette, M. A. *et al.* Radium isotopes as tracers of iron sources fueling a Southern Ocean phytoplankton bloom. *Deep-Sea Res. II* **54,** 1989–1998 (2007).
54. Dulaiova, H., Ardelan, M. V., Henderson, P. B. & Charette, M. A. Shelf-derived iron inputs drive biological productivity in the southern Drake Passage. *Glob. Biogeochem. Cycles* **23,** GB4014 (2009).
55. Dierssen, H. M., Smith, R. C. & Vernet, M. Glacial meltwater dynamics in coastal waters west of the Antarctic peninsula. *Proc. Natl Acad. Sci. USA* **99,** 1790–1795 (2002).
56. Schwertmann, U., Stanjek, H. & Becher, H. H. Long-term *in vitro* transformation of 2-line ferrihydrite to goethite/hematite at 4, 10, 15 and 25 degrees C. *Clay Miner.* **39,** 433–438 (2004).
57. Howard, A. G. & Statham, P. *Inorganic Trace Analysis: Philosophy and Practice* (Wiley, 1993).
58. Green, W. J., Stage, B. R., Preston, A., Wagers, S., Shacat, J. & Newell, S. Geochemical processes in the Onyx River, Wright Valley, Antarctica: major ions, nutrients, trace metals. *Geochim. Cosmochim. Acta* **69,** 839–850 (2005).

Acknowledgements

This research is part of the UK Natural Environment Research Council, NERC funded DELVE (NERC grant NE/I008845/1) and associated NERC PhD studentship to JH, and Weathering Science Consortium (NE/C004566/1) projects. AT was funded by a NERC studentship and MOSS scholarship. PN was supported by grants from the Carnegie Trust for University of Scotland and The University of Edinburgh Development Trust. Additional support was provided by the Leverhulme Trust, via a Leverhulme research fellowship to JLW. We thank all of those assisted with fieldwork at LG. We would also like to thank Dr Mike Ward, Dr Adriana Matamoros Veloza and Dr Samuel Allshorn at the University of Leeds for their help in laboratory analysis, and Dr Matthew Cooper and Dr Andy Milton for help at the NOC Plasma Mass Spectrometry lab.

Author contributions

All authors made significant contributions to the research presented here. J.L.W. and M.T. conceived the project. J.R.H., R.R., A.T., P.N., K.L., J.T. and J.L.W. collected the field data. J.R.H. and J.L.W. wrote the manuscript. J.R.H. undertook lab analysis. L.G.B. provided significant help and invaluable advice in lab analysis. P.S. and R.R. aided in developing the field methods.

Additional information

Supplementary Information accompanies this paper at http://www.nature.com/naturecommunications

Competing financial interests: The authors declare no competing financial interests.

Reprints and permission information is available online at http://npg.nature.com/reprintsandpermissions/

How to cite this article: Hawkings, J. R. *et al.* Ice sheets as a significant source of highly reactive nanoparticulate iron to the oceans. *Nat. Commun.* 5:3929 doi: 10.1038/ncomms4929 (2014).

Appendix E

Hawkings *et al.*, 2015 (Geochem. Persp. Let.)

Geochemical Perspectives Letters

The effect of warming climate on nutrient and solute export from the Greenland Ice Sheet

J.R. Hawkings[1]*, J.L. Wadham[1], M. Tranter[1], E. Lawson[1,2], A. Sole[3], T. Cowton[3,4], A.J. Tedstone[4], I. Bartholomew[4], P. Nienow[4], D. Chandler[1], J. Telling[1]

OPEN ACCESS

doi: 10.7185/geochemlet.1510

Abstract

Glacial meltwater runoff is likely an important source of limiting nutrients for downstream primary producers. This has particular significance for regions surrounding the Greenland Ice Sheet, which discharges >400 km^3 of meltwater annually. The Arctic is warming rapidly but the impact of higher discharge on nutrient export is unknown. We present four years of hydrological and geochemical data from a large Greenland Ice Sheet catchment that includes the two highest melt years on record (2010, 2012). Measurements reveal significant variation in dissolved solute (major ion) and estimated dissolved macronutrient (nitrogen, phosphorus and silica) fluxes, with increases in higher melt years. Labile particulate macronutrients dominate nutrient export, accounting for ~50 % of nitrogen and >80 % of both phosphorus and silica. The response of ice sheet nutrient export to enhanced melting is largely controlled by particle bound nutrients, the future supply of which is uncertain. We propose that the Greenland Ice Sheet provides an underappreciated and annually dynamic source of nutrients for the polar oceans, with changes in meltwater discharge likely to impact marine primary productivity in future decades.

Received 10 March 2015 | Accepted 19 June 2015 | Published 23 June 2015

Introduction

Recent estimates predict global mean surface warming of up to 4.8 °C above the 1986-2005 mean by 2100, with the polar regions subject to more extreme increases (Collins *et al.*, 2013). Already, the Greenland Ice Sheet has experienced

1. Bristol Glaciology Centre, School of Geographical Sciences, University of Bristol, University Road, Bristol, BS8 1SS, UK
* Corresponding author (email: jon.hawkings@bristol.ac.uk)
2. School of Geography, University of Nottingham, University Park, Nottingham, NG7 2RD, UK
3. Department of Geography, The University of Sheffield, Western Bank, Sheffield, S10 2TN, UK
4. School of Geoscience, University of Edinburgh, Drummond Street, Edinburgh, EH8 9XP, UK

increased surface temperatures, with the five highest melt seasons on record occurring since 2000 (Tedesco *et al.*, 2013). In 2012, surface melting was the most widespread in over 100 years (Tedesco *et al.*, 2013). By 2100, the annual freshwater flux from the Greenland Ice Sheet could exceed 1000 km^3 a^{-1}, making it one of the world's largest sources of freshwater (Fettweis *et al.*, 2013).

Currently, we lack information about the impact of meltwater on downstream biogeochemical cycles, even though the coastal waters surrounding the ice sheet harbour highly productive ecosystems, that are strong CO_2 sinks (Rysgaard *et al.*, 2012). Recent work has highlighted the importance of glacier meltwater, including delivery of essential nutrients to the polar oceans (Bhatia *et al.*, 2013; Wadham *et al.*, 2013; Hawkings *et al.*, 2014; Lawson *et al.*, 2014). However, whether glacier melting provides an important negative climate feedback through its effect on marine primary production and CO_2 drawdown remains unknown.

Future changes to Greenland Ice Sheet hydrology will probably impact the export of solute and reactive sediments to the polar oceans. Much of the meltwater drains from the surface to the ice sheet bed, chemically weathering the subglacial sediments (Bartholomew *et al.*, 2011). Supraglacial lake drainage events are particularly important because they rapidly channel large quantities of meltwater to the ice sheet bed, flushing out stored, solute-rich, subglacial waters (Bartholomew *et al.*, 2011; Hawkings *et al.*, 2014). Supraglacial lake formation and the migration of drainage systems inland in a warming climate (Leeson *et al.*, 2015) could expose new subglacial areas to meltwater flushing, potentially enhancing solute evacuation. Glaciers are effective at fracturing and grinding bedrock (Cowton *et al.*, 2012), producing turbid meltwaters with abundant, very fine suspended particles, *i.e.* >1 g L^{-1} (Cowton *et al.*, 2012). Suspended material has recently been identified as a potential source of labile nutrients to near coastal regions (Hodson *et al.*, 2004; Bhatia *et al.*, 2013; Hawkings *et al.*, 2014; Wehrmann *et al.*, 2014) but data are sparse.

In this study, we present a full suite of geochemical and hydrological data from Leverett Glacier, a large (~600 km^2), land terminating, outlet glacier of the Greenland Ice Sheet (details in Supplementary Information). The data cover four years (2009-2012) where melting intensity varied (Fig. 1), including the two highest melt seasons on record. This is the most comprehensive dataset yet on major ion and nutrient concentrations from a glacial system.

Results and Discussion

Hydrological data (discharge, electrical conductivity and suspended material concentration) were collected for all four years (2009-2012) at a stable bedrock section ~2.2 km downstream of the glacier mouth. Major ion data are available for 2009, 2010 and 2012 and we used them to interpolate concentrations for 2011. Nutrient flux for 2009, 2010 and 2011 was estimated from 2012 data using a correlation with electrical conductivity. Further details are provided below and in Supplementary Information.

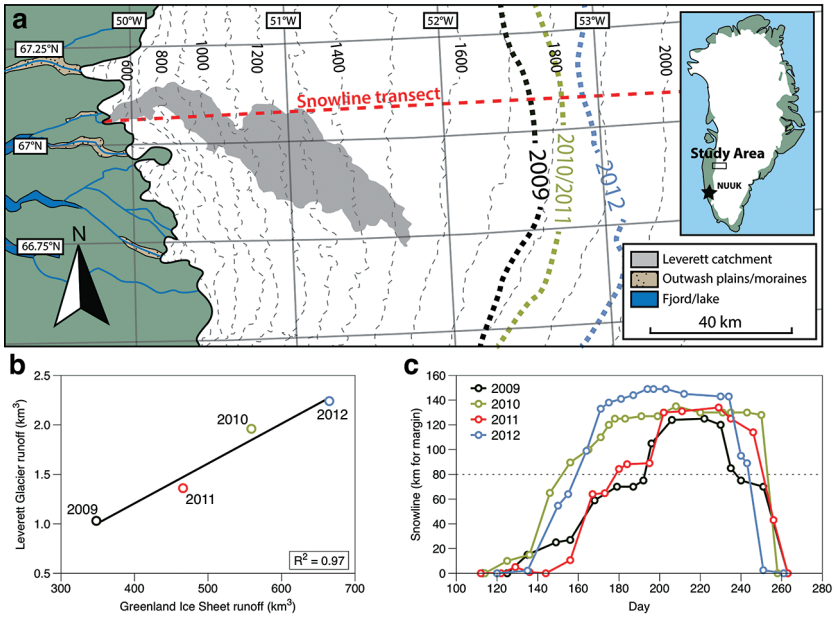

Figure 1 Field site and basic hydrological data. **(a)** Leverett Glacier with the snowline transect used to determine the point where snow covers the ice surface, derived from MODIS imagery. Dashed lines represent elevation contours. The catchment area was determined from a surface digitial elevation model (Palmer *et al.*, 2011). **(b)** Leverett Glacier meltwater discharge (Table 1) versus modelled Greenland Ice Sheet runoff (Tedesco *et al.*, 2013). **(c)** Leverett Glacier snowline; open circles represent observed position; connecting lines are linear estimates of retreat, interpolated between the measurements. Estimated catchment extent is represented by the dotted line at ~80 km.

Hydrology

The 2010 and 2012 ablation seasons produced the largest volumes of meltwater on record (Tedesco *et al.*, 2013). This is reflected in Leverett Glacier discharge (Fig. S-1), which was proportional to annual ice sheet runoff (R^2 = 0.97; Fig. 1b). The snowline also reached maximum elevation in 2012, 14 km further inland than in 2010 and 2011 (Table 1; Fig. 1c). 2009 and 2011 can be considered "average" melt years, with discharge proportional to the mean meltwater flux over the past decade. 2010 and 2012, with significantly above average discharge, were "extreme" melt years. This characterisation provides a benchmark for evaluating future trends because the frequency of extreme seasons is likely to increase (Fettweis *et al.*, 2013).

Table 1 Flux and hydrological data.

	Units	Year			
		2009	2010	2011	2012
Greenland Ice Sheet runoff *	km^3	348	559	466	665
Leverett Glacier discharge	km^3	0.94	1.79	1.10	2.03
Snowline above catchment	est. days	45	100	73	85
Snowline retreat from margin	km	125	135	135	149
Solute Flux	eq	3.0×10^8	5.6×10^8	3.2×10^8	5.6×10^8
Sediment Flux	t	3.7×10^6	2.6×10^6	3.0×10^6	2.2×10^6
Dissolved inorganic nitrogen †	t	25	46	26	48
Dissolved silica †	t	130	230	120	230
Dissolved inorganic phosphorus†	t	6.2	12	6.7	12
Dissolved inorganic nitrogen ‡	t	22	41	25	47
Dissolved silica ‡	t	110	220	130	240
Dissolved inorganic phosphorus‡	t	7.8	15	8.9	16
Exchangeable NH_4**	t	19-58	13-41	15-47	11-35
Amorphous silica**	t	18,000-44,000	12,000-31,000	14,000-36,000	11,000-26,000
NaOH extractable phosphorus**	t	20-130	14-92	16-110	12-78

All estimates are shown to Decimal Day 230/231, *i.e.* 17 August.
Estimates are reported with 2 significant digits.
eq = molar equivalent
t = tons of dry element
Snowline: the boundary where snow covers the underlying ice. Down glacier from this point is exposed ice, where the snow cover has melted.
* Greenland Ice Sheet runoff estimates from Tedesco *et al.* (2013).
** Sediment fluxes given as range based on minimum and maximum extractable nutrient concentrations.
† Fluxes estimated with electrical conductivity.
‡ Fluxes estimated using discharge weighted mean.

Solute flux

We estimated total solute export for all years from the electrical conductivity (EC) of the meltwater (Fig. S-3). The major ion (Ca^{2+}, Mg^{2+}, K^+, Na^+, Cl^-, SO_4^{2-}, HCO_3^-) concentrations are a linear function of conductivity with R^2 = 0.87 (2009), 0.77 (2010) and 0.98 (2012) (Figs. S-3 and S-4). We have a full hydrological dataset (discharge, EC and suspended material) from 2011 but major ion data are missing so using the concentration-conductivity correlation for data from 2009, 2010 and 2012 (n = 368; R^2 = 0.89), we estimated 2011 solute concentrations (Fig. S-3). Solute flux was estimated by cumulatively summing the total solute concentration

at each conductivity measurement time step (Fig. 2). We differentiated supraglacial solute from the total solute flux to assess the importance of subglacial sources (Fig. 2a). The estimates suggest that flushing of stored subglacial waters and rapid weathering of subglacial sediments by dilute supraglacial meltwater account for >95 % of the solute export from the catchment.

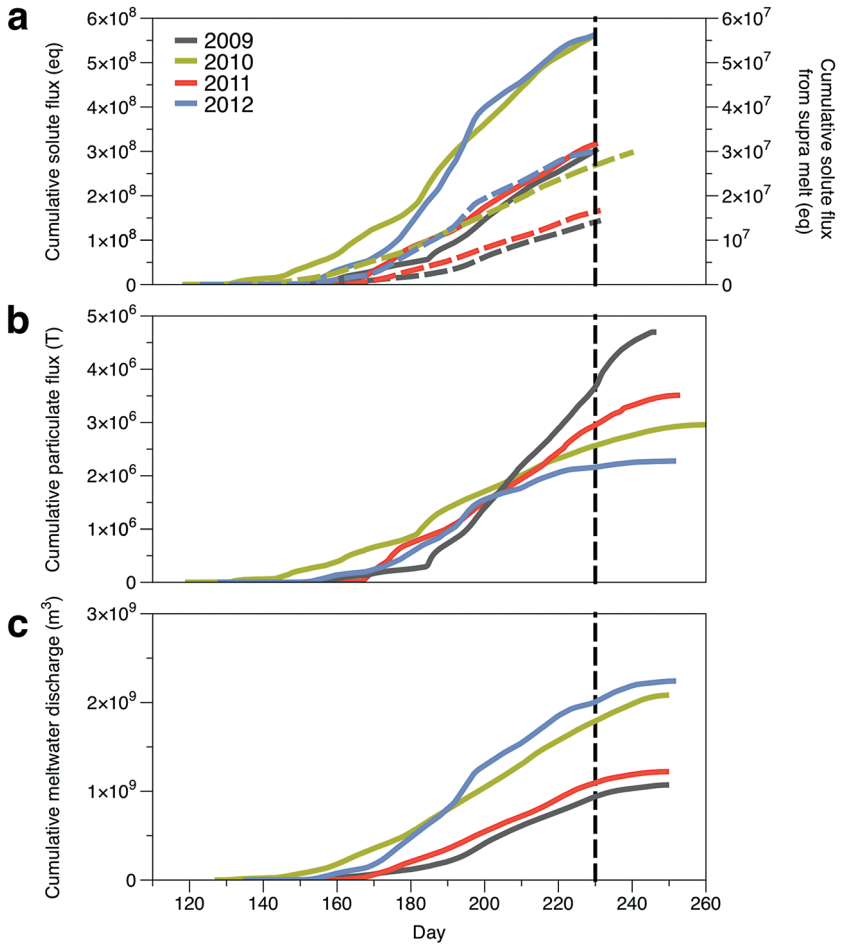

Figure 2 Cumulative solute and sediment flux. **(a)** Solid lines show solute flux (Ca^{2+}, Mg^{2+}, K^+, Na^+, Cl^-, SO_4^{2-}, HCO_3^-); dashed lines represent the estimated portion originating from supraglacial meltwater (right axis). **(b)** Cumulative particle borne flux. **(c)** Cumulative meltwater discharge. Day 230 (dashed line) was the limit of the dataset interpretation. Values at the dashed line correspond to data presented in Table 1 and Figure 1b.

A key discovery is that solute flux during the two extreme melt years was ~90 % higher than for the average years, indicating that solute export scales with discharge. Thus, it is likely that increased melting will increase solute fluxes from the Greenland Ice Sheet. Most of the solute is delivered during peak melt periods during the ablation season (Fig. S-5). Solute pulses are also released during supraglacial lake drainage events (Fig. S-5; Bartholomew *et al.*, 2011). Enhanced solute discharge during extreme years likely results from i) drainage of concentrated subglacial waters stored in poorly connected regions, *e.g.*, deeper into the ice sheet, ii) higher flushing rates and iii) rapid weathering of reactive subglacial sediments by large volumes of supraglacial meltwater. We next ascertain if nutrient fluxes follow the same trend.

Dissolved nutrient fluxes

Nutrient fluxes for all years were estimated from the 2012 dataset, the only complete macronutrient record available. For the most common, namely NH_4^+, NO_3^-, Si and PO_4^{3-}, we also estimated annual flux by correlation with conductivity, as for major ion concentrations. This is justified by the good correlation of conductivity with nutrient concentrations (Fig. S-6). If the function holds for 2012, we assume it also holds for the other years. Si and P are released during rock weathering and dissolved inorganic nitrogen is also enhanced by subglacial biogeochemical processes, such as microbially mediated nitrification (NO_3^-) and mineralisation of organic matter (NH_4^-; Wynn *et al.*, 2007). For example, mean nitrogen concentrations attributable to subglacial processes (~1 µM) are similar to supraglacial processes (~1.3 µM). Nitrogen correlates linearly with conductivity ($R^2 = 0.74$; Fig. S-6). To account for the seasonal evolution in meltwater composition, we used two regressions (Fig. S-6) for dissolved silica ($R^2 = 0.72$ for early season and $R^2 = 0.34$ for bulk season runoff), and phosphate ($R^2 = 0.61$ and 0.59, respectively). We propose that these differences arise from the change in source of the subglacial water as the melt season progresses, *i.e.* close to ice margins early in the season to more isolated inland subglacial waters as the season progresses. The source influences the subglacial flowpath length, hence water residence times and pH/redox conditions.

Higher dissolved nutrient flux correlates with higher discharge years. Inorganic nitrogen (86 % ± 9.8 %), dissolved silica (85 % ± 0.1 %) and phosphate (86 % ± 11.9 %) are higher in extreme melt years than for average years. This is significant and demonstrates the potential for nutrient release by a warming climate.

A different approach for estimating nutrient flux is to combine discharge weighted mean concentrations and total discharge flux (Hawkings *et al.*, 2014). Estimates from this method and the EC-based method are similar (Table 1). The weighted mean dissolved nitrogen and silica fluxes were marginally lower (~7 % and ~5 %) and phosphate flux was higher (~23 %), probably because of late melt season influence, when phosphate concentrations were high and where the bulk of the discharge occurred.

An important assumption is that the correlation of nutrient concentration with conductivity is consistent over the years. We have a limited dataset for NO_3^- and Si from 2009. Results are sparse so estimates are crude but they serve as a benchmark for comparison. Flux derived from 2009 data for NO_3^-N is 12 tons, compared with 15 tons estimated using 2012 data. Flux for dissolved Si is 180 tons, compared with 130 tons estimated using 2012 measurements (Table 1). Both are well within an order of magnitude, which offers confidence that our estimates from 2012 data are reasonable.

Nutrient flux on particles

Glaciers effectively fracture and grind bedrock into high surface area, highly reactive, clay and silt sized particles, some of which are transported in runoff as suspended material (Gurnell and Clark, 1987; Brown *et al.*, 1996). By using data derived from the labile nutrients in the 2012 suspended material (n > 25), we estimated the range of nutrient concentrations associated with the particulate fraction (Table 1; Fig. 3). We assumed that the 2009-2011 mean extractable nutrient concentrations lie within the 2012 minimum and maximum concentrations, which is reasonable because the runoff comes from the same catchment and the mineral composition is relatively constant (Hawkings *et al.*, 2014).

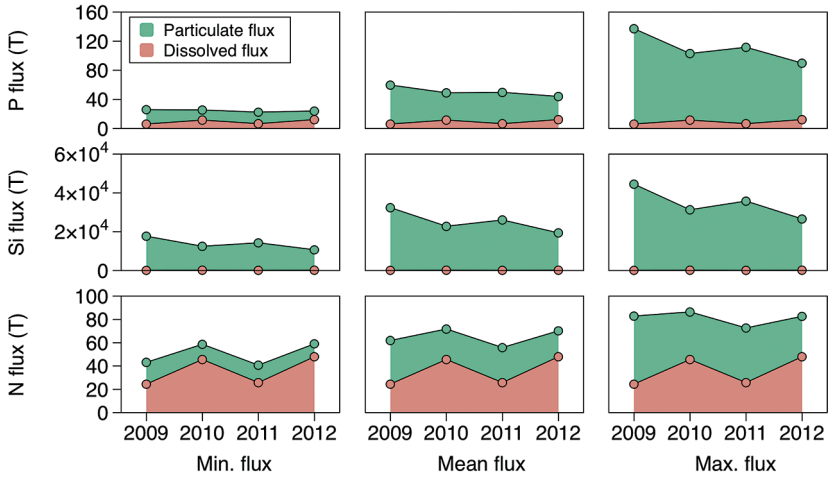

Figure 3 Estimated nutrient flux. Minimum (left column), mean (middle) and maximum (right) possible values give an impression of the range for phosphate, silicate and nitrogen compounds. Dissolved flux was determined using the electrical conductivity correlation.

Particulate bound nutrients account for a large portion of the estimated nutrient flux (Table 1; Fig. 3), which is significant in all years. The particulate transported fraction correlates with the nutrient source (lithogenic or atmospheric)

and the tendency for the ion to complex. Nutrients derived directly from rocks associate more with solids, *i.e.* for Si, >99 % and for P, ~80 % of the total flux. Nitrogen, which has a supraglacial component, is transported less on solids, *i.e.* <50 %. Our results are consistent with the low solubility of Si and the high affinity for P absorption onto solids, such as iron (oxyhyd)roxides. Ammonium is only weakly absorbed and nitrate remains preferentially in solution. This suggests that annual nitrogen flux is more sensitive to changes in ice sheet water discharge than particle flux.

We have demonstrated that, as in riverine systems (Mayer *et al.*, 1998; Ruttenberg, 2014), a high fraction of ice sheet nutrient export is associated with suspended material. This is consistent with previous research from Arctic glaciers (Hodson *et al.*, 2004) and supports recent assertions that the impact of terrigeneous material on the oceans is underestimated in global element cycling (Jeandel and Oelkers, 2015). Our results underline the need for more information about ice sheet sediment flux dynamics. As in previous studies, we observed highly variable annual sediment fluxes, which do not correlate well with discharge on a catchment basis (Fig. 2; Gurnell and Clark, 1987). Sediment flux might be less influenced by total meltwater discharge and more sensitive to meltwater access to fresh, subglacial sediment sources (Cowton *et al.*, 2012). However, evidence from past deglaciation events indicates that climate warming increases sediment export (Jeandel and Oelkers, 2015) and analysis of sediment plumes from meltwater rivers demonstrates a higher sediment flux in recent years (Hudson *et al.*, 2014).

The extent of biological consumption of the nutrients bound to particles before deposition and subsequent burial is unknown. Particulates from meltwater are extremely fine, *e.g.*, >95 % of particles can be <32 µm in size (Brown *et al.*, 1996), so surface area is high and nutrient transport in the buoyant, fresh water plumes in near coastal regions is likely to be significant. Evidence from recent polar studies shows that particle borne nutrients are carried far offshore (Schroth *et al.*, 2014; Wehrmann *et al.*, 2014) and nutrients deposited with glacial sediments in fjords can be resuspended in the water column (Wehrmann *et al.*, 2014). However, the scarcity of data means that the contribution of particle bound nutrients on oceanic productivity near Greenland remains uncertain.

Terrestrial and marine studies have shown that large fractions (75-95 %) of amorphous Si can be dissolved and recycled (Treguer *et al.*, 1995; Gibson *et al.*, 2000). Amorphous Si is an order of magnitude more soluble in saline solutions than in fresh water (Icenhower and Dove, 2000; Loucaides *et al.*, 2008) and recycling is favoured in estuaries (Loucaides *et al.*, 2008). NaOH extractable phosphate is commonly termed "algae available" (DePinto *et al.*, 1981) and its bioavailability has previously been demonstrated (Bostrom *et al.*, 1988). High salinity in ocean and fjord waters also favours P and NH_4 desorption (Garner *et al.*, 1991; Hodson *et al.*, 2004; Zhang and Huang, 2011), enhancing their bioavailability. Thus, annual sediment flux is an important factor in downstream productivity.

Conclusions

Changes in the hydrological output from the Greenland Ice Sheet in a warming climate could have significant effect on solute and nutrient delivery to near coastal regions. Our data, from Leverett Glacier, a large representative ice sheet catchment, indicate that bulk solute and dissolved nutrient fluxes will increase as "extreme" melt year frequency increases. A significant fraction of nutrients, especially silica and phosphorous, will be transported by suspended particles. The extent of their influence depends on desorption before burial, bioavailability and change in the ice sheet particulate flux, which are currently uncertain. Our study demonstrates that retreating snowline and higher meltwater input into less efficiently drained subglacial regions are likely to increase the dissolved macronutrient flux. Particle bound nutrients have been largely overlooked but contribute significant mass to nutrient cycling. Increased warming, thus increased meltwater runoff, will likely impact regional nutrient availability, and thus, the carbon cycle.

Acknowledgements

This research was part of the UK Natural Environment Research Council Project, DELVE (NERC grant NE/I008845/1) and the associated PhD studentship to JH. EL, AT, TC and IB were funded by NERC studentships and a MOSS scholarship. PN was supported by the Carnegie Trust for The University of Scotland and The University of Edinburgh Development Trust. Additional support was provided by the Leverhulme Trust, in a research fellowship to JLW. We thank all of those who assisted with fieldwork at Leverett Glacier and the technical staff in LOWTEX labs, School of Geographical Sciences, University of Bristol. We are grateful to our anonymous reviewers for constructive comments on the manuscript.

Editor: Susan S.L. Stipp

Additional Information

Supplementary Information accompanies this letter at www.geochemicalperspectivesletters.org/article1510

Reprints and permission information is available online at http://www.geochemicalperspectivesletters.org/copyright-and-permissions

Cite this letter as: Hawkings, J.R., Wadham, J.L., Tranter, M., Lawson, E., Sole, A., Cowton, T., Tedstone, A.J., Bartholomew, I., Nienow, P., Chandler, D., Telling, J. (2015) The effect of warming climate on nutrient and solute export from the Greenland Ice Sheet. *Geochem. Persp. Let.* 1, 94-104.

Author Contributions

All authors contributed. JLW and MT conceived the project. JRH, EL, AS, TC, IB, AT, PN, DC and JLW collected field data. JRH, JRH, EL and JT undertook the lab analysis. JRH, JLW and MT wrote the paper.

References

Bartholomew, I., Nienow, P., Sole, A., Mair, D., Cowton, T., Palmer, S., Wadham, J. (2011) Supraglacial forcing of subglacial drainage in the ablation zone of the Greenland ice sheet. *Geophysical Research Letters* 38, L08502.

Bhatia, M.P., Kujawinski, E.B., Das, S.B., Breier, C.F., Henderson, P.B., Charette, M.A. (2013) Greenland meltwater as a significant and potentially bioavailable source of iron to the ocean. *Nature Geoscience* 6, 274-278.

Bostrom, B., Persson, G., Broberg, B. (1988) Bioavailability of different phosphorus forms in freshwater systems. *Hydrobiologia* 170, 133-155.

Brown, G.H., Tranter, M., Sharp, M.J. (1996) Experimental investigations of the weathering of suspended sediment by Alpine glacial meltwater. *Hydrological Processes* 10, 579-597.

Collins, M., Knutti, R., Arblaster, J., Dufresne, J.-L., Fichefet, T., Friedlingstein, P., Gao, X., Gutowski, W.J., Johns, T., Krinner, G., Shongwe, M., Tebaldi, C., Weaver, A.J., Wehner, M. (2013) Long-term Climate Change: Projections, Commitments and Irreversibility. In: Stocker, T.F., Qin, D., Plattner, G.-K., Tignor, M., Allen, S.K., Boschung, J., Nauels, A., Xia, Y., Box, V., Midgley, P.M. (Eds.) *Climate Change 2013: The Physical Science Basis. Contributions of Working Group I to the Fifth Assessment Report of the Intergovernmental Panel on Climate Change*. Cambridge University Pess, Cambridge, UK and New York, NY, USA.

Cowton, T., Nienow, P., Bartholomew, I., Sole, A., Mair, D. (2012) Rapid erosion beneath the Greenland ice sheet. *Geology* 40, 343-346.

DePinto, J.V., Young, T.C., Martin, S.C. (1981) Algal-available phosphorus in suspended sediments from Lower Great Lakes Tributaries. *Journal of Great Lakes Research* 7, 311-325.

Fettweis, X., Franco, B., Tedesco, M., van Angelen, J.H., Lenaerts, J.T.M., van den Broeke, M.R., Gallee, H. (2013) Estimating the Greenland ice sheet surface mass balance contribution to future sea level rise using the regional atmospheric climate model MAR. *Cryosphere* 7, 469-489.

Gardner, W., Seitzinger, S., Malczyk, J. (1991) The effects of sea salts on the forms of nitrogen released from estuarine and freshwater sediments: Does ion pairing affect ammonium flux? *Estuaries* 14, 157-166.

Gibson, C.E., Wang, G., Foy, R.H. (2000) Silica and diatom growth in Lough Neagh: the importance of internal recycling. *Freshwater Biology* 45, 285-293.

Gurnell, A.M., Clark, M.J. (1987) *Glacio-fluvial sediment transfer: An Alpine Perspective*. Wiley & Sons, Chichester.

Hawkings, J.R., Wadham, J.L., Tranter, M., Raiswell, R., Benning, L.G., Statham, P.J., Tedstone, A., Nienow, P., Lee, K., Telling, J. (2014) Ice sheets as a significant source of highly reactive nanoparticulate iron to the oceans. *Nature Communications* 5.

Hodson, A.J., Mumford, P., Lister, D. (2004) Suspended sediment and phosphorus in proglacial rivers: bioavailability and potential impacts upon the P status of ice-marginal receiving waters. *Hydrological Processes* 18, 2409-2422.

Hudson, B., Overeem, I., McGrath, D., Syvitski, J.P.M., Mikkelsen, A., Hasholt, B. (2014) MODIS observed increase in duration and spatial extent of sediment plumes in Greenland fjords. *The Cryosphere* 8, 1161-1176.

ICENHOWER, J.P., DOVE, P.M. (2000) The dissolution kinetics of amorphous silica into sodium chloride solutions: Effects of temperature and ionic strength. *Geochimica et Cosmochimica Acta* 64, 4193-4203.

JEANDEL, C., OELKERS, E.H. (2015) The influence of terrigenous particulate material dissolution on ocean chemistry and global element cycles. *Chemical Geology* 395, 50-66.

LAWSON, E.C., BHATIA, M.P., WADHAM, J.L., KUJAWINSKI, E.B. (2014) Continuous summer export of nitrogen-rich organic matter from the Greenland Ice Sheet inferred by ultra high resolution mass spectrometry. *Environmental Science & Technology* 48, 14248-14257.

LEESON, A.A., SHEPHERD, A., BRIGGS, K., HOWAT, I., FETTWEIS, X., MORLIGHEM, M., RIGNOT, E. (2015) Supraglacial lakes on the Greenland ice sheet advance inland under warming climate. *Nature Climate Change* 5, 51-55.

LOUCAIDES, S., VAN CAPPELLEN, P., BEHRENDS, T. (2008) Dissolution of biogenic silica from land to ocean: Role of salinity and pH. *Limnology and Oceanography* 53, 1614-1621.

MAYER, L.M., KEIL, R.G., MACKO, S.A., JOYE, S.B., RUTTENBERG, K.C., ALLER, R.C. (1998) Importance of suspended particulates in riverine delivery of bioavailable nitrogen to coastal zones. *Global Biogeochemical Cycles* 12, 573-579.

PALMER, S., SHEPHERD, A., NIENOW, P., JOUGHIN, I. (2011) Seasonal speedup of the Greenland Ice Sheet linked to routing of surface water. *Earth and Planetary Science Letters* 302, 423-428.

RUTTENBERG, K. (2014) The global phosphorus cycle. *Treatise on Geochemistry* 8, 499-558.

RYSGAARD, S., MORTENSEN, J., JUUL-PEDERSEN, T., SØRENSEN, L.L., LENNERT, K., SØGAARD, D.H., ARENDT, K.E., BLICHER, M.E., SEJR, M.K., BENDTSEN, J. (2012) High air–sea CO2 uptake rates in nearshore and shelf areas of Southern Greenland: Temporal and spatial variability. *Marine Chemistry* 128–129, 26-33.

SCHROTH, A.W., CRUSIUS, J., HOYER, I., CAMPBELL, R. (2014) Estuarine removal of glacial iron and implications for iron fluxes to the ocean. *Geophysical Research Letters* 41, 3951-3958.

TEDESCO, M., FETTWEIS, X., MOTE, T., WAHR, J., ALEXANDER, P., BOX, J.E., WOUTERS, B. (2013) Evidence and analysis of 2012 Greenland records from spaceborne observations, a regional climate model and reanalysis data. *Cryosphere* 7, 615-630.

TREGUER, P., NELSON, D.M., VANBENNEKOM, A.J., DEMASTER, D.J., LEYNAERT, A., QUEGUINER, B. (1995) The silica balance in the world ocean – a reestimate. *Science* 268, 375-379.

WADHAM, J., DE'ATH, R., MONTEIRO, F.M., TRANTER, M., RIDGWELL, A., RAISWELL, R., TULACZYK, S. (2013) The potential role of the Antarctic Ice Sheet in global biogeochemical cycles. *Earth and Environmental Science Transactions of the Royal Society of Edinburgh* 104, 55-67.

WEHRMANN, L.M., FORMOLO, M.J., OWENS, J.D., RAISWELL, R., FERDELMAN, T.G., RIEDINGER, N., LYONS, T.W. (2014) Iron and manganese speciation and cycling in glacially influenced high-latitude fjord sediments (West Spitsbergen, Svalbard): Evidence for a benthic recycling-transport mechanism. *Geochimica et Cosmochimica Acta* 141, 628-655.

WYNN, P.M., HODSON, A.J., HEATON, T.H.E., CHENERY, S.R. (2007) Nitrate production beneath a High Arctic Glacier, Svalbard. *Chemical Geology* 244, 88-102.

ZHANG, J.Z., HUANG, X.L. (2011) Effect of temperature and salinity on phosphate sorption on marine sediments. *Environmental Science & Technology* 45, 6831-6837.

Geochemical Perspectives Letters

The effect of warming climate on nutrient and solute export from the Greenland Ice Sheet

J.R. Hawkings[1]*, J.L. Wadham[1], M. Tranter[1], E. Lawson[1,2], A. Sole[3], T. Cowton[3,4], A.J. Tedstone[4], I. Bartholomew[4], P. Nienow[4], D. Chandler[1], J. Telling[1]

Supplementary Information

The Supplementary Information includes:

- Study Site and Methods
- Figures S-1 to S-6
- Supplementary Information References

Study Site and Methods

Study area

Research was conducted at Leverett Glacier (LG; Fig. 1a; 67.06 °N, 50.17 °W), a large, land terminating glacier on the southwestern margin of the Greenland Ice Sheet (GrIS). The catchment extends >80 km into the ice sheet and is estimated to cover an area of >600 km^2 (Palmer *et al.*, 2011; Cowton *et al.*, 2012). Leverett overlies bedrock of Archean gneiss and granite, common to much of Greenland (Henriksen *et al.*, 2009). Catchment hydrology is typical of large Greenland outlet glaciers and is described elsewhere (Chandler *et al.*, 2013). A catchment hydrological record was maintained during the 2009-2012 summer ablation seasons, with monitoring of discharge, electrical conductivity (EC) and turbidity (suspended material), recorded at 5-10 minute intervals (Fig. S-1).

1. Bristol Glaciology Centre, School of Geographical Sciences, University of Bristol, University Road, Bristol, BS8 1SS, UK
* Corresponding author (email: jon.hawkings@bristol.ac.uk)
2. School of Geography, University of Nottingham, University Park, Nottingham, NG7 2RD, UK
3. Department of Geography, The University of Sheffield, Western Bank, Sheffield, S10 2TN, UK
4. School of Geoscience, University of Edinburgh, Drummond Street, Edinburgh, EH8 9XP, UK

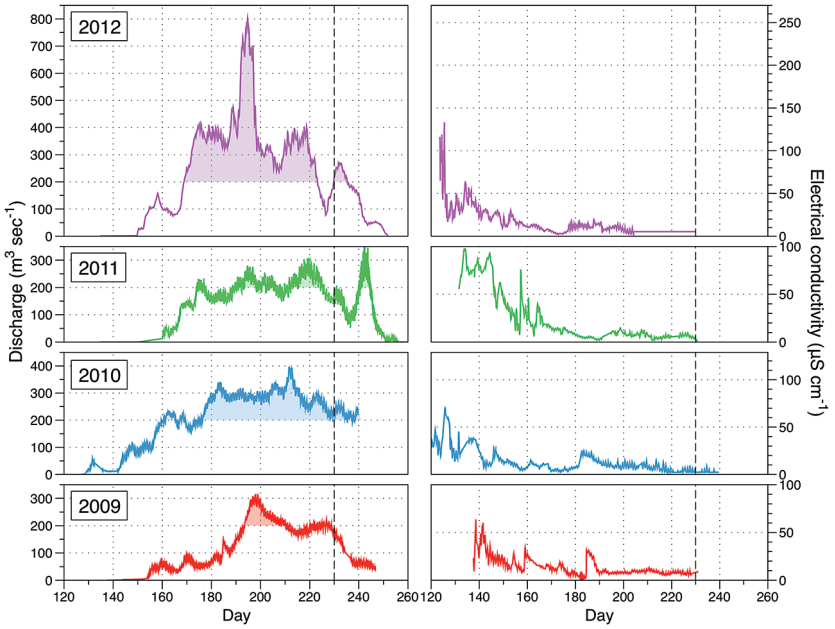

Figure S-1 Leverett Glacier discharge hydrographs and electrical conductivity. Shaded areas in the discharge plots show when discharge exceeded 200 m^3 sec^{-1}. The dashed line represents the cut off date used for flux estimates.

Water sample collection and filtration

Bulk meltwater samples for geochemical analysis were collected at least once a day (2009, 2010, 2012), from a sampling site located ~1 km (2012) or ~2 km (2009, 2010) downstream from the Leverett Glacier terminus, throughout the main melt period (May-August). Our confidence that these waters represent the bulk discharge is based on the drainage of Leverett from a single portal. The composition of point samples taken there were within the uncertainty of those taken further downstream.

Grab samples were immediately passed through 47 mm 0.45 µm cellulose nitrate filters (Whatman®), mounted on a PES filtration stack (Nalgene™), that had been rinsed 3 times with the sample. The filtrate was immediately frozen in clean HDPE 30 mL Nalgene™ bottles that had been rinsed 3 times with the filtered sample. Major ion analysis (Ca^{2+}, Mg^{2+}, K^+, Na^+, Cl^-, SO_4^{2-}, HCO_3^-) and NO_3^- was completed within three months of collection. We used a Thermo Scientific™ Dionex™ DX-500 (2009, 2010) or a Thermo Scientific™ Dionex™ capillary ICS-5000 (2012), fitted with simultaneous anion and cation columns.

Measurement accuracy was ~ ±4 % and precision was ~ ±7 % for the DX-500, and ~ ±3 % and ~ ±3 % for the ICS-5000. Dissolved macronutrients were measured from the 2012 samples using a LaChat QuickChem® 8500 flow injection analyser system using low level detection methods (Si, PO_4^-) or by manual colormetric techniques (NH_4^+), as described by Le and Boyd (2012). All samples were field blank corrected where the blank concentrations were above the detection limit of the instrument. In total, 408 samples were analysed for major ions and 75 samples, for nutrient concentrations. In 2012, snow and supraglacial meltwaters draining into a moulin ~30 km from the catchment margin were sampled for geochemical analysis (n = 32), using the same methods as the bulk geochemical samples. Snow samples were placed in new Whirl-Pak® bags (Nasco) and left in a water bath to melt. Samples were filtered, as above, as soon as melting was complete.

Sediment nutrient extractions

Particulate bound nutrient samples were taken during the 2012 melt season (n = 25 for P and Si, n = 39 for N). Briefly, a meltwater sample of 300-400 mL was filtered through a 0.45 µm cellulose nitrate filter (PSi and PP; Whatman®) or a 0.7 µm glass microfibre filter. Suspended particulate material was retained for the commonly used labile nutrient extractions, "algae available" P (Hodson *et al.*, 2004), exchangeable NH_4 (PN; Maynard *et al.*, 2007), and amorphous Si (PSi; DeMaster, 1981). Particulate material was removed carefully by gentle scraping from the filter, and weighed. Mean extractable concentrations were combined with the total sediment flux from Leverett Glacier, to determine the labile particulate nutrient flux.

"Algae available" phosphorus extraction

Owing to its importance as an essential nutrient, phosphorus extraction techniques are well documented in the literature (Dorich *et al.*, 1980; DePinto *et al.*, 1981; Sharpley *et al.*, 1991; Ekholm and Krogerus, 2003; Hodson *et al.*, 2004). Here we used a common extraction method that aims to determine the amount that is bioavailable (Bostrom *et al.*, 1988; Hodson *et al.*, 2004). We adapted the standard method to allow for analysis of very small quantities of sediment, *i.e.* "micro-extraction". Briefly, 1.5 mL of 0.1 M NaOH solution was added to ~50 mg of sediment, that was accurately measured to ±0.001 g using a high precision/accuracy balance. We used 2 mL microcentrifuge tubes, which allow similar sediment to extractant ratios to those used by others (Hodson *et al.*, 2004). Microcentrifuge tubes were capped and placed on a reciprocating (rotary) shaker at 200 rpm for 16 hours. Tubes were then centrifuged at 2600 rpm for 10 minutes, the supernatant was transferred to new 2 mL tubes using a 1 mL plastic syringe (PP/PE) and filtered through a syringe filter (Whatman® Puradisc PP).

Exchangeable ammonium extraction

We adopted the method described by Maynard *et al.* (2007) and applied elsewhere (Telling *et al.*, 2011, 2012, 2014). 10 mL of 2.0 M KCl solution was added to 0.7 µm filters (GF/F Whatman®) in a 15 mL plastic centrifuge tube. Tubes were capped and placed on a reciprocating (rotary) shaker (160 rpm) for 30 minutes. Solutions were then decanted into fresh plastic tubes, centrifuged, filtered through a 0.45 µm syringe filter (Whatman® Puradisc PP) and frozen at -20 °C until analysis. All sediment from filters was retained, rinsed with Milli-Q deionised water (18.2 MΩ cm^{-1} Millipore) to remove extract solution and dried in an oven overnight at ~50 °C to provide dry sediment weights. These were cross checked against weights expected from hydrological suspended sediment records, *i.e.* 300 mL of water was filtered so an expected weight could be generated from the recorded meltwater suspended material. Nine blanks were treated in the same manner as the samples, using the same types of filter, to test for filter contamination.

Amorphous silica extraction

This is the first study to present data on extraction of amorphous silica in glacial sediments. Here we use a method commonly employed in marine and riverine systems that was developed by DeMaster (1981) and validated for terrestrial soils and sediments (Sauer *et al.*, 2006). The technique uses 0.1 M Na_2CO_3, a weak base, which maximises dissolution of amorphous Si, with minimal impact on crystalline material. About 30 mg of sediment was accurately weighed into a 60 mL HDPE bottle (Nalgene®) and 50 mL of 0.1 M Na_2CO_3 solution was added. Bottles were placed in a hot water bath (85 °C) and 1 mL aliquots were removed after 1, 2, 3 and 5 hours. Aliquots were refrigerated in 2 mL microcentrifuge tubes at 4 °C until analysis, less than 24 hours later. Just prior to analysis, 0.5 mL of sample was neutralised with 4.5 mL 0.021 M HCl in plastic centrifuge tubes. Three blanks were processed alongside the samples to check for method contamination. Amorphous silica was determined by using the intercept of the regression line drawn through Si concentrations obtained from the time series aliquots; amorphous silica dissolves within the first hour of the extraction procedure (DeMaster, 1981).

Analysis of extract solutions and filtered meltwater

Phosphorus and silica extraction solutions were measured on a LaChat QuickChem® 8500 flow injection analyser system (Method Numbers 31-115-01-1-I for P and 31-114-27-1D for Si). The coefficient of variation (CoV) for the method was ±0.5 % for silica (based on seven replicate standards) and ±3.2 % for dissolved orthophosphate (five replicate standards). Limits of detection were 0.3 µM (8.4 µg Si L^{-1}) and 0.01 µM (0.3 µg P L^{-1}). Ammonium was determined using a Bran and Luebbe Autoanalyzer 3 (for extractants) or by the manual salicylate method (Le and Boyd, 2012). The Luebbe Autoanalyzer 3 method had a CoV of ±1.5 % (eight

replicate standards) and a detection limit of 0.5 µM (6.4 µg N L^{-1}). The manual method had a CoV of ±4.9 % (five replicate standards) and a limit of detection of 0.6 µM (8.4 µg N L^{-1}). All samples were blank corrected where blank concentrations were higher than the detection limits.

Contribution of supraglacial solute to total solute flux

Measured mean major ion concentration in supraglacial melt (snow and ice melt from 2012, n = 32) was 15 µeq L^{-1} (±7 µeq L^{-1}). There is no reason to expect there to be significant annual variation in these concentrations, which are more than an order of magnitude lower than mean bulk meltwaters (~400 µeq L^{-1}). The mean supraglacial major ion value of 15 µeq L^{-1} was multiplied by catchment discharge at each time step and cumulatively summed (Fig. 2) to derive solute fluxes from supraglacial sources.

Catchment hydrological monitoring and meltwater/sediment fluxes

Leverett Glacier runoff was hydrologically gauged throughout the 2009-2012 summer melt seasons, from late April or early May at the onset of melting, through to late August or early September. Briefly, the discharge, electrical conductivity and turbidity (suspended material concentration) of the meltwater river were logged every 5 minutes at a stable bedrock section ~2.2 km downstream from the glacier terminus (Cowton *et al.*, 2012). Discharge was determined using the method described by Bartholomew *et al.* (2011). A wired water pressure sensor monitored stage, which was converted into discharge using a (stage-discharge) rating curve of Rhodamine WT dye dilution injections. Twenty nine dye dilutions were used in 2009 and 2010, 26 in 2011 and 41 in 2012. Leverett meltwater and particulate material fluxes were determined by multiplying discharge and suspended material concentrations at the 5 minute time points by 300 (to derive values for each second over the 5 minute period between new recordings) and summed over the entire melt season. For comparison, modelled meltwater runoff data for the Greenland Ice Sheet were taken from Tedesco *et al.* (2013).

Snowline determination

Snowline retreat throughout the 2009-2012 melt seasons was monitored using MODIS (moderate resolution imaging spectroradiometer) on the Terra platform. Surface reflectance band 1-2 images (Product Number MOD09GQ) were processed using the QGIS analysis package, to determine snowline extent (Fig. S-2). Maximum snowline position from monitored years is shown in Figure 1. A minimum of 18 cloud free images were used per year to determine snowline migration.

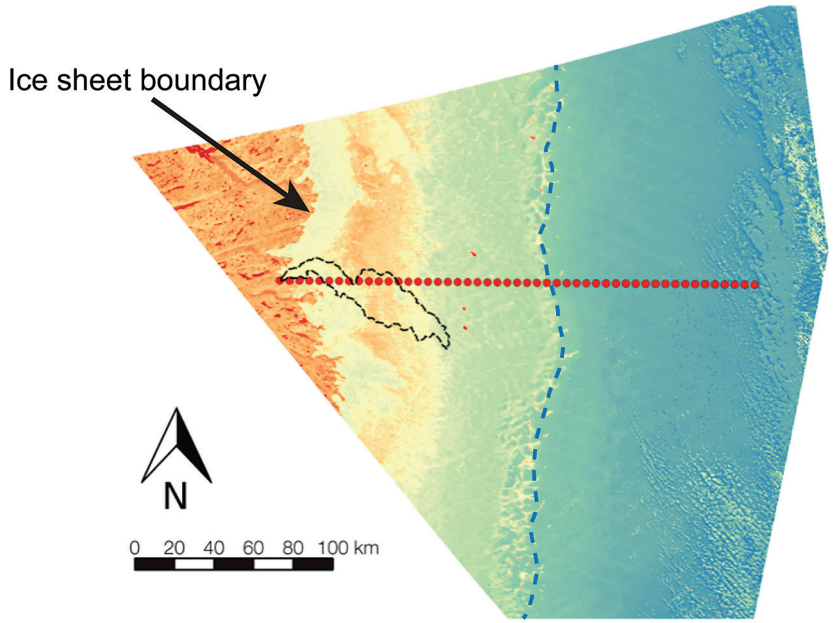

Figure S-2 An example of the MODIS satellite imagery used to determine snowline extent. Data are from surface reflectance bands 1-2 (Product Number MOD09GQ). Leverett Glacier moves from east to west. The estimated catchment area is outlined in black (Palmer *et al.*, 2011) and the snowline transect is displayed by the red dotted line (space between each dot = 5 km). False colour imaging differentiates between snow (dark blue) and ice (light blue). The margin of the ice sheet is evident at the border of the red colouring (black arrow). The blue dashed line represents the interpreted position of the snowline. The image displayed is from 21 July 2012. Fig. 1a provides more information about the catchment.

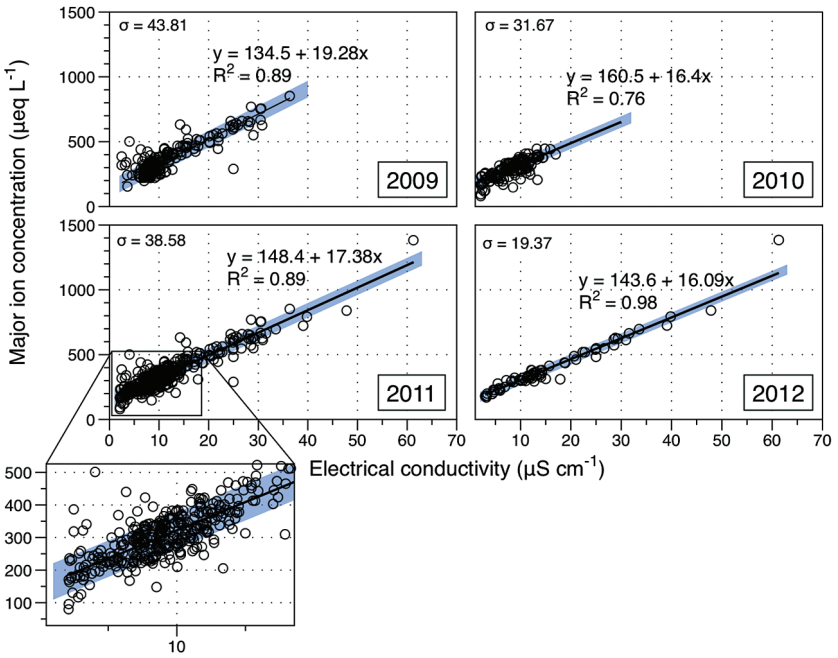

Figure S-3 Regression plots for major ions as a function of electrical conductivity. Shaded blue lines represent the standard error (σ, also written in the top left of plots). The 2011 regression plot (bottom left), which encompasess data from 2009, 2010 and 2012, is magnified to demonstrate the linear relationship of electrical conductivity with major ions in the dilute waters.

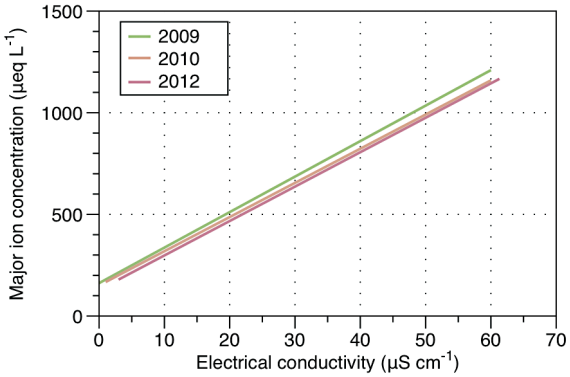

Figure S-4 Comparison of regression plots for the major ions for 2009, 2010 and 2012, where data are available. The differences in the regression equations used to determine major ion concentrations are very small.

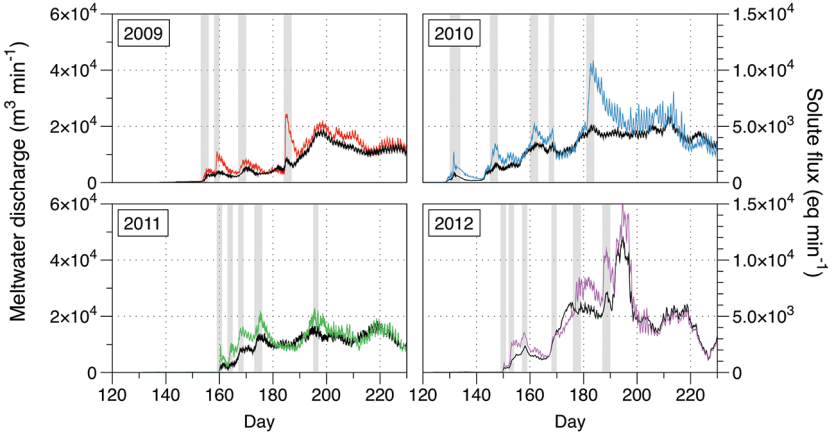

Figure S-5 Temporal variation in meltwater discharge and estimated solute flux. Coloured lines indicate solute flux calculated by the EC based method (eq min^{-1}), and black lines, meltwater discharge (m^3 min^{-1}), during the 2009-2012 melt seasons. Shaded areas correspond to meltwater pulse events. These are associated with spring events, *i.e.* the annual opening of the subglacial drainage system, or rapid drainage of meltwater from supraglacial lake drainage events. These meltwater pulses flush concentrated waters from the subglacial drainage system (Bartholomew *et al.*, 2011 and Hawkings *et al.*, 2014).

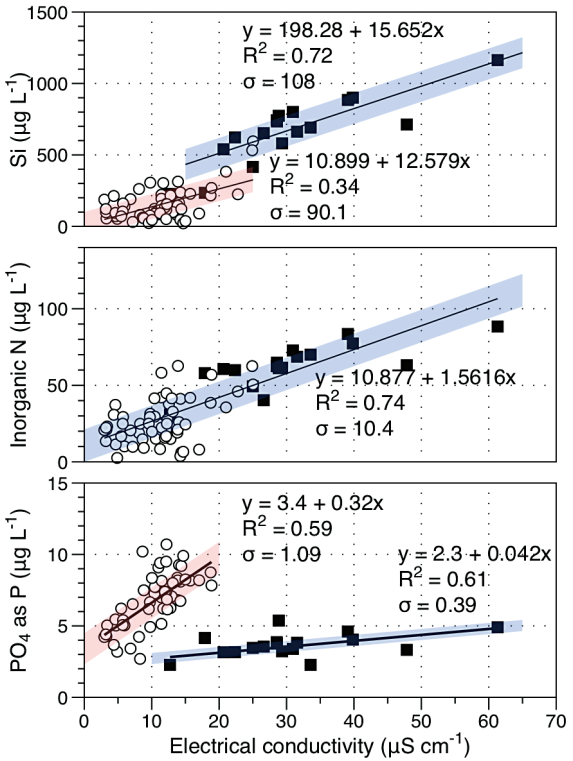

Figure S-6 Regression plots for nutrient concentrations as a function of electrical conductivity. The regression plots for Si and PO_4^{3-} represent early (blue) versus later season (red) hydrological and associated biogeochemical changes. Early season regressions are applied to time points before Day 153 in 2009, Day 128 in 2010, Day 160 in 2011 and Day 150 in 2012, which are before the initial change in drainage hydrology occurred, *i.e.* the spring event (Figs S-1 and S-5). Shaded areas show associated standard error.

Supplementary Information References

Bartholomew, I., Nienow, P., Sole, A., Mair, D., Cowton, T., Palmer, S., Wadham, J. (2011) Supraglacial forcing of subglacial drainage in the ablation zone of the Greenland ice sheet. *Geophysical Research Letters* 38, L08502.

Bostrom, B., Persson, G., Broberg, B. (1988) Bioavailability of different phosphorus forms in freshwater systems. *Hydrobiologia* 170, 133-155.

Chandler, D.M., Wadham, J.L., Lis, G.P., Cowton, T., Sole, A., Bartholomew, I., Telling, J., Nienow, P., Bagshaw, E.A., Mair, D., Vinen, S., Hubbard, A. (2013) Evolution of the subglacial drainage system beneath the Greenland Ice Sheet revealed by tracers. *Nature Geoscience* 6, 195-198.

Cowton, T., Nienow, P., Bartholomew, I., Sole, A., Mair, D. (2012) Rapid erosion beneath the Greenland ice sheet. *Geology* 40, 343-346.

DeMaster, D.J. (1981) The supply and accumulation of silica in the marine-environment. *Geochimica Et Cosmochimica Acta* 45, 1715-1732.

DePinto, J.V., Young, T.C., Martin, S.C. (1981) Algal-available phosphorus in suspended sediments from Lower Great Lakes Tributaries. *Journal of Great Lakes Research* 7, 311-325.

Dorich, R.A., Nelson, D.W., Sommers, L.E. (1980) Algal availability of sediment phosphorus in drainage water of the Black Creek Watershed. *Journal of Environmental Quality* 9, 557-563.

Ekholm, P., Krogerus, K. (2003) Determining algal-available phosphorus of differing origin: routine phosphorus analyses versus algal assays. *Hydrobiologia* 492, 29-42.

Hawkings, J.R., Wadham, J.L., Tranter, M., Raiswell, R., Benning, L.G., Statham, P.J., Tedstone, A., Nienow, P., Lee, K., Telling, J. (2014) Ice sheets as a significant source of highly reactive nanoparticulate iron to the oceans. *Nature Communications* 5.

Henriksen, N., Higgins, A.K., Kalsbeek, F., Pulvertaft, T.C.R. (2009) Greenland from Archaean to Quaternary Descriptive text to the 1995 Geological map of Greenland, 1:2 500 000. In: Garde, A.A. (Ed.) *Geological Survey of Denmark and Greenland Bulletin*, 2nd edition. 18, 9-116.

Hodson, A.J., Mumford, P., Lister, D. (2004) Suspended sediment and phosphorus in proglacial rivers: bioavailability and potential impacts upon the P status of ice-marginal receiving waters. *Hydrological Processes* 18, 2409-2422.

Le, P.T.T., Boyd, C.E. (2012) Comparison of phenate and salicylate methods for determination of total ammonia nitrogen in freshwater and saline water. *Journal of the World Aquaculture Society* 43, 885-889.

Maynard, D.G., Kalra, Y.P., Crumgaugh, J.A. (2007) Nitrate and exchangeable ammonium nitrogen. In: Carter, M.R., Gregorich, E.G. (Eds.) *Soil Sampling and Methods of Analysis*. CRC Press, Boca Raton, Florida, 25-38.

Palmer, S., Shepherd, A., Nienow, P., Joughin, I. (2011) Seasonal speedup of the Greenland Ice Sheet linked to routing of surface water. *Earth and Planetary Science Letters* 302, 423-428.

Sauer, D., Saccone, L., Conley, D.J., Herrmann, L., Sommer, M. (2006) Review of methodologies for extracting plant-available and amorphous Si from soils and aquatic sediments. *Biogeochemistry* 80, 89-108.

Sharpley, A.N., Troeger, W.W., Smith, S.J. (1991) The measurement of bioavailable phosphorus in agricultural runoff. *Journal of Environmental Quality* 20, 235-238.

Tedesco, M., Fettweis, X., Mote, T., Wahr, J., Alexander, P., Box, J.E., Wouters, B. (2013) Evidence and analysis of 2012 Greenland records from spaceborne observations, a regional climate model and reanalysis data. *Cryosphere* 7, 615-630.

Telling, J., Anesio, A.M., Tranter, M., Irvine-Fynn, T., Hodson, A., Butler, C., Wadham, J. (2011) Nitrogen fixation on Arctic glaciers, Svalbard. *Journal of Geophysical Research* 116, G03039.

Telling, J., Stibal, M., Anesio, A.M., Tranter, M., Nias, I., Cook, J., Bellas, C., Lis, G., Wadham, J.L., Sole, A., Nienow, P., Hodson, A. (2012) Microbial nitrogen cycling on the Greenland Ice Sheet. *Biogeosciences* 9, 2431-2442.

Telling, J., Anesio, A.M., Tranter, M., Fountain, A., Nylen, T., Hawkings, J., Singh, V.B., Kaur, P., Musilova, M., Wadham, J.L. (2014) Spring thaw ionic pulses boost nutrient availability and microbial growth in entombed Antarctic Dry Valley cryoconite holes. *Frontiers in Microbiology* 5, 694.

Appendix F

Dehecq *et al.*, 2015 (Remote Sens. Environ.)

This paper provides further context to the ice motion methodology used in Chapter 6.

Remote Sensing of Environment 162 (2015) 55–66

Contents lists available at ScienceDirect

Remote Sensing of Environment

journal homepage: www.elsevier.com/locate/rse

Deriving large-scale glacier velocities from a complete satellite archive: Application to the Pamir–Karakoram–Himalaya

Amaury Dehecq [a,*], Noel Gourmelen [b], Emmanuel Trouve [a]

[a] Universite de Savoie, Polytech Annecy-Chambery, LISTIC, BP 80439, 74944 Annecy-le-Vieux cedex, France
[b] School of GeoSciences, University of Edinburgh, Edinburgh EH8 9XP, UK

ARTICLE INFO

Article history:
Received 21 June 2014
Received in revised form 27 January 2015
Accepted 29 January 2015
Available online xxxx

Keywords:
Remote sensing
Feature-tracking
Surface velocity
Mountain glaciers
Landsat
Himalaya
Karakoram

ABSTRACT

Mountain glaciers are pertinent indicators of climate change and their dynamics, in particular surface velocity change, is an essential climate variable. In order to retrieve the climatic signature from surface velocity, large-scale study of temporal trends spanning multiple decades is required. Satellite image feature-tracking has been successfully used to derive mountain glacier surface velocities, but most studies rely on manually selected pairs of images, which is not adequate for large datasets. In this paper, we propose a processing strategy to exploit complete satellite archives in a semi-automated way in order to derive robust and spatially complete glacier velocities and their uncertainties on a large spatial scale. In this approach, all available pairs within a defined time span are analysed, preprocessed to improve image quality and features are tracked to produce a velocity stack; the final velocity is obtained by selecting measures from the stack with the statistically higher level of confidence. This approach allows to compute statistical uncertainty level associated with each measured image pixel.
This strategy is applied to 1536 pairs of Landsat 5 and 7 images covering the 3000 km long Pamir–Karakoram–Himalaya range for the period of 1999–2001 to produce glacier annual velocity fields. We obtain a velocity estimate for 76,000 km^2 or 92% of the glacierized areas of this region. We then discuss the impact of coregistration errors and variability of glacier flow on the final velocity. The median 95% confidence interval ranges from 2.0 m/year on the average in stable areas and 4.4 m/year on the average over glaciers with variability related to data density, surface conditions and strain rate. These performances highlight the benefits of processing of a complete satellite archive to produce glacier velocity fields and to analyse glacier dynamics at regional scales.

1. Introduction

Mountain glaciers have a high societal impact; first on a local scale as they influence the water resources (Immerzeel, Beek, & Bierkens, 2010) and economical activity (Barros et al., 2014) of a region, but also at a global scale by contributing to changes in the global sea level (Gardner et al., 2013). Moreover, mountain glaciers are sensitive to climate forcing and are thus relevant indicators of past and present climate changes (IPCC, 2013). Satellite imagery, with its global coverage and repeated acquisition, represents a unique opportunity to quantify the spatial and temporal changes affecting mountain glaciers. In particular, feature-tracking using repeated images allows us to construct velocity fields which are valuable information to understand dynamical processes such as the response to climate changes, glacier surges or development of glacial lakes and associated hazards (Paul et al., 2013).

Many studies have proven the capabilities of feature-tracking applied to repeated satellite images to measure glacier velocities. Scambos, Dutkiewicz, Wilson, and Bindschadler (1992) applied normalized cross-correlation of Landsat TM images to measure the velocity of ice streams in Antarctica. Kääb (2002) and Berthier et al. (2005) show that it is possible to apply this method to mountain glaciers, using respectively ASTER and SPOT images. High resolution images as well as an improved algorithm, that determines the position of the correlation maximum from 1/2nd to 1/20th of a pixel (Strozzi, Luckman, Murray, Wegmuller, & Werner, 2002), allow the tracking of much smaller surface features with a precision in yearly velocity of a few cm/year, equivalent to the precision obtained by synthetic aperture radar interferometry (InSAR) (Goldstein, Engelhardt, Kamb, & Frolich, 1993) and multiple aperture InSAR (MAI) (Gourmelen et al., 2011). Particular attention has been given to improving the techniques of feature-tracking. Preprocessing steps to enhance and improve the performances of the tracking include principal component analysis, high-pass filters (Scambos et al., 1992; Berthier et al., 2005) or edge-detection (Ahn & Howat, 2011). Several studies focused on the choice of the feature-tracking algorithm (Heid & Kääb, 2012a; Strozzi et al., 2002), reduction of the orthorectification errors (Scherler, Leprince, & Strecker, 2008) or on optimizing the parameters for the feature-tracking (Debella-Gilo & Kääb, 2012). However, automatation of the processing in order to reduce user interaction remains a challenge (Ahn & Howat, 2011; Debella-Gilo & Kääb, 2012; Heid & Kääb, 2012a).

* Corresponding author.
E-mail address: amaury.dehecq@univ-savoie.fr (A. Dehecq).

http://dx.doi.org/10.1016/j.rse.2015.01.031
0034-4257/

The large amount of currently available and future remote sensing data has led to a large variety of applications. Copland et al. (2009) produced velocity fields on a regional scale, for all glaciers within the central Karakoram region for the period of 2006–2007, thereby giving an instantaneous picture of the glacier velocity in this region. This technique has also been applied to SAR images, to study specific areas such as the Mont-Blanc glaciers (Fallourd et al., 2011), the Everest region (Luckman, Quincey, & Bevan, 2007) and the Baltoro glacier (Quincey et al., 2009). Heid and Kääb (2012b) exploit the long time span of Landsat images to investigate the link between variations in mass balance and velocity over the period of 1985–2011 for 6 selected regions across the globe. However, they also outline the problem of the representativeness of the selected regions and the need to increase the efforts at a regional scale. Several studies have processed larger number of images to produce velocity fields at a regional scale. Willis, Melkonian, Pritchard, and Ramage (2012) processed 124 manually selected ASTER images to produce a velocity field for the 3593 km^2 Northern Patagonian Icefield and the period of 2000–2011. They obtain a composite velocity by averaging the stack of velocities weighted by the uncertainty of each velocity. Burgess, Forster, and Larsen (2013) apply feature-tracking to 344 pairs of ALOS images acquired between 2007 and 2010 but only 60 pairs are manually retained to produce a final mosaic velocity of the Alaska range glaciers. Scherler, Bookhagen, and Strecker (2011b) produce centre flow line velocities for several parts of the Himalayan range by computing the mean of a stack of velocities obtained from feature-tracking of 657 ASTER and SPOT images for the period of 2000–2008. Nevertheless, all of these studies always rely on manually selected images and the repetivity of the satellite imagery archive has not been exploited yet.

In this paper, we present a processing strategy to derive a robust and spatially dense velocity field over an extended region from a complete satellite archive. First, we give a broad outline of the method, we then apply this strategy to the Landsat 5 and 7 archive to produce glacier annual velocity fields over the Pamir–Karakoram–Himalaya (PKH) over a three-year period. This allows us to assess the performance and uncertainties of the strategy.

2. Data and methods

In this section, we describe the processing strategy including the selection of image pairs, the preprocessing steps to reduce the dimensionality of the problem and enhance the useful information, the feature-tracking algorithm and the fusion of the multi-temporal results (Fig. 1). The method can be applied to any satellite imagery archive with sufficient repetition in the acquisition as for example ASTER, SPOT or the upcoming Sentinel 1 and 2 missions of the European Space Agency that will provide repeated images of the Earth surface. In this paper we focus on the Landsat series that represents the longest continuous satellite archive, with acquisitions of the Earth surface from 1972 to nowadays and a repeat-cycle of 16 to 18 days at medium-resolution (15 to 60 m) and a quasi-global coverage.

2.1. Selection of image pairs

The main idea of the method is to process all available data without manual selection for several reasons. First, selecting the images beforehand with consideration of the quality of the scene is very time consuming and subjective and could lead to a loss of valuable information. Here we propose to process all data and to filter the results based on the quality of the feature-tracking. Secondly, a single pair rarely gives an spatially complete result due to shadows, clouds or sensor saturation that induce outliers or gaps in the resulting data. But several pairs might be complementary, allowing a more spatially complete estimate of the velocity field. Thirdly, we can exploit data redundancy to reduce the uncertainty in the results.

Thus images are selected solely based on the date and time of acquisition and location. Pairs are then formed with a specific time span. In order to produce, for example, annual velocity fields, we select pairs separated by one year, or multiples of a year, to minimize the effects of the seasonal variability. It also increases the chances that the two images have a similar surface condition (linked to snow cover) which will improve the performance of the feature-tracking. Finally, the time span has to be large enough so that the displacement is significant with reference to the pixel size. Here, we obtain an annual velocity for year T by selecting all pairs of the form $(T-1; T)$ and $(T; T+1)$, as well as $(T-1; T+1)$, so that all velocity measured are centred around year T. For example, the Landsat 5/7 repeat cycle is 16 days, and 23 cycles represent 368 days, so not exactly one year, so we process pairs that have temporal baselines of $368-16$, 368 and $368+16$ days for one year and $736-16$, 736 and $736+16$ days for 2 years. Thus each image is paired with up to 6 other images. This allows us to compensate for some missing or poor quality images.

2.2. Preprocessing

2.2.1. Image coregistration

We assume that the images are corrected for topographic distortion, i.e. that the displacement observed between two images is actual horizontal motion and not influenced by topography. But as some images are not exactly georeferenced, they are first coregistered to a reference image. We chose to use the Global Land Survey as a reference data set that has a positional accuracy better than 50 m (Tucker, Grant, & Dykstra, 2004). Coregistration consists the following: computing the offsets on a regular grid (typically 100×100 estimates), fitting a degree 2 polynomial and resampling to the reference image grid using Sinc interpolation. The resampling is done only if more than 10% of the pixels have offsets higher than 0.5 pixels in order to preserve the actual radiometry of images that are already well coregistered. Higher order offsets may still appear, mainly due to instrumental uncertainties that cannot be corrected due to the whiskbroom Landsat acquisition system (Scherler et al., 2008), but as long as they are not coherent between images, they will be efficiently filtered out by the proposed strategy. All images of the same frame are then cropped to a common region to ensure that the correlation windows are the same from pair to pair and the measurement always corresponds to the same region. We use the coordinates of the frame corners provided by the USGS in shapefile format (https://landsat.usgs.gov/tools_wrs-2_shapefile.php) to consistently crop the images.

2.2.2. Principal component analysis

Images are then enhanced in order to improve the quality of the feature-tracking algorithm. Different steps have been proposed as follows: principal component analysis (PCA) to reduce the dimensionality of multi-spectral images, edge filters to enhance crevasse contours and high-pass filters for removing larger scale variations (Ahn & Howat, 2011; Berthier, Raup, & Scambos, 2003; Scambos et al., 1992).

The PCA is the procedure of projecting a set of different observations of the same variable, possibly correlated, into a new set of uncorrelated observations. It is constructed so that the first component maximizes the variance of the variable, then the second component maximizes the variance while being orthogonal to the first etc. It is interesting as it enhances the signal into a single value but the choice of the bands to be merged is a difficult task as it depends on the gain of the acquisition, the surface conditions of the glacier (e.g. clean or debris-covered) and the sensor. Heid and Kääb (2012a) use the Landsat panchromatic band because of its higher resolution whereas Scambos et al. (1992) and Berthier et al. (2003) apply a principal component analysis (PCA) on near-infrared and visible bands (1–5 for TM and ETM+) and use the first component, but this method does not explore the choice of the bands. Necsoiu et al. (2009) produce a combination of ASTER bands 1 and 2 to improve the performance of the correlation with

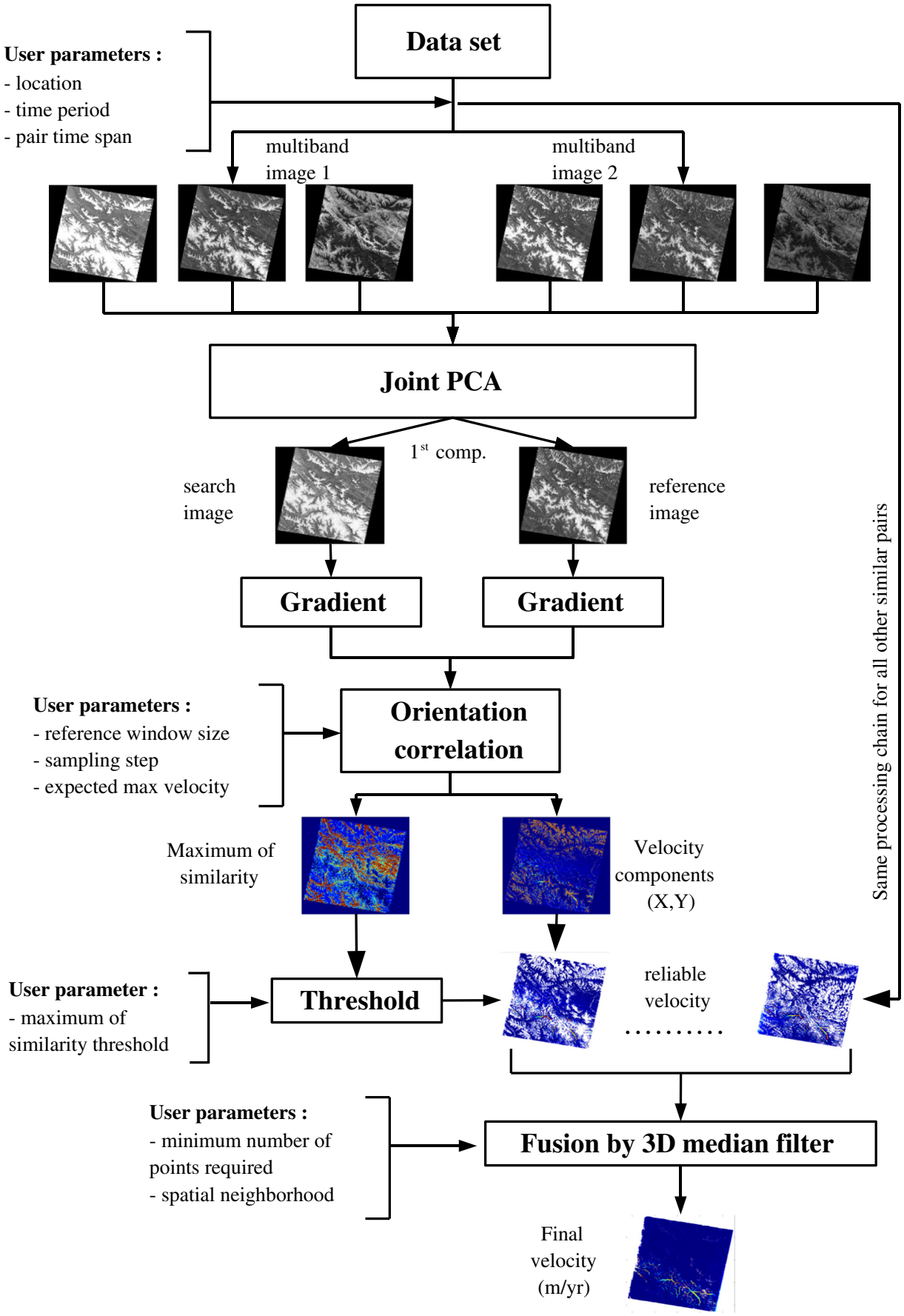

Fig. 1. Processing strategy to derive glacier velocities from a complete multispectral satellite archive.

SPOT panchromatic images. Redpath, Sirguey, Fitzsimons, and Kääb (2013) determine the best band or band combination by comparing the result of the feature-tracking of ASTER images with ground truths.

As we are seeking a method that can be exploited globally, we decide not to rely on ground truth for this step but rather on the performance of the feature-tracking itself. First, a few representative scenes of the studied region are selected. For each of these scenes, the feature-tracking is run for each band individually and the performance assessed using the success rate as defined in Section 2.5. Once the best band or bands according to this criteria are determined, several band combinations can be considered. Every combination is then compared to the others using the same criteria and eventually an optimal band or band combination can be chosen. The results of this method for our study case are detailed in Section 3.

Finally, we noticed that the result of the PCA can vary much from image to image, mostly due to changes in snow cover. In order to avoid correlating different band combinations, we perform the PCA on a concatenation of the 2 images of the pair instead of performing it for each image individually. This choice ensures that the same physical signal (same combination of spectral bands) is introduced in the correlation step. The PCA has thus to be applied for each pair specifically.

2.2.3. Intensity gradient

Two Sobel kernels of size 3×3 are applied to compute the intensity gradient in the x and y directions, which enhances surface features such as crevasses and serac or debris cover. The gradients are normalized in order to produce an orientation image, which is the input for the feature-tracking algorithm described below. The different enhancement steps are illustrated in Fig. 2.

2.3. Feature-tracking

Feature-tracking is a method that allows the estimation of a displacement between a first image called reference image and a second image or search image. First, a window Ω_r is chosen in the reference image centred around pixel (i, j). Then a window of same size is extracted from the search image but translated by (p, q) pixels within a specified search window Ω_s and compared to Ω_r using a function of similarity. This operation is repeated for different values of (p, q) and the position of the maximum of similarity, interpolated to a fraction of pixel, is a measure of the displacement.

2.3.1. Algorithm

After a comparison between 6 different methods, Heid and Kääb (2012a) showed that the method called "orientation correlation" proposed in Fitch, Kadyrov, Christmas, and Kittler (2002) has the best performance over mountain glaciers. Thus we focus only on this algorithm that is fast, illumination invariant and not sensitive to uniform areas such as in the saturated accumulation zones or the null-stripes that appear in the Landsat 7 ETM+ images after May 2003. In this algorithm, a synthetic complex image, called orientation image, is formed by setting the real and imaginary parts to the gradients in the x and y directions of the image intensity (I), respectively, and normalizing the quantity in order to take only the orientation into account (Fitch et al., 2002):

$$f = \begin{cases} \dfrac{g_x + i g_y}{\sqrt{g_x^2 + g_y^2}} \\ 0, \qquad \text{if } g_x = g_y = 0 \end{cases} \tag{1}$$

$$\text{where } g_x = \frac{\partial I}{\partial x},\ g_y = \frac{\partial I}{\partial y}. \tag{2}$$

Because the input images are complex, we perform a complex cross-correlation between the two orientation images. The similarity function is given for each pixel (p, q) by:

$$CO(p, q) = \frac{1}{n}\left| \sum_{(i,j)\in\Omega_r} f_r(i, j) f_s^*(i + p, j + q) \right| \tag{3}$$

where n is the number of points in the reference window Ω_r, f_r (f_s) the orientation image of the reference (search) image and f_s^* is the complex conjugate of f_s (this formula is simplified by the fact that the images being correlated are already normalized). Concretely, we match the orientation of the intensity gradient that is contained in the phase of the orientation image (see Fig. 2 right). We use the coherence tracking function proposed by Strozzi et al. (2002) that allows to track the gradient orientation which is contained in the phase of the orientation image. The coherence is computed in the Fourier domain and the maximum interpolated to a fraction of a pixel. The program also returns the signal-to-noise ratio (SNR) i.e. the ratio between the correlation maximum and the average value in the search window which is a commonly used proxy for the confidence of the matching (Quincey, Copland, et al., 2009; Strozzi et al., 2002).

2.3.2. Parameter setting

The optimum parameters for the feature-tracking, i.e. the reference and search window sizes must then be chosen. The choice of the reference window size is complex since it must be large enough to avoid correlating only noise but small enough to avoid deformation of the

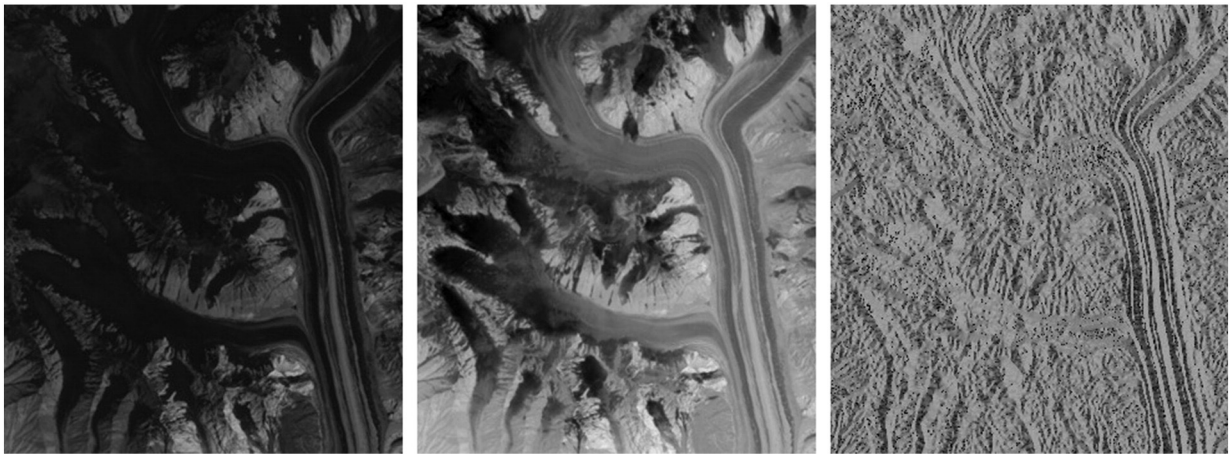

Fig. 2. Example of enhancement procedure for Landsat images over northern tributaries of the Baltoro glacier (Karakoram): Landsat mid-infrared band 5 (left) has the best performance in the Karakoram (see Section 3.2.2), selecting the first component of a PCA of bands 4 & 5 results in brightening of the accumulation zones (middle), the gradient orientation displays enhanced glacier features (right).

matched objects inside the window. We perform the offset-tracking for a few selected pairs and different reference window sizes γ_r and choose the lowest value that minimizes the errors in stable areas. It ensures that the window is large enough with respect to the image resolution while retaining the highest possible spatial resolution. This choice might not be optimal for all glaciers because it depends on the texture and size of the glaciers, but more sophisticated methods such as locally adaptive reference window sizes (Debella-Gilo & Kääb, 2012) are computationally too expensive for processing a large number of images.

The search window is chosen to be larger than the expected maximum displacement but small enough not to increase unnecessarily the computation time. For an expected maximum velocity V_{max} and a time span Δt between two images of pixel size R, the search window size is set to $\gamma_s = 2V_{max}\Delta t/R + \gamma_r$.

2.4. Postprocessing

After processing all the selected pairs, it is important to filter the displacement vectors and to merge all results into a single value. In the following sections, we propose a method to exploit the redundancy in the series of pairs in order to efficiently remove outliers and produce a more robust velocity field with very little user interaction.

2.4.1. Outliers removal

Mismatches or outliers are identified and removed using a threshold value of SNR. The choice of the threshold is a compromise between removing most of the mismatches while retaining the interesting information. The threshold can be easily determined by looking at the residuals in stable areas (see MAD in Section 2.5). We show in Section 3.2.3 that the residuals are high for low thresholds and drop dramatically to reach an asymptote in the range of the coregistration errors. Thus, we recommend to compute the MAD in stable areas for different SNR thresholds and select the lowest threshold that approaches the asymptote.

2.4.2. Fusion into a single velocity

At this stage, we have a set of displacement fields that may contain gaps but also redundant values. The idea is to exploit the redundancy of information and physical properties of the glaciers to merge this set into a single, more robust velocity. We propose to compute a median of all neighbouring values both in a spatial and temporal neighbourhood, for each x and y component of the velocity. To ensure that the median is statistically significant and in order to remove spatially isolated pixels, we do not retain the value of the velocity if the number of points used to compute the median is less than a certain value Nmin. This method relies on two assumptions. First, because pairs were selected with similar time spans within a specified period, we assume that the measured velocity does not vary much from pair to pair. Secondly, we assume that the shear of the ice is low and that adjacent pixels on a glacier do not have large velocity differences. This is arguable at the edge of the glaciers where the moving ice is adjacent to the stable moraine and there might be a strong gradient. Nevertheless, a median filter preserves edges and thus glacier contours. The size of the spatial window for the median filtering depends on the image resolution and the number of pairs available (the more points we have, the smaller the window can be) and the size of the glaciers. For mountain glaciers, this spatial window should not exceed a few hundred metres.

This method offers several advantages. First, the median is not sensitive to isolated outliers and thus is able to filter out aberrant values that were not removed in the first stage. The use of a median filter to discard aberrant values is common in glaciology (Ahn & Howat, 2011; Copland et al., 2009; Heid & Kääb, 2012a), but this method still requires supervision by an expert to select the threshold and is region-dependent (Heid & Kääb, 2012a). By adding more information with a set of displacement fields, we can minimize the expert interaction. Secondly, several factors (orthorectification errors, shadows, clouds) can induce matches with high confidence, because the features actually match between the two images, but are not related to actual terrain motion. This is often the main source of errors when applying feature-tracking to satellite images. But because these errors are not coherent from pair to pair, the median is not affected and the result of the fusion is still robust.

At last, in order to merge together velocity fields over a large region, with possible overlap and different projections (for example, different Landsat frames are projected on different UTM zones), we recommend to set a global grid and to merge the velocity fields by taking the median value of neighbour estimates, both spatially and in the stack of pairs, at each node of the grid.

2.5. Performance assessment indices

In this section, we define the indices that are used throughout the study to evaluate the velocity fields. As noted by Burgess et al. (2013), the presence of mismatches in the velocity fields tends to stretch the tails of the velocity distribution. It is thus important to use robust statistical estimators (Rousseeuw & Hubert, 2011). It is the reason why we suggest to use the median and median absolute deviation (MAD) instead of the mean and standard deviation.

In the following, velocity estimates are considered as valid after applying the SNR threshold. Glaciers are delimited using version 3.2 of the Randolph Glaciers Inventory outlines (Pfeffer et al., 2014) except for some parts of the Karakoram where we used manually edited outlines due to a misalignment between the outlines and the actual glacier location. The performance assessment indices we retained are the following:

- The success rate SR, which is the percentage of valid velocity estimates on glaciers.
- The normalized median absolute deviation (MAD) of the velocity is as follows:

$$\mathrm{MAD} = 1.483 \times \mathrm{med}(|V - \mathrm{med}(V)|) \quad (4)$$

which is a robust equivalent of the standard deviation. When not mentioned, it is computed for the velocity magnitude V, or for each component of the velocity when a different behaviour is expected for the two components. In particular, in stable areas, i.e. off glaciers, where the velocity V is supposed to be null, the MAD is as follows:

$$\mathrm{MAD}_{off} = 1.483 \times \mathrm{med}_{(i,j)\in\Omega_{off}}(|V(i,j)|) \quad (5)$$

where Ω_{off} is the ensemble of points off glaciers. This is a proxy for the uncertainty of the measurement.

Table 1
Selected test pairs for the choice of the preprocessing and feature-tracking parameters.

Area	Path/row	Sensor	First date	Second date	Image 1	Image 2
Karakoram	148/35	LE7	25/02/2000	27/02/2001	LE71480352000056SGS01	LE71480352001058SGS00
Everest	140/41	LE7	30/10/2000	17/10/2001	LE71400412000304SGS00	LE71400412001290SGS00
Kunlun Shan	145/35	LT5	10/08/2007	15/08/2009	LT51450352007222IKR00	LT51450352009227KHC00

- The dispersion: during the fusion step, the MAD can be calculated at each velocity location.

$$\sigma(i,j) = 1.483 \times \mathrm{med}_{t\in T}\left(\left|V(i,j,t) - \overline{V}(i,j)\right|\right) \quad (6)$$

where T is the set of N velocity estimates V(i,j,t) merged to obtain the median velocity $\overline{V}(i,j)$ at pixel (i,j). This is indicative of the variability between the different velocity estimates.

- The coherence of the velocity vectors that contributed to the median, i.e. if they point in the same direction. We define the velocity vector coherence (VVC) as follows:

$$VVC(i,j) = \frac{\left\|\sum_{t\in T} \vec{V}(i,j,t)\right\|}{\sum_{t\in T} \left\|\vec{V}(i,j,t)\right\|}. \quad (7)$$

According to the triangle inequality, VCC is in the interval [0,1], equal to 1 if all vectors are perfectly aligned and tend to 0 if they point in random directions.

2.6. Uncertainty

Uncertainties of the single-pair velocity fields are dominated by the precision of the feature-tracking algorithm, the image to image registration and the temporal variability of glacier flow. But the uncertainty of the final, i.e. the median velocity over the considered period, is known to decrease with the number of estimates. Suppose a sample of size N drawn from a normally distributed population with variance σ_n, the sample median converges asymptotically to a normal distribution with standard deviation $\sigma_m = \sqrt{\frac{\pi}{2}}\frac{\sigma_n}{\sqrt{N}}$ (Chu, 1955). Here, we cannot make the hypothesis of a normal distributed velocity because of the possible presence of outliers, but because the different measurements are independent and symmetrically distributed, we assume that the 95% confidence interval of each component of the final velocity follows a similar law:

$$t_{95} = k\frac{\sigma}{N^{\alpha}} \quad (8)$$

where σ is the MAD of the N velocities used to compute the median velocity, t_{95} the 95% confidence interval, i.e. the difference between the 97.5th quantile and the 2.5th quantile of the final velocity distribution, and k and α parameters to be determined. Applying a logarithm to this equation, we obtain a linear relationship as follows:

$$\log\left(\frac{t_{95}}{\sigma}\right) = p_0 + p_1 \log(N). \quad (9)$$

We propose to compute the 95% confidence interval in the stable areas, where the true velocity is known to be null, for each value of N. The relationship between t_{95}, σ and N is then fitted to Eq. (9) using a least-square regression. This relationship is extrapolated to glacier areas to compute the 95% confidence interval of each component of the final velocity.

Table 2
Success rate of the feature-tracking over glaciers for each individual Landsat band (upper part) or different PCA combinations and component (lower part). The best value for each column is highlighted in bold. For the 15 m band 8, the reference window has been set to 16 × 16 and 32 × 32 pixels to keep an identical window size in pixels and metres respectively.

	Everest	Karakoram	Kunlun
Band 1	8	7	4
Band 2	10	13	10
Band 3	9	8	8
Band 4	24	9	*15*
Band 5	*42*	*40*	9
Band 8 (r16)	19	14	
Band 8 (r32)	25	17	
1,2,3,4,5	37	48	15
1,2,3,4	24	14	15
4,5	**44**	**48**	**15**

3. Results

3.1. Data set

We assess the ability of the processing strategy to produce glacier annual velocity fields over a large region. We thus process all Landsat pairs available between 1999 and 2001 over the Pamir–Karakoram–Himalaya (PKH) extending over 3000 km. As mentioned earlier, we process all pairs of images with a time span in the list 368 − 16, 368, 368 + 16, 736 − 16, 736 and 736 + 16 days. It represents 1382 images, 1536 pairs, covering 68 Landsat frames. The location of the studied region and the processed frames is shown in Fig. 5. We use the Level 1T images, which are already terrain corrected using ground control points (GCPs) and digital elevation models (DEMs) and available at no cost on the USGS website in GeoTIFF format in UTM projection. We

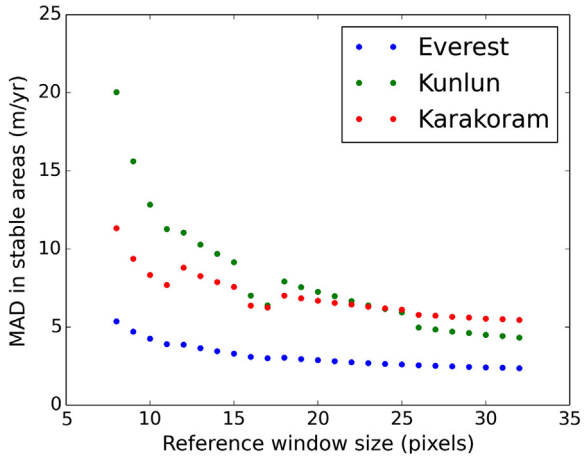

Fig. 3. MAD of the velocity in stable areas as a function of the reference window size γ_r for the three test pairs and an SNR threshold of 5.

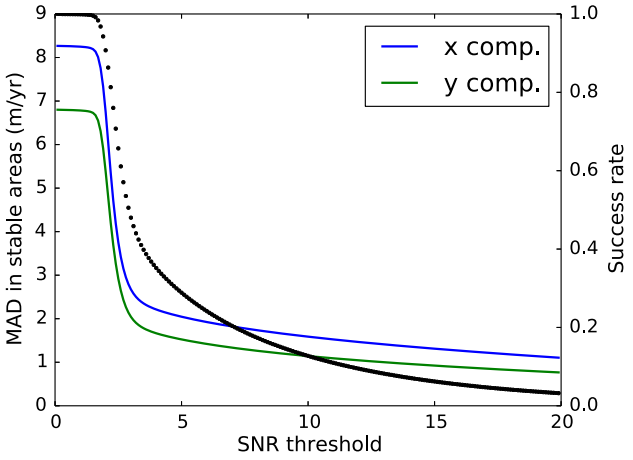

Fig. 4. MAD of each component of the velocity in stable areas (plain lines) and success rate (black dots) for different SNR thresholds.

downloaded the images using the Bulk Download Application available on the USGS website (https://lta.cr.usgs.gov/BulkDownloadApplication) that allows downloading a large set of images at once. Each image is roughly 8000 × 7000 pixels (or 16,000 × 14,000 for the panchromatic) and each scene is over 600 MB in size. The processing of a pair takes approximately 15 min on an 8 cores desktop computer and the entire processing took 16 days.

3.2. Parameter setting

Because it would be time-consuming to define specific parameters for each of the available pairs, a few representative test pairs with a low cloud cover and good contrast have been selected to set the parameters that will be applied to all scenes. We selected three test pairs that are representative of different glacier types in the PKH (Table 1). A first frame covering a large part of the Karakoram, north-west of the Himalaya is selected because it hosts some of the largest mountain glaciers. The second frame covers the Everest region that features smaller glaciers with an important debris cover which is an interesting property for feature tracking. The last frame over the Kunlun Shan features mostly clean-ice glaciers. Two different sensors, LE7 and LT5 have also been selected to account for possible differences.

3.2.1. Feature-tracking parameters

The most critical parameter for the feature-tracking is the size of the reference window γ_r. Fig. 3 shows the MAD in stable areas as a function of the reference window size for the three test pairs and an SNR threshold of 5. It clearly shows that for values of γ_r below 12, the measured offsets are noisy, which is likely due to the small window size. Choosing higher values of γ_r would reduce the noise even more, but it would also decrease the resolution of the results and increase the risk of deformation within the reference window, which is not desirable.

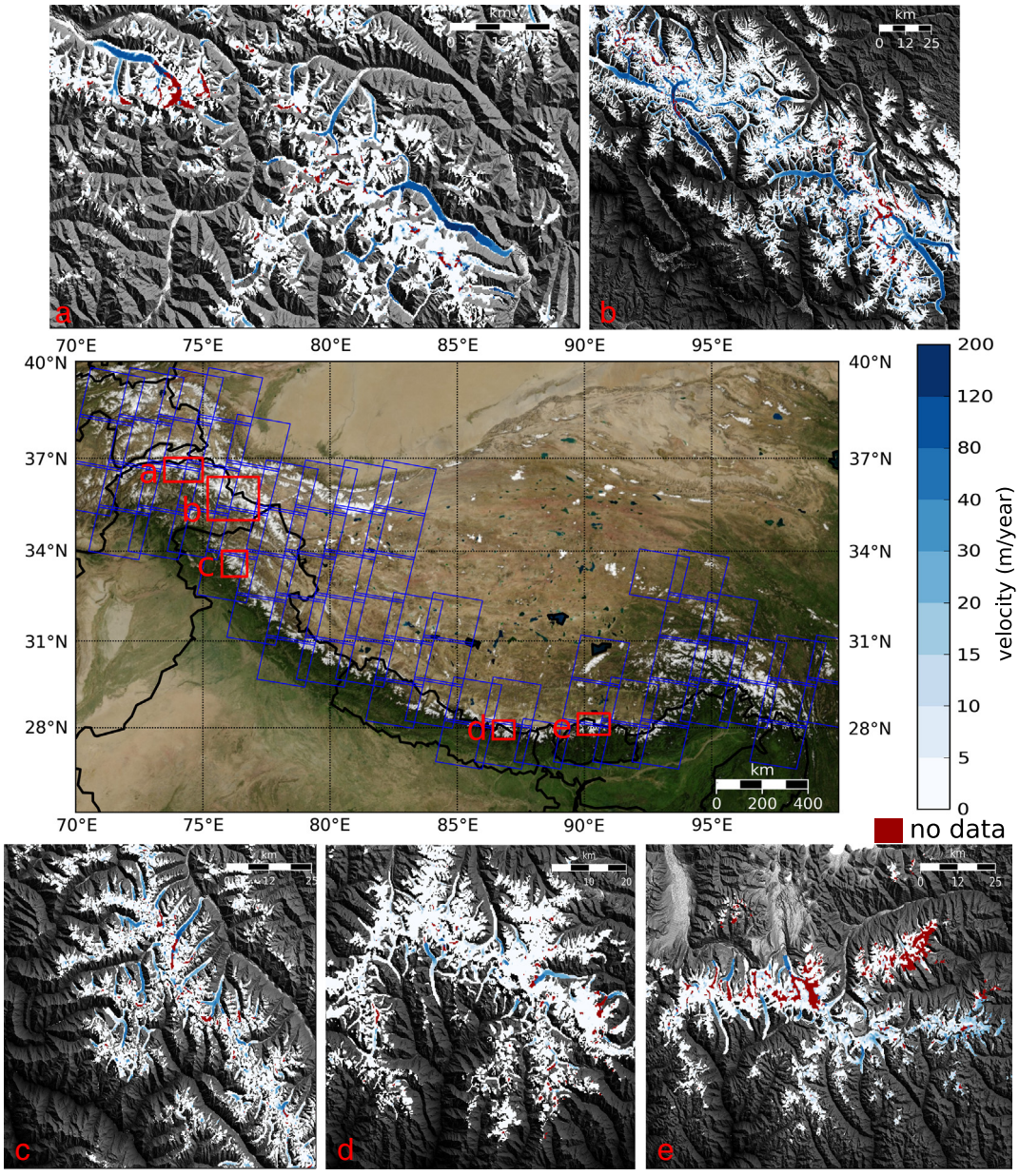

Fig. 5. Map of the studied region: blue polygons show processed Landsat frames, red squares highlight the position of the inserts a to e (a: Hindu-Kush, b: Karakoram, c: Jammu-Kashmir, d: Everest, e: Bhutan). Inserts show annual glacier velocity fields for the year 2000 within the RGI masks (blue colour scale). Red points are region without velocity estimate. (For interpretation of the references to colour in this figure legend, the reader is referred to the web version of this article.)

We thus set the reference window to 16 × 16 pixels (480 m × 480 m) that approaches a minimum in MAD while not being excessively large. Although not necessary, using a power of 2 optimizes the computation of the feature-tracking algorithm in Fourier domain. The search window is set to allow tracking displacements that are below 300 m/year, which is the case for most of the studied glaciers with the exception of the surging glaciers (Quincey et al., 2011). So it varies from 30 to 48 pixels depending on the pair time span. Images time span and search window are tuned to maximize precision and long-term trend, for study aimed at the study of glaciers with rapidly changing dynamics (e.g. surging glaciers) these parameters can be adapted; e.g. the inclusion of pairs with shorter time span or larger search windows. We set the spacing between 2 correlation patches to half the reference window, so 8 pixels.

3.2.2. Band selection

We select the best band or band combination following the method described in Section 2.2, for the three test pairs. The success rate for each pair and band 1 to 5 (and panchromatic when available) are shown in Table 2, upper part, for an SNR threshold of 5. We observe that the visible bands 1 to 3 have low performance, this is due to saturation on snow and clean-ice. Then, band 5 gives the best results for the Everest and Karakoram region whereas band 4 is more interesting for the Kunlun region. The panchromatic band has better performances than the bands 1 to 3 but is still very saturated and doesn't give the best results on snow and ice. This ranking is not affected by the choice of the SNR threshold. This difference comes from differences in glacier types. The Kunlun scene contains essentially clean-ice glaciers, which have a very low and almost uniform signal in band 5 (mid-infrared) and explain the poor performance for this band. On the contrary, the Everest and Karakoram regions contain many debris-covered glaciers which have a more homogenous response between all bands, but band 5 has a higher contrast in accumulation zones. In summary, band 5 has overall best performance in the accumulation areas where all others are saturated, except in shadows and over clean-ice where band 5 captures a very low signal (Fig. 2). In those areas, band 4 has a higher contrast, thus band 4 and 5 seem to be complementary.

We then perform the same tests for the first component of different PCA combinations as follows: the 1–5 combination that is used by Scambos et al. (1992) or Berthier et al. (2003), a combination that excludes band 5 and a combination of only bands 4–5. Results are shown in Table 2 lower part.

They show that the combination of bands 4–5 has the best performance in all regions and it consistently performs better than any of the single bands. It seems to profit from the complementarity of bands 4 and 5. This is not the case for the PCA (1, 2, 3, 4, 5) that has sometimes worse performances than the best band, as for example the Everest pair. So this band combination is not the best choice for studying mountain glaciers of different cover types. The results for PCA (1, 2, 3, 4) confirm that band 5 brings valuable information and shouldn't be excluded. In fact, it is the only band that differs significantly from all others on snow and ice and allows to increase the variance of the PCA. Again, these are robust conclusions for different choices of the SNR threshold (we tested 3, 5 and 7).

In conclusion, the first component of PCA (4,5) is the band combination that has the most robust performance over mountain glaciers.

3.2.3. SNR threshold

Once the feature-tracking parameters and the preprocessing steps are chosen, we can run the feature-tracking for each available pair to compute velocity fields and an associated SNR. These intermediate results allow us to set the SNR threshold used to remove residuals. Fig. 4 shows the MAD in stable areas for each component of the velocity and the success rate for different SNR thresholds for all processed pairs. Low values of SNR mean that the reference and matching window don't match and the associated offsets are very noisy. But it is interesting to note that the MAD drops suddenly for SNR threshold higher than 3 and reaches an asymptote. The value of the asymptote represents the mean residuals for single pairs velocities, here it is in the range of 1–2 m/year and is slightly different for the x and y component. They are due to remaining orthorectification errors but thanks to the coregistration step they are reduced compared to estimated uncertainty in Landsat image to image registration (Lee, Storey, Choate, & Hayes, 2004; Storey & Choate, 2004). The success rate drops in the same way but continues to decrease for higher SNR threshold. Thus, we choose an SNR threshold of 4 that allows to substantially filter outliers while not removing too many interesting points.

3.2.4. Fusion

The individual velocity fields are then merged together using a median filter. The median velocity of each component is computed within all velocity fields and a spatial neighbourhood. Because the Landsat frames over this large region are projected on different UTM zones, the median velocity is computed on a 240 m Lambert conformal conic grid. Each velocity estimate within a radius of $\sqrt{2} \times 240 = 340$ m is then included in the median, which means up to the nine closest neighbours are retained. Finally, if the number of data points used to compute the median is lower than Nmin = 5, we discard the measurement because the median is not robust enough.

3.3. Final velocity fields

The final velocity estimated for the PKH and the year 2000 (period of 1999–2001) is presented in Fig. 5 for several subregions. A velocity has been estimated for 76,000 km^2 or 92% of the total glacierized areas within this region. Main gaps (red patches) correspond to the accumulation zones with low texture and specific glaciers flowing faster than 300 m/year, especially in the Karakoram. The pattern of the velocity fields are in good agreement with previous works, in particular Copland et al. (2009), Heid and Kääb (2012a) and Rankl, Kienholz, and Braun (2014) in the Karakoram (insert b), Quincey, Luckman, and Benn (2009) and Scherler et al. (2011b) in the Everest region (insert d), Kääb (2005) in Bhutan (insert e).

4. Discussion

4.1. Contribution of the fusion versus single pairs

In this section, we assess the performance of the processing of the complete archive compared to the results of single pairs for the frame 148/35 (East Karakoram) and the year 2000 (pairs within the period of 1999–2001). The data set is 26 images and 29 pairs. Fig. 6 represents

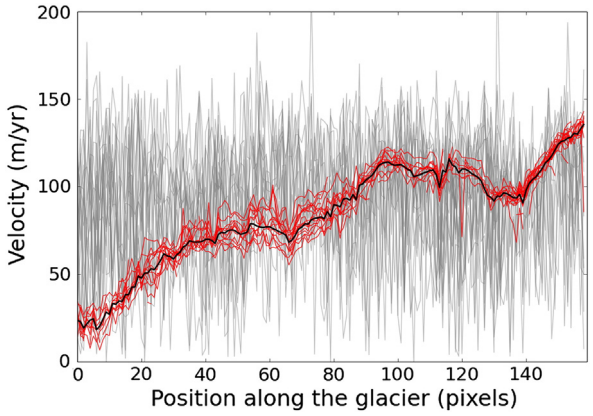

Fig. 6. Velocity profiles along the Baltoro glacier (35°42′29″N, 76°23′21″E) for the 29 available pairs for the years 1999 to 2001: unfiltered (grey), after selecting values with an SNR higher than 4 (red) and applying the spatio-temporal median (black).

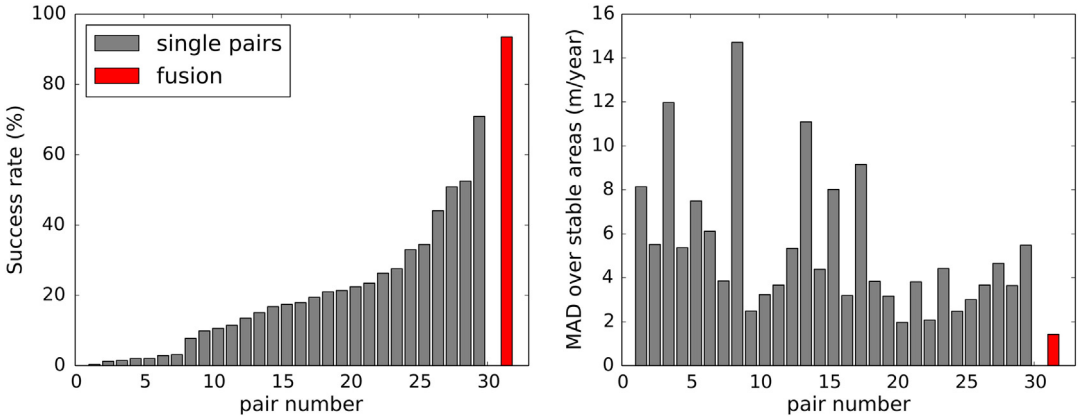

Fig. 7. Left: Success rate for each individual pair, in ascending order and for the result of the fusion (red). Right: MAD in stable areas for same pairs in same order. (For interpretation of the references to colour in this figure legend, the reader is referred to the web version of this article.)

the effect of each step of the postprocessing for a velocity profile along the Baltoro glacier. The raw velocity fields (in grey) contain many aberrant values due to clouds and shadows in the images that need to be filtered out. Applying an SNR threshold of 4 removes most of them, but some outliers still remain and it does not ensure that the displacements are physically acceptable. By including more information, the spatio-temporal filtering method has several advantages as follows: it efficiently removes outliers, it fills most gaps that may appear and gives a robust single value for each location.

More quantitatively, Fig. 7 (left) shows the success rate for each single pair and the fusion. The best single pair or optimum pair (i.e. the pair with the highest success rate) allows an estimate of the velocity of 71% of the glacierized regions, main gaps are due to saturation in accumulation areas. Meanwhile, the result of the fusion returns a velocity estimate for 94% of the points. The fusion outperforms all individual pairs by exploiting the complementarity between different pairs.

Fig. 7 (right) shows the MAD in stable areas for each pair individually and for the result of the fusion. The MAD for the optimum pair is 5.5 m/year and the mean MAD for all single pairs 5.4 m/year, mainly due to orthorectification errors. The fusion has the advantage of reducing this noise that is not correlated between successive pairs. As a consequence, the MAD for the fusion is 1.4 m/year, gaining a factor of almost 4 on the optimum pair.

4.2. Uncertainties

In this section we show how the fusion approach allows to reduce the uncertainty of the final velocity fields with the example of the Karakoram subregion (74–78°E, 34.5–37°N). Fig. 8 shows the dispersion of the single velocities around the median (cf. Eq. 6). It highlights the two main sources of uncertainties. The first source of uncertainty is coregistration errors that are visible in the shape of large rectangles displaying the contours of the Landsat frames or correlated with the topography. Despite the coregistration with the GLS images, the mean dispersion over stable areas is 4.1 m/year. The second source of uncertainty is the variability in glacier flow over the three year period. Glaciers are clearly visible in the figure in the shape of yellow or red tongues. In particular, a large variability is observed on the central Rimo glacier (as noted with an *) of approximately 40 m/year. This is coherent with the reported surging behaviour of this glacier during that period (Bhambri et al., 2013). The mean dispersion over glaciers is 6.4 m/year.

The uncertainty of the final velocity, i.e. the median velocity, is impacted by the dispersion of the velocities but is reduced with an increasing number of observations. Fig. 9 (left) shows the 95% confidence interval t_{95} of the final velocity in stable areas as a function of the number of points used to compute the median. When few velocity estimates are available, i.e. the measurement is spatially isolated or very few pairs

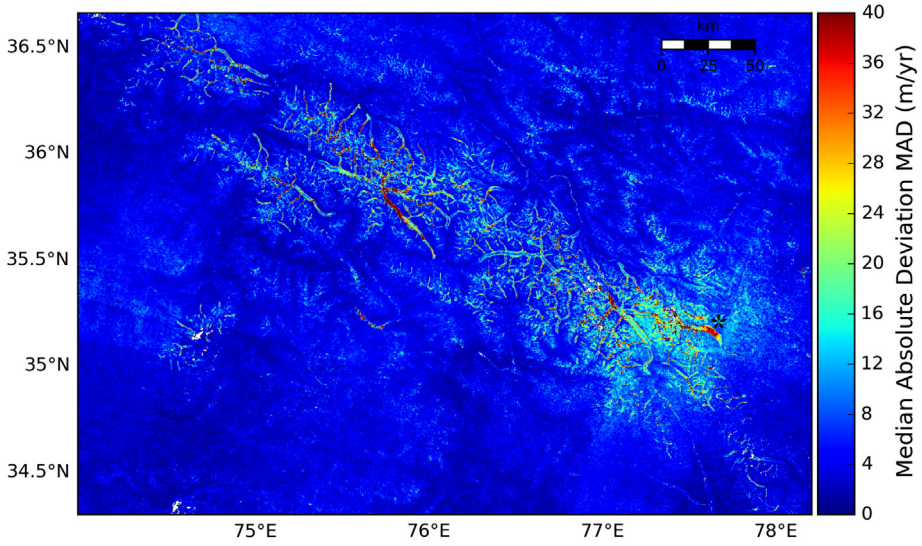

Fig. 8. Dispersion of the velocities estimated from all pairs for the Karakoram and the period of 1999–2001.

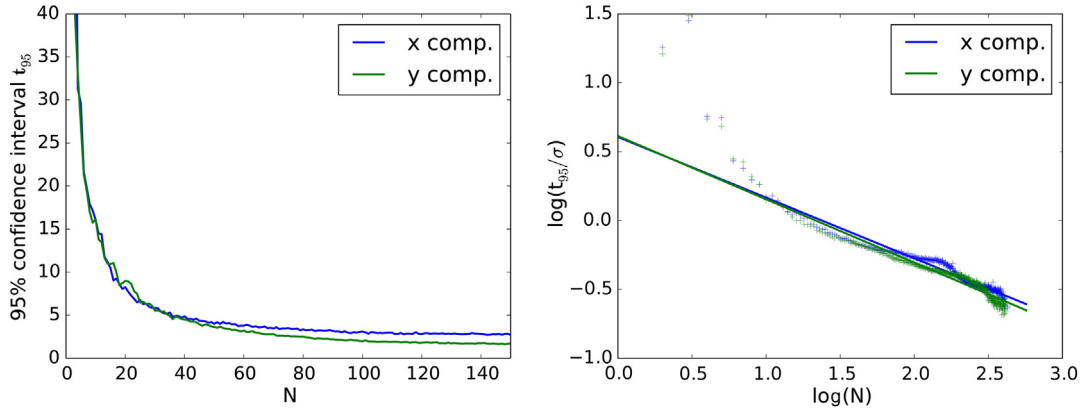

Fig. 9. Residuals in stable areas as a function of the number of available velocity estimates for the Karakoram subregion.

allows for a measurement, the residuals reach over 20 m/year but as the number of merged velocity estimates increases, the confidence in the measurements reaches a few m/year. Fig. 9 (right) shows the linear relationship between $\log(t_{95}/\sigma)$ and $\log(N)$. The relationship is strong except for N below 5 ($\log(N) \leq 0.7$). Actually, for a low number of samples, the median and MAD are more difficult to estimate and their distributions diverge from the normal distribution. For these values, our method underestimate the uncertainty and we recommend to remove these points. For $N \geq 5$, the parameters of the regression are summarized in Table 3.

This allows us to compute a 95% confidence interval as a function of σ and N. Fig. 10 shows the result for the Karakoram region. The uncertainty map has a similar shape as σ (Fig. 8), but is weighted by N; in particular, on stable grounds where there are generally more measurements (less problems of saturation), the uncertainty is reduced whereas in snow covered areas, the low contrast reduces the number of measurements and uncertainty remains relatively high. The median uncertainty is 2.0 m/year in stable areas. Over glaciers, the median uncertainty is 4.4 m/year, from a few m/year on some glacier tongues to 10 m/year in some accumulation zones. The uncertainty is also higher on glacier edges (as visible in the inset of Fig. 10), due to higher strain rates and thus a more variable velocity within the reference window. Some grid patterns are also visible: they are due to the fact that the UTM and Lambert conic grids are not superposed and the number of neighbours varies periodically.

At last, the velocity vector coherence is illustrated in Fig. 11 for the Karakoram region. Frame patterns or features correlated with topography remain in stable areas and are indicative of coregistration errors. Nevertheless, the coherence is much higher on glaciers which mean that the merged velocity vectors are well aligned and that we can be confident in the direction of the velocity field.

5. Conclusions

In this paper, we present a processing strategy to estimate mountain glacier velocities from a complete satellite archive. We select all possible pairs for a specific time span, avoiding the lengthy task of manually selecting the best available images. The pairs are then submitted to the same preprocessing steps and a feature-tracking algorithm is performed to produce surface velocity fields. Successful measurements are selected solely based on the quality of the correlation, and merged together. First, the most aberrant displacement values are rejected based on the confidence function returned by the feature-tracking algorithm; all points below a certain threshold are removed. Secondly, the results are filtered based on the spatial and temporal consistency of the displacement. A median filter is applied to the resulting stack of velocities on a pixel by pixel basis within a spatio-temporal neighbourhood to obtain the final glacier velocity field.

This strategy has been applied to produce glacier annual velocity fields from a data set of 1536 pairs of Landsat 5 and 7 images acquired within a 3 year period and covering the Pamir–Karakoram–Himalaya region extending over 3000 km. Results on a single Landsat frame shows that the percentage of successful measurements increases from 71% of glacierized area for the best available pair, to 94% for the merged results. In overall, it allows us to obtain a velocity estimate for 76,000 km^2 or 92% of the glacierized areas of this region. We then estimate the impact of the coregistration errors and variability of glacier flow on the final velocity over the Karakoram region (300×200 km). The median 95% confidence interval is reduced to 2.0 m/year in stable areas and 4.4 m/year over glaciers thanks to the redundancy in the measurements.

The strategy has been applied to Landsat images but is flexible and could easily be applied to various sensors with different pixel resolution or wavelength, including radar. This would be particularly valuable for the upcoming Sentinel 1–2 missions of the European Space Agency that will provide repeated images of the Earth surface. This strategy can also be applied to derive not only annual but seasonal velocities using set of pairs with shorter time span. More complex postprocessing strategy as for example time series inversion (Lanari et al., 2007) to select the coherent displacements along the time series could be implemented, potentially allowing to derive the seasonal velocity variations.

The analysis of complete satellite archives open new perspectives for the study of glacier's dynamics against physical parameters such as length, slope and debris cover, for the study of glacier response to climate changes, glacial geomorphology, erosion (Scherler, Bookhagen, & Strecker, 2011a), glacial hazards (Bolch, Buchroithner, Peters, Baessler, & Bajracharya, 2008) and the estimation of the contribution of surface mass balance and ice fluxes to the observed glacier thinning/thickening (Berthier & Vincent, 2012).

Acknowledgements

Glacier outlines are downloaded from the GLIMS database http://glims.org/RGI/ except for the outlines in the Baltoro area which are courtesy of Julie Gardelle. We would like to thank the USGS for making the Landsat archive freely available at http://earthexplorer.usgs.gov/. We are grateful to Urs Wegmüller and Charles Werner for their precious help in improving the feature-tracking code. Comments and suggestion of three anonymous reviewers greatly improved the quality of the

Table 3
Parameters for the linear regression between $\log(t_{95}/\sigma)$ and $\log(N)$.

Component	α	k	R^2
x	0.44	4.0	0.94
y	0.46	4.1	0.94

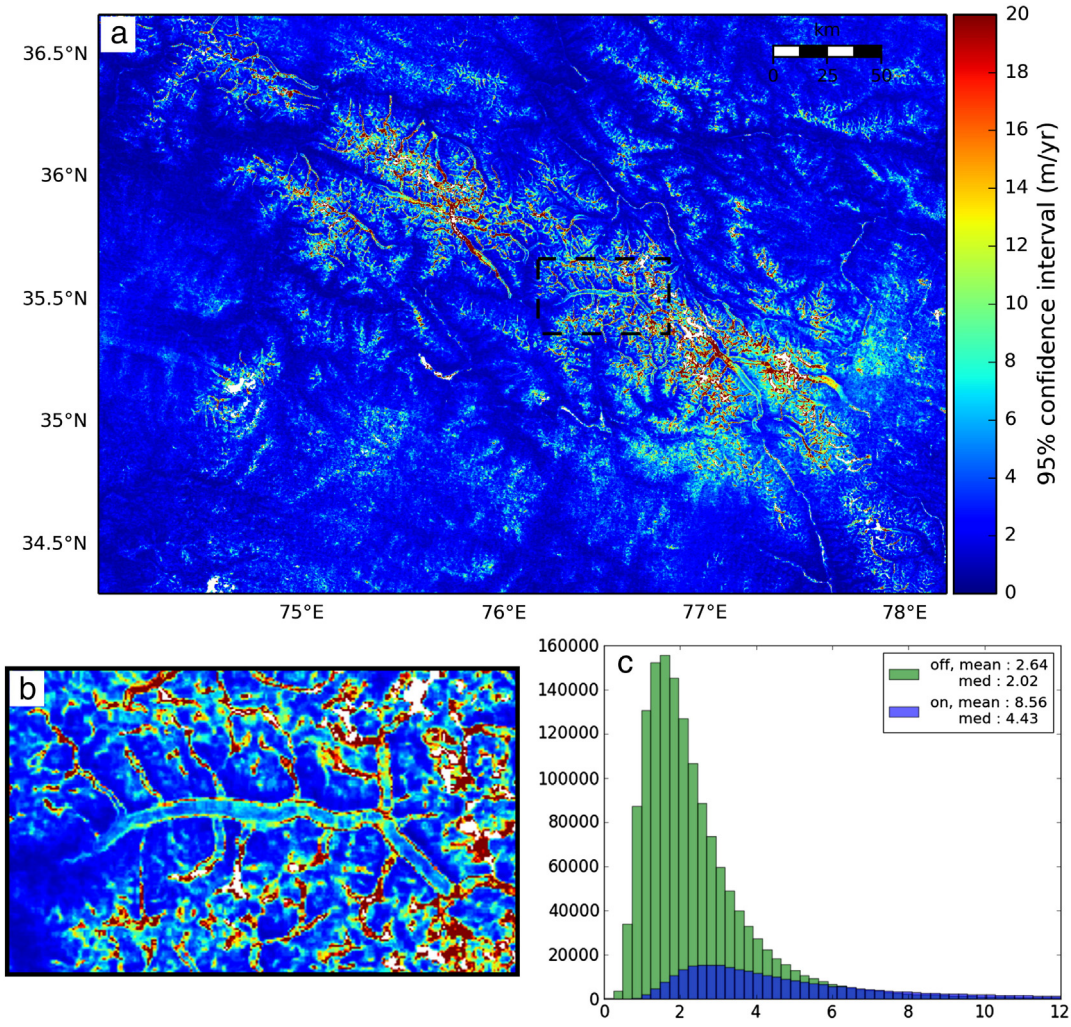

Fig. 10. (a) Uncertainty of the final velocity for the Karakoram and the period of 1999–2001, (b) zoom over the Baltoro glacier (dash line), (c) histogram of the uncertainty on and off glacier.

paper. All processing with the exception of the feature-tracking have been performed using Python and GDAL. We thank the Tera_SAR (Mastodons CNRS) project for their support. A. Dehecq aknowledges a PhD fellowship from the French Space Agency (CNES) and the Assemblée des Pays de Savoie (APS). This work is supported by the GdR ISIS, a TOSCA CESTENG project 2013-15 and the Dragon10302

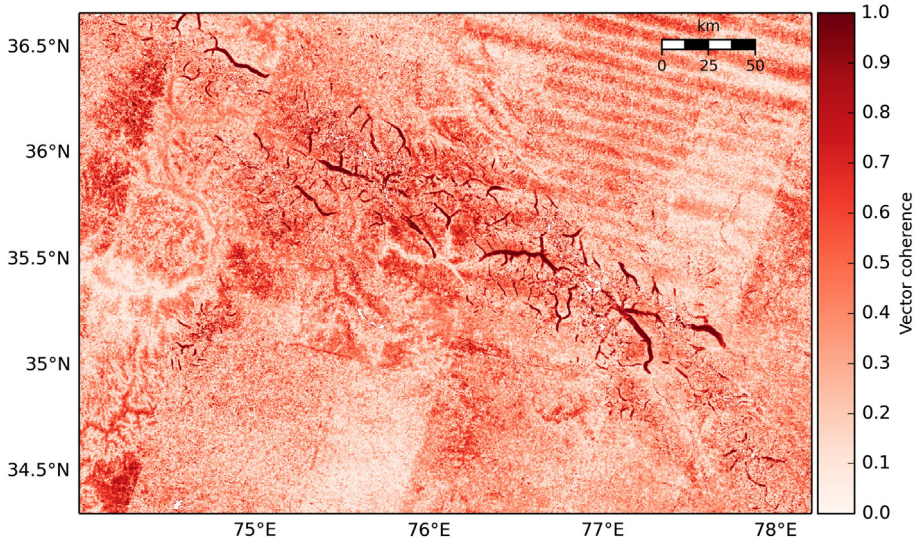

Fig. 11. Velocity vector coherence for the Karakoram region. A value of 1 means perfect alignment of all the vectors contributing to the median velocity, 0 means completely random directions.

project, a partnership between the European Space Angency (ESA) and the National Remote Sensing Center of China (NRSCC).

References

Ahn, Y., & Howat, I. M. (2011). Efficient automated glacier surface velocity measurement from repeat images using multi-image/multichip and null exclusion feature tracking. *IEEE Transactions on Geoscience and Remote Sensing*, *49*, 2838–2846 (URL: http://ieeexplore.ieee.org/xpls/abs_all.jsp?arnumber=5738677).

Barros, V., Field, C., Dokken, D., Mastrandea, M., Mach, K., Bilir, T., et al. (2014). IPCC 2014: Climate change 2014: Impacts, adaptation, and vulnerability. Part B: Regional aspects. *Contribution of Working Group II to the Fifth Assessment Report of the Intergovernmental Panel on Climate Change*. Cambridge, United Kingdom and New York, NY, USA: Cambridge university press (ed).

Berthier, E., Raup, B., & Scambos, T. (2003). New velocity map and mass-balance estimate of Mertz Glacier, east antarctica, derived from Landsat sequential imagery. *Journal of Glaciology*, *49*, 503–511. http://dx.doi.org/10.3189/172756503781830377.

Berthier, E., Vadon, H., Baratoux, D., Arnaud, Y., Vincent, C., Feigl, K. L., et al. (2005). Surface motion of mountain glaciers derived from satellite optical imagery. *Remote Sensing of Environment*, *95*, 14–28 (URL: http://www.sciencedirect.com/science/article/pii/S0034425704003463).

Berthier, E., & Vincent, C. (2012). Relative contribution of surface mass-balance and ice-flux changes to the accelerated thinning of Mer de Glace, French alps, over 1979–2008. *Journal of Glaciology*, *58*, 501–512. http://dx.doi.org/10.3189/2012JoG11J083.

Bhambri, R., Bolch, T., Kawishwar, P., Dobhal, D. P., Srivastava, D., & Pratap, B. (2013). Heterogeneity in glacier response in the upper Shyok valley, northeast Karakoram. *The Cryosphere*, *7*, 1385–1398. http://dx.doi.org/10.5194/tc-7-1385-2013 (URL: http://www.the-cryosphere.net/7/1385/2013/).

Bolch, T., Buchroithner, M. F., Peters, J., Baessler, M., & Bajracharya, S. (2008). Identification of glacier motion and potentially dangerous glacial lakes in the Mt. Everest region/Nepal using spaceborne imagery. *Natural Hazards and Earth System Sciences*, *8*, 1329–1340. http://dx.doi.org/10.5194/nhess-8-1329-2008 (URL: http://www.nat-hazards-earth-syst-sci.net/8/1329/2008/).

Burgess, E. W., Forster, R. R., & Larsen, C. F. (2013). Flow velocities of Alaskan glaciers. *Nature Communications*, *4* (URL: http://www.nature.com/ncomms/2013/130716/ncomms3146/full/ncomms3146.htm l?message-global=remove WT.ec_id=NCOMMS-20130717).

Chu, J. T. (1955). On the distribution of the sample median. *The Annals of Mathematical Statistics*, *26*, 112–116 (URL: http://www.jstor.org/stable/2236761).

Copland, L., Pope, S., Bishop, M. P., Shroder, J. F., Clendon, P., Bush, A., et al. (2009). Glacier velocities across the central Karakoram. *Annals of Glaciology*, *50*, 41–49 (URL: http://www.ingentaconnect.com/content/igsoc/agl/2009/00000050/00000052/ art00006).

Debella-Gilo, M., & Kääb, A. (2012). Locally adaptive template sizes for matching repeat images of earth surface mass movements. *ISPRS Journal of Photogrammetry and Remote Sensing*, *69*, 10–28 (URL: http://www.sciencedirect.com/science/article/pii/S092427161200038X).

Fallourd, R., Harant, O., Trouv, E., Nicolas, J. M., Gay, M., Walpersdorf, A., et al. (2011). Monitoring temperate glacier displacement by multi-temporal TerraSAR-x images and continuous GPS measurements. *IEEE Journal of Selected Topics in Applied Earth Observations and Remote Sensing*, *4*, 372–386. http://dx.doi.org/10.1109/JSTARS.2010.2096200.

Fitch, A. J., Kadyrov, A., Christmas, W. J., & Kittler, J. (2002). Orientation correlation. *Proceedings of the British Machine Conference* (pp. 11.1–11.10). BMVA Press. http://dx.doi.org/10.5244/C.16.11 (URL: http://citeseerx.ist.psu.edu/viewdoc/download?doi=10.1.1.19.7698 rep=re p1 type=pdf).

Gardner, A. S., Moholdt, G., Cogley, J. G., Wouters, B., Arendt, A. A., Wahr, J., et al. (2013). A reconciled estimate of glacier contributions to sea level rise: 2003 to 2009. *Science*, *340*, 852–857. http://dx.doi.org/10.1126/science.1234532.

Goldstein, R. M., Engelhardt, H., Kamb, B., & Frolich, R. M. (1993). Satellite radar interferometry for monitoring ice sheet motion: Application to an antarctic ice stream. *Science*, *262*, 1525–1530 (URL: http://www.sciencemag.org/content/262/5139/1525.short).

Gourmelen, N., Kim, S. W., Shepherd, A., Park, J. W., Sundal, A. V., Björnsson, H., et al. (2011). Ice velocity determined using conventional and multiple-aperture InSAR. *Earth and Planetary Science Letters*, *307*, 156–160 (URL: http://www.sciencedirect.com/science/article/pii/S0012821X11002421).

Heid, T., & Kääb, A. (2012a). Evaluation of existing image matching methods for deriving glacier surface displacements globally from optical satellite imagery. *Remote Sensing of Environment*, *118*, 339–355 (URL: http://www.sciencedirect.com/science/article/pii/S0034425711004214).

Heid, T., & Kääb, A. (2012b). Repeat optical satellite images reveal widespread and long term decrease in land-terminating glacier speeds. *The Cryosphere*, *6*, 467–478. http://dx.doi.org/10.5194/tc-6-467-2012 (URL: http://www.the-cryosphere.net/6/467/2012/).

Immerzeel, W. W., Beek, L. P. H. v., & Bierkens, M. F. P. (2010). Climate change will affect the Asian water towers. *Science*, *328*, 1382–1385. http://dx.doi.org/10.1126/science.1183188 (URL: http://www.sciencemag.org/content/328/5984/1382).

IPCC (2013). *Group I contribution to the IPCC Fifth Assessment Report (AR5), Climate Change 2013: The physical science basis.* Geneva, Switzerland: Intergovernmental Panel on Climate Change.

Kääb, A. (2002). Monitoring high-mountain terrain deformation from repeated air- and spaceborne optical data: Examples using digital aerial imagery and ASTER data. *ISPRS Journal of Photogrammetry and Remote Sensing*, *57*, 39–52 (URL: http://www.sciencedirect.com/science/article/pii/S0924271602001144).

Kääb, A. (2005). Combination of SRTM3 and repeat ASTER data for deriving alpine glacier flow velocities in the Bhutan Himalaya. *Remote Sensing of Environment*, *94*, 463–474. http://dx.doi.org/10.1016/j.rse.2004.11.003 (URL: http://linkinghub.elsevier.com/retrieve/pii/S0034425704003475).

Lanari, R., Casu, F., Manzo, M., Zeni, G., Berardino, P., Manunta, M., et al. (2007). An overview of the small baseline subset algorithm: A DInSAR technique for surface deformation analysis. *Pure and Applied Geophysics*, *164*, 637–661. http://dx.doi.org/10.1007/s00024-007-0192-9.

Lee, D., Storey, J., Choate, M., & Hayes, R. (2004). Four years of Landsat-7 on-orbit geometric calibration and performance. *IEEE Transactions on Geoscience and Remote Sensing*, *42*, 2786–2795. http://dx.doi.org/10.1109/TGRS.2004.836769.

Luckman, A., Quincey, D., & Bevan, S. (2007). The potential of satellite radar interferometry and feature tracking for monitoring flow rates of Himalayan glaciers. *Remote Sensing of Environment*, *111*, 172–181 (URL: http://www.sciencedirect.com/science/article/pii/S0034425707002842).

Necsoiu, M., Leprince, S., Hooper, D. M., Dinwiddie, C. L., McGinnis, R. N., & Walter, G. R. (2009). Monitoring migration rates of an active subarctic dune field using optical imagery. *Remote Sensing of Environment*, *113*, 2441–2447 (URL: http://www.sciencedirect.com/science/article/pii/S0034425709002168).

Paul, F., Bolch, T., Kääb, A., Nagler, T., Nuth, C., Scharrer, K., et al. (2013). The glaciers climate change initiative: Methods for creating glacier area, elevation change and velocity products. *Remote Sensing of Environment*. http://dx.doi.org/10.1016/j.rse.2013.07.043 (URL: http://www.sciencedirect.com/science/article/pii/S0034425713003532).

Pfeffer, W. T., Arendt, A. A., Bliss, A., Bolch, T., Cogley, J. G., Gardner, A. S., et al. (2014). The Randolph glacier inventory: A globally complete inventory of glaciers. *Journal of Glaciology*, *60*, 537 (URL: http://www.igsoc.org/journal/60/221/j13J176.pdf).

Quincey, D. J., Braun, M., Glasser, N. F., Bishop, M. P., Hewitt, K., & Luckman, A. (2011). Karakoram glacier surge dynamics. *Geophysical Research Letters*, *38*, L18504 (URL: http://www.agu.org/pubs/crossref/2011/2011GL049004.shtml).

Quincey, D. J., Copland, L., Mayer, C., Bishop, M., Luckman, A., & Belo, M. (2009a). Ice velocity and climate variations for Baltoro glacier, Pakistan. *Journal of Glaciology*, *55*, 1061–1071 (URL: http://www.ingentaconnect.com/content/igsoc/jog/2009/00000055/00000194/ art00011).

Quincey, D. J., Luckman, A., & Benn, D. (2009b). Quantification of Everest region glacier velocities between 1992 and 2002, using satellite radar interferometry and feature tracking. *Journal of Glaciology*, *55*, 596–606 (URL: http://www.ingentaconnect.com/content/igsoc/jog/2009/00000055/00000192/ art00002).

Rankl, M., Kienholz, C., & Braun, M. (2014). Glacier changes in the Karakorum region mapped by multimission satellite imagery. *The Cryosphere*, *8*, 977–989. http://dx.doi.org/10.5194/tc-8-977-2014 (URL: http://www.the-cryosphere.net/8/977/2014/).

Redpath, T. A. N., Sirguey, P., Fitzsimons, S. J., & Kääb, A. (2013). Accuracy assessment for mapping glacier flow velocity and detecting flow dynamics from ASTER satellite imagery: Tasman glacier, New Zealand. *Remote Sensing of Environment*, *133*, 90–101 (URL: http://www.sciencedirect.com/science/article/pii/S0034425713000485).

Rousseeuw, P. J., & Hubert, M. (2011). Robust statistics for outlier detection. *Wiley interdisciplinary reviews: Data mining and knowledge discovery*, *1*, 73–79. http://dx.doi.org/10.1002/widm.2 (URL: http://onlinelibrary.wiley.com/doi/10.1002/widm.2/abstract).

Scambos, T. A., Dutkiewicz, M. J., Wilson, J. C., & Bindschadler, R. A. (1992). Application of image cross-correlation to the measurement of glacier velocity using satellite image data. *Remote Sensing of Environment*, *42*, 177–186 (URL: http://www.sciencedirect.com/science/article/pii/003442579290101O).

Scherler, D., Bookhagen, B., & Strecker, M. R. (2011a). Hillslope-glacier coupling: The interplay of topography and glacial dynamics in high Asia. *Journal of Geophysical Research, Earth Surface*, *116*, F02019. http://dx.doi.org/10.1029/2010JF001751 (URL: http://onlinelibrary.wiley.com/doi/10.1029/2010JF001751/abstract).

Scherler, D., Bookhagen, B., & Strecker, M. R. (2011b). Spatially variable response of Himalayan glaciers to climate change affected by debris cover. *Nature Geoscience*, *4*, 156–159. http://dx.doi.org/10.1038/ngeo1068.

Scherler, D., Leprince, S., & Strecker, M. R. (2008). Glacier-surface velocities in alpine terrain from optical satellite imagery—accuracy improvement and quality assessment. *Remote Sensing of Environment*, *112*, 3806–3819. http://dx.doi.org/10.1016/j.rse.2008.05.018 (URL: http://linkinghub.elsevier.com/retrieve/pii/S0034425708001934).

Storey, J., & Choate, M. (2004). Landsat-5 bumper-mode geometric correction. *IEEE Transactions on Geoscience and Remote Sensing*, *42*, 2695–2703. http://dx.doi.org/10.1109/TGRS.2004.836390.

Strozzi, T., Luckman, A., Murray, T., Wegmuller, U., & Werner, C. L. (2002). Glacier motion estimation using SAR offset-tracking procedures. *IEEE Transactions on Geoscience and Remote Sensing*, *40*, 2384–2391 (URL: http://ieeexplore.ieee.org/xpls/abs_all.jsp?arnumber=1166597).

Tucker, C. J., Grant, D. M., & Dykstra, J. D. (2004). NASA's global orthorectified Landsat data set. *Photogrammetric Engineering and Remote Sensing*, *70*, 313–322 (URL: http://lpais.fii.gob.ve/files/orto_lansat_nasa.pdf).

Willis, M. J., Melkonian, A. K., Pritchard, M. E., & Ramage, J. M. (2012). Ice loss rates at the northern patagonian icefield derived using a decade of satellite remote sensing. *Remote Sensing of Environment*, *117*, 184–198 (URL: http://www.sciencedirect.com/science/article/pii/S0034425711003440).